The Marine Carbon Cycle of the Scotia Sea, Southern Ocean

Elizabeth Jones

Thesis submitted in fulfilment of the requirements

for the degree of Doctor of Philosophy

University of East Anglia

School of Environmental Sciences

2010

Abstract

From 2006 to 2009, over 2,500 measurements of the sea surface fugacity of CO_2 (fCO_2) in the Scotia Sea were collected from a new Centre for observation of Air Sea Interactions and fluXes (CASIX) underway fCO_2 instrument onboard RRS *James Clark Ross*. This novel fCO_2 timeseries contributes to alleviating the paucity of fCO_2 data in the Southern Ocean. A key component of this work was a 1,400 km repeat transect, occupied in austral spring 2006, summer 2008 and autumn 2009. An at-sea intercomparison was conducted to determine the accuracy and suitability of the CASIX instrument for oceanic fCO_2 measurements and contributions to global databases. The first deep carbonate measurements of the Scotia Sea were made in summer 2008. A distinct Winter Water layer was observed and used to provide sea surface carbonate parameters for the preceding winter (2007), completing the seasonal dataset. Upper Circumpolar Deep Water represented a voluminous reservoir of dissolved inorganic carbon (DIC) and nitrate in the Antarctic Circumpolar Current (ACC), outcropping at the Southern ACC Front and the Southern Boundary. As a result, low pH and carbonate ion concentrations in sub-surface waters forced a large seasonal amplitude in aragonite saturation, which may hasten the onset of ocean acidification in the Scotia Sea.

A strong relationship existed between sea ice, ice edge phytoplankton blooms and fCO_2. Moderate sea ice advance and early retreat set up conditions most favourable for bloom development and biological carbon uptake. Residual seasonal deficits in DIC during the summer thaw indicated that calcium carbonate precipitation had taken place in the sea ice brines. Combined with biological carbon uptake, this 'sea ice carbon pump' created substantial fCO_2 undersaturation in the meltwaters. An 'island mass effect' and extensive diatom blooms downstream of South Georgia created a strong summertime sink for atmospheric CO_2 of 15.1 ± 5.7 mmol m^{-2} d^{-1}. Substantial seasonal depletion in DIC promoted the uptake of 1.3 ± 0.5 Tg C from the atmosphere during summer 2008, which was the strongest region of biological carbon uptake to date in ice-free waters of the Southern Ocean. On an annual basis, the Scotia Sea from 62.6° to 49.5°S represented a large sink for atmospheric CO_2 of 6.2 ± 2.1 mmol m^{-2} d^{-1}. The data presented here firmly establish the Scotia Sea as a 'mosaic' of archetypal Southern Ocean environments. The region can be considered as a natural mesocosm in order to infer future distributions of air-sea CO_2 fluxes, pH and aragonite undersaturation for the contemporary and future Southern Ocean.

Contents

Figures

Tables

Acknowledgements

"... mackerel skies and mares tails means tall ships go to short sails ..."

I would like to express a sincere thank you to Dorothee Bakker for making my three and half year voyage full of mackerel skies. I am extremely grateful for your guidance, inspiration and devotion and for allowing me to set my compass in any direction. Thank you to Andy Watson for encouraging me to think beyond the horizon. You both gave me the opportunity to be part of a dynamic research community and to work in such an inspirational place.

Nick Hardman-Mountford and Ute Schuster spent much time navigating me through the world of CO_2 measurements, to which I am exceedingly grateful. Thank you to Hugh Venables who committed time and expertise on many levels and helped to improve this work right to the end. A huge thank you to Angus Atkinson and Sophie Fielding for welcoming me into unchartered waters of life at sea with the British Antarctic Survey. I am also very grateful to the people who supported this research: Simon Wright, Doug Trevett, Mark Preston and Jim Fox for assisting in the maintenance of the underway pCO_2 instruments; Gareth Lee for his technical expertise in seawater analysis; Mick Whitehouse, Beki Korb and Maria Nielsdóttir for memorable experiences at sea and their complimentary datasets.

I would also like to thank all of the people who have prevented me from ending up in the doldrums: Marie Racault for being an amazing friend, running partner and companion when working late; Amandine Caruana for bringing Mediterranean sunshine into the office, whatever the weather; Alba Gonzales-Posada, Karel Castro-Morales and Sophie Chollet for always making me smile, both at sea and on dry land; James Clark, Dave Sproson, Jenny Graham, Matt Jones, Greg Colbourn and Lee Gumm for countless crazy days and crazy nights; the brunettes of '464', Chloé Kessi and Kim Findlay-Cooper, your smiles and hugs made life plain sailing; Mark Stinchcombe for making me laugh anytime, anywhere and Rosa Blanch for helping me to fly high and dive deep for many 'flamingo and nitrogen' filled years.

I would like to acknowledge my parents for instilling in me a desire to explore and understand the world around me and my brother for being the best companion on these journeys. And finally to my sailor, for your endless support, even when you were 9,000 miles away, and for always believing in me. Thank you for opening my eyes to the South and for showing me warmth in the coldest place on Earth.

1. Introduction

1.1. Context

Human (anthropogenic) activity is rapidly changing the concentration of certain gases in the atmosphere, such as carbon dioxide (CO_2), chlorofluorocarbons, methane and nitrous oxide. Prior to the Industrial Revolution in the 18th century, atmospheric concentrations of CO_2 fluctuated naturally between 180 ppm (parts per million or μmol mol^{-1}) during glacial periods and 300 ppm during interglacial periods, for at least the last 650,000 years (Siegenthaler et al., 2005). However, since this time there has been significant anthropogenic perturbation to this natural cycle. Combustion of fossil fuels, cement manufacturing and changes in land use have led to an unprecedented increase in the concentration of atmospheric CO_2 to about 388 ppm today (Dr. Pieter Tans, NOAA/ESRL (www.cmdl.noaa.gov/gmd/ccgg/trends)). Of the 340-420 Pg C (Pg = 10^{15} g) emitted to the atmosphere during this period it is estimated that only 45% has remained in the atmosphere (IPCC, 2007). The remainder has been removed by the oceanic biosphere, through the physical and biological carbon pumps (section 1.5.4) and the terrestrial biosphere, therefore mitigating the atmospheric increase and associated global warming.

A leading motivation to understand the marine carbon cycle is the importance of the oceans as a dynamic reservoir that regulates the concentration of CO_2 in the atmosphere. Oceanic uptake of CO_2 acts as a buffer to the increasing atmospheric CO_2 concentrations as most of the CO_2 that diffuses into the oceans reacts with the seawater to form a series of inorganic carbon species (section 1.5.2). Global ocean carbon observations indicated that since the industrialisation of 1800 the oceans have absorbed 48% of the anthropogenic CO_2 emissions (Sabine et al., 2004). Recently, studies have indicated a reduction in oceanic CO_2 uptake (Sabine et al., 2004; Canadell et al., 2007; Le Quéré et al., 2007), however contradicting results highlight the difficulty in forecasting future changes to the climatically dynamic carbon cycle (Zickfeld et al., 2007; Law et al., 2008; Zickfeld et al., 2008).

Although the oceanic uptake of CO_2 will dampen the extent of global warming, the effect of increased CO_2 on ocean chemistry is leading to ocean acidification (Caldeira and Wickett, 2003; Feely et al., 2004; Orr et al., 2005). The evolution of the oceanic carbon sink and how it

will evolve in the future are important issues concerning climate change and ocean acidification.

In the early 1980s it was established that the Southern Ocean had a larger influence on atmospheric CO_2 concentrations compared to other ocean basins (Sarmiento and Toggweiler, 1984; Siegenthaler and Wenk, 1984). This is a consequence of the distinct interleaving between the surface and the deep ocean at high latitudes, through water mass ventilation and formation, imprinting the biogeochemical traits of high latitude surface waters on the deep ocean (Sarmiento and Gruber, 2006). The unique circulation of the Antarctic Circumpolar Current (ACC) is a pivotal component of this surface-to-deep ocean framework, exchanging heat, momentum and carbon between the atmosphere and the deep ocean and forming a link between the major ocean basins. Sea ice dynamics drive the overturning circulation through deep and bottom water formation (Sarmiento et al., 1998) and mixing and upwelling, over complex seafloor topography, enhances ventilation of water masses in the ACC (Naveira Garabato et al., 2007). Accompanied by low temperatures and wind-driven deep mixing, these processes facilitate the physical uptake (section 1.5.4.2) and removal of atmospheric CO_2 to the deep sea, which is the dominant mechanism for uptake of anthropogenic CO_2 (Watson and Orr, 2003).

Observing the long-term trends of oceanic CO_2 is crucial to monitor the evolution of the global oceanic carbon sink. Repeat sections and time series stations have proven to be essential components to this research issue, e.g., three of the Joint Global Ocean Flux Study (JGOFS) time-series stations (BATS (Bates et al., 1996), HOT (Feely et al., 2002; Feely et al., 2006) and KERFIX (Jeandel et al., 1998)) and voluntary observing ship routes (Schuster and Watson, 2007). Several different methods (ocean observations, ocean models and atmospheric inversions) have estimated the global oceanic carbon uptake as around 2 Pg C yr^{-1} (Le Quéré and Metzl, 2003; Takahashi et al., 2009).

To date, numerous investigations have generated extensive databases of air and sea surface partial pressure of CO_2 (pCO_2) measurements over the global ocean (IOCCP, 2007; Takahashi et al., 2009). Using an interpolation method, the computed climatological distribution of the air-sea pCO_2 difference (ΔpCO_2) showed that the Southern Ocean (62-50°S) acted as a sink of 0.06 Pg C yr^{-1} for the reference year 2000 (Takahashi et al., 2009). This is an order of magnitude less than the 0.60 Pg C yr^{-1} predicted for the reference year 1995 (Takahashi et al., 2002). This decrease from 24% to 4% of the global CO_2 sink is dominated by increased data

coverage in the sea ice region, where summer biological carbon uptake is heavily counteracted by winter CO_2 release through deep water upwelling (Takahashi et al., 2009). This highlights the complexities of the Southern Ocean, in terms of constraining the CO_2 sink with comparatively sparse observations compared to other ocean basins, e.g., North Atlantic (Schuster and Watson, 2007) and the North Pacific (Midorikawa et al., 2005), and the influence of sea ice, upwelling and biological processes.

It is firmly established that the Southern Ocean hosts the formation and mixing of the densest waters of the oceanic overturning circulation, which is linked to the climatically vulnerable deep ocean ventilation and CO_2 uptake (Watson and Orr, 2003; Naveira Garabato et al., 2007; Meredith at al., 2008). An improved understanding of the contemporary marine carbon cycle of the Southern Ocean is critical to better constrain the uptake of anthropogenic CO_2 (Takahashi et al., 2009), and transport of carbon to the deep ocean, and to better predict the effects of future CO_2 emissions on marine organisms (Royal Society, 2005).

From low productivity waters of the ACC flowing in from Drake Passage to areas of high productivity associated with sea ice retreat (Korb et al., 2005; Smith and Comiso, 2008), hydrographic fronts (Comiso et al., 1993; Tynan et al., 1998; Strass et al., 2002; Ward et al., 2002; Holm-Hansen et al., 2004b; Shim et al., 2006) and submarine arcs and islands (Moore and Abbot, 2000; Strass et al., 2002; Holm-Hansen et al., 2004b; Korb and Whitehouse, 2004; Korb et al., 2004; Korb et al., 2008; Dulaiova et al., 2009; Ardelan et al;., 2010), the Scotia Sea is a mosaic of archetypal Southern Ocean environments. The region is important for the mixing of deep water masses of the ACC with recently ventilated waters from the Weddell Sea (Hoppema et al. 1995; Hoppema et al., 1998; Stoll et al., 1999; Naveira Garabato et al., 2007) that become incorporated into the global ocean overturning circulation (Carmack and Foster, 1975; Naveira Garabato et al., 2002a). Carbon-rich deep waters upwell within the ACC and are transported south- and northwards before sinking close to the Antarctic continent, as dense bottom waters, or north of the Polar Front, as intermediate waters (Speer et al., 2000).

The region around South Georgia is one of the most biologically active in the Southern Ocean, as the enhanced phytoplankton biomass supports a rich and valuable fisheries (Atkinson et al., 2001). Frequented by the UK research fleet, the Scotia Sea is an ideal ‘mesocosm’ to investigate the myriad of processes that affect the contemporary marine carbon cycle of the Southern Ocean, in the context of dynamic physical regimes and valuable biological

environments. Previous international research efforts, e.g., Geochemical Ocean Section Study (GEOSECS), JGOFS and the World Ocean Circulation Experiment (WOCE) have improved the understanding of the processes that influence the uptake of atmospheric CO_2 in the ocean (Craig, 1972; Craig, 1974; Wallace, 2001). Following on from these, two UK research endeavours are the CARBON-OPS project: www.bodc.ac.uk/carbon-ops/ and the British Antarctic Survey (BAS) Discovery-2010 programme: http://www.antarctica.ac.uk/bas_research/our_research/previous_research/gsac/discovery_2020.php.

The operational UK air-sea carbon flux observation capability, CARBON-OPS, mission was to collect surface water pCO_2 measurements in waters frequented by ships of the UK research fleet (Hardman-Mountford et al., 2008). Integral to this was the development of autonomous pCO_2 instruments, commissioned by the Centre for observation of Air-Sea Interactions and fluXes (CASIX), Plymouth Marine Laboratory and Dartcom (section 2.5.4). The objective of the Discovery-2010 programme was to understand the seasonal structure and function of different food webs, in contrasting regions of productivity, and to infer the effects on the transfer of CO_2 from the atmosphere to the deep ocean. This was to be realised through high frequency surface sampling and deep hydrographic stations along a 1,400 km transect across the Scotia Sea (section 2.3). The transect was occupied in austral spring (November-December) 2006, summer (January-February) 2008 and autumn (March-April) 2009. Winter (September) 2007 conditions were inferred from parameters measured within the Winter Water during summer (2008). The transect traversed through numerous archetypal Southern Ocean environments: sea ice, meltwaters, hydrographic fronts, high-nutrient low-chlorophyll (HNLC) waters, open ocean regimes of the ACC and intense phytoplankton blooms.

In October 2006, a new CASIX underway pCO_2 system was installed on the BAS research vessel RRS *James Clark Ross*, integrating carbon measurements into the Discovery-2010 programme (Fig. 2.2). Since then, sea surface pCO_2 has been measured on 20 cruises in the Scotia Sea region from 2006-2009 (Table 2.1), establishing a new seasonal timeseries. The first deep carbonate measurements of the Scotia Sea were made during the second occupation of the transect. The combination of sea surface pCO_2 data and deep carbonate vertical profiles presented a unique opportunity to investigate the marine carbon cycle of the Scotia Sea from a seasonal and inter-annual perspective.

1.2. The Southern Ocean

1.2.1. Antarctic Circumpolar Current

The Southern Ocean is characterised by a unique circulation dominated by the Antarctic Circumpolar Current (ACC). The ACC flows continuously around the Antarctic continent for about 25,000 km with a volume flow in the order of 130-140 Sv through Drake Passage (1 Sv = 10^6 m^3 s^{-1}) (Rintoul et al., 2001). This unbounded flow allows the transfer of heat, dissolved constituents and plankton around Antarctica and between the three major ocean basins (Nowlin and Klinck, 1986). The eastward flow of the ACC is dynamically linked to the global overturning circulation, through the movement of the major water masses in the ACC (Fig. 1.1).

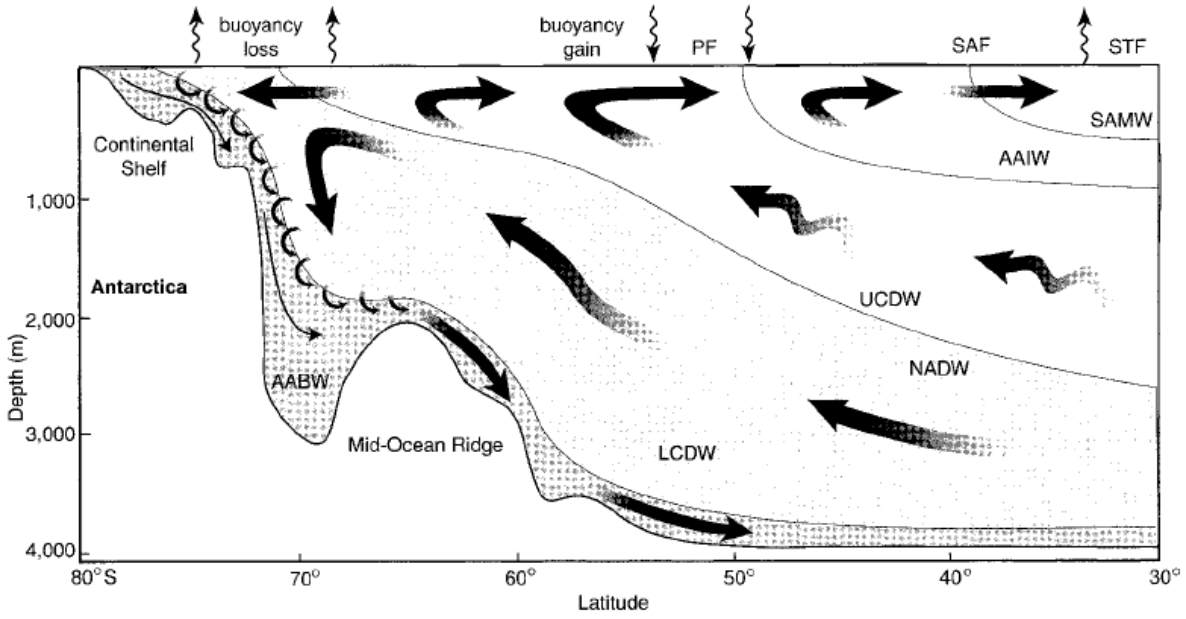

Figure. 1.1. Meridional overturning circulation in the Southern Ocean (Speer et al., 2000). Key water masses are identified: Sub-Antarctic Mode Water (SAMW), Antarctic Intermediate Water (AAIW), Upper Circumpolar Deep Water (UCDW), North Atlantic Deep Water (NADW), Lower Circumpolar Deep Water (LCDW) and Antarctic Bottom Water (AABW).

1.2.2. Water masses

Global ocean circulation is governed by the vertical and horizontal movement of large water masses. Individual water masses can be identified and traced throughout the global ocean by distinct characteristics, such as temperature and salinity, retained from surface conditions

present at the source at the time of formation. Upper water masses are usually composed of water from the mixed layer and water above the permanent thermocline. Antarctic Surface Water (AASW) has a surface temperature < 5 °C and a sub-surface potential temperature minimum (θ_{min}) of about 2 °C as a result of the winter mixed layer not being thermally eroded during the summer. The dominant water mass in the Southern Ocean is Circumpolar Deep Water (CDW) that occupies mid-levels of the ACC. CDW is formed from North Atlantic Deep Water (NADW), a dense water mass produced close to the northern limits of the Atlantic that flows along the ocean basin into the Southern Ocean. CDW can be distinguished into two main types; Upper Circumpolar Deep Water (UCDW), corresponding to a potential temperature maximum (θ_{max}) and an oxygen minimum, and Lower Circumpolar Deep Water (LCDW), corresponding to a salinity maximum. Many of the sloping isopycnals associated with the strong flow of the ACC reach shallower depths in the south (about 60°S) and provide a mechanism for UCDW and LCDW to reach the surface (Rintoul et al., 2001). This provides a pathway for the nutrient-rich deep water to enter the euphotic zone (section 1.4.1).

The poleward transport and shoaling of CDW is an important component of the overturning circulation in the Southern Ocean (Fig. 1.1). As UCDW upwells it is entrained into the AASW through vertical mixing. These surface waters are transported north and east in the wind-driven Ekman layer until it sinks again as Antarctic Intermediate Water (AAIW) north of the Polar Front (Speer et al., 2000). Upwelled LCDW continues to flow south towards the Antarctic continent where the water properties become influenced by ocean-atmosphere-ice processes. Here the dense Antarctic Bottom Water (AABW) is formed, as the water sinks out of the upper ocean due to increased density from sea ice formation and wind-driven cooling (Gill, 1973; Carmack and Foster, 1975; Weiss et al., 1979). AABW is the most widespread of all water masses as it has been found in all three major ocean basins. These water mass interactions set up a north-south circulation pattern that consists of two opposing, rotating cells: deep water is imported into the Southern Ocean from the north and intermediate and bottom water is exported out of the Southern Ocean (Speer et al., 2000). A detailed discussion of the hydrographic and biogeochemical traits of some of the principle water masses is presented in Chapter 4.

1.2.3. Fronts

The transport of the ACC is not uniform over the latitudes but is concentrated into several circumpolar jets or fronts, which are seen as increased gradients in the sloping isopycnal surfaces. The fronts are often defined by near surface criteria such as temperature, salinity, oxygen and concentrations of nutrients. The surface expression may not always be above the sub-surface current, which is the important part of the front in terms of transport and delimiting biogeochemical zones.

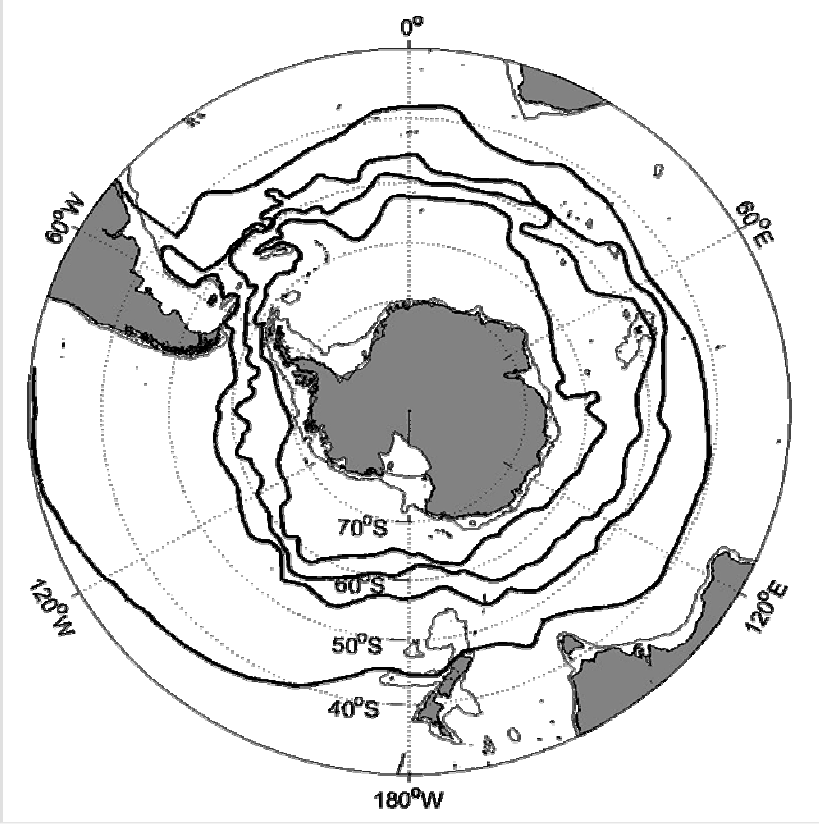

Figure. 1.2. The Southern Ocean and average circumpolar extent of the hydrographic fronts, from north to south, the sub-Antarctic Front, the Polar Front, the Southern Antarctic Circumpolar Front and the Southern Boundary adapted from Orsi et al. (1999). The boundaries of the Antarctic Circumpolar Current are the Polar Front and the Southern Boundary.

There are many different definitions of the ACC fronts based on different water mass characteristics and the spatial and temporal variability in the surface expressions due to the meandering nature of the fronts. Early hydrographic sections identified a band of converging

water in the Southern Ocean, which was called the Antarctic Convergence (Deacon, 1982). Based on Ekman drifts in the upper ocean and wind speed data, a second feature was identified to the south of the wind stress maximum, called the Antarctic Divergence (Deacon, 1982; Rintoul et al., 2001). More recently, the convergence was classified as the Polar Front, forming a band of converging water called the Polar Frontal Zone (PFZ), separating sub-Antarctic waters to the north from Antarctic waters to the south (Whitworth and Nowlin, 1987). The PF is a circumpolar jet with velocities in the order of 0.5-1.0 m s^{-1} (Belkin and Gordon, 1996). It is identified by the northern terminus of a 2 °C temperature minimum layer at 100-300 m depth.

Further south, the southern ACC front (SACCF) is identified by the limit of a θ_{max} > 1.8 °C deeper than 500 m and salinity greater than 34.73 along a salinity maximum deeper than 800 m (Orsi et al., 1995). A third front is the Southern Boundary of the ACC (SB), replacing the older term of the Antarctic Divergence (Orsi et al., 1995). The oceanic region from the PF to the SB is the Antarctic Zone (AAZ) (Pollard et al., 2002). In the Atlantic sector, the SB lies just north of the Weddell-Scotia Confluence (WSC), and band of weakly stratified, relatively homogenous water that extends from the tip of the Antarctic Peninsula to about 30°E (Patterson and Sievers, 1980; Whitworth et al., 1994) and separates the eastward-flowing ACC to the north and the Weddell Gyre to the south (Orsi et al., 1995).

This SB is characterised by the southern terminus of UCDW. Closest to Antarctica is the narrow, wind-driven Antarctic Coastal Current that flows westwards around the continent. These definitions provide a guide for the identification of the Southern Ocean fronts, however as the fronts meander, fragment and coalesce the characteristics are likely to exhibit longitudinal and temporal variations (Sokolov and Rintoul, 2007). The vertical hydrographic and biogeochemical characteristics of the principle fronts is presented in Chapter 4.

1.2.4. Geographical zonation

1.2.4.1. Southern Ocean sectors

The Southern Ocean (defined here as the area south of the Polar Front) can be divided into several geographic sectors defined by longitude (Arrigo et al., 1998); the Atlantic Ocean sector (60°W-20°E), the Indian Ocean sector (20-90°E) and the Pacific Ocean sector (90-

160°E). In the Atlantic sector, two smaller oceanic regions are the Scotia Sea (60-50°S 60-24°W) and the Weddell Sea (65-60°S 60°W-30°E). Regions of the open ocean in all sectors can be defined on the basis of sea ice coverage (Arrigo et al., 1998). The marginal ice zone (MIZ) refers to the region between the ice edge and the ice free open ocean (Chapter 5). The seasonal ice zone (SIZ) is the region bound by the latitudinal limits of maximum and minimum sea ice extent (Chapter 7).

1.2.4.2. The Scotia Sea

The Scotia Sea is a relatively small ocean basin in the Atlantic sector of the Southern Ocean (Fig. 1.3).

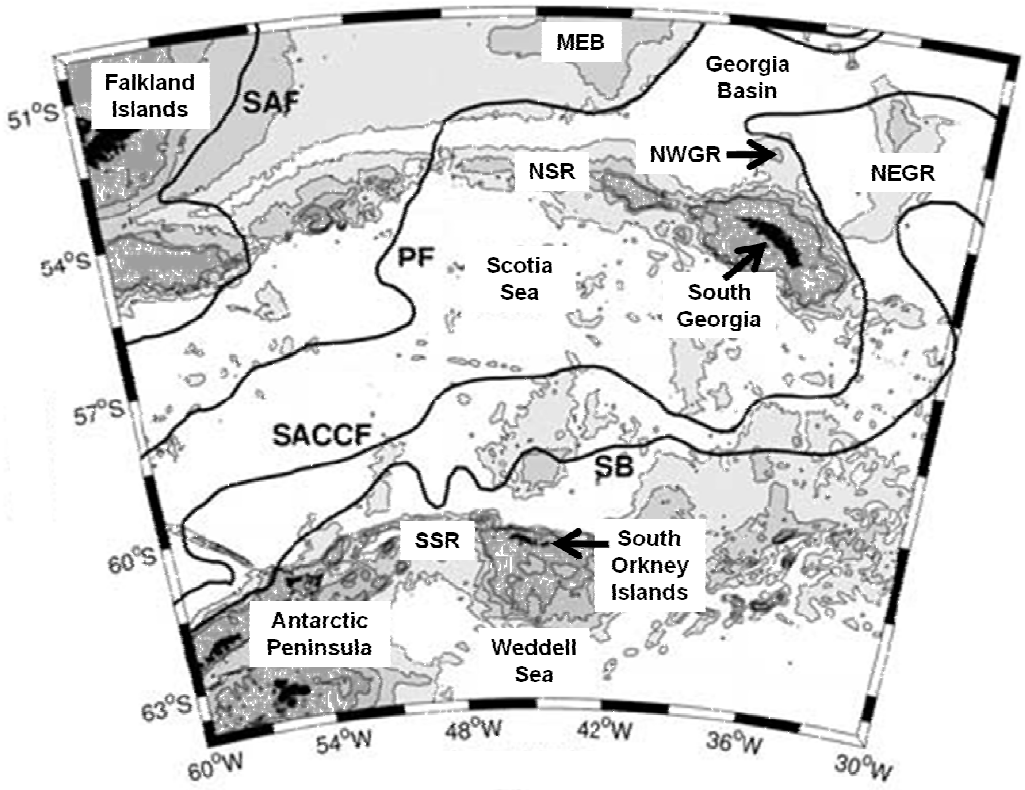

Figure. 1.3. The Scotia Sea showing the average locations of the hydrographic fronts, from north to south: the sub-Antarctic Front (SAF), the Polar Front (PF), the Southern ACC Front (SACCF) and the Southern Boundary (SB) adapted from Meredith et al. (2003a). Some important topographic features are identified: Maurice Ewing Bank (MEB), the North East Georgia Rise (NEGR), the North West Georgia Rise (NWGR), North Scotia Ridge (NSR) and the South Scotia Ridge (SSR). The 1000, 2000 and 3000 m isobaths are marked.

The northern, southern and eastern extents of the basin are bound by rugged bathymetry, which has been implicated in the biological and physical characteristics of this region. Running from the north to the south east of the basin is the Scotia Ridge, a submarine arc extending from Tierra del Fuego, at the southern tip of South America, to the Antarctic Peninsula with land mass protrusions at South Georgia, on the North Scotia Ridge (NSR), and the South Orkney Islands on the South Scotia Ridge (SSR).

To the west, the Scotia Sea is open to Drake Passage where the ACC fronts are at their narrowest meridional extension that spread out upon the westerly passage across the basin. The flow of the PF and SACCF is strongly constrained by the bathymetry of the NSR (Thorpe et al., 2002; Meredith et al., 2003a; Meredith et al., 2003b; Smith et al., 2010) (Fig. 1.7), further discussed in Chapter 6.

1.2.4.3. The Weddell Sea

The Weddell Sea, south of the WSC in the Atlantic sector, is dominated by a cyclonic gyre, bound to the west and south by the Antarctic continent but open to the north and east for interaction with waters of the ACC (Fig. 1.3). The action of the prevailing winds and the resulting gyre leads to diverging flow and significant upwelling. The Weddell Sea is an important region for ventilation of deep waters and is generally regarded as the principal source of AABW (Gill, 1973; Carmack and Foster, 1975). CDW from the ACC is advected into the gyre to the east and is locally referred to as Warm Deep Water (WDW), which can be distinguished by maxima in temperature, salinity, nutrients and dissolved inorganic carbon (Deacon, 1979; Whitworth and Nowlin, 1987; Gouretski and Danilov, 1993; Hoppema et al., 1997; Schröder and Fahrbach, 1999). The geochemical properties of the deep and bottom waters can be used as tracers to investigate carbon uptake through the MOC in the Southern Ocean (Weiss et al., 1979; Hoppema et al., 1998; Naveira Garabato et al., 2002a).

Deep and bottom water formation occurs over the Antarctic continental shelf, which leads to large modifications to the CDW injected into the gyre through ocean-ice-atmosphere interactions (Schröder and Fahrbach, 1999). The newly ventilated deep and bottom waters overspill the South Scotia Ridge and flow through the WSC into the Scotia Sea to become incorporated into the deep current of the South Atlantic (Locarnini et al., 1993; Orsi et al., 1999; Naveira Garabato et al., 2002a; Meredith et al., 2008). These processes transport carbon

into the deep ocean and signify the role of the Weddell Sea in the ventilation of the global ocean.

1.3. Mixed layer processes

The mixed layer, or mixing layer, refers to waters of the upper ocean with relatively low vertical density gradients (Brainerd and Gregg, 1995). The homogeneity of the mixed layer is due to turbulence within the upper water column as a result of wind stress and heat loss at the sea surface (Donlon and Robinson, 1997). The depth of the mixed layer is influential for a range of factors, including sea surface temperature, gas exchange, nutrient supply and light availability. Beneath the mixed layer the temperature decreases rapidly with depth to form a permanent thermocline. During the winter reduced sea surface temperatures and rough sea states cause a deepening of the mixed layer, even down to the permanent thermocline. With the onset of spring, increasing sea surface temperatures and calmer conditions allow the water column to become stratified forming a shallow surface layer and capping off the remnant of the winter mixed layer beneath. These processes lead to the characteristic potential temperature profiles of the AASW, with the distinct θ_{min} of the Winter Water beneath the summer mixed layer (Fig. 4.2).

Deepening of the mixed layer occurs when turbulence erodes the stratification that was initially present at the base of the mixed layer. Mixing processes tend towards a more homogenous water column and can be distinguished by the different magnitudes of the processes, from slow molecular diffusion to rapid turbulent mixing. Turbulent mixing acts on the bulk water at a faster rate compared to molecular diffusion, and is the dominant mixing process in the oceans. Turbulence is associated with several factors ranging from waves, wind-driven surface currents (Chen et al., 1994) and the influence of undulating bathymetry to density-driven convection currents (Donlon and Robinson, 1997) and eddies. The strength of the turbulence and degree of stratification will affect the extent to which the mixed layer is eroded and deepened.

In high latitude oceans two principal processes increase the density of surface waters: the rejection of saline brines during sea ice formation and cooling from cold winds blowing over the sea surface (Foster, 1972). As the density of surface water is increased the system becomes gravitationally unstable and the water sinks out of the upper layers, transporting dissolved constituents into the underlying water column (Rysgaard et al., 2007).

1.4. Marine productivity

1.4.1. Elements of life

All oceanic organisms are composed of the major elements carbon (C), hydrogen (H), nitrogen (N), oxygen (O) and phosphorous (P), and silicon (Si) in some species (Falkowski et al., 2003). The free-floating phytoplankton are the dominant primary producers in the ocean that utilise light to synthesise organic compounds from CO_2 during photosynthesis. Solar energy drives photosynthesis using the dominant photosynthetic pigment chlorophyll-a. Respiration is the reverse process where organic compounds are metabolised to release energy, forming CO_2 as a by-product. Photosynthesis can only be carried out during periods of daylight whereas respiration continues both day and night.

Phytoplankton have certain minimum requirements of these elements (nutrients) in order to form organic matter. Nitrogen is usually sourced from dissolved nitrate (NO_3^-), nitrite (NO_2^-), or ammonia (NH_3); phosphorous is sourced from either dissolved organic phosphorous or from one of the inorganic species, such as orthophosphate (PO_4^{3-}). Certain phytoplankton groups such as diatoms require silicon, which is obtained from a variety of dissolved silicate compounds, such as silicic acid ($Si(OH)_4$). Micronutrient (trace element) requirements include iron (Fe), manganese (Mn), cobalt (Co) and copper (Cu), which are essential to life processes but exist in seawater in trace quantities. Iron is an essential element for phytoplankton in the electron transfer reactions of the photosynthetic pathways (Strzepek and Harrison, 2004) and the action of nitrate reductase enzymes (Lalli and Parsons, 1997). The concentrations of all of these elements in seawater depend on the rate of photosynthesis, respiration, decomposition, advection, upwelling and atmospheric deposition.

Sea surface concentrations of nitrate (Fig. 1.4) and phosphate in the Southern Ocean are higher compared to surface waters of the rest of the global ocean. There is a similar pattern for the distribution of silicate (Fig. 1.5). This can be accounted for by consideration of the meridional overturning circulation patterns (section 1.2.2). The structure of fronts and upwelling of CDW and deep vertical mixing in the ACC brings high nutrient concentrations to the surface waters, southwards of 60°S. As the Ekman transport moves these waters northwards, nitrate and silicate are utilised by organisms in the upper ocean, setting up northward gradients of these nutrients in the AASW.

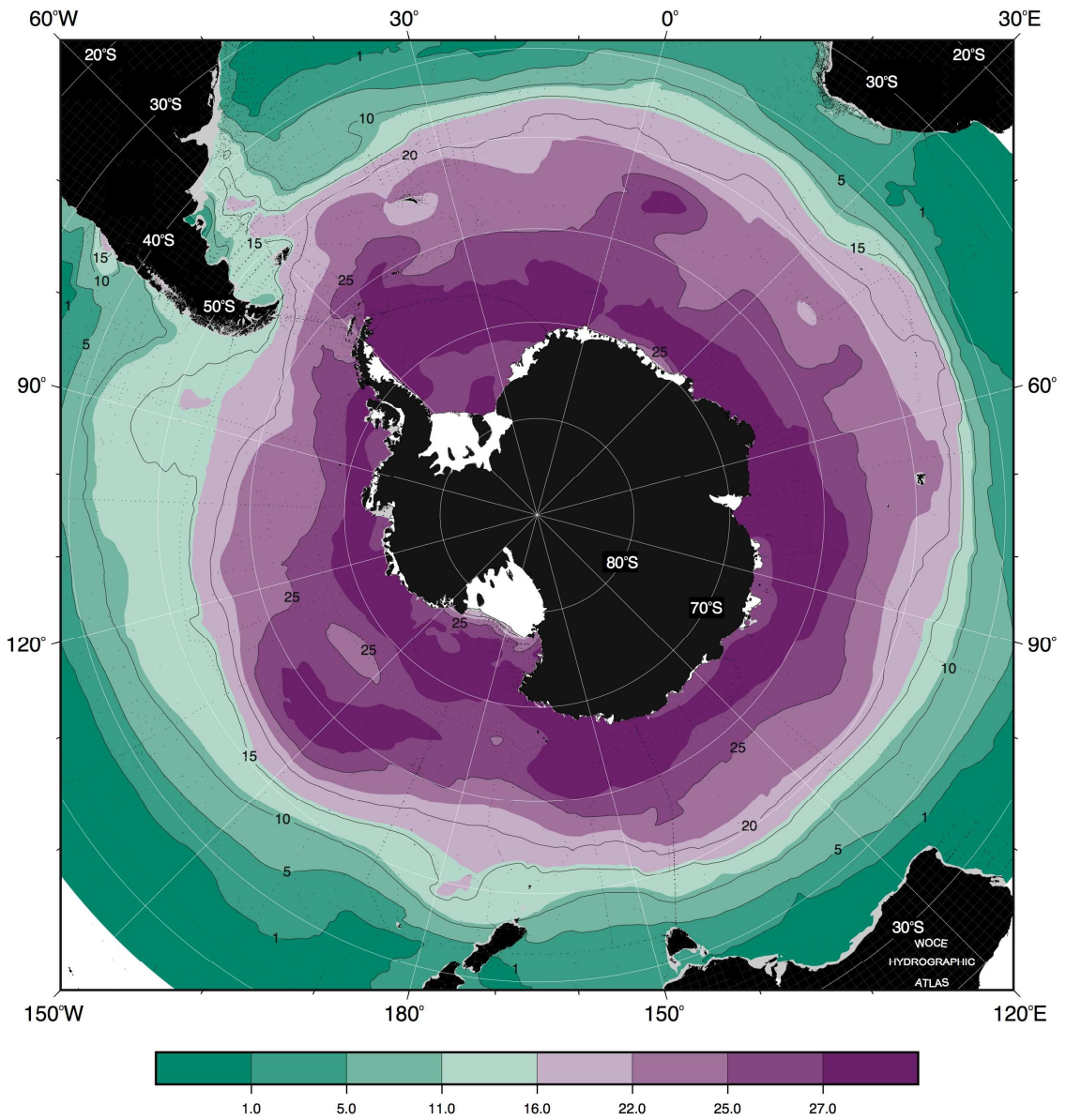

Figure. 1.4. Map of the annual mean nitrate (μmol kg^{-1}) concentration in the upper water column (50 m) of the Southern Ocean based on the WOCE Southern Ocean Atlas 1998 (Conkright et al., 2002). The distribution of phosphate is predominantly the same as for nitrate, but at $1/16^{th}$ of the concentration based on the Redfield ratio (Redfield, 1963), so is not presented.

The vertical distributions of nitrate, phosphate and silicate across the ACC are presented and discussed in Chapter 4.

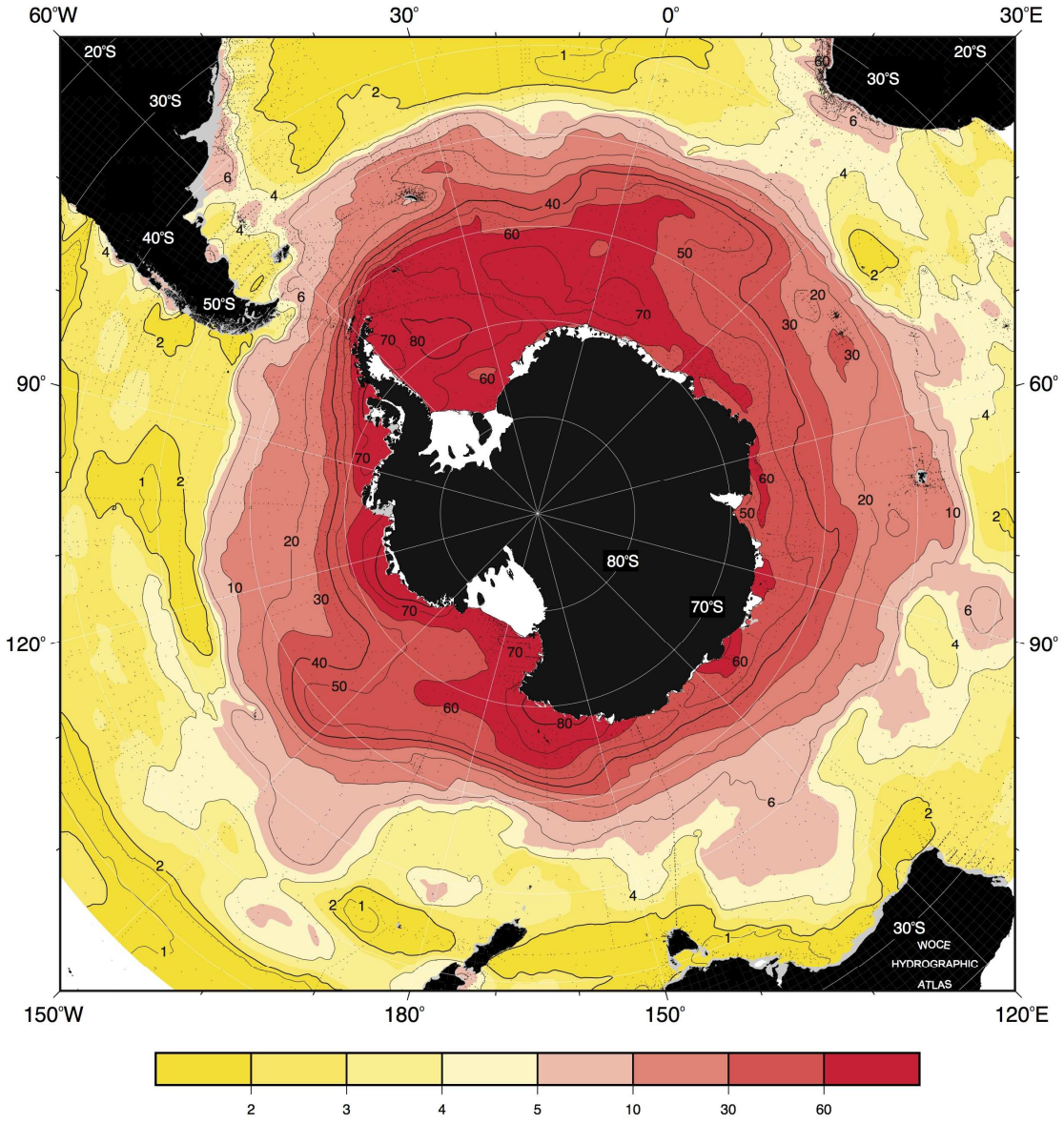

Figure. 1.5. Map of the annual mean silicate (μmol kg^{-1}) concentration in the upper water column (50 m) of the Southern Ocean based on the WOCE Southern Ocean Atlas 1998 (Conkright, 2002).

1.4.2. Phytoplankton productivity and distribution

Primary production is the net biological carbon uptake by phytoplankton, determined from the gross primary production (photosynthesis) corrected for respiration. Rates of primary production are useful tools in predicting the biogenic flux of organic carbon into the deep ocean. Regions of low primary production are efficient in recycling organic matter and therefore contribute to a low carbon export out of the upper ocean (Sarmiento and Gruber,

2006). Current estimates of annual primary production in the Southern Ocean have varied widely from close to zero to 170 g C m^{-2}, in open ocean and coastal regions, respectively (Wefer and Fischer, 1991; Arrigo et al., 1998; Priddle et al., 1998).

1.4.3. Limits to growth

1.4.3.1. High-nutrient low-chlorophyll (HNLC) conditions

Oceanic regions where essential nutrients are present in high concentrations, usually have associated high productivity, and are termed eutrophic. Waters that have low concentrations of one or more of the essential macronutrients and low primary production are termed oligotrophic. A paradox situation arises in regions of high concentrations of macronutrients where primary productivity is too low to deplete them at the end of the growing season. These regions are referred as high-nutrient low-chlorophyll (HNLC) waters (Martin et al., 1990; de Baar, 1994; Johnson et al., 1997; Boyd et al., 1999; Boyd et al., 2001).

The Southern Ocean is the largest HNLC region due to the persistence of high levels of macronutrients (Figs. 1.4 and 1.5) and large areas of relatively low phytoplankton biomass. This consideration is particularly important due to the formation of deep water masses in the Southern Ocean (section 1.2) and, therefore, the surface nutrient distributions are strongly influential in determining the chemical properties of the deep ocean. Several hypotheses have been proposed to explain the HNLC conditions of the Southern Ocean: deficits in trace elements such as dissolved iron (Martin, 1990), insufficient light for phytoplankton growth (Sakshaug et al., 1991; Tranter, 1982) and grazing pressure from zooplankton (Dubischar and Bathmann, 1997), which are discussed below. The effects of temperature are also considered.

1.4.3.2. Iron

The hypothesis that iron is a limiting micronutrient in HNLC regions has been well established through numerous natural and artificial iron enrichment experiments (de Baar et al., 1995; Boyd et al., 2000; Gervais and Riebesell, 2002; Boyd et al., 2004; Coale et al., 2004; de Baar et al., 2005; Boyd et al., 2007). A wider implication of iron fertilisation is the increased efficiency of the biological (organic carbon) pump and enhanced uptake of atmospheric CO_2 (Watson et al., 2000; Boyd et al., 2004; Bakker et al., 2007; Jouandet et al., 2008).

Iron is a reactive micronutrient and is rapidly removed from the ocean by biological utilisation and chemical scavenging by sinking particles (Sarmiento and Gruber, 2006). The sources of iron to surface waters of the Southern Ocean are atmospheric deposition of dust particles (Duce and Tindale, 1991; Johnson, 2001), upwelling and turbulent diffusion (Hoppema et al., 2003; Blain et al., 2007), the interaction of water masses with sediments and advection (Nolting et al., 1991; Johnson et al., 1999; Sanudo-Wilhelmy et al., 2002; Dulaiova et al., 2009; Ardelan et al., 2010), melting sea ice, (de Baar et al., 1990; Martin, 1990; Löscher et al., 1997; Sedwick and DiTullio, 1997; Lannuzel et al., 2008), icebergs (Smith et al., 2007; Geibert et al., 2010) and a minor contribution from hydrothermal vents (Jickells et al., 2005; Tagliabue et al., 2010).

As atmospheric dust deposition has been reported as the governing factor in surface iron concentrations, the low levels of iron in the Southern Ocean are therefore explained by the low dust inputs (Duce and Tindale, 1991; Jickells et al, 2005; Meskhidze et al., 2007). This is largely a result of the westerly winds circulating over the Southern Ocean having little interaction with the land masses of South America, Africa and Australia and suggests that oceanic sources of iron are dominant in the Southern Ocean. The vertical distribution of iron in the ocean is typical to that of other nutrients, with relatively low concentrations in the upper ocean and high concentrations in deep waters (Sarmiento and Gruber, 2006). Increasing concentrations with depth means that upwelling and vertical mixing in the Southern Ocean will supply iron to the surface waters. However, the ratio of iron to nitrate in upwelled waters is usually insufficient to fulfil the biological requirements due to the low solubility and short lifetime of the bio-available iron (Jickells et al., 2005).

1.4.3.3. Light

Organic matter production is predominantly due to photosynthesis, which requires sunlight. If the light supply is inadequate for photosynthesis, then respiration will be the dominant process and there will be no biological carbon uptake. Therefore, phytoplankton productivity is limited to the upper ocean (euphotic zone) where there is sufficient light for photosynthesis. During the polar autumn and winter, the sun is either absent or low on the horizon resulting in low irradiance and light limitation to phytoplankton (van Oijen et al., 2004). Stormy conditions, typical of high latitudes during the winter, inhibit light penetration through the formation of deep mixed layers. Sea ice cover, in winter, and phytoplankton self-shading during the

growing season, also act to inhibit light penetration in these regions. These factors would lead to light limitation (Aumont and Bopp, 2006; Mitchell et al., 1991), although it is unlikely to be the dominant limiting factor (Boyd et al., 2007).

1.4.3.4. Grazing

Zooplankton grazing in the upper ocean has a direct effect on phytoplankton concentrations. Metal enrichment experiments in the Scotia and Weddell Seas suggested that in late spring and summer grazing was a dominant control of phytoplankton communities (Buma et al., 1991). This hypothesis was further examined by monitoring the *in situ* affect of copepod and salp populations in a phytoplankton bloom (Dubischar and Bathmann, 1997). When conditions favoured rapid phytoplankton growth there was a time lag in the response of the slower-growing zooplankton. Hence, zooplankton only acted to reduce the population of phytoplankton after bloom conditions had already been attained. Therefore, with the exception of salp blooms and krill swarms, zooplankton generally have a minor grazing impact on Southern Ocean phytoplankton (Atkinson et al., 2001 and references cited therein). An outcome of phytoplankton ingestion is the production of faecal pellets (particulate organic carbon), which sink out of the upper ocean and contribute to the flux of organic carbon to the deep ocean (section 1.5.4.1).

1.4.3.5. Temperature

Temperature is a controlling factor on phytoplankton growth as photosynthetic rates increase exponentially with increasing temperature, within a certain range to which cells are adapted (Reay et al., 2001). It would seem reasonable to predict that rates of primary production in the Southern Ocean would increase along the temperature gradients in this region. However, high chlorophyll-a concentrations have been detected across a wide range of surface seawater temperatures (Smith and Nelson, 1986; Kang et al., 2001; Korb et al., 2005), suggesting that temperature is not a principle limiting factor on phytoplankton biomass (Arrigo and van Dijken, 2004).

1.4.3.6. Co-limitation between potential factors

Iron has been shown to be the principle limiting factor for phytoplankton biomass in the Southern Ocean, however co-limitation between iron and light, and sometimes silicate (for

diatoms) and grazing, is likely. The iron hypothesis states that low iron concentrations lead to a shift towards smaller phytoplankton cells to increase the surface area to volume ratio and reduce the iron stress (Morel et al., 1991; Fennel et al., 2003). Phytoplankton of smaller cell sizes and reduced growth rates are more easily grazed by zooplankton (Timmermans et al., 2001). The involvement of iron in the photosynthesis pathway means that iron requirement is a function of light availability (Raven et al., 1990; Sunda et al., 1997; Boyd et al., 1999; Maldonado et al., 1999). It is therefore likely phytoplankton communities limited by one factor become stressed when another factor becomes limiting.

1.4.4. Exceptions to HNLC conditions

1.4.4.1. Productive waters of the Southern Ocean

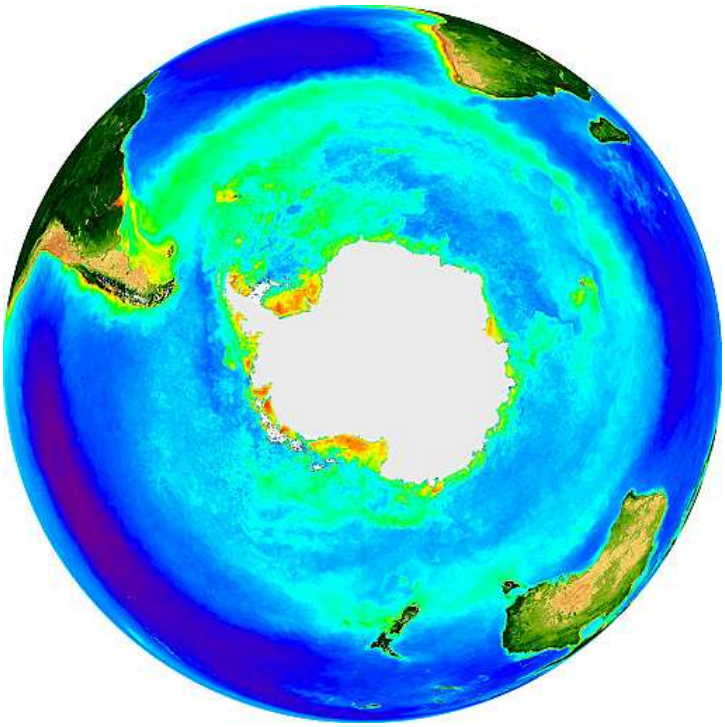

Figure. 1.6. Sea surface chlorophyll-a (mg m^{-3}) composite (1997-2007) during austral summer from the Sea-viewing Wide Field-of-view Sensor (SeaWiFS) ocean colour satellite (http://oceancolor.gsfc.nasa.gov/SeaWiFS/).

Alleviation of the HNLC conditions occurs by removal of one of the limiting factors. In the broad HNLC belt of the Southern Ocean, high productivity occurs within the vicinity of fronts (Bathmann et al., 1997; Boyd et al., 1995; Strass et al., 2002), at the sea ice edge and in the

wake of icebergs (Smith and Nelson, 1985; Korb et al., 2005; Smith et al., 2007) and in the wake of islands and submerged topographic features (Comiso et al., 1993; Moore and Abbot, 2000; Strass et al., 2002; Holm-Hansen et al., 2005; Tyrell et al., 2005; Blain et al., 2007; Pollard et al., 2007; Sokolov and Rintoul, 2007; Korb et al., 2008). Investigation into these areas helps to understand the processes that act to alleviate the HNLC conditions and promote phytoplankton productivity (Fig. 1.6).

1.4.4.2. Frontal zones

Enhanced chlorophyll-a concentrations have been associated with frontal mixing zones (Strass et al., 2002; Smetacek et al., 1997; Moore et al., 1999b). Fronts are associated with sloping isopycnals, upwelling and eddy mixing, which provide pathways for nutrients to be mixed into the surface waters (Moore and Abbott, 2002; Naveira Garabato et al., 2002b; Pollard et al., 2002; Strass et al., 2002; Hoppema et al., 2003) and often advected downstream (de Baar et al., 1995; Moore et al., 1999b; Daly et al., 2001; Hewes et al., 2008).

Correlations between dissolved iron and chlorophyll-a concentrations have been used to explain increases in primary production at the ACC fronts in the Scotia Sea due to advected iron enriched water masses within the frontal jet (Boyd et al., 1995; de Baar et al., 1995; Löscher et al., 1997; van Leeuwe et al., 1997; Pollard et al., 2002; Strass et al., 2002) and the uplifting isopycnals bringing nutrient-rich UCDW into the upper ocean (Löscher et al., 1997; Tynan, 1998; Pollard et al., 2002; Hoppema et al., 2003). Phytoplankton blooms observed at 6°W in the region of the PF coincided with elevated iron concentrations (up to 4 nM), which are likely to be sourced from South Georgia and the North Scotia Ridge (de Baar et al., 1995; Korb et al., 2004). Sediment trap data have indicated that primary production at the major fronts facilitates increased export of POC through the organic carbon pump (Wefer and Fischer, 1991).

1.4.4.3. Sea ice

Sea ice in the Southern Ocean exerts a major influence on phytoplankton productivity. Retreating ice edges, polynyas and icebergs are common sites of elevated phytoplankton biomass (Smith and Nelson, 1986; Moore et al., 1999b; Kang et al., 2001; Korb et al., 2005; Smith et al., 2007) due to factors including the production of a meltwater stratified surface layer (Smith and Nelson, 1985; Holm-Hansen and Mitchell, 1991; Sakshaug et al., 1991;

Lancelot et al., 1993), release of ice algae that acts as an inoculum (Smith and Nelson, 1985; Ackley and Sullivan, 1994) and the release of bioavailable iron (de Baar et al., 1990; Martin, 1990; Sedwick and DiTullio, 1997; Lannuzel et al., 2008). However, blooms are not systematically found at retreating ice edges during austral spring and summer (Boyd et al., 1995; Bakker et al., 1997; Bathmann, 1998). The occurrence of ice edge blooms in the Scotia Sea is discussed in Chapter 5 (section 5.5) and Chapter 7 (section 7.14).

1.4.4.4. Islands

Extensive phytoplankton blooms in the Southern Ocean are often associated with topographic features such as islands and seamounts (Moore et al., 1999b; Moore and Abbot, 2000; Comiso et al., 1993; Korb et al., 2004; Holm-Hansen et al., 2005; Tyrell et al., 2005; Blain et al., 2007; Pollard et al., 2007; Sokolov and Rintoul, 2007). These are sites of natural iron fertilisation where there is permanent interaction between water masses and the land, such as the upwelling and advection of waters in the ACC that have been in contact with shallow topography (de Baar et al., 1995; Loscher et al., 1997; Bucciarelli et al., 2001 ; Hoppema et al., 2003; Coale et al., 2004; Blain et al., 2007).

In addition to effects on downstream chlorophyll-a concentrations, the bathymetry around South Georgia (Thorpe et al., 2002; Meredith et al., 2003a; Meredith et al., 2003b; Meredith et al., 2005), Kerguelen (Park and Gamberoni, 1995) and the Crozet islands (Pollard and Read, 2001) has substantial effects on the circulation of the region. This is generally called the ‘island mass effect’. Previous investigations into Southern Ocean island blooms have confirmed natural iron fertilisation downstream of the Crozet islands (Planquette et al., 2007; Pollard et al., 2007) and Kerguelen (Blain et al., 2007; Bucciarelli et al., 2001) and substantial biological carbon uptake within the blooms that form (Bakker et al., 2007; Jouandet et al., 2008).

The island of South Georgia is situated on the NSR within the AAZ of the Scotia Sea, between the PF to the north and the SACCF to the south (section 1.2.4.2). The high-speed fronts and the wider, slower moving waters of the ACC are perturbed in the vicinity of South Georgia, due to the underlying bathymetry (Thorpe et al., 2002; Meredith et al., 2003a; Meredith et al., 2003b; Smith et al., 2010) (Fig. 1.7). Waters of the PF approaching the western face of South Georgia are deflected northwards due to the influence of the NSR, before returning to an

easterly course. Similarly, the southwestern approach of the SACCF is directed along the shelf edge to the east, after which it continues in an easterly course. Waters off the northwest shelf of South Georgia become enclosed in an area of weaker circulation and have longer residence times compared to the faster flowing waters within the PF and the SACCF (Thorpe et al., 2002).

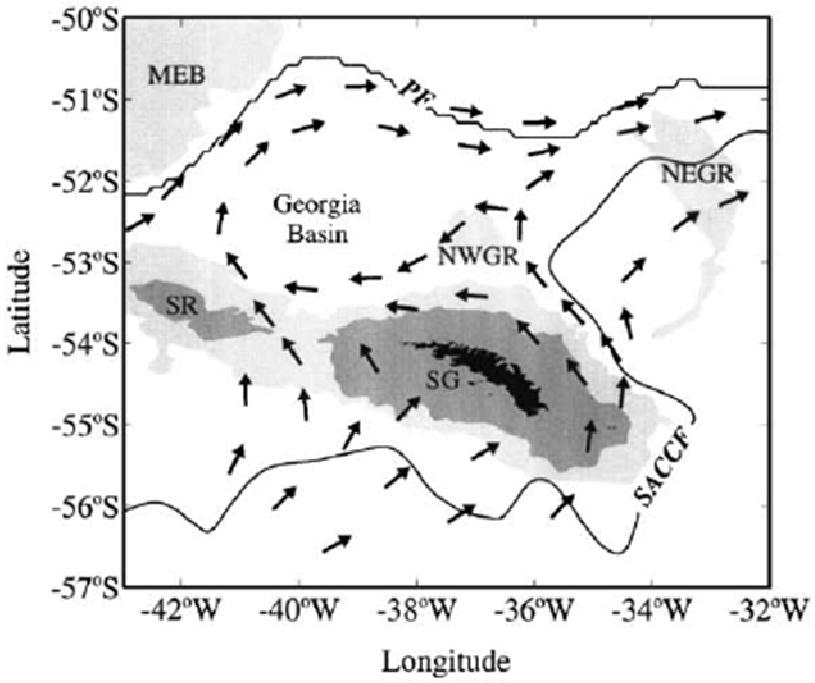

Figure 1.7. The island mass effect around South Georgia (SG) demonstrated using flow patterns from the FRAM model (Trathan et al., 1997) and drifter buoy data (Meredith et al., 2003a), adapted from Korb et al. 2004. The locations of the Maurice Ewing Bank (MEB), Northwest Georgia Rise (NWGR), the Northeast Georgia Rise (NEGR) and Shag Rocks (SR) are indicated. Bathymetry depths up to 500 m (dark grey) and depths up to 2,500 m (light grey).

Large and intense phytoplankton blooms regularly occur for 4 to 6 months in the wake of South Georgia (Atkinson et al., 2001; Korb and Whitehouse, 2004; Korb et al., 2004; Whitehouse et al., 2008). The circulation features of the PF and SACCF promote macronutrient resupply and iron enrichment to the surface waters by the upwelling of CDW or from sub-surface waters in contact with shelf sediments (Holm-Hansen et al., 2005). Mechanisms for potential iron enrichment to the surface waters include inputs from the

SACCF (Thorpe et al., 2002; Meredith et al., 2003b), circulation over elevated bathymetry such as the Northwest Georgia Rise and upwelling of deeper water from the ACC (Meredith et al., 2003a; Ward et al., 2002; Whitehouse et al., 2008).

The enhanced productivity downstream of South Georgia, contrasting with upstream HNLC conditions (Korb and Whitehouse, 2004), in conjunction with physiological assessments of the phytoplankton communities (Holeton et al., 2005; Korb et al., 2008), provides strong evidence for iron fertilisation (Moore and Abbott, 2002; Korb et al., 2004). In comparison to the biological carbon uptake associated with the Kerguelen and Crozet blooms, a first assessment of the affect of the extensive phytoplankton blooms downstream of South Georgia on the marine carbon cycle of the Scotia Sea is presented in Chapter 6.

1.5. The marine carbon cycle

1.5.1. The contemporary marine carbon cycle

The marine carbon cycle is a dynamic and complex component of the global carbon cycle. It is vital to have a clear understanding of the marine carbon cycle in order to better predict how the cycling of carbon will respond to increasing atmospheric levels of CO_2 and climatic changes. The global oceans represent the largest reservoir of carbon (~38,000 Pg C, Fig. 1.8) and therefore exert a dominant control on atmospheric CO_2 levels over timescales of millennia (Zeebe and Wolf-Gladrow, 2001).

During the pre-Industrial period (prior to the year 1800) no direct carbon measurements were made and hence the ocean carbon cycle at this time has been inferred from indirect geochemical evidence with reference to present day carbon cycle dynamics. During at least the last 11,000 years the concentration of CO_2 in the atmosphere has been relatively stable with inter-annual variations in the order of 20 ppm (Joos and Prentice, 2004). As the global ocean overturning circulation operates on timescales of about 1,000 years and CO_2 air-sea exchange has timescales of about 1 year (Broecker and Peng, 1982), the ocean must have been in a dynamic steady state with the atmosphere during the pre-Industrial period (Fig. 1.8). Pre-industrial sea surface pCO_2 is estimated to have comparable spatial and temporal variability as the current oceanic pCO_2 measurements with a flux across the air-sea interface of about 70 Pg C yr^{-1} (Sarmiento and Gruber, 2006). Model estimates propose that prior to 1800, oceans in

the northern hemisphere were a sink for atmospheric CO_2, whereas the Southern Ocean was a net source of CO_2 to the atmosphere (Sarmiento and Gruber, 2006).

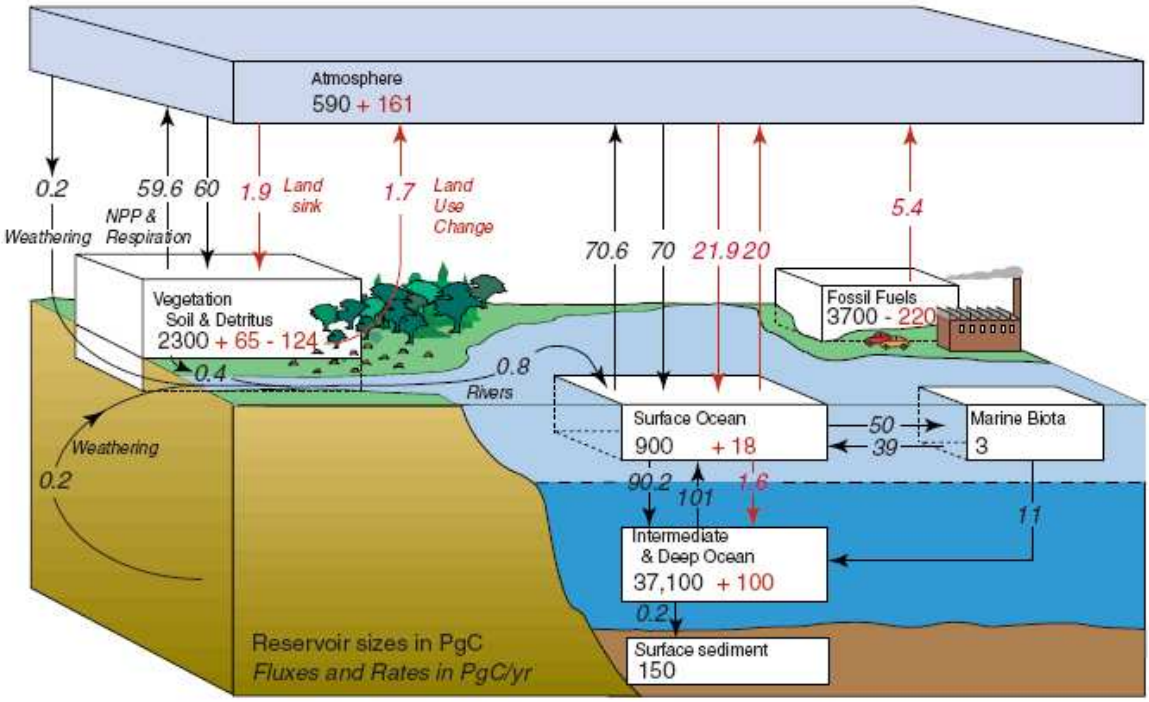

Figure 1.8. The global carbon cycle (IPCC, 2007) adapted from Sarmiento and Gruber (2002). Black arrows and values indicate natural carbon fluxes (Pg C yr^{-1}) and reservoirs (Pg C) and red arrows and values show the anthropogenic imprint.

Increases in atmospheric CO_2 since the Industrial Revolution have driven the ocean to uptake CO_2 from the atmosphere, steering surface seawater towards thermodynamic equilibrium with the atmospheric pCO_2 (Fig. 1.8). The results of numerous investigations show that the role of the contemporary ocean in the global carbon cycle is now a net sink for CO_2 of 1.5-2.0 Pg C yr^{-1} (Takahashi et al., 2009, and references cited therein).

1.5.2. The carbon dioxide system in seawater

The carbon dioxide system in seawater is one of the most important chemical equilibria in the ocean, and can be described using four variables: the fugacity of CO_2 (fCO_2), dissolved inorganic carbon (DIC), total alkalinity (TA) and pH. These parameters can be determined by direct or indirect methods that differ in both the accuracy and precision of data collection

(Millero, 1995). Knowledge of any two of the four parameters is sufficient to determine the other two to get a full appreciation of the whole carbon dioxide system.

Exchange of CO_2 between the atmosphere and surface ocean takes place until the pCO_2 in the seawater and overlying air is in thermodynamic equilibrium. The amount of dissolved (aqueous) CO_2 is proportional to the pCO_2 exerted by seawater. The fCO_2 is determined from pCO_2 and the CO_2 equation of state to account for the non-ideal nature of CO_2 in the gas phase (section 2.5.5). The fCO_2 is generally about 1% lower than pCO_2 (Zeebe and Wolf-Gladrow, 2001). The difference in fCO_2 in the surface ocean and overlying marine air (ΔfCO_2) is used with wind speed and the gas transfer velocity to calculate the flux of CO_2 across the air-sea interface. The flux calculation process and different gas transfer velocity formulations are discussed in section 2.15.

When CO_2 dissolves in seawater it becomes hydrated ($CO_2(aq)$) and then forms carbonic acid (H_2CO_3) from the reaction with seawater. Most of the carbonic acid rapidly dissociates to produce bicarbonate (HCO_3^-) and a hydrogen ion (H^+) and again to produce carbonate (CO_3^{2-}) and another H^+. Free H^+ can then react with carbonate to yield more bicarbonate. As a result, enhanced CO_2 uptake in the ocean increases the concentrations of H_2CO_3, HCO_3^-, H^+, decreases the concentration of CO_3^{2-} with a net effect of lowering the pH.

$$CO_2(g) \xleftrightarrow{K_0} CO_2(aq) \qquad \text{Equation 1.1.}$$

$$CO_2(aq) + H_2O(l) \longleftrightarrow H_2CO_3(aq) \qquad \text{Equation 1.2.}$$

$$H_2CO_3(aq) \xleftrightarrow{K_1} H^+(aq) + HCO_3^-(aq) \qquad \text{Equation 1.3.}$$

$$HCO_3^-(aq) \xleftrightarrow{K_2} H^+(aq) + CO_3^{2-}(aq) \qquad \text{Equation 1.4.}$$

The notations (g), (aq) and (l) indicate the state of the species, i.e. a gas, aqueous solution and a liquid, respectively.

The thermodynamics of the carbonate system have been thoroughly investigated and the equilibrium relationships between the various carbon dioxide species are well defined (DOE, 2007):

$$K_0 = [CO_2\ ] / \ fCO_2(g) \qquad \text{Equation 1.5.}$$

$$K_1 = [H^+(aq)][HCO_3^-(aq)] / [CO_2] \qquad \text{Equation 1.6.}$$

$$K_2 = [H^+(aq)][CO_3^{2-}(aq)] / [HCO_3^-(aq)] \qquad \text{Equation 1.7.}$$

where K_0 is the equilibrium constant for the solubility of CO_2 and K_1 and K_2 are the first and second dissociation constants of carbonic acid. [CO_2] represents the combined concentration of CO_2(aq) and H_2CO_3(aq), which are not differentiated by the equilibrium constants. The square brackets represent the total stoichiometric concentrations of the species. The temperature dependency of the CO_2 system reactions in seawater is very strong (Fig. 1.9).

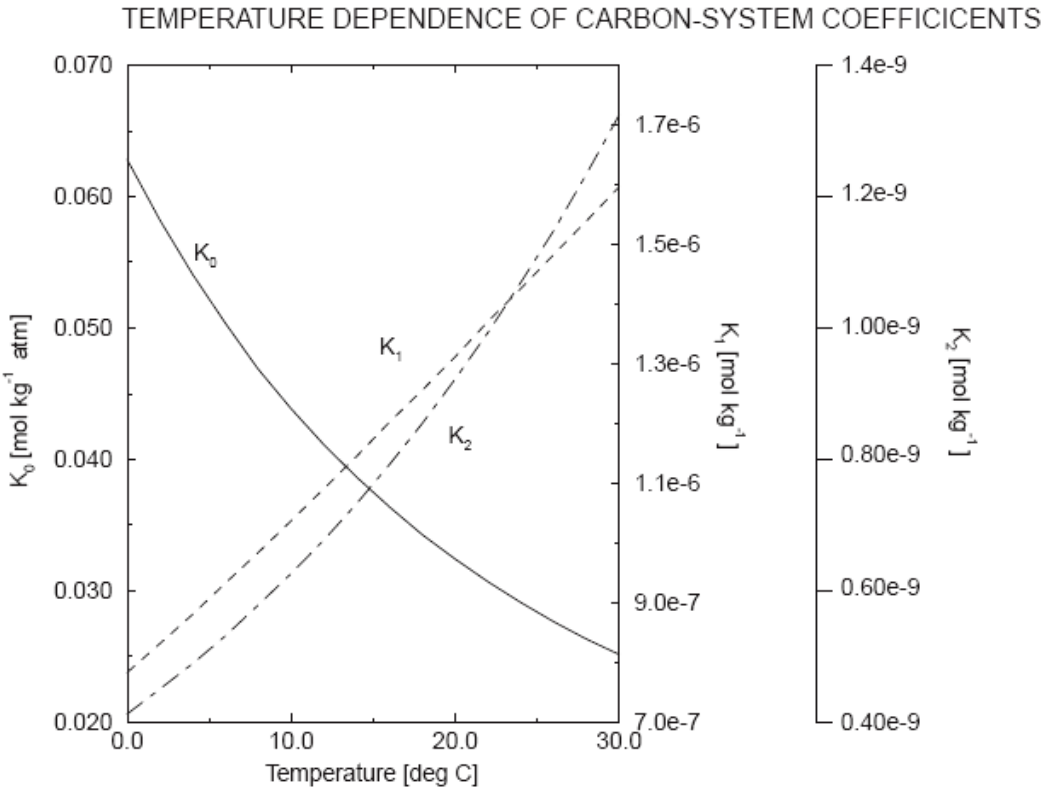

Figure 1.9. Plot of the CO_2 solubility (K_0, mol kg^{-1}) and the equilibrium constants of the first (K_1, mol kg^{-1}) and second (K_2, mol kg^{-1}) mechanisms of the carbonic acid dissociation pathway as a function of temperature (Sarmiento and Gruber, 2006).

Dissolved inorganic carbon (DIC), or total CO_2, exists in seawater in three major forms: bicarbonate (HCO_3^-), carbonate (CO_3^{2-}) and aqueous CO_2 (CO_2(aq)), which includes carbonic acid (H_2CO_3):

$$DIC = \left[HCO_3^-(aq)\right] + \left[CO_3^{2-}(aq)\right] + \left[CO_2(aq)\right] \qquad \text{Equation 1.8.}$$

Due to the presence of the carbonate equilibria, dissolved CO_2 gas is present in only small amounts in seawater. The bicarbonate and carbonate ions represent the greatest reservoir of DIC in seawater. At pH 8.2, about 88% of the carbon is HCO_3^-, 11% is CO_3^{2-} and about 0.5% is in the form of dissolved CO_2. The analytical techniques for the determination of DIC are described in section 2.8.1.

Total alkalinity (TA) is a description of the charge balance of seawater that measures the concentration of all bases that can be protonated during an acid titration to the carbonic acid endpoint (Millero, 2007):

$$\begin{aligned} TA = {} & \left[HCO_3^-(aq)\right] + 2\left[CO_3^{2-}(aq)\right] + 2\left[B(OH)_4^-(aq)\right] + \left[OH^-(aq)\right] + \left[HPO_4^{2-}(aq)\right] + \\ & 2\left[PO_4^{3-}(aq)\right] + \left[SiO(OH)_3^-(aq)\right] + \left[NH_3(aq)\right] + \left[HS^-(aq)\right] + \ldots - \\ & \left[H^+(aq)\right]_F - \left[HSO_4^-(aq)\right] - \left[HF(aq)\right] - \left[H_3PO_4(aq)\right] - \ldots \end{aligned}$$

Equation 1.9.

The ellipses (...) represent additional minor acid or base species that are either unidentified or exist in trace amounts. For seawater, the most important bases are [HCO_3^-], [CO_3^{2-}] and [$B(OH)_4^-$]. The analytical techniques for the determination of TA are described in section 2.8.2. The concentrations of the major ions vary with salinity however, their relative proportions remain almost constant.

The final parameter of the carbonate system is the total hydrogen ion concentration, reported as pH:

$$pH = -\log_{10}\left[H^+\right] \qquad \text{Equation 1.10.}$$

The definition of pH is complicated by the chemical properties and the ionic activity of seawater and therefore different pH scales were created. Three pH scales are commonly used, based on buffer solutions of artificial seawater (Hansson, 1973): free pH (pH_F), total pH (pH_T) and seawater pH (pH_{SWS}):

$$pH_F = -\log_{10}\left[H^+\right]_F \qquad \text{Equation 1.11.}$$

$$pH_T = -\log_{10}\left(\left[H^+\right]_F + \left[HSO_4^-\right]\right) \qquad \text{Equation 1.12.}$$

$$pH_{SWS} = -\log_{10}\left(\left[H^+\right]_F + \left[HSO_4^-\right] + \left[HF\right]\right) \qquad \text{Equation 1.13.}$$

The total scale, pH_T, is a measure of total $[H^+]$ and includes a contribution from hydrogen sulphate and will be used to discuss pH distributions in the Scotia Sea (Chapters 2 and 7).

1.5.3. Distribution of carbon in the ocean

The incentive to better understand the marine carbon cycle is the importance of the oceans in controlling the concentration of CO_2 in the atmosphere, thus influencing the climate system. An initial consideration is the distribution of pCO_2 in the sea surface as it is the air-sea interface that is the dynamic link between the atmospheric and oceanic reservoirs. Air-sea exchange of CO_2 is a comparatively slow process, it takes about 6 months to equilibrate a 40 m mixed layer (Zeebe and Wolf-Gladrow, 2001) and hence over- and undersaturation of fCO_2 can readily occur in seawater relative to the rather stable atmospheric CO_2 content.

The surface water pCO_2 of the global oceans varies geographically and seasonally from about 150 to 550 μatm, which is 50-60% above and below the current global mean atmospheric value of about 388 ppm (Dr. Pieter Tans, NOAA/ESRL (www.cmdl.noaa.gov/gmd/ccgg/trends)). Therefore, the direction of the air-sea CO_2 flux is dominated by changes in oceanic pCO_2. Global and regional air-sea CO_2 fluxes were calculated for a nominal year 2000 (Fig. 1.10) to reveal an average annual global oceanic uptake of 1.42 Pg C yr^{-1} (Takahashi et al., 2009).

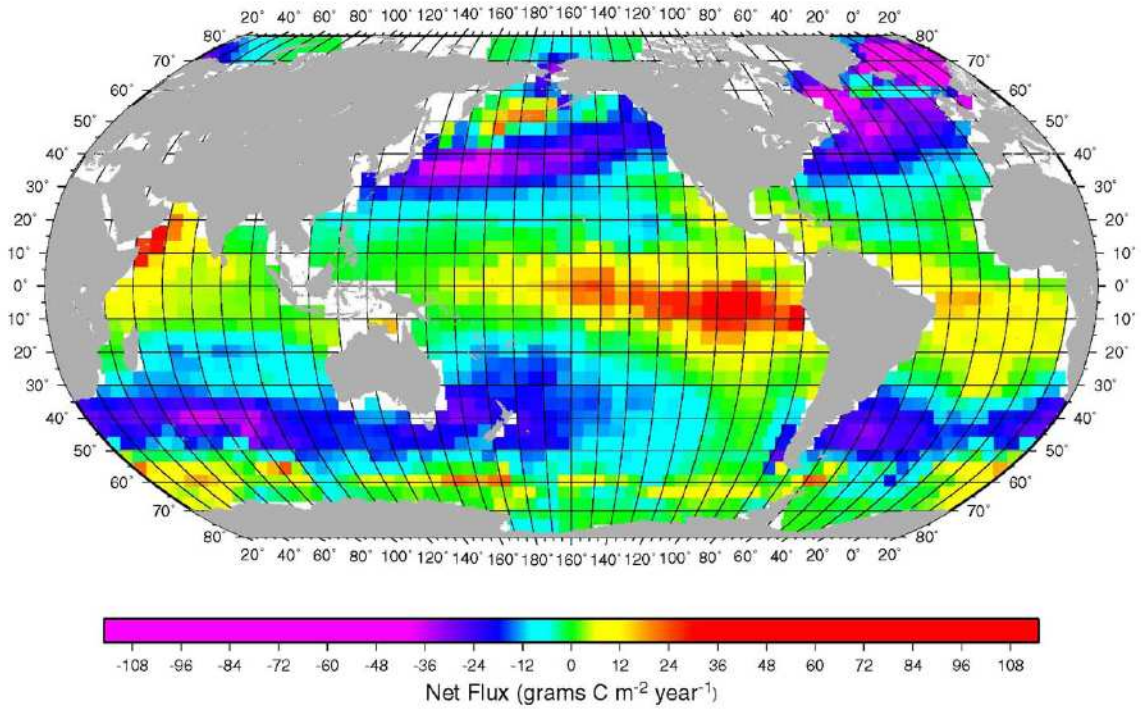

Figure 1.10. Global climatology of the mean annual air-sea CO_2 flux (g C m^{-2} yr^{-1}) based on interpolation of ΔpCO_2 for the reference year 2000 (Takahashi et al., 2009).

Global climatological air-sea CO_2 fluxes calculated for austral summer in the reference year 2000 show regions of strong CO_2 uptake in the Southern Ocean, particularly in the Atlantic sector (Fig. 1.11a). This indicates that these regions are net sinks for atmospheric CO_2 and, given the time of year, this has been attributed predominantly to biological carbon uptake (Takahashi et al., 2009). This pattern is in marked contrast to the equatorial Pacific, where there is net outgassing of CO_2 as a result of upwelling of sub-surface CO_2 enriched waters and intense solar heating of the newly formed surface waters. Other net CO_2 source regions include the tropical Atlantic and Indian oceans throughout the year. The high latitude oceans are regions of intense CO_2 uptake during the summer through the action of the physical and organic carbon pumps (Fig. 1.11a).

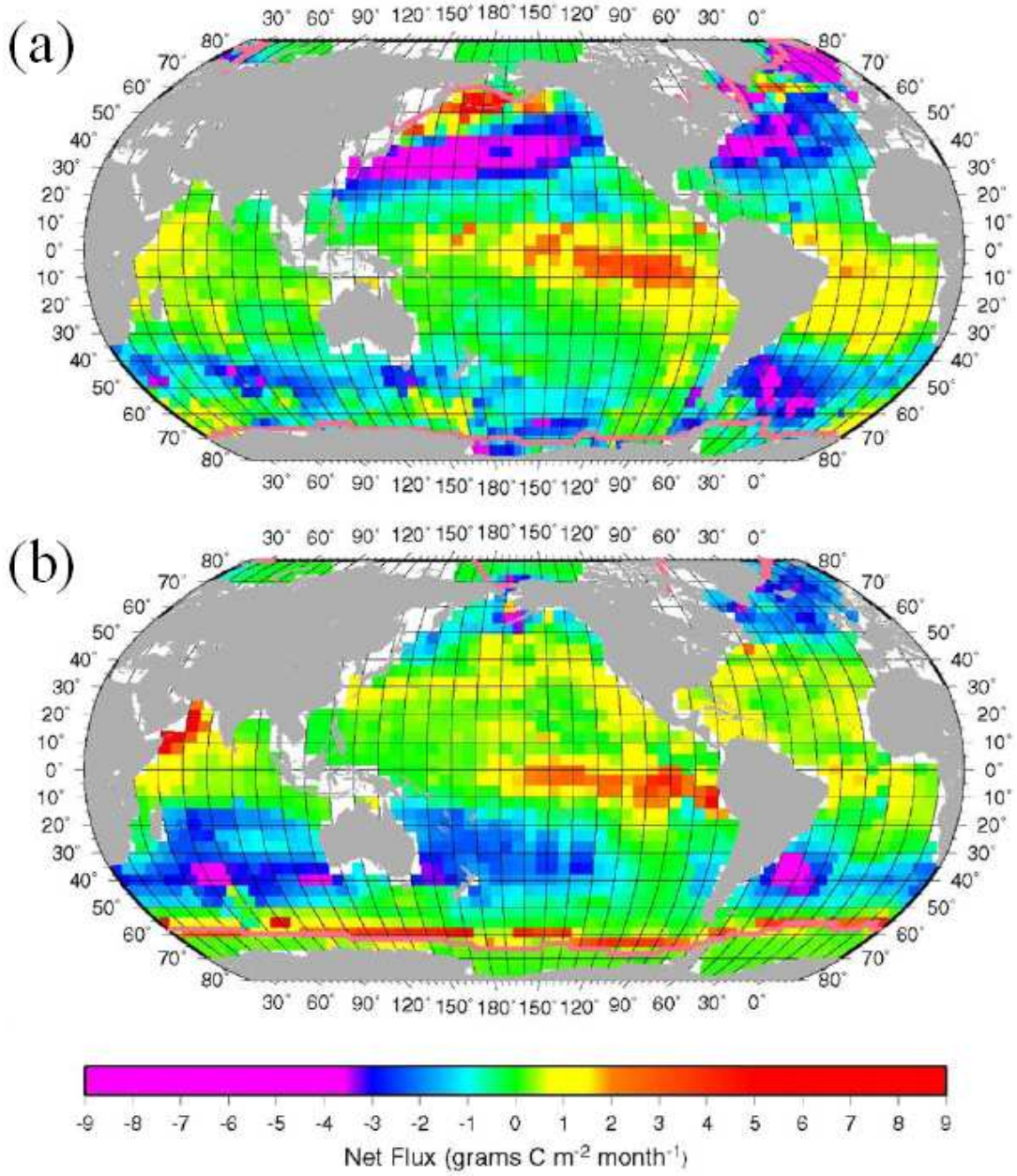

Figure 1.11. Global climatology of the mean air-sea CO_2 flux (g C m^{-2} $month^{-1}$) in (a) February and (b) August based on interpolation of ΔpCO_2 for the reference year 2000 (Takahashi et al., 2009).

During winter in the Southern Ocean, continued upwelling and deep vertical mixing entrains DIC-rich waters at the surface, with the net effect of eliminating this CO_2 uptake. A circumpolar band of moderate source waters develops at about 60°S during austral winter (Fig. 1.11b). This represents CO_2 outgassing from supersaturated waters, especially beneath the seasonal sea ice cover. Poleward of the CO_2 source band, sea ice is present for longer and the

CO_2 flux is largely inhibited by the sea ice barrier and tends to zero. As the sea ice recedes during spring and summer, photosynthetic activity reduces the sea surface pCO_2 and drives strong CO_2 uptake in the seasonally ice-free waters (Chapters 5 and 7).

The pCO_2 of the mixed layer is in exchange with CO_2 in the atmosphere and is largely controlled by changes in temperature, salinity, DIC and alkalinity. The efficiency of the ocean to absorb CO_2 is related to how much CO_2 can be converted to DIC. This is measured by a buffering capacity described by the Revelle Factor (*RF*) as given by Eqn. 1.14 (Revelle and Suess, 1957):

$$RF = \frac{\left(\delta pCO_2 / pCO_2\right)}{\left(\delta DIC / DIC\right)} \qquad \text{Equation 1.14.}$$

The Revelle Factor is defined as the ratio of the relative change in pCO_2 (δpCO_2/ pCO_2) to the relative change in DIC (δDIC/ *DIC*) (Zeebe and Wolf-Gladrow, 2001). In the global ocean, Revelle Factors are governed by atmospheric CO_2 concentrations and temperature and are typically between 8-15 (Broecker et al., 1979). Therefore, the relative change in pCO_2 is larger than the relative change in DIC. Waters with low Revelle Factors are four times more efficient at taking up CO_2 than waters with very high Revelle Factors. High latitude waters are characterised by high Revelle Factors in the order of 10-15 (Sabine et al., 2004), mainly due to the temperature dependency of solubility of CO_2 (Eqn. 1.5) in seawater (Fig. 1.9).

Processes affecting the carbonate system in the ocean are CO_2 uptake and release (physical carbon pump), photosynthesis (organic carbon pump), respiration and the formation and dissolution of calcium carbonate minerals (carbonate pump) (Zeebe and Wolf-Gladrow, 2001). These processes produce an uneven distribution of DIC in the ocean and set the rates at which carbon moves between the oceanic and atmospheric reservoirs (Fig. 1.8).

1.5.4. The oceanic carbon pumps

1.5.4.1. The biological carbon pumps

The biogenic production of organic matter and carbonate minerals in the upper ocean and their subsequent transport to depth are referred to as the biological carbon pumps (Fig. 1.1). The

photosynthetic fixation of CO_2 by phytoplankton and the flux of particulate organic carbon (POC) to depth is referred to as the organic carbon pump (Eppley, 1972). This mechanism of biological carbon uptake utilises aqueous CO_2 (CO_2(aq), Eqn. 1.1) and generates a CO_2 sink in the upper ocean. The efficiency of the organic carbon pump is largely controlled by the availability of light and important nutrients (section 1.4).

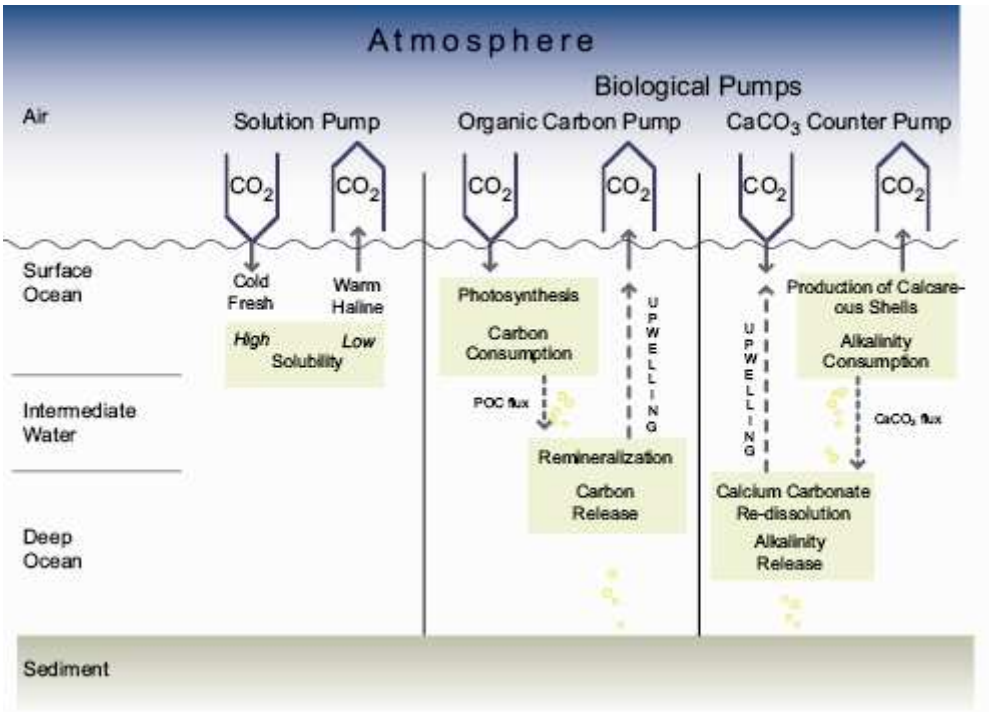

Figure 1.12. Schematic of the physical (solution) pump, the organic carbon pump and the calcium carbonate ($CaCO_3$) 'counter' carbon pump (Heinze et al., 1991), adapted from IPCC (2007). Abbreviations used: POC, particulate organic carbon.

Calcification (Eqn. 1.15) and the subsequent transport of calcium carbonate ($CaCO_3$) minerals to depth is referred to as the carbonate 'counter' pump. In contrast to the organic carbon pump, this mechanism utilises bicarbonate (HCO_3^-, Eqn. 1.15) and releases CO_2 in the upper ocean, reduces the alkalinity and acts as a potential source on short timescales (Elderfield, 2002).

$$Ca^{2+}(aq) + 2HCO_3^-(aq) \longleftrightarrow CaCO_3(s) + CO_2(aq) + H_2O\,(l) \qquad \text{Equation 1.15.}$$

The $CaCO_3$ formed is one of two crystalline forms, calcite or aragonite. The aragonite crystalline structure is thermodynamically less stable and is about 50% more soluble in

seawater compared to calcite (Mucci, 1983). Three groups of organisms dominate the carbonate pump in the open ocean through the formation of calcium carbonate exoskeletons: (1) coccolithophores are phytoplankton that produce an outer sphere of calcite plates, (2) foraminifera are heterotrophic zooplankton that secrete calcite shells and (3) pteropods are heterotrophic zooplankton that produce shells of the less stable $CaCO_3$ phase aragonite. The pteropods are one of the major calcifyers in the Southern Ocean that contribute to the Southern Ocean biological pump and to the export flux of carbonates from the upper ocean to the deep sea (Fabry, 1990).

The degree of saturation (Ω) of $CaCO_3$ in the ocean is defined as the ratio of the ionic activity product of calcium ($Ca^{2+}(aq)$) and carbonate ($CO_3^{2-}(aq)$) over the stoichiometric solubility product ($K_{sp}^{CaCO_3}$) for either calcite or aragonite:

$$\Omega = \frac{\left(\left[Ca^{2+}(aq)\right]\left[CO_3^{2-}(aq)\right] \right)}{K_{sp}^{CaCO_3}} \qquad \text{Equation 1.16.}$$

When the ocean is supersaturated with respect to $CaCO_3$ ($\Omega > 1$), the formation of calcareous material is favoured. Conversely, if the ocean becomes undersaturated with respect to $CaCO_3$ ($\Omega < 1$), then dissolution of calcareous material can occur. Saturation states are typically low at high latitudes as the solubility of $CaCO_3$ increases with decreasing temperature and increasing pressure. Oceanic surface waters are supersaturated with respect to calcite and aragonite. At decreasing temperatures and increasing pressure, the solubility of both carbonate mineral phases increases. In the water column, the depth at which seawater becomes undersaturated with respect to $CaCO_3$ is called the carbonate saturation horizon. The large variations in the distribution of the carbonate saturation horizon are primarily a consequence of variations in the distribution of carbonate ions (Sarmiento and Gruber, 2006).

As DIC is utilised during photosynthesis and calcification, the carbonate equilibria thermodynamically shift to produce free CO_2 from the DIC pool (Eqns. 1.2-1.4). These reactions deplete DIC, utilise H^+ and subsequently increase the pH in surface waters (Fig. 4.4). The sinking of cold, saline water provides a method of transport of POC and PIC from the surface waters to the deep ocean (Fig. 1.1), where DIC is returned to the marine carbon cycle

through remineralisation and dissolution at depth (Redfield et al., 1963). Remineralisation of organic matter reduces the concentration of carbonate, leading to the distribution of carbonate in the ocean being opposite to that of the macronutrients i.e. high in surface waters and low in the deep ocean (Sarmiento and Gruber, 2006). Combined with relatively slow ventilation, deep waters become DIC-rich and carbonate poor, relative to surface waters.

Relative to the variability in DIC, alkalinity has much smaller variations (Fig. 6.9). The main processes controlling the distribution of alkalinity in the ocean are freshwater inputs (sea ice melt and precipitation), freshwater removal (sea ice formation and evaporation), the carbonate pump in the upper ocean and the dissolution of the carbonate minerals at depth (Lee et al., 2006). As a result, alkalinity is typically lower in surface waters compared to deep waters. Identifying the processes that control the distribution of alkalinity is becoming increasingly important for understanding the effects of anthropogenic CO_2 uptake on the ocean carbonate chemistry (Feely et al., 2004).

The organic carbon pump can represent a mechanism of removal of carbon from the atmosphere, relative to timescales of anthropogenic perturbations. Under dynamic steady state conditions, the removal and transport of POC to deep waters is balanced by outgassing of CO_2 from upwelled waters. However, an increase in the organic carbon pump can represent a mechanism of carbon sequestration if the POC is exported out of the upper ocean, away from strong upwelling regions. Export of the particulate inorganic carbon (PIC) through the carbonate pump represents a mechanism of long-term carbon removal through dissolution and sedimentation at depth.

1.5.4.2. The physical carbon pump

The physical (solution) pump refers to the thermodynamic uptake of CO_2 at the air-sea interface and the physical processes that transport it to the deep ocean (Watson and Orr, 2003). As surface seawater is transported to high latitudes it becomes cooled, which enhances the thermodynamic uptake of CO_2 through the response of the equilibrium constants (K_0, K_1 and K_2, section 1.5.2) to cooler water (Fig. 1.9). The physical pump acts as a sink of atmospheric CO_2 through the juxtaposition of increased CO_2 concentrations of the sinking water, which have been in contact with the present day atmosphere, and the lower CO_2 concentrations of upwelled water, which were exposed to pre-Industrial levels of CO_2 (Sabine et al., 2004).

1.6. Anthropogenic CO_2

Since the beginning of the Industrial Revolution the natural carbon cycle has undergone large perturbations through anthropogenic emissions of CO_2 (IPCC, 2007). Oceanic uptake of CO_2 acts as a buffer to the increasing atmospheric CO_2 concentrations through the reactions of the carbonate equilibria (section 1.5.2). Using global DIC measurements (Key et al., 2004) and a tracer-based separation technique, it is estimated that 118 ± 19 Pg of anthropogenic CO_2 has accumulated in the ocean between 1800 and 1994 (Sabine et al., 2004). This uptake is not uniform throughout the global ocean and high inventories in the North Atlantic and in the Southern Ocean in the region of 50°S (Fig. 1.13) are attributed to water mass formation, transporting anthropogenic CO_2 into the ocean interior (Fig. 1.9).

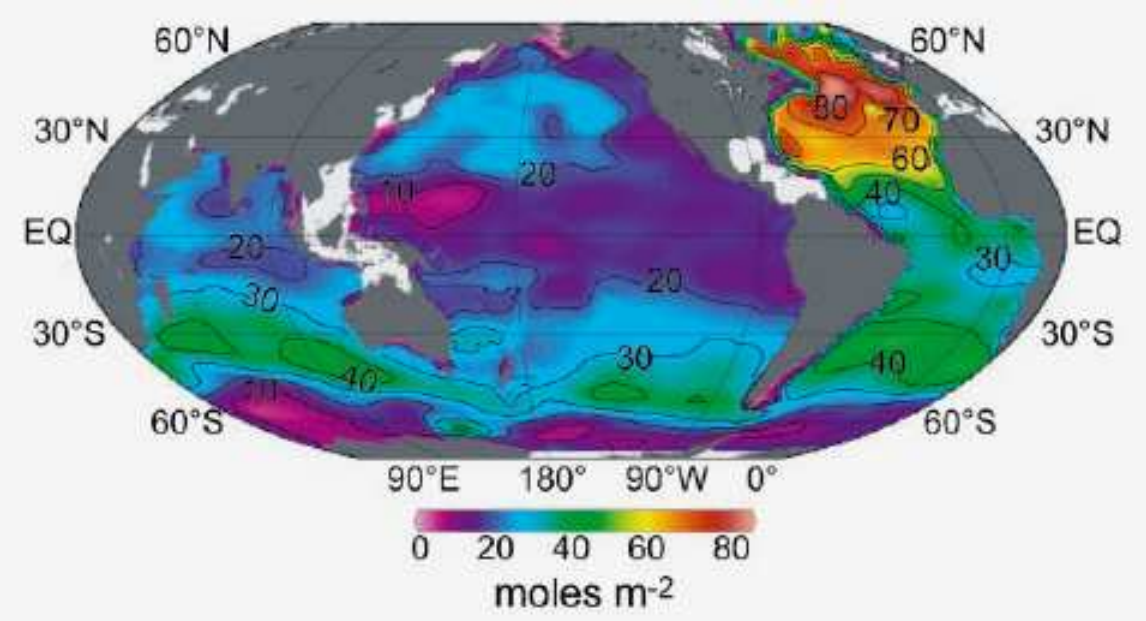

Figure 1.13. Column inventory of anthropogenic CO_2 in the global ocean (mol m^{-2}) (Sabine et al., 2004).

Based on the anthropogenic CO_2 inventory estimates of Sabine et al. (2004), the average Revelle Factor (Eqn. 1.14) of the global ocean surface has increased by about one unit compared to pre-Industrial values. This indicates that CO_2 uptake by the contemporary ocean is less efficient than the pre-Industrial ocean. A decrease in the buffering capacity of the oceans is accompanied by depletion in carbonate and decreased pH leading to 'the other CO_2 problem' of ocean acidification (Doney et al., 2009).

1.7. Ocean acidification

Although oceanic uptake of anthropogenic CO_2 will mitigate the extent of global warming, the direct effect of CO_2 on ocean chemistry has significant impacts of marine ecosystems. Numerous investigations have indicated that oceanic anthropogenic CO_2 uptake and the concomitant modifications to the carbonate system (section 1.5.2) have adverse consequences for calcifying organisms (Royal Society, 2005). Invasion of anthropogenic CO_2 from the atmosphere increases the DIC through the production of bicarbonate (Eqn. 1.17), leading to a reduction in the carbonate ion concentration, decreased pH and a lowering of the calcium carbonate saturation state:

$$CO_2 + H_2O + CO_3^{2-} \longleftrightarrow 2HCO_3^- \qquad \text{Equation 1.17.}$$

If the sea surface fCO_2 concentrations continue to increase alongside the atmospheric CO_2 increase, a doubling of the pre-Industrial atmospheric CO_2 concentration will result in a 30% reduction in carbonate ion concentration in the surface ocean (Sabine et al., 2004). These changes on the ocean carbonate chemistry have already led to increased impacts of ocean acidification (Orr et al., 2005; Royal Society, 2005).

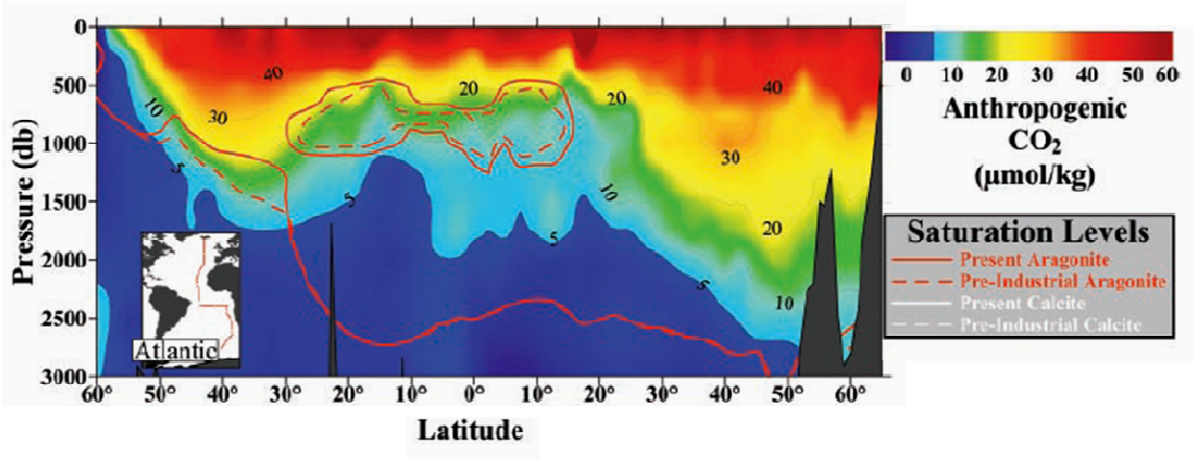

Figure 1.14. The vertical distribution of anthropogenic CO_2 (µmol kg^{-1}) as a function of latitude along a north-south transect (insert map) in the Atlantic ocean (Sabine et al., 2004), adapted from Feely et al. (2004). The present day (red solid line) and pre-Industrial (red dashed line) saturation horizons for aragonite are shown.

The uptake of anthropogenic CO_2 has resulted in the shoaling of the aragonite saturation horizon by several hundred meters (Feely et al., 2004). If present trends in anthropogenic CO_2 continue, then surface waters of the Southern Ocean will become undersaturated with respect to aragonite. This would first occur during the winter when sea surface fCO_2 levels are highest due to cold temperatures (Fig. 1.9) and vertical mixing into the sub-surface waters supplied with upwelled DIC-rich CDW (section 1.2). These wintertime sea surface conditions are discussed for the Scotia Sea in Chapter 7.

The effects of anthropogenic CO_2 uptake on calcifying organisms are not well understood. Investigations into calcification under different CO_2 conditions have indicated that the rate of calcification in numerous organisms is reduced under elevated CO_2 levels (see summaries in Feely et al., (2004) and Fabry et al. (2008) and references therein). However, contradicting results suggest that uncertainties still exist in this area (Iglesias-Rodriguez et al., 2008). Based on the majority of the laboratory analyses (Riebesell et al., 2000) and mesocosm experiments (Engel et al., 2005), evidence suggests that the direct effects of increased seawater fCO_2 include a decrease in the marine rates of calcification in response to the subsequent reduction in carbonate ion concentration, calcium carbonate saturation state and pH (Riebesell et al., 2000). In accordance with the carbonate reaction mechanism (Eqn. 1.11) this would reduce the production of natural CO_2 from the ocean, with significant implications for the marine ecosystem (Royal Society, 2005).

Uptake of anthropogenic CO_2 has led to a reduction in average surface ocean pH by about 0.1 units, corresponding to an increase in H^+ of about 30% (Orr et al., 2005). Under the IPCC emission scenarios (Houghton, 2001), average surface ocean pH could decrease by 0.3-0.4 units from the pre-Industrial values by the end of the century (Caldeira and Wickett, 2003). Combining predicted future changes to surface ocean carbonate chemistry, forced with the IPCC IS92a "business as usual" CO_2 emission scenario (Orr et al., 2005), and global gridded DIC data (Key et al., 2004), the Southern Ocean south of about 60°S will become undersaturated with respect to aragonite by 2050 (Orr et al., 2005). The aragonite saturation horizon could shoal from its current average depth of about 730 m (Fig. 1.14) to the surface of the Southern Ocean (Fabry et al., 2008). It is predicted that Southern Ocean surface waters will reach aragonite undersaturation when seawater fCO_2 reaches about 450-560 μatm (Fabry et al., 2008; McNeil and Matear, 2008).

Field and laboratory data are limited on the response of calcification in pteropods under conditions of high CO_2 and decreased aragonite saturation state, although ongoing research hopes to address this (Bednarsek, in preparation). At present, a laboratory study has shown that high CO_2 conditions and the subsequent decreasing aragonite saturation state promotes the dissolution of the thin aragonite shells (Feely et al., 2004; Orr et al., 2005). With the shoaling of the aragonite saturation horizon, pteropods in the Southern Ocean could become one of the first major planktonic calcifyers to be exposed to critically low concentrations of carbonate in surface waters.

1.8. The Scotia Sea and the marine carbon cycle

Furthering the understanding of the marine carbon cycle and the long-term removal of carbon is paramount in order to better predict the effects of future emissions on the marine ecosystems of the Southern Ocean. The difficulty of constraining the Southern Ocean CO_2 sink can only be alleviated by increased data coverage, with temporal requirements of autumn and winter data, and spatial requirements of the sea ice regions. Experimental evidence suggests that the effects of increased CO_2 on ocean carbon chemistry is leading to ocean acidification (Riebesell et al., 2000; Engel et al., 2005). Limited investigations have been carried out to assess the *in situ* occurrence of ocean acidification in the oceanic environment, despite several studies that consider the future onset of ocean acidification in the Southern Ocean (Feely et al., 2004; Orr et al., 2005; McNeil and Matear, 2008).

The contribution of the Scotia Sea to the overturning circulation and global uptake of CO_2 is routed in the transport, mixing and ventilation of different water masses, from Drake Passage and the Weddell Sea, in the ACC (Carmack and Foster, 1975; Naveira Garabato et al., 2002a). Hydrographic sections have already evaluated the changing roles of the North Atlantic in the uptake and storage of carbon (Brown, 2008). Despite the numerous high resolution hydrographic data in the Scotia Sea (Naveira Garabato et al., 2002a; Naveira Garabato et al., 2007; Meredith at al., 2008), the requirement for vertical distributions of carbon is yet to be fulfilled.

Many questions regarding the role of sea ice in the carbon cycles of the polar oceans remain unsolved. The sea ice carbon pump hypothesis, derived from observations in Arctic sea ice, states that inorganic carbon is rejected in brines during sea ice formation and that dissolution

of carbonate minerals leads to enhanced CO_2 uptake during ice melt (Rysgaard et al., 2007; Rysgaard et al., 2009). Carbonate minerals have been detected in Antarctic sea ice (Papadimitriou et al., 2007; Dieckmann et al., 2008), however the affect of carbonates on the marine carbon cycle in the Southern Ocean is still speculative.

Regions of high productivity associated with receding sea ice (Korb et al., 2005; Smith and Comiso, 2008), hydrographic fronts (Comiso et al., 1993; Tynan et al., 1998; Strass et al., 2002; Ward et al., 2002; Holm-Hansen et al., 2004b; Shim et al., 2006) and submarine arcs and islands (Moore and Abbot, 2000; Strass et al., 2002; Holm-Hansen et al., 2004b; Korb and Whitehouse, 2004; Korb et al., 2004; Korb et al., 2008; Dulaiova et al., 2009; Ardelan et al;., 2010) establish the Scotia Sea as sustaining one of the most active biological carbon pumps. Natural iron fertilisation and biologically mediated carbon uptake has been identified in the intense phytoplankton blooms at the sub-Antarctic islands of Crozet (Bakker et al., 2007; Planquette et al., 2007) and Kerguelen (Blain et al., 2007; Jouandet et al., 2008). A similar 'island mass effect' is observed at South Georgia as the circulation is tightly constrained by bathymetry (Thorpe et al., 2002; Meredith et al., 2003a; Meredith et al., 2003b; Smith et al., 2010). Waters downstream of South Georgia are amongst the most productive in the Southern Ocean, where extensive blooms regularly occur (Atkinson et al., 2001; Korb and Whitehouse, 2004; Korb et al., 2008; Whitehouse et al., 2008). As a result, this region is associated with strong carbon sinks in the Southern Ocean (Schlitzer et al., 2002; Takahashi et al., 2009), which has yet to be acutely quantified by *in situ* carbon measurements.

This thesis attempts to address these issues. The Scotia Sea is a model 'mesocosm' to investigate the processes that affect the marine carbon cycle of the Southern Ocean. The sea surface pCO_2 data and vertical carbonate chemistry data collected onboard RRS *James Clark Ross* from 2006-2009 are presented. The cross fertilisation of the Discovery-2010 and CARBON-OPS programmes enabled the collection of over 2,500 sea surface pCO_2 measurements across a mosaic of archetypal oceanic environments of the Southern Ocean (Fig. 8.1). This established a new surface water pCO_2 timeseries to alleviate the paucity of pCO_2 data in this region. The new CASIX underway pCO_2 instrument is acutely tested during an at-sea intercomparison, subsequently launching an additional instrument into the oceanic pCO_2 community (Chapter 3). Vertical carbonate chemistry profiles are presented alongside hydrographic data in order to identify the principle water masses, hydrographic fronts and the

contemporary carbonate characteristics of the Scotia Sea, from the surface to the deep ocean (Chapter 4). Passage through sea ice cover allowed a unique analysis of changes in the carbonate chemistry of Antarctic sea ice during the summer thaw (Chapter 5). In comparison to the substantial biological carbon uptake in the blooms downstream of the sub-Antarctic islands of Kerguelen and Crozet, a first assessment of the affect of the extensive South Georgia phytoplankton blooms on the marine carbon cycle of the Scotia Sea is presented (Chapter 6). The novel seasonal fCO_2 data allowed an assessment of the controls on the marine carbon cycle from the transition from winter CO_2 source to summer CO_2 sink and provided an insight into how the annual marine carbon cycle of the Southern Ocean might respond to future climate change (Chapter 7).

2. Methodology

2.1. Abstract

In October 2006 a new Centre for observation of Air-Sea Interactions and fluXes (CASIX) underway partial pressure of carbon dioxide (pCO_2) system was installed on the British Antarctic Survey (BAS) research and supply vessel, RRS *James Clark Ross*. From 2006 to 2009, sea surface pCO_2 data was collected on 14 research cruises in the Scotia Sea, Southern Ocean. A 1,400 km transect across the Scotia Sea was initiated in spring 2006, with repeat occupations in summer 2008 and autumn 2009 as part of the BAS Discovery-2010 programme: integrating Southern Ocean ecosystems into the Earth System. During summer 2008, the carbonate system was analysed through determination of dissolved inorganic carbon and total alkalinity, through which a suite of other carbonate parameters (pH, carbonate ion concentration and aragonite saturation) and seasonal biogeochemical changes could be calculated. The methodologies used for sample collection, analysis of carbonate data and acquisition of satellite data from 2006 to 2009 are presented. The methodology demonstrated that the carbonate data collected and analysed as part of this research are of comparable accuracy and precision to those described by international guidelines.

2.2. Introduction

A 1,400 km transect across the Scotia Sea (Fig. 2.1) was occupied during cruise JR161 in spring (November-December) 2006, JR177 in summer (January-February) 2008 and JR200 in autumn (March-April) 2009 as part of the British Antarctic Survey (BAS) Scotia Sea FOODWEBS, a component project of the Discovery-2010 programme: integrating Southern Ocean ecosystems into the Earth System: http://www.antarctica.ac.uk/bas_research/our_research/previous_research/gsac/discovery_2010.php.

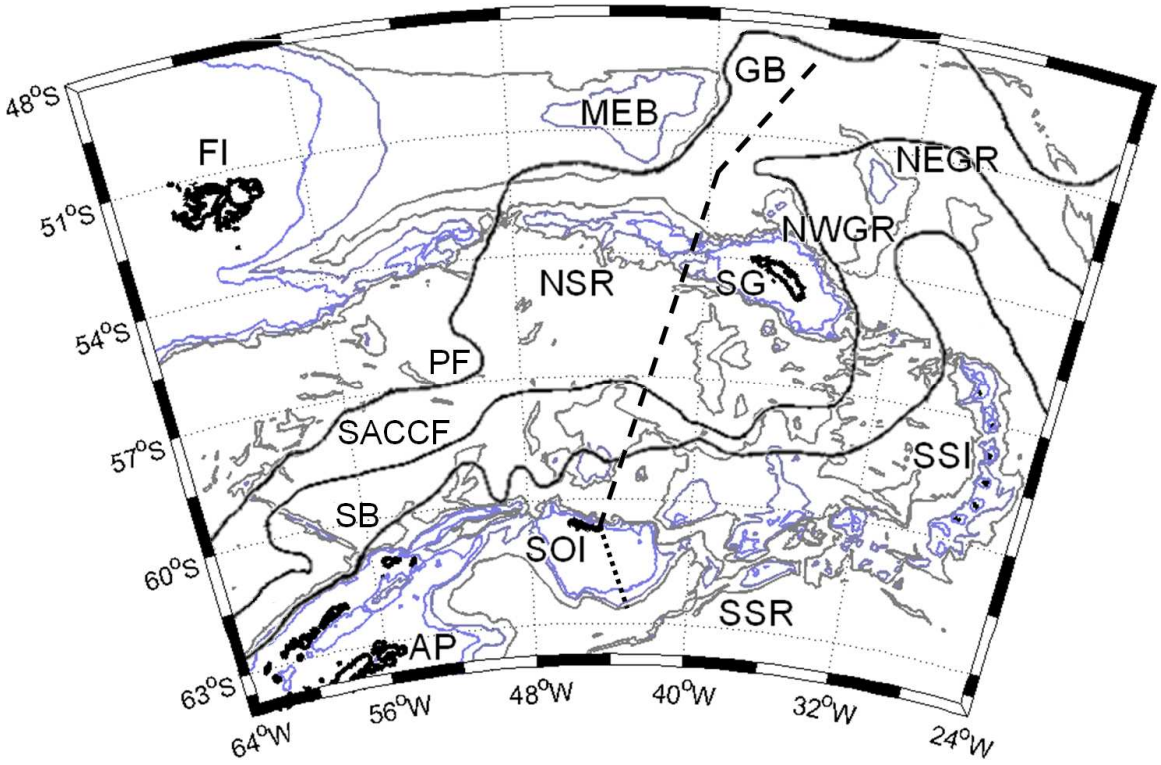

Figure 2.1. A schematic of the Scotia Sea showing the approximate location of the repeat transect (dashed line) and the extended transect (dotted line) from JR177. Some important topographic features are identified: Antarctic Peninsula (AP), South Orkney Islands (SOI), South Scotia Ridge (SSR), South Sandwich Islands (SSI), North Scotia Ridge (NSR), South Georgia (SG), Northwest Georgia Rise (NWGR), Northeast Georgia Rise (NEGR), Georgia Basin (GB), Maurice Ewing Bank (MEB) and the Falkland Islands (FI). Antarctic Circumpolar Current (ACC) fronts are shown schematically, adapted from Meredith et al. (2003a): the Southern Boundary (SB, Orsi et al., 1995), Southern ACC Front (SACCF, Thorpe et al., 2002) and the Polar Front (PF, Moore et al., 1999). Depth contours are at 1000, 2000 and 3000 m (GEBCO, 2001).

In October 2006 a new Centre for observation of Air-Sea Interactions and fluXes (CASIX) underway partial pressure of carbon dioxide (pCO_2) system was installed on the BAS research and supply vessel, RRS *James Clark Ross* (Fig. 2.2). Since then sea surface pCO_2 data has been collected on 20 cruises in five sub-regions of the Southern Ocean (Table 2.1). Of these, 14 cruises have taken place in the Scotia Sea: one pilot study, three core seasonal cruises and ten secondary cruises.

Figure 2.2. The RRS *James Clark Ross* showing the outline of the CASIX underway pCO_2 system.

The objective of the Discovery-2010 programme was to understand the seasonal structure and function of different food webs, in contrasting regions of productivity, and to infer the effects on the transfer of carbon dioxide (CO_2) from the atmosphere to the deep ocean. This was realised through high frequency surface sampling and deep hydrographic stations. Sea surface pCO_2 measurements were made during all three core seasonal cruises, from the CASIX underway pCO_2 system (JR161, JR177 and JR200) and a University of East Anglia (UEA) underway pCO_2 system (JR177). In the following chapter, the methodologies used for seawater sample collection, carbonate analyses and acquisition of satellite data from 2006 to 2009 will be described.

Table 2.1. Cruises of RRS *James Clark Ross* in the Southern Ocean from 2006 to 2009 with underway pCO_2 data.

Cruise	*Region(s)*	*Year*	*Dates*	*Comments*
JR152/159	Scotia Sea	2006	2 Oct-20 Oct	Pilot study
JR161	Scotia Sea	2006	20 Oct-1 Dec	Spring core cruise
JR163/164	Scotia Sea	2006	5 Dec-2 Jan	Secondary cruise
JR157/166	Falkland Plateau	2007	4 Jan – 22 Jan	
JR158	Scotia Sea Antarctic Peninsula	2007	22 Jan-22 Feb	Secondary cruise
JR165/170	Drake Passage Antarctic Peninsula	2007	22 Feb-16 Apr	
JR167/168	Scotia Sea	2007	16 Apr-12 May	Secondary cruise
JR209	Falkland Plateau	2007	20 Oct-24 Oct	
JR184	Scotia Sea	2007	30 Oct-29 Nov	Secondary cruise
JR193/196	Scotia Sea Antarctic Peninsula	2007	29 Nov-07 Dec	Secondary cruise
JR185	Scotia Sea	2007	18 Dec-21 Dec	Secondary cruise
JR177	Scotia Sea	2008	02 Jan-17 Feb	Summer core cruise pCO_2 intercomparison
JR179	Drake Passage Antarctic Peninsula	2008	22 Feb-11 Apr	
JR186	Scotia Sea	2008	11 Apr- 25 Apr	Secondary cruise
JR218	Falkland Plateau	2008	6 Nov-10 Nov	
JR187	Scotia Sea	2008	14 Nov-3 Dec	Secondary cruise
JR194/197	Antarctic Peninsula Scotia Sea	2008	12 Dec-31 Dec	Secondary cruise
JR188	Scotia Sea	2009	31 Dec-7 Jan	Secondary cruise
JR224	Falkland Plateau	2009	11 Jan-19 Feb	
JR200	Scotia Sea	2009	11 Mar-17 Apr	Autumn core cruise

2.3. Cruise descriptions

2.3.1. Pilot study

A pilot study was carried out during October 2006 (JR152/159) where the CASIX pCO_2 instrument was installed and tested onboard (Table 2.1).

2.3.2. Core seasonal cruises

The three core seasonal cruises provided the data that are the primary focus of this research, a contribution to the BAS Discovery-2010 programme (section 2.2). The programme involved deep hydrographic stations and high resolution underway sampling along a 1,400 km transect from the South Orkney Islands (SOI) to 49°S, which was occupied during austral spring 2006 (JR161), summer 2008 (JR177) and autumn 2009 (JR200) (Fig. 2.1). During JR177, the transect was extended south of the SOI to the southern edge of the South Scotia Ridge (SSR) at about 63°S.

For each cruise, the RRS *James Clark Ross* sailed southeast from the Falkland Islands (FI) to the SOI to begin the northward transect, passing to the west of South Georgia and up to the Polar Front (PF) before returning to the FI. Across the three seasons, the transects encompassed numerous archetypal Southern Ocean environments: the marginal ice zone (MIZ), from sea ice cover to regions of substantial sea ice melt, frontal systems, open ocean regimes and intense phytoplankton blooms. The Southern Boundary was identified at about 59°S (Chapter 4), which marked the transition from the Weddell-Scotia Confluence (WSC) into waters of the Antarctic Circumpolar Current (ACC). The PF marked the northern limit of the ACC within the Antarctic Zone (AAZ) of the Scotia Sea.

Hydrographic stations were occupied in regions of contrasting productivity after inspection of near-real time satellite chlorophyll-a images from the Natural Environment Research Council Earth Observation Data Acquisition and Analysis Service (NEODAAS). As the aim of the FOODWEBS project was to investigate the seasonality in the biological, chemical and physical oceanography, the core cruises were carried out during representative seasonal months to capture characteristic conditions of spring, summer and autumn (Table 2.1). Satellite data were valuable to study the advance and retreat of sea ice and the seasonal progression of phytoplankton blooms.

In addition to the new CASIX underway pCO_2 system, an established UEA underway pCO_2 system was run in parallel during JR177 in order to conduct an at-sea pCO_2 instrument intercomparison to determine the suitability of the CASIX instrument for oceanic pCO_2 measurements (Chapter 3). The carbonate system, from the surface to the deep ocean, was analysed during JR177 through determination of dissolved inorganic carbon and total alkalinity (Chapter 4). These were the first deep carbonate measurements of the Scotia Sea and are presented alongside vertical sections of the hydrographic parameters to identify the water masses and hydrographic fronts in the region. The corresponding distributions of the carbonate parameters were used to investigate the processes that govern the marine carbon cycle in the MIZ (Chapter 5) and in extensive phytoplankton blooms (Chapter 6). Samples collected at the depth of the potential temperature minimum, within the Winter Water (WW), during summer 2008 (JR177) were used to determine surface biogeochemical conditions during the preceding winter (2007). This completed the seasonal dataset for the Scotia Sea and enabled an investigation into the variability of the marine carbon cycle in the context of seasonal biological and physical processes and future ocean acidification (Chapter 7).

2.3.3. Secondary cruises

The ten secondary cruises were conducted as part of other science programmes and logistic operations of the RRS *James Clark Ross* in the Scotia Sea and provided supplementary underway pCO_2 data to those described above (Table 2.1). The sea surface pCO_2 data are shown alongside the data collected from the core seasonal cruises to complement the major findings of this research (Chapter 8).

2.4. Underway and station sampling

Continuous measurements of temperature and salinity in surface water were made on all cruises (Table 2.1) using an underway oceanlogger with an intake 6.5 m below the surface. High resolution, vertical profiles of potential temperature and salinity (Fig. 4.2) were obtained during the downcast of a conductivity, temperature, depth (CTD) sensor (Seabird SBE9 +). All salinity values reported here are on the practical salinity scale.

The summer mixed layer depth (MLD) is defined here as the depth where the potential density exceeds that measured at 10 m by 0.05 kg m^{-3} (Brainerd and Gregg, 1995). This definition was selected to provide a depth that is located between the active mixing layer and the seasonal

mixed layer. The winter mixed layer depth (WMLD), marking the remnant of the WW, is defined here as the depth of the potential temperature minimum (θ_{min}). Mixed layer depths were calculated from 2 dbar profiles of potential temperature and salinity from the CTD deployment at each station. During JR177, 360 CTD samples and 60 underway samples were taken in total (Tables 2.2-2.3).

Table 2.2. Hydrographic stations of the Weddell-Scotia Confluence (WSC) during cruise JR177: station number, classification, date, location and bottom depth. Station classification: Southern Boundary (SB). Samples is the total number of Niskins sampled from the CTD at the specified depths. For 10 depths (m): 5 10 30 50 80 120 160 200 400 600 and for 20 depths: 5 10 20 30 40 50 60 80 100 120 140 160 180 200 400 600 800 1000 1500 2000. Notes: (1) changed deep samples to 2 × 1000 m and 1 × 1200 m; (2) Niskins 4 (2000 m), 5 (1500 m) and 6 (1000 m) all had loose caps and were not sampled; (3) two casts were carried out due to a malfunction halfway through the first cast.

CTD	*Date*	*Start time*	*Latitude*	*Longitude*	*Classification*	*Depth*	*Samples*	*Note*
	2008	*hh:mm*	*°S*	*°W*		*m*		
02	04 Jan	07:50	60.498	48.193	Open water	1396	20	1
05	08 Jan	09:07	60.208	44.408	Open water	5543	20	2
08	09 Jan	13:41	60.431	44.593	Open water	999	10	
09	10 Jan	01:52	61.198	44.408	Meltwater	319	10	
10	10 Jan	09:54	61.665	44.053	Ice edge	570	10	
12	10 Jan	22:59	62.355	43.529	Sea ice	1238	10	3
14	11 Jan	09:30	62.608	43.234	Sea ice	3075	10	
16	13 Jan	09:14	59.936	44.239	Open water	4784	10	
17	15 Jan	07:32	59.689	44.054	Open water	4172	20	
21	17 Jan	00:25	59.144	43.694	SB	3611	10	

Table 2.3. Hydrographic stations of the Antarctic Zone (AAZ) during cruise JR177: station number, classification, date, location and bottom depth. Station classification: Southern Antarctic Circumpolar Current Front (SACCF), Antarctic Circumpolar Current (ACC), high-nutrient low-chlorophyll (HNLC), North Scotia Ridge (NSR), South Georgia (SG). Samples as for Table 2.2. Notes: (1) a deep chlorophyll-a maximum was identified; (2) 5 m bottle was fired at 10 m due to rough weather; (3) Niskin 24 (5 m) was leaking and not sampled.

CTD	*Date*	*Start time*	*Latitude*	*Longitude*	*Classification*	*Depth*	*Samples*	*Note*
	2008	*hh:mm*	*°S*	*°W*		*m*		
25	19 Jan	07:02	58.023	42.985	SACCF	2831	20	
28	20 Jan	21:41	57.758	42.801	ACC	2904	10	
30	22 Jan	04:43	57.140	42.433	HNLC	3700	10	
33	22 Jan	15:57	56.843	42.257	HNLC	4248	20	1
35	23 Jan	13:10	55.902	41.720	ACC	3595	10	2
37	25 Jan	11:50	55.207	41.246	ACC bloom	3246	20	
41	28 Jan	20:11	54.913	41.173	ACC	3442	10	3
42	29 Jan	10:31	54.591	40.997	ACC	3301	10	
43	29 Jan	15:09	54.216	40.813	NSR	2461	10	
44	29 Jan	19:06	53.897	40.645	NSR	1233	10	
46	30 Jan	11:18	53.155	40.276	NSR	4052	10	
48	01 Feb	07:24	52.857	40.097	NSR	3811	20	
51	02 Feb	21:28	52.727	40.147	SG bloom	405	10	
53	04 Feb	08:10	52.627	39.102	SG bloom	3750	20	
55	09 Feb	15:45	53.714	37.964	SG shelf	126	10	
58	11 Feb	17:45	53.567	34.962	SG shelf	3610	10	
59	11 Feb	21:50	53.691	35.258	SG shelf	3602	10	

2.5. Atmospheric and seawater CO_2

2.5.1. The pCO_2 principle and instruments

The principle of measuring seawater pCO_2 is based on the equilibration of a headspace with a continuous stream of seawater and subsequent determination of the CO_2 mixing ratio (xCO_2) in the sampled headspace air. The infra-red adsorption properties of CO_2 are used to determine xCO_2 in the sampled air. The determination of pCO_2 is dependent on temperature, pressure and water vapour content. The partial pressure of an ideal gas is defined as the product of xCO_2 and total pressure of the gas phase. To account for the non-ideal nature of CO_2, the fugacity of CO_2 (fCO_2) should be used comparing to other parameters of the carbonate system (sections 2.8 and 2.12) (Zeebe and Wolf-Gladrow, 2001; DOE, 2007).

Quasi-continuous measurements of the pCO_2 in surface seawater and marine air were made using the new CASIX pCO_2 instrument (2006-2009), developed at the Plymouth Marine Laboratory in collaboration with Dartcom, and a long-running UEA pCO_2 instrument (summer 2008) designed and built at the University of East Anglia. Sampling of marine air is very similar for both instruments and will be described first, followed by details of the individual instrument design and continuing with features common to both instruments and the pCO_2 calculation process. The accuracy and precision of both instruments is discussed in section 3.4.

2.5.2. Atmospheric CO_2

To sample the marine air a ¼″ outer diameter Dekabon tubing air line was run to each instrument from the central bridge at 15 m height. The inlet was finished with a Whatman 1.0 μm PTFE filter in order to remove solid particulates and a plastic funnel to ensure that any moisture that collects drips off the larger rim to prevent the comparatively narrow line from becoming frozen. The samples were pumped through the 90 m air lines before entering the cooling system of each instrument for analysis in the laboratory. It is important to record the relative wind speed and direction to confirm that the air being sampled is not contaminated by ship exhaust gases.

2.5.3. UEA underway pCO_2 system

The detailed design of the UEA underway pCO_2 system has previously been described in Cooper et al. (1998) and changes incorporated between 2001 and 2007 are reported in Schuster and Watson (2007). Surface seawater from the underway supply is introduced at a rate of 4 L min^{-1} into a percolating, packed bed equilibrator (Fig. 2.3). The system is maintained at ambient atmospheric pressure through a coiled vent positioned in the top of the equilibrator. The air from the equilibrator head space is circulated through a dual channel, non-dispersive infra-red (IR) analyser, a LICOR 7000 (LICOR Inc., USA) to measure the xCO_2 and water content simultaneously. The xCO_2 is measured relative to a dry and CO_2 free reference cell. The LICOR is calibrated using three secondary BOC gas standards of nominal CO_2 concentrations of 250, 350 and 450 µmol mol^{-1} in artificial air (21% O_2, 79% N_2). All BOC gases were calibrated against certified, high precision, primary standards from the National Oceanic and Atmospheric Administration (NOAA) (Table 2.4). The mixing ratios of the calibration gases were selected to bracket the 'natural' range of seawater CO_2.

Samples from the equilibrator headspace and marine air are partially dried by passing through a cold trap at 2 °C, prior to analysis in the LICOR. Drying the air eliminates the possibility of condensation in the tubing and minimises the uncertainty related with water vapour contamination. Analyses of all parameters were carried out at a flow of 100 ml min^{-1} through the LICOR at a slight overpressure ('flush' conditions). A final analysis for each parameter was made at atmospheric pressure under 'non-flush' conditions. The flow and overpressure did not have a discernable effect on the CO_2 and H_2O measurements.

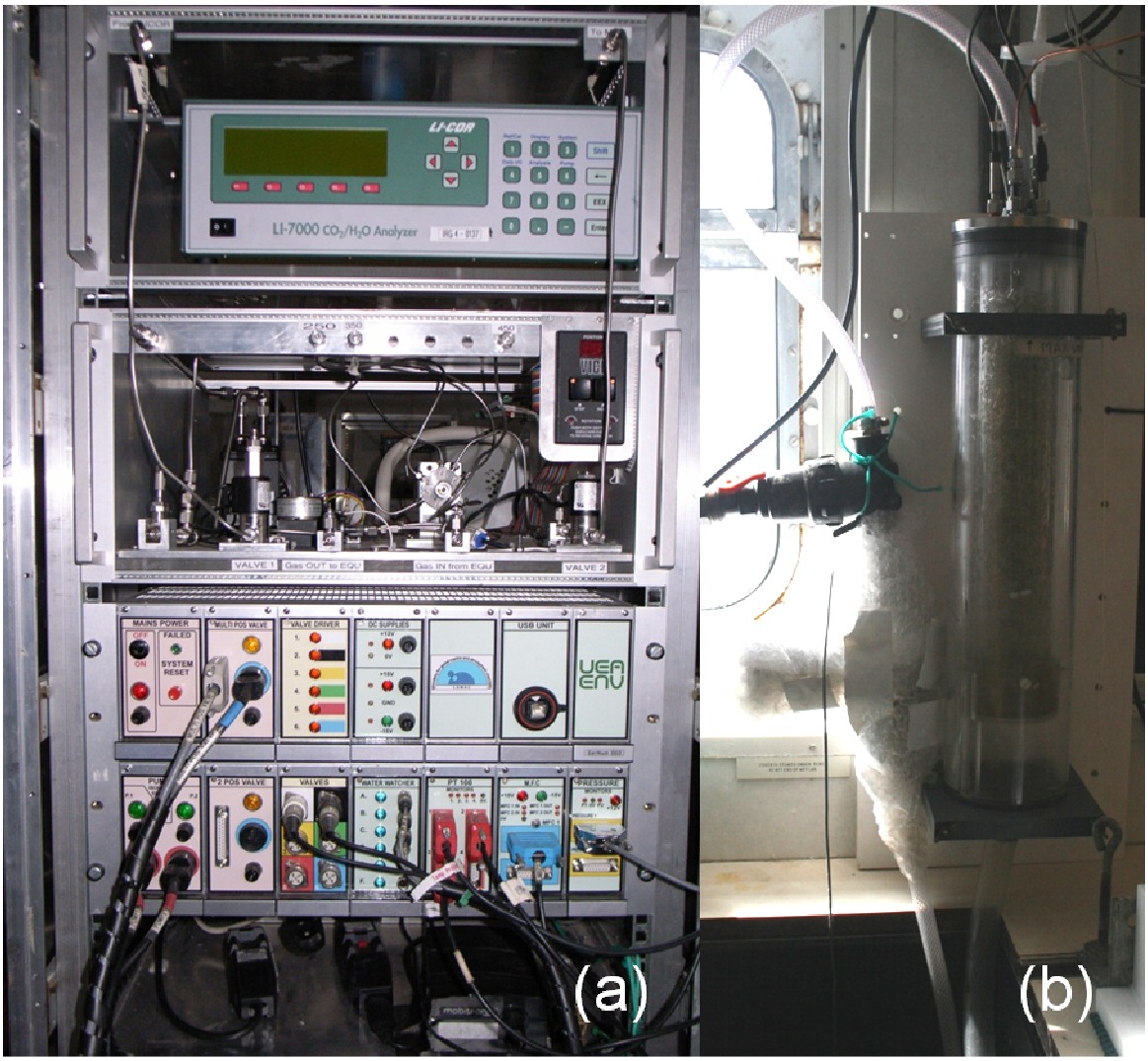

Figure 2.3. Main parts of the University of East Anglia (UEA) underway pCO_2 system, (a) the LICOR 7000, sampling components and electronics unit and (b) the equilibrator and oxygen optode.

The measurement routine begins by calibrating the system with one of the gas standards, with a priority order of analysis as 250, 450, 350 and then a 0 CO_2 ppm in artificial air (21% O_2, 79% N_2) standard. The CO_2 and H_2O content is determined every minute during a 30 minute cycle, with 29 minutes of continual flushing at a slight overpressure and 1 minute with non-flush conditions at ambient pressure. Once a standard has been run, the system alternates between equilibrator headspace and marine air readings (3 × 32 minutes). The CO_2 and H_2O content is determined every minute during a 32 minute cycle, with 31 minutes of continual flushing at a slight overpressure and 1 minute with non-flush conditions at ambient pressure.

A second standard is then run and the analysis cycle repeats itself with a complete calibration of the instrument every 6 hours. All raw data are time stamped by a Garmin GPS module mounted on the starboard side of the ship. Ancillary data from the ship's underway oceanlogger and meteorological station are added during the data processing. Gaps in the data are due to the seawater supply being turned off in ice or very shallow water, contamination from the ship exhaust gases, replacement of instrument components and pressure leak testing or calibrations.

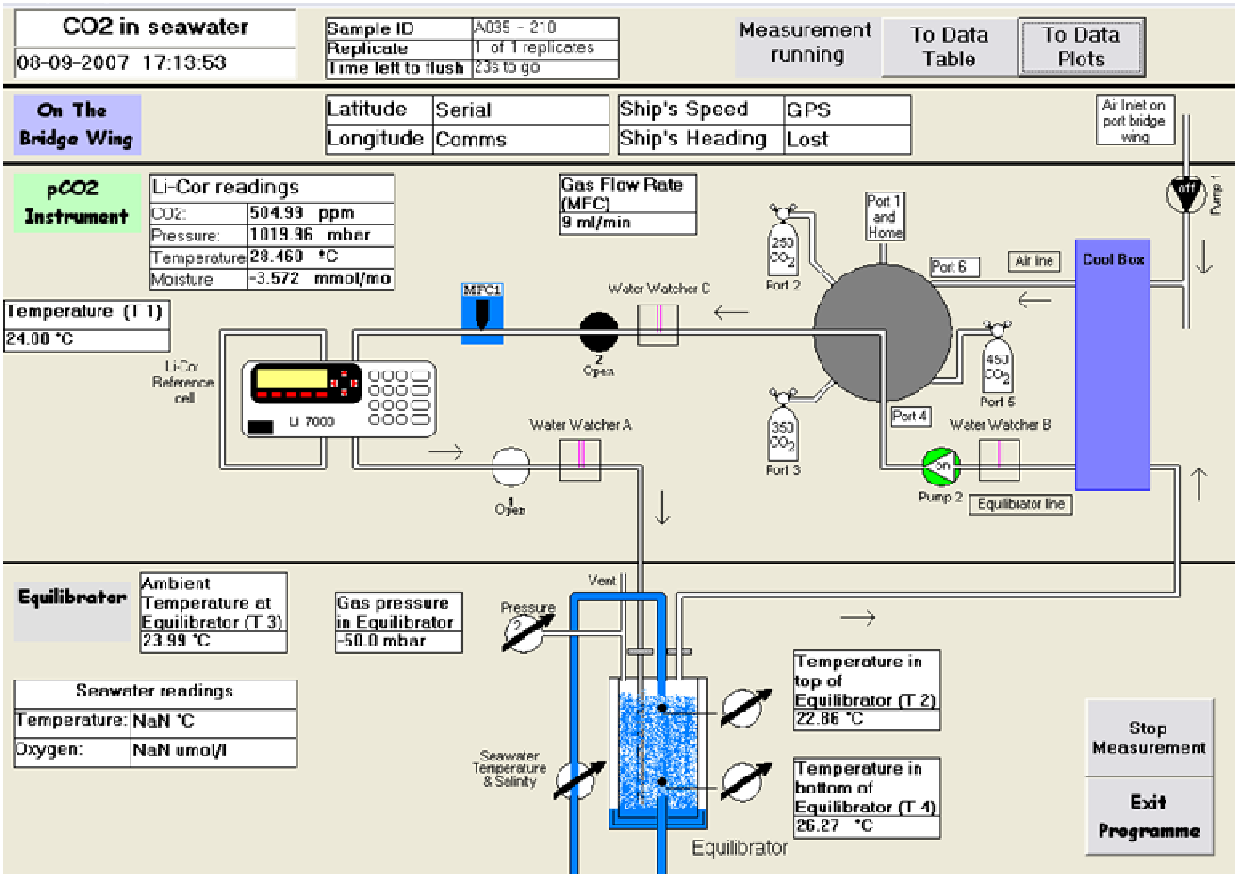

Figure 2.4. The software control screen for the UEA pCO_2 system.

2.5.4. CASIX underway pCO_2 system

The design and set-up of the new CASIX underway pCO_2 system is based on some of the principles outlined in Cooper et al. (1998). Surface seawater from the ship's underway supply is introduced at a rate of approximately 6 L min^{-1} into a non-vented, percolating, packed bed equilibrator (Fig. 2.5). The air from the equilibrator head space is circulated through a LICOR 840, which is calibrated using two secondary BOC gas standards of approximately 250 and

450 µmol CO_2 mol^{-1} in artificial air (21% O_2, 79% N_2). All BOC gases were calibrated against certified, high precision, primary standards from NOAA using a LICOR 6262 (Table 2.5). Nitrogen is used as the zero reference gas.

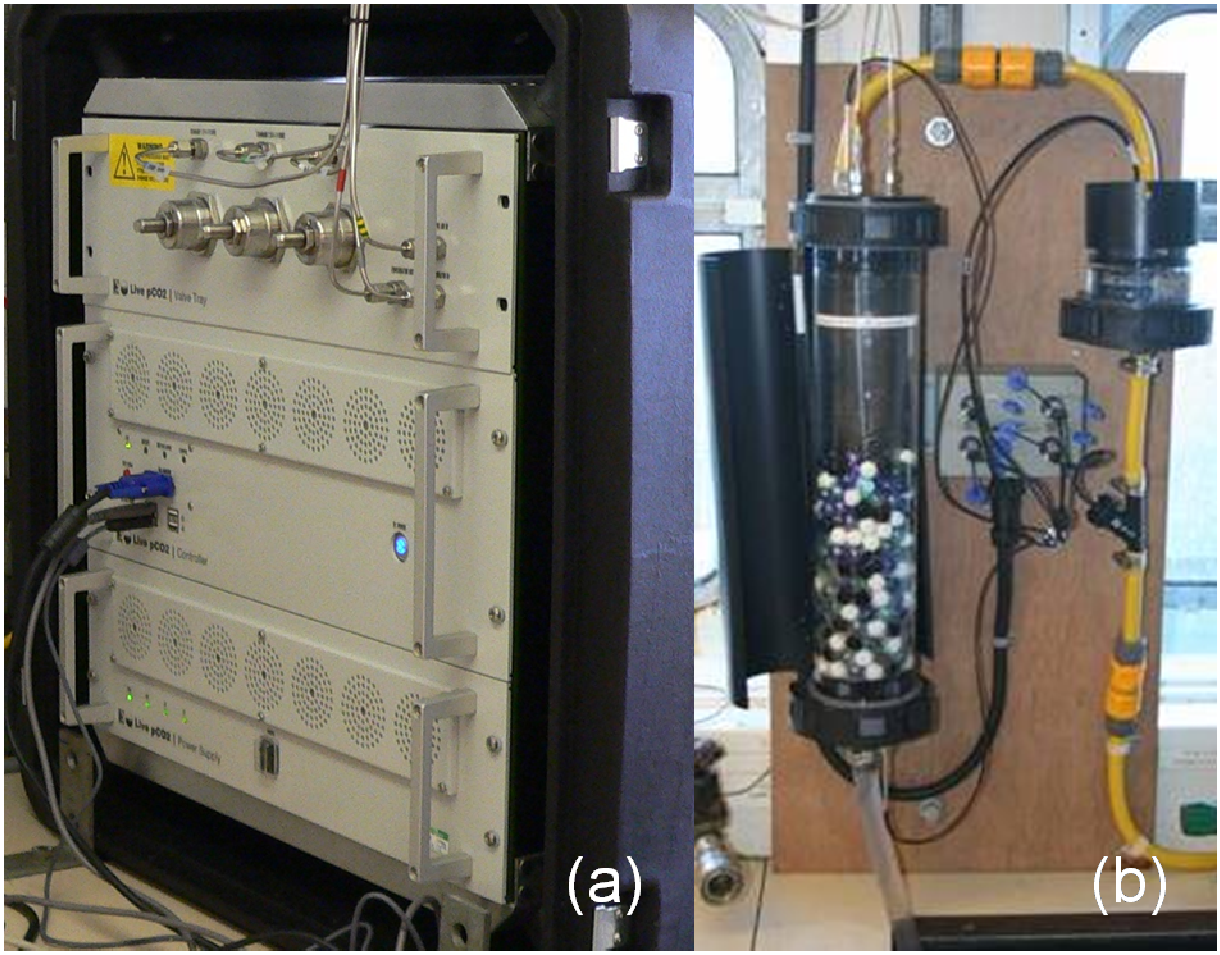

Figure 2.5. Main parts of the CASIX underway pCO_2 system, (a) the valve trays and electronics unit and (b) the equilibrator and oxygen optode.

Samples from the equilibrator headspace and marine air were partially dried by passing through a Peltier condenser system, prior to analysis in the LICOR. Analyses of all parameters were carried out at a flow of 200 ml min^{-1} through the LICOR at a slight overpressure. The measurements are made in the following sequence: equilibrator headspace air, ancillary data acquisition, marine air and gas standards. The routine for sampling of equilibrator air was 2 minutes of continual flushing and 2 minutes with non-flush conditions, repeated 4 times (4 × 4 minutes), followed by 2 minutes of continual flushing and 2 minutes of LICOR rest, sample and vent (1 × 4 minutes). The routine for marine air sampling is 4 minutes of continual

flushing and 1 minute of LICOR rest, sample and vent with non-flush conditions at ambient pressure (1 × 5 minutes). One of the gas standards is then run with 2 minutes of continual flushing and 1 minute of LICOR rest, sample and vent (1 × 3 minutes). The cycle is repeated every 30 minutes, alternating between the two gas standards, with a priority order of analysis of the 250 and 450 standards and then the nitrogen. The instrument is fully calibrated every 90 minutes. Ancillary data from the ship's underway oceanlogger and meteorological station are integrated directly into the pCO_2 output file. Gaps in the data as previously explained (section 2.5.3).

2.5.5. Determination of fCO_2

LICOR millivolt (mV) readings are converted into mole fraction mixing ratios using internal algorithms that are specific to each LICOR model. The raw xCO_2 values in µmol mol^{-1} (parts per million, ppm) are corrected for the water vapour content (xH_2O) in mmol mol^{-1} (parts per thousand, ppt) to account for the IR band broadening effects of water vapour:

$$xCO_{2\ dry} = \frac{xCO_{2\ raw}}{1 - \left(xH_2O / 1000\right)} \qquad \text{Equation 2.1.}$$

The dried xCO_2 readings are corrected to account for drift in the LICOR by linear interpolation between the nearest gas standards xCO_2, which are corrected to their calibrated values (section 2.6.1). The pCO_2 is determined with the ambient pressure (P, atm) and is proportional to xCO_2 . Air in the equilibrator headspace is assumed to be at 100% humidity, like air overlying the sea surface. Therefore, the pCO_2 in the equilibrator headspace at 100% humidity must be reduced to account for the 'apparent' increased CO_2 concentration as a result of the removal of the water vapour:

$$pCO_{2\ Teq\ wet} = xCO_{2\ dry}\left(P - pH_2O\right) \qquad \text{Equation 2.2.}$$

where pH_2O is the water vapour pressure in air overlying seawater of a given salinity at the temperature of equilibration (Teq, K) (Weiss and Price, 1980):

$$pH_2O = 0.981 \exp\left(14.32602 - \frac{5306.83}{Teq}\right) \qquad \text{Equation 2.3.}$$

The pCO_2 measured in the equilibrator is correct for the temperature of equilibration (*Teq*). For oceanographic research it is necessary to correct the pCO_2 to the temporally co-located sea surface temperature (SST, K), representing the bulk temperature of the mixed layer (Takahashi et al., 1993):

$$pCO_{2\ SST\ wet} = pCO_{2\ Teq\ wet} \exp\left(0.0423\ (SST - Teq)\right) \qquad \text{Equation 2.4.}$$

The fCO_2 is determined from the pCO_2 alongside the total pressure (*P*, atm), the first virial coefficient of CO_2 (*B*, $m^3\ mol^{-1}$), the cross virial coefficient (δ, $m^3\ mol^{-1}$), the molar gas constant (*R*, $J\ K^{-1}\ mol^{-1}$) and the temperature (*T*, K) as outlined in Zeebe and Wolf-Gladrow (2001) and DOE (2007):

$$fCO_2 = pCO_2 \exp\left(P\,\frac{B + 2\delta}{RT}\right) \qquad \text{Equation 2.5.}$$

The fugacity coefficient (the ratio of fugacity to partial pressure) is a function of temperature and composition of the gas phase and in most cases is very close to 1. From inspection of the calculation procedure (Eqns. 2.2-2.5), seawater fCO_2 is highly dependent on temperature. Therefore, it is critical to have accurate temperature measurements both in the equilibrator, where the actual CO_2 concentration is being measured, and at the sea surface. To minimise errors sourced from temperatures, it is important that the water in the equilibrator be as close to sea surface temperature as possible. This is achieved by using a high flow rate of seawater to reduce the extent to which the water is warmed (Table 3.1). This research uses sea surface temperatures as measured by the underway oceanlogger temperature sensor located in the hull of RRS *James Clark Ross* at 6.5 m depth (Fig. 2.2). Equilibrator temperature is the average of two platinum resistant thermometers placed in the upper and lower parts of the seawater stream in the equilibrator. A discussion of equilibrator and sea surface temperatures follows in sections 2.6.3 and 2.6.4, respectively.

2.6. Instrument calibrations

2.6.1. BOC gas standards

For calibration of the BOC cylinders, high precision, primary standards from NOAA are used that cover the nominal mixing ratios of 250, 350 and 450 µmol CO_2 mol^{-1} for the UEA instrument and 250 and 450 µmol CO_2 mol^{-1} for the CASIX instrument. All tubing was flushed with nitrogen prior to the calibrations to ensure that all lines were fully dried. The calibration routine began and finished with the NOAA standards, running the series of BOC gas standards in between in ascending order of CO_2 mixing ratios.

The main cycle time for each gas was approximately 30 minutes to allow sufficient flushing of the lines and stabilisation of readings. Logging of data from the LICOR 7000 was every minute and for the LICOR 840 was every 10 seconds. The near-final 20 minutes worth of readings were used to calculate the mean and standard deviation for each BOC cylinder. The response of the LICOR was determined using linear regression of the absolute NOAA calibrated xCO_2 values and the LICOR output xCO_2 for the NOAA standards (Fig. 2.6). The resultant relationship was then applied to all raw xCO_2 readings for each of the BOC gas standards to give a calibrated value, with associated standard deviation (Tables 2.4 and 2.5).

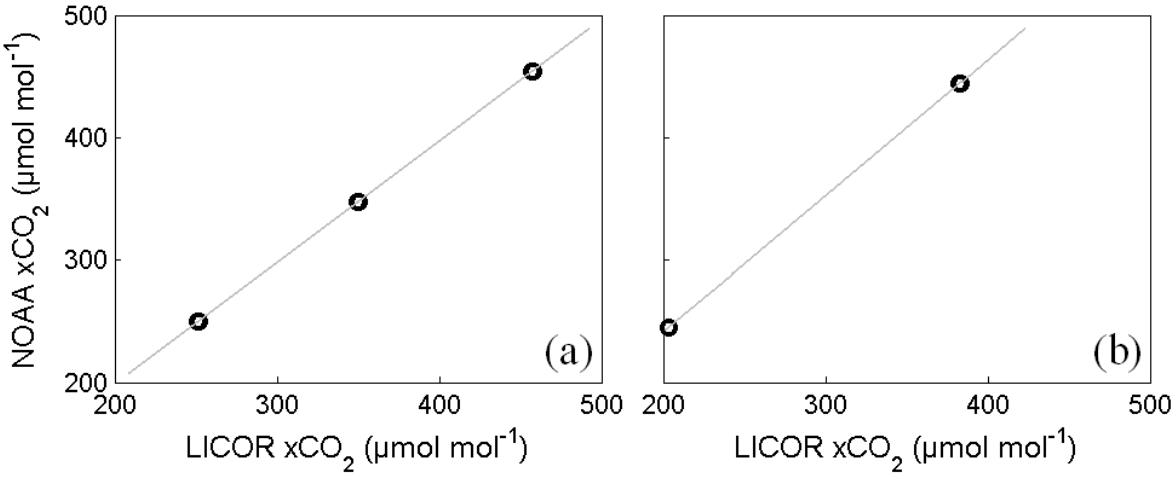

Figure 2.6. Calibration curves for NOAA cylinders using a (a) LICOR 7000 and a (b) LICOR 840. The response of the LICOR, based on absolute NOAA readings, was 0.99(xCO_2raw) + 0.25 and 1.11(xCO_2raw) + 19.39 for the LICOR 7000 and 840, respectively.

Table 2.4. BOC gas calibration dates and xCO_2 for UEA instrument standards used on JR177. Standard deviations are shown in parentheses.

Cylinder ID	*Standard*	*Date 1*	*xCO_2 1*	*Date 2*	*xCO_2 2*
			$\mu mol\ mol^{-1}$		*$\mu mol\ mol^{-1}$*
25B16	250	20.06.07	249.12 (0.06)	01.08.08	248.85 (0.03)
35B01	350	20.06.07	356.46 (0.04)	01.08.08	356.56 (0.04)
45B16	450	10.08.07	457.36 (0.04)	01.08.08	457.11 (0.06)

Table 2.5. BOC gas calibration date and xCO_2 for CASIX instrument standards. Standard deviations are shown in parentheses.

Cylinder ID	*Standard*	*Date 1*	*xCO_2 1*	*Date 2*	*xCO_2 2*
			$\mu mol\ mol^{-1}$		*$\mu mol\ mol^{-1}$*
111903	250	24.07.06	250.15 (0.13)	10.09.07	250.21 (0.33)
150464	250	17.07.07	255.41 (0.30)	-	-
129451	450	24.07.06	449.03 (0.08)	17.07.07	449.79 (0.15)
143967	450	17.07.07	452.25 (0.15)	-	-

2.6.2. LICOR accuracy and precision

The response of the LICORs during the run of the NOAA cylinders is shown in a series of control charts, detailing the two sets of analyses for each NOAA standard, means and standard deviations (Figs. 2.7 and 2.8). Control charts are used to demonstrate whether the instrument measurement is 'in control' and if the data display unbiased, natural variability (DOE, 2007). Upper and lower control limits are determined as ± 3 standard deviations of the mean and they provide an indication of problematic data. Each NOAA cylinder was run twice during the calibration day, at the beginning and end and the LICOR xCO_2 is plotted sequentially by analysis number to evaluate the stability of the LICOR over the calibration period.

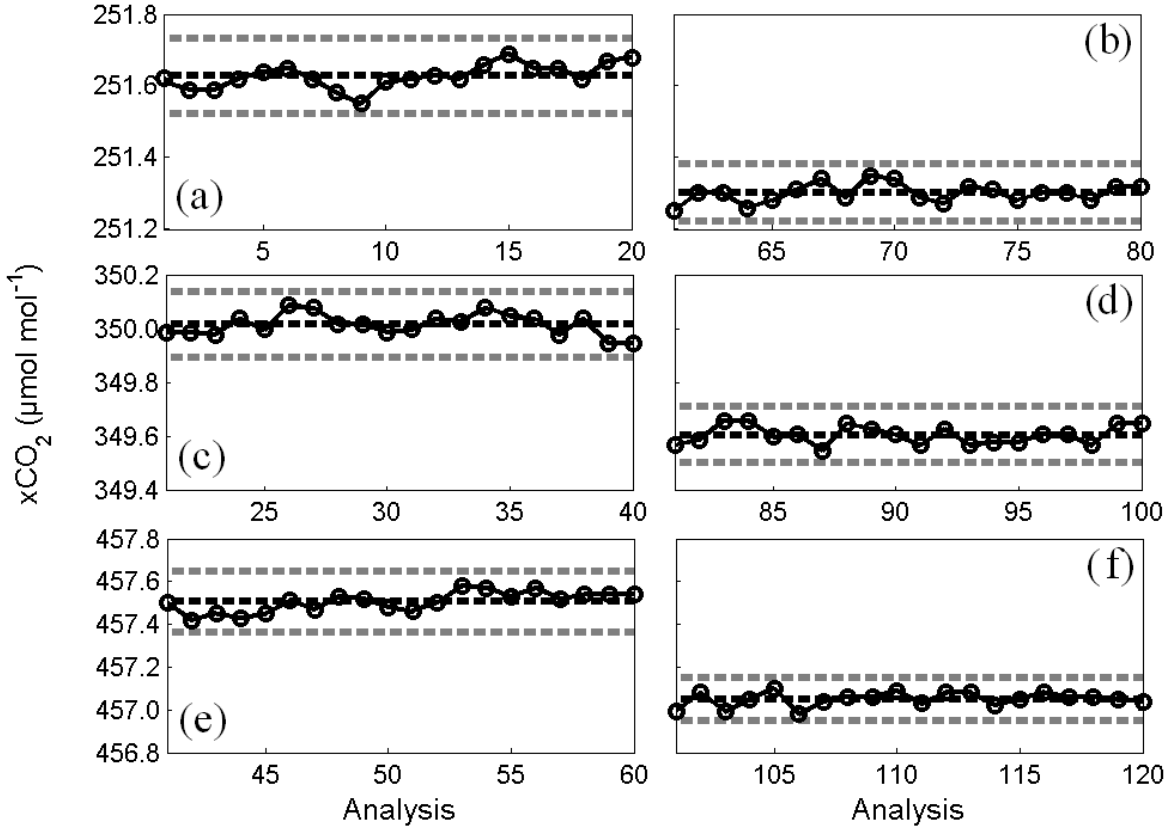

Figure 2.7. Control chart of $x\mathrm{CO_2}$raw measured by the LICOR 7000 during 20 minutes (one value per minute) from the NOAA cylinders (a) first run 250 standard, (b) second run 250 standard, (c) first run 350 standard, (d) second run 350 standard, (e) first run 450 standard and (f) second run 450 standard. First run refers to the set of analyses of NOAA standards at the start of the BOC cylinder calibration, and the second run to the set of analyses of NOAA standards at the end of the BOC calibration session. The black dashed line indicates the mean and grey dashed lines indicate upper and lower control limits (± 3 standard deviations of the mean).

The charts reveal that all points are well within the control limits and therefore that the LICOR measurement is in control. The individual $x\mathrm{CO_2}$ readings for each run had little variation with values tightly fitting round the mean. This indicates that the LICOR 7000 measurements were continually stable over a range of $x\mathrm{CO_2}$ concentrations. The analyses show that the second run of each NOAA cylinder has a lower mean $x\mathrm{CO_2}$, still retaining little variability between successive $x\mathrm{CO_2}$ measurements. This decrease indicates the magnitude of the LICOR drift over a 10 hour period and highlights the necessity to run standard gases frequently, in order to calibrate the LICOR, during sampling. The accuracy of the LICOR, determined from the

maximum difference between the certified NOAA xCO_2 values and the calibrated LICOR xCO_2 values is 0.40 μmol mol^{-1}. The precision for the xCO_2 measurements (average standard deviation of the 6 NOAA runs) using the LICOR 7000 is determined as 0.04 μmol mol^{-1} (Fig. 2.7).

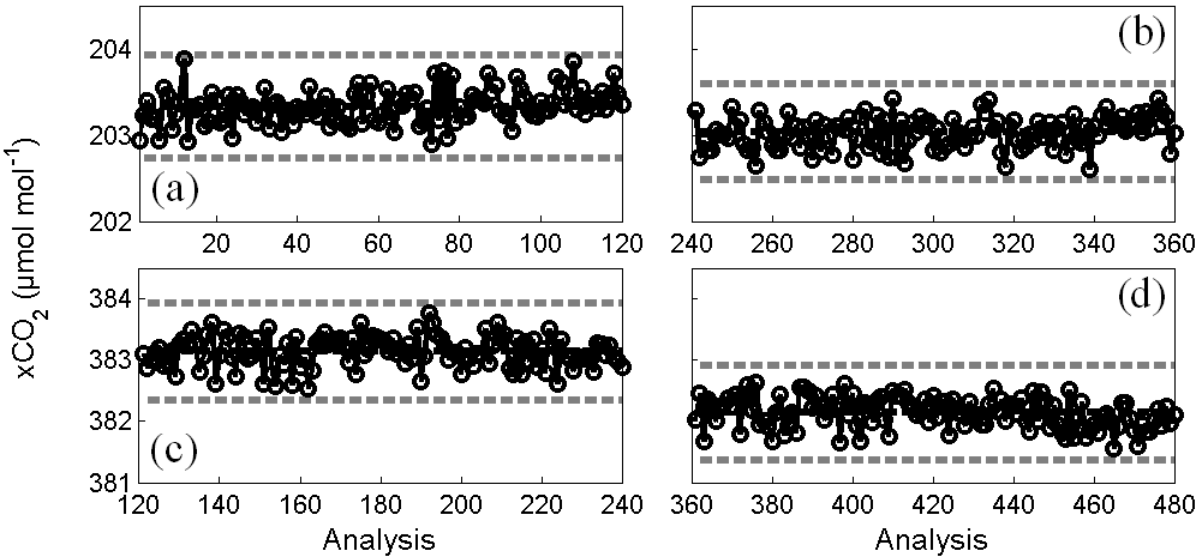

Figure 2.8. Control chart of xCO_2raw measured by the LICOR 840 during 20 minutes (six values per minute) from the NOAA cylinders (a) first run 250 standard, (b) second run 250 standard, (c) first run 450 standard and (d) second run 450 standard. First and second runs as for Figure 2.7. The black dashed line indicates the mean and grey dashed lines indicate upper and lower control limits (± 3 standard deviations of the mean).

The charts reveal that all points are just within the control limits and therefore that the LICOR measurement is in control. Compared to the LICOR 7000, the individual xCO_2 readings for each cylinder run showed more variation, which appeared to increase with increasing CO_2 concentration. The analyses show that the second run of each NOAA cylinder has a slightly lower mean xCO_2, still retaining variability between successive xCO_2 measurements. This indicates the magnitude of the LICOR drift over a 4 hour period and again reinforces the requirement of regular LICOR calibration. The accuracy of the LICOR 840, determined from the maximum difference between the certified NOAA xCO_2 values and the calibrated LICOR xCO_2 values is 1.28 μmol mol^{-1}. The precision for the xCO_2 measurements (average standard deviation of the 4 NOAA runs) is estimated as 0.23 μmol mol^{-1} (Fig. 2.8).

2.6.3. Equilibrator temperature

The calibration of the UEA platinum resistant thermometers (Pt100) required both Pt100s to be held in a temperature calibration bath alongside a calibrated mercury (Hg) thermometer (accurate to 0.1 °C). The bath was set to different temperatures and the thermometers were allowed to reach a stable temperature over 30 minutes. Logging of the Pt100 data was every minute. For each set temperature, the final 10 minutes worth of readings were used to calculate the mean and standard deviation for each Pt100 at the given temperature. The response of the Pt100s was determined using linear regression of the absolute temperature from the Hg thermometer and the Pt100 voltage output (Fig. 2.9). The resultant offset was then applied to all voltage readings for each Pt100 sensor to give a calibrated temperature reading.

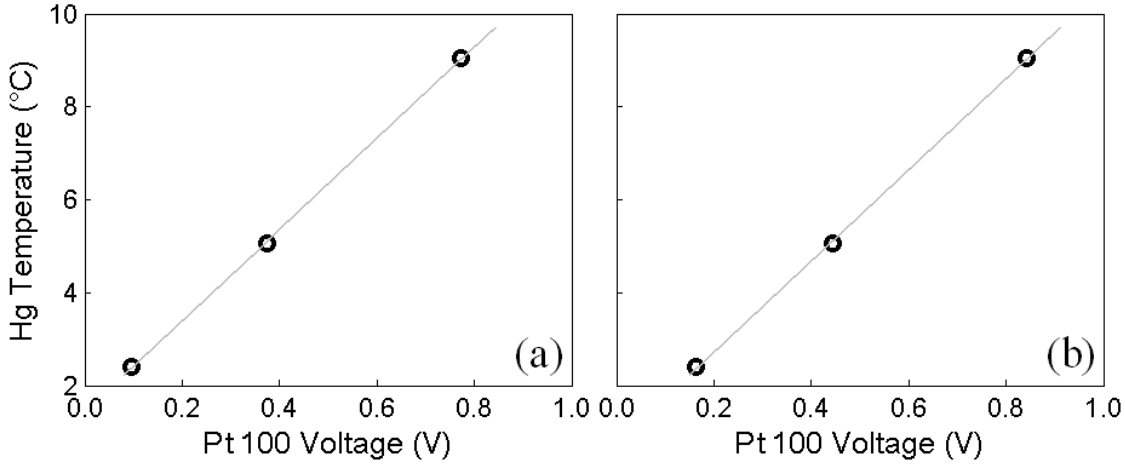

Figure 2.9. Calibration curves for the (a) upper Pt100 temperature sensor and the (b) lower Pt100 temperature sensors on the UEA pCO_2 instrument during JR177. The response of the sensors, based on absolute mercury (Hg) thermometer readings, was T = 0.98V + 1.4 and T = 0.98V + 0.8 for the upper and lower sensors, respectively.

Plots of the upper and lower Pt100 temperatures during the calibration are shown in a series of control charts (Figs. 2.10). The Pt100 sensor response is plotted sequentially by analysis number to evaluate the sensor stability over the calibration period.

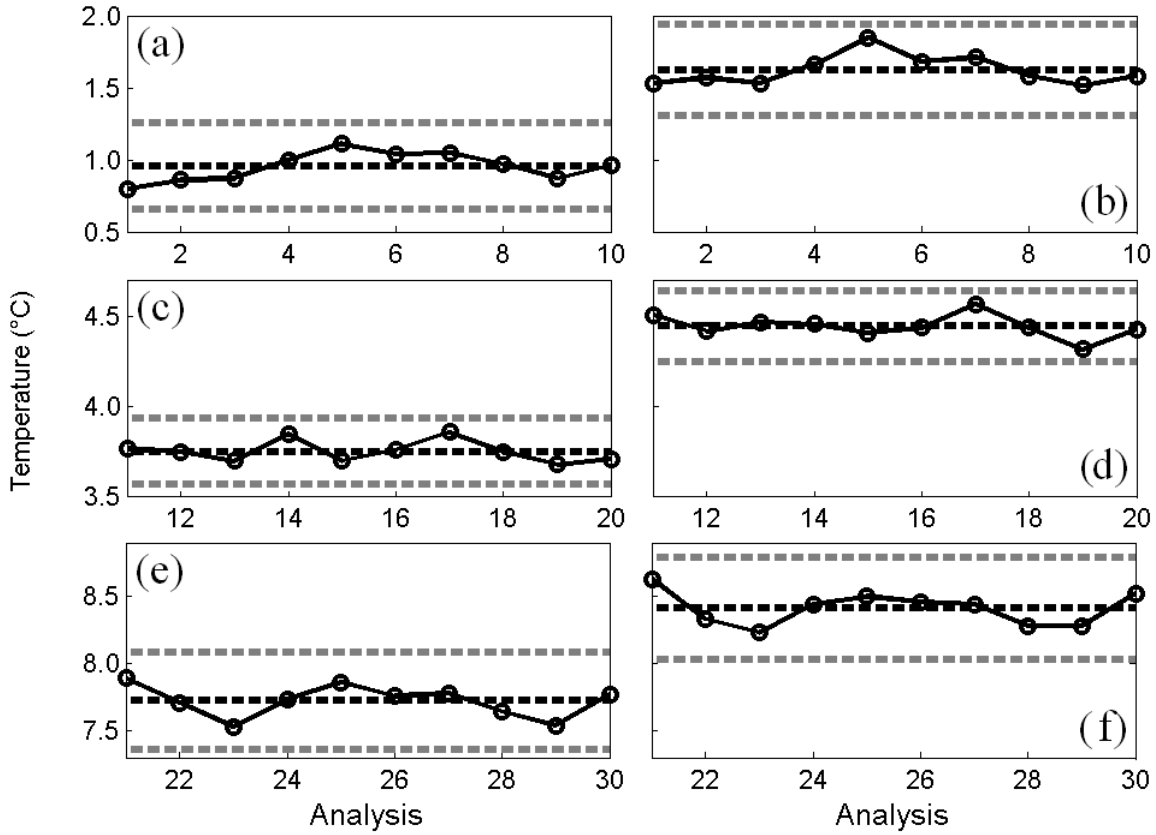

Figure 2.10. Control charts of the raw temperature measured by the upper (a, c, e) and lower (b, d, f) Pt100 sensors of the UEA instrument at three set temperatures. The black dashed line indicates the mean and grey dashed lines indicate upper and lower control limits (± 3 standard deviations of the mean).

The charts reveal that all points are within the control limits and that the temperature measurement is in control. The individual readings for both sensors had little variation with each of the values tightly fitting round the mean. This indicates that the Pt100 temperature measurements were stable over the selected range of set temperatures. The raw measurements (using the previous calibration) show a difference of about 0.5 °C between the two sensors, which is corrected for using the appropriate calibration equation (Fig. 2.9). The accuracy of the Pt100s, determined from the maximum difference between the absolute mercury thermometer temperature and the calibrated Pt100 temperature, is 0.2 °C. The precision of the Pt100 measurements (average standard deviation of 6 Pt100 analyses) is determined as 0.1 °C (Fig. 2.10). The calibrations of the CASIX platinum resistant thermometers (PRTs) followed a similar method and were found to have a matching accuracy and precision of 0.2 °C and 0.1 °C, respectively.

2.6.4. Sea surface temperature

During cruise JR177, sea surface temperature data from the underway oceanlogger (6.5 m below surface) were compared to the potential temperature from the CTD Seabird SBE9+ sensor at hydrographic station 18, north of the SB (Fig. 2.1), where the CTD was suspended at 5 m for 30 minutes. Logging of the underway temperature data was every 5 seconds and all data were used to calculate the accuracy and precision of the oceanlogger temperature sensor.

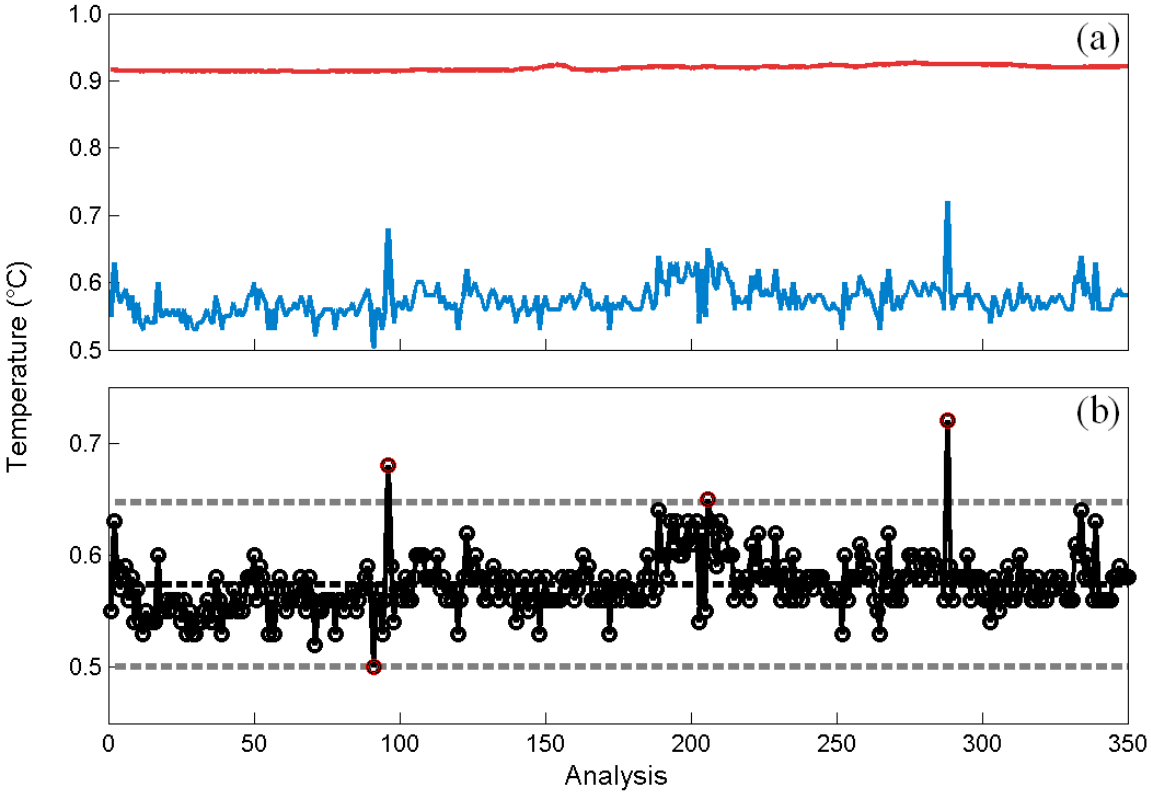

Figure 2.11. Investigating the underway temperature (blue in (a)) data from the oceanlogger by (a) comparison with the CTD temperature (red), (b) control chart of underway temperature response during the 30 minute investigation. The black dashed line indicates the mean and the grey dashed lines indicate upper and lower control limits (± 3 standard deviations of the mean). The red outlined points (b) represent flagged data based on the control limit criteria.

The control chart of the underway temperature reveals four data points that fall outside the control limits (Fig. 2.11b). These appear to occur at random times and show large deviations compared to all other data. Inspection of other oceanlogger parameters and discussion with onboard physicists did not reveal any technical or oceanographic reason to exclude the data. The outliers were attributed to natural fluctuations or noise in the electronics or calibration of

the sensor. Overall, the oceanlogger temperature sensor was in control during the investigation period with 99% of the data falling within the control limits. Despite the inclusion of the outlier values, the accuracy of the oceanlogger temperature sensor, determined from the maximum difference between the CTD potential temperature and the corrected underway temperature is 0.14 °C. The precision for the temperature measurements (average standard deviation during 30 minutes) is determined as 0.02 °C (Fig. 2.11).

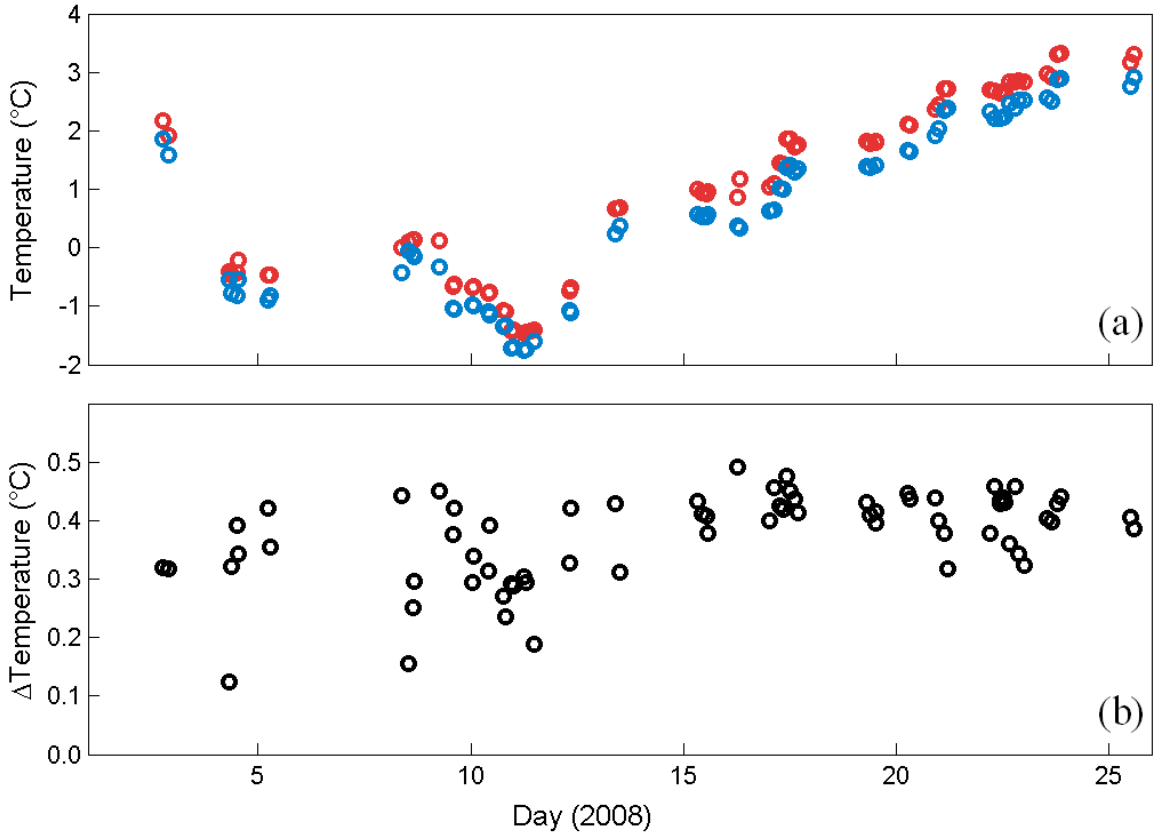

Figure 2.12. (a) downcast and upcast 6 m CTD potential temperature (°C, red) and oceanlogger sea surface temperature (°C, blue) and (b) the difference between the CTD temperature and the oceanlogger temperature (°C) for hydrographic stations 1-37 during JR177.

The mean offset of the underway temperature was determined as -0.37 °C from the difference between the CTD temperature (taken as absolute, checked against high precision SBE35 temperature sensor) and the oceanlogger temperature for CTD 18 (Fig. 2.11a). To investigate the nature of the temperature offset, CTD and underway temperature were compared for hydrographic stations 1-37 (Fig. 2.12a). Spanning 26 days of the cruise and a temperature range from -2 °C to 3 °C, the offset was independent of temperature and had no drift over time

(Fig. 2.12b). A correction of +0.37 °C was applied to all raw temperature readings to give calibrated underway temperature datasets for the Antarctic season 2007/08 (October 2007-May 2008). The same comparison was carried during JR161 and JR200 where offsets of -0.40 and +0.003 °C were applied to give calibrated underway temperature datasets for the Antarctic seasons of 2006/07 and 2008/09, respectively.

2.7. Seawater sampling

Samples for dissolved inorganic carbon (DIC) and total alkalinity (TA) analysis were collected according to the Standard Operating Procedures for oceanic CO_2 measurements (DOE, 2007). Vertical profile samples were taken from the 24 × 10 L Niskin bottles mounted onto the CTD rosette on the upcast of the CTD during cruise JR177 (Tables 2.2 and 2.3). Seawater was collected from the Niskin, using Tygon tubing that had been soaked in seawater, into pre-cleaned 250 ml or 500 ml borosilicate glass bottles. Each sample bottle was rinsed with Niskin water and the bottles were filled bottom-up at a slow rate to minimise the formation of bubbles and were allowed to overflow by at least one bottle volume. The tube was drawn out slowly and bottle sealed with a ground glass stopper that had been rinsed with Niskin water.

A small volume was extracted to create a head space of 1% of the bottle volume and 0.02% vol/vol saturated mercuric chloride ($HgCl_2$) solution was immediately added to fix the sample and prevent further biological activity that would otherwise alter the composition of organic and inorganic carbon. The bottle was re-sealed with the glass stopper, greased in Apiezon L (silicon) grease, shaken to disperse the $HgCl_2$ and stored in a dark location at ambient temperature for shipment to the UK. Underway samples were collected following the same technique, using Tygon tubing connected to the ship's seawater supply on a bypass from the pCO_2 instruments. Replicate samples were taken where possible, both from the same source at the same time or different sources at the same time.

2.8. Seawater analysis

Seawater analyses for DIC and TA were carried out using a VINDTA (Versatile INstrument for the Determination of Titration Alkalinity, Marianda, Kiel, Germany). VINDTA instruments were originally designed for the determination of titration (total) alkalinity, however later models combined this with analysis for DIC (Fig. 2.13). The whole system was maintained at 25 °C by a continual flow of temperature controlled water through the water jackets of the glassware. A Certified Reference Material (CRM) was analysed in duplicate for DIC and TA at the beginning and end of each sample analysis day to monitor the accuracy of the analysis (DOE, 2007). Seawater samples were analysed in duplicate where possible (approximately 70% of samples).

Figure 2.13. (page 85) The VINDTA instrument, detailing principle components for the analysis of total alkalinity (TA) and dissolved inorganic carbon (DIC). The electrodes are both connected to the Titrino and acid for TA analysis is added by the Metrohm piston burette (not shown). Various level sensors are not shown.

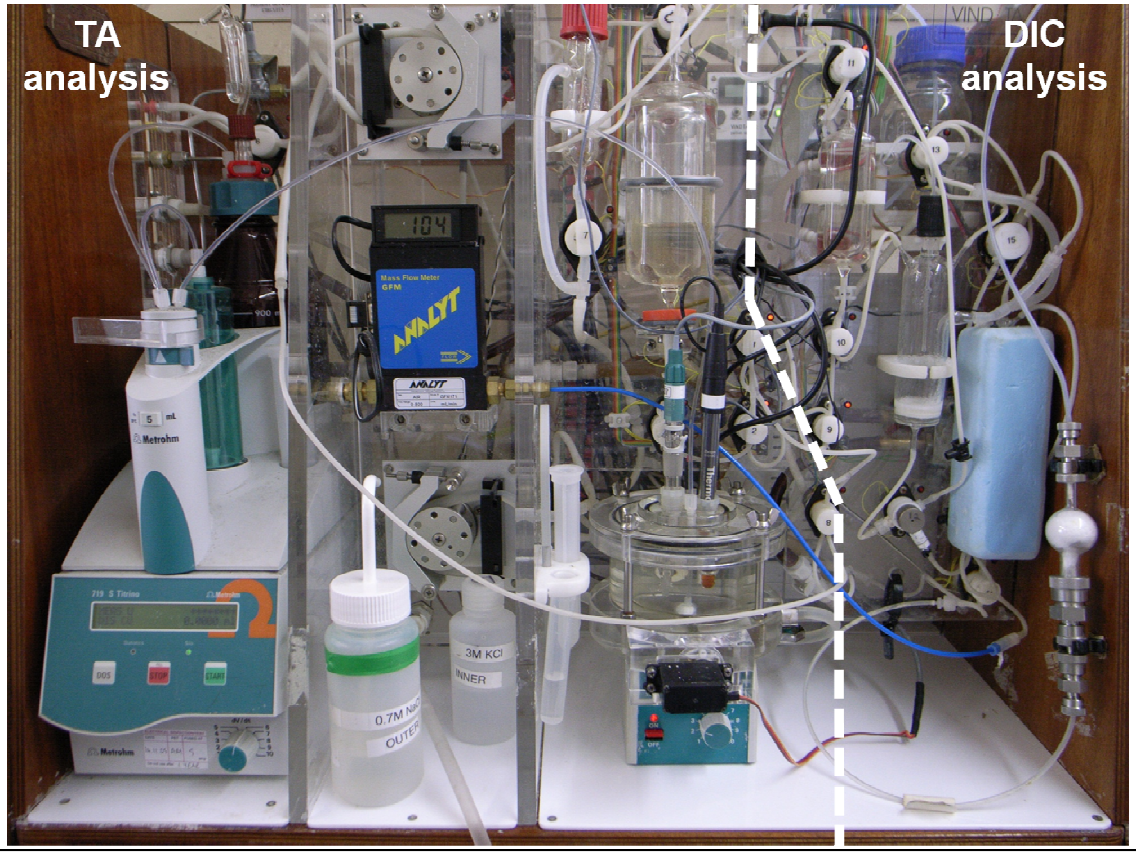
TA
analysis
DIC
analysis
3M KCl
INNER
0.7M NaCl
OUTER

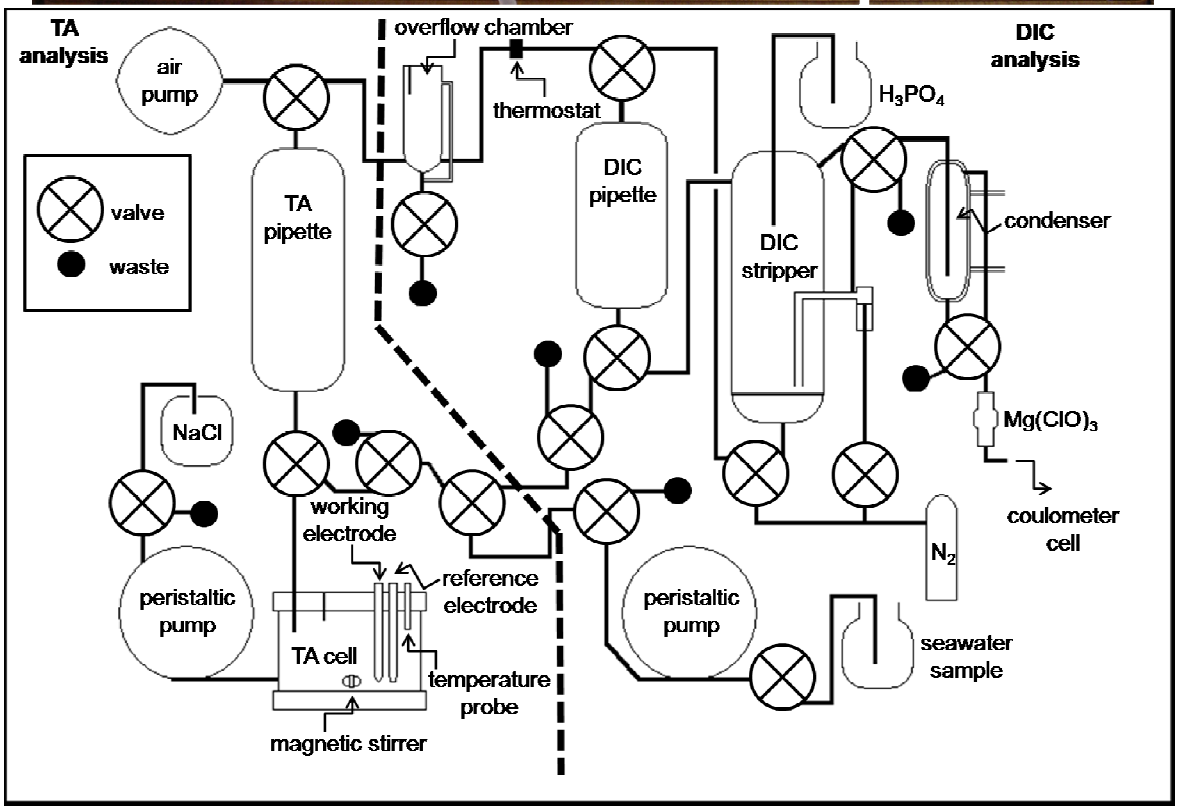
TA
analysis
air
pump
valve
waste
overflow chamber
thermostat
TA
pipette
DIC
pipette
DIC
stripper
DIC
analysis
H_3PO_4
condenser
$Mg(ClO)_3$
coulometer
cell
N_2
NaCl
working
electrode
reference
electrode
peristaltic
pump
TA cell
temperature
probe
magnetic stirrer
peristaltic
pump
seawater
sample

2.8.1. Dissolved inorganic carbon

The concentration of DIC was determined using the principles of coulometric analysis (Johnson et al., 1987). The analysis was conducted with a VINDTA interfaced with a coulometer (model 5100, UIC, USA) (Fig. 2.13). To begin DIC analysis a background count is first determined by running a nitrogen carrier gas (O_2- and CO_2-free) through the extraction system and into the coulometer cell. The background level is determined as the number of counts detected in one minute from the nitrogen purging the system. Seawater is extracted from the sample bottle, held in a thermostat bath at 25°C, until the calibrated pipette is filled and hence the volume of sample could be accurately determined. The sample is then dispensed into a borosilicate glass stripping chamber where it is acidified with phosphoric acid (1.5 ml, 8.5%) to convert all dissolved inorganic carbon species to gaseous CO_2. The solution is purged with nitrogen to strip out the CO_2 and the gas stream is passed through a Peltier cooler and a drier column (magnesium perchlorate) to remove any water vapour. The gas is then bubbled into the main coulometer cell. The cell consists of a glass beaker with a smaller, side arm extension, connected by a glass frit (Fig. 2.14).

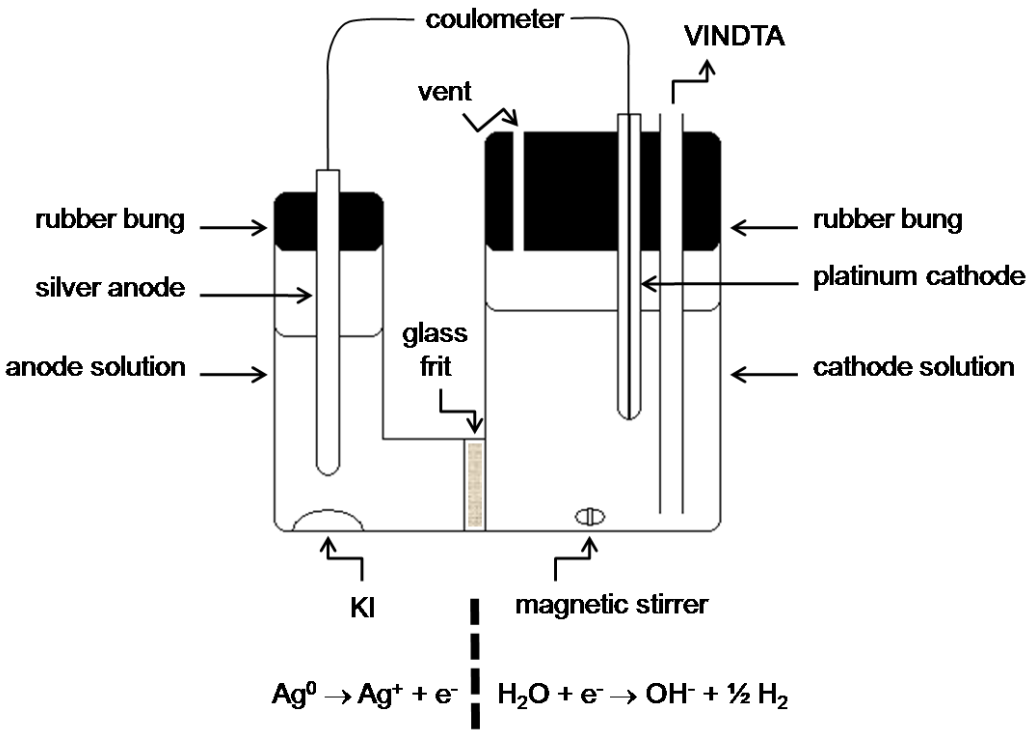

Figure 2.14. Schematic of the coulometer cell for the determination of dissolved inorganic carbon (DIC) detailing the reactions that take place at each electrode. The nitrogen carrier gas enters the coulometer cell through the tubing connection labelled VINDTA.

The main beaker is setup with a platinum cathode immersed in a solution of water, ethanolamine, and tetraethylammonium bromide in dimethyl sulfoxide, with a thymolphthalein indicator (100 ml). The side arm of the cell contains a silver anode suspended in a saturated solution of saturated potassium iodide, dimethyl sulfoxide (about 20 ml) and potassium iodide (KI) crystals (about 2 ml). The cell is positioned in the coulometer light path to maximise transmittance. A current is then applied across the cell and the amount of CO_2 in the carrier gas stream is determined by reaction with ethanolamine to form hydroxyethylcarbonic acid (Eqn. 2.6):

$$CO_2 + HO(CH_2)_2NH_2 \rightarrow HO(CH_2)_2NHCOO^- + H^+ \qquad \text{Equation 2.6.}$$

The reaction is followed by monitoring the pH of the solution through transmittance of the thymolphthalein indicator at about 610 nm. The coulometer maintains maximum transmittance by liberating hydroxide ions at the cathode, by the electrolysis of water (Eqn. 2.7), and dissolving the silver anode to produce an electron (Eqn. 2.8) to generate current within the cell (Fig. 2.13):

$$H_2O + e^- \rightarrow \frac{1}{2}H_2(g) + OH^- \qquad \text{Equation 2.7.}$$

$$Ag(s) \rightarrow Ag^+ + e^- \qquad \text{Equation 2.8.}$$

The hydroxide ions produced at the cathode titrate with the acid formed in the cathode solution (Eqn. 2.7). The coulometer 'interprets' the titration reaction as counts, based on the current, under Faraday's Law. The final coulometer value is achieved when the coulometer sample counts per unit time reach the value of the background level, marking the titration end-point. At the beginning of each day of analysis, the coulometer was primed with a series of six 'test' seawater samples until the analysis time and instrument response had stabilised.

Analyses were conducted as either a series of underway samples or one full CTD station per day to maintain internal consistency. A CRM from batches 76 or 81 (DOE, 2007) was analysed in duplicate at the beginning and end of each day, corresponding to two CRM bottles per CTD cast and per 20 underway samples. The CRM replicate analyses provided an assessment of instrument accuracy and precision each day and over the course of whole analysis period. Upon completion of the daily analysis, the cell and frit were cleaned with

acetone and deionised water under a slight pressure and dried overnight at 60°C. The drying agent, magnesium perchlorate ($Mg(ClO_4)_2$, Fig. 2.12), was replaced daily to minimise water vapour passing into the cell and introducing noise to the count signal. A correction of 1.0002 is made to each final DIC measurement to account for the dilution of the seawater by the addition of 0.02% saturated mercuric chloride solution.

A total of 53 CRM bottles were analysed for DIC in duplicate. Plots of the CRM responses during the analysis period are shown in a series of control charts, detailing the individual analyses, means and standard deviations for each bottle (Figs. 2.15 and 2.16). Individual CRM analyses are plotted sequentially to evaluate the stability of the DIC measurement process for CRM batch 76 (Fig. 2.16a) and batch 81 (Fig. 2.16b).

Figure 2.15. (page 89) Control charts of CRM response during DIC analysis, showing (a) batch 76 in-bottle replicates, (b) batch 81 in-bottle replicates, (c) batch 76 bottle standard deviations, (d) batch 81 bottle standard deviations, (e) batch 76 corrected replicates, (f) batch 81 corrected replicates, (g) batch 76 corrected bottle standard deviations and (h) batch 81 corrected bottle standard deviations. Upper and lower control limits as for Fig. 2.7. Red outlined points (a-d) represent flagged data based on the control limit criteria.

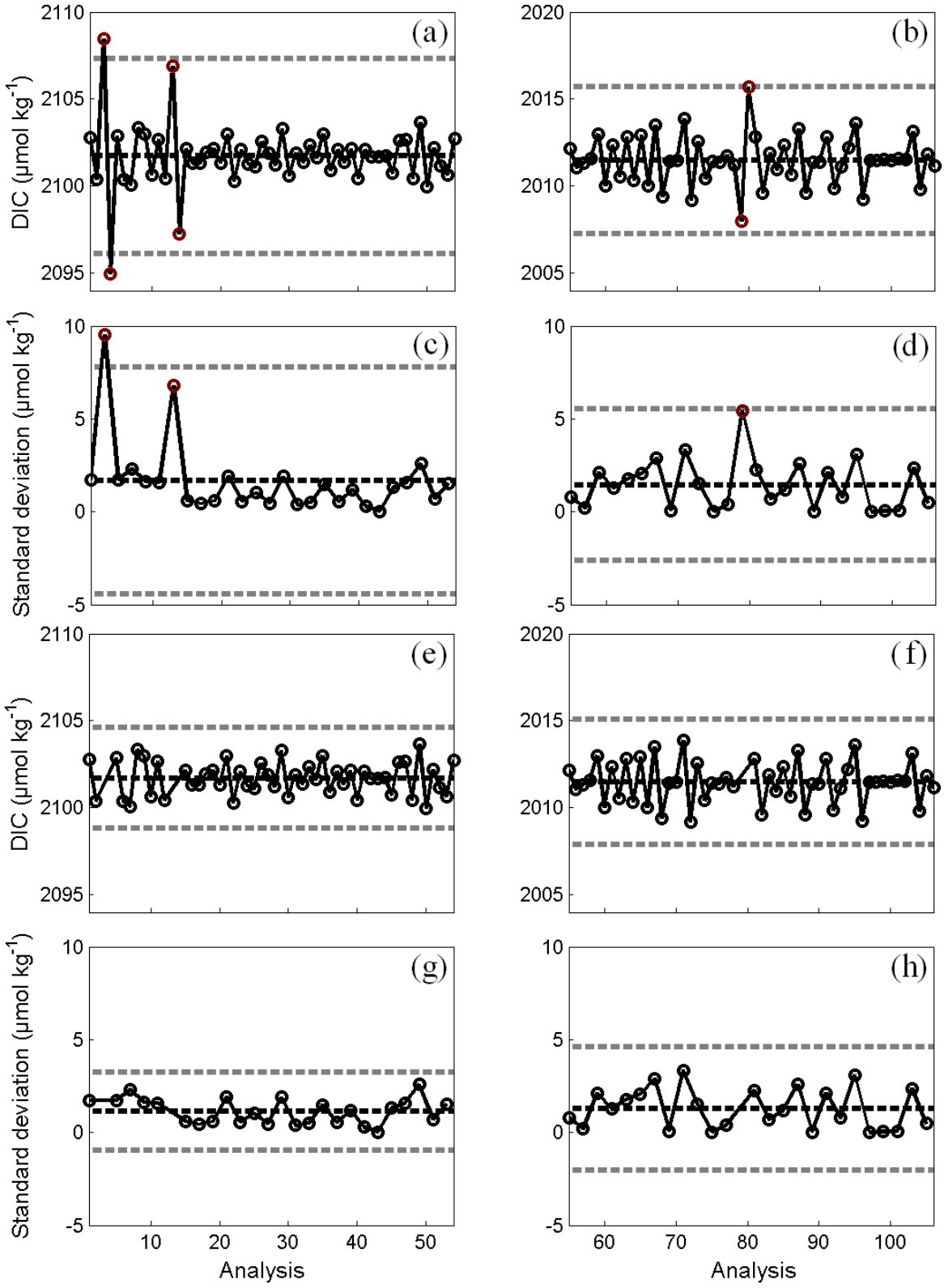
(a)
(b)
(c)
(d)
(e)
(f)
(g)
(h)
DIC (µmol kg-1)
Standard deviation (µmol kg-1)
Analysis
2110
2105
2100
2095
2020
2015
2010
2005
10
5
0
-5
10
20
30
40
50
60
70
80
90
100

Both sets of charts reveal data points that fall very close to the control limits. These correspond to three individual CRM bottles that showed considerable deviations compared to all other bottle data (Fig. 2.15c-d). Inspection of laboratory notebooks and instrument output revealed that each of the bottles were run first on a given analysis day after a short break and suggest that the instrument may have still been in a stabilising period. As the flagged data originated from one bottle on three separate days, it was decided that the data should be removed from further analysis as the second CRM analysed on each of the days performed well within the control limits. The 'corrected' CRM values can now be used with confidence to evaluate the accuracy of the DIC measurements, determined from the maximum difference between the certified DIC values and the corrected VINDTA measured DIC values as 2.4 μmol kg^{-1}.

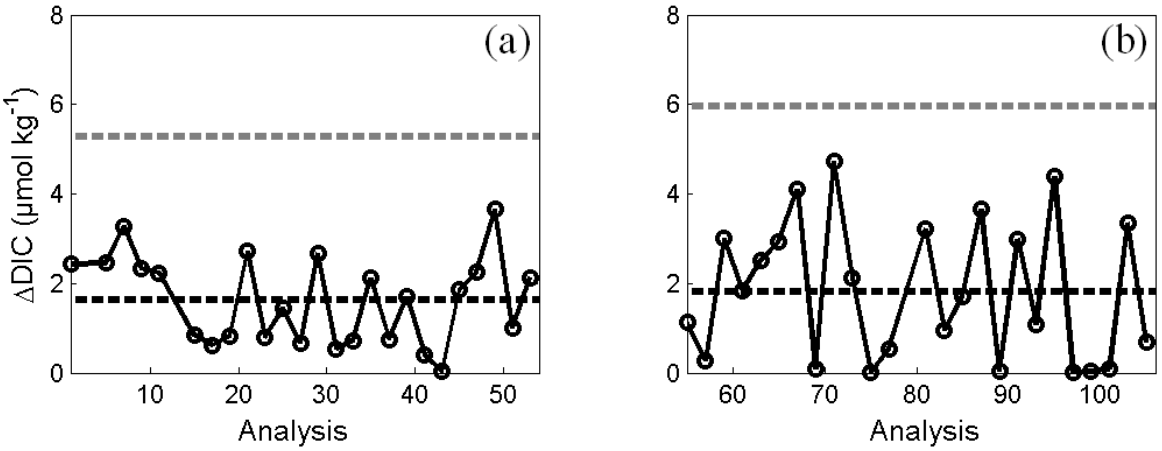

Figure 2.16. Control chart of the corrected DIC difference (ΔDIC) between in-bottle replicates for (a) batch 76 (b) batch 81. The black dashed line indicates the mean and the grey dashed line indicates the upper control limit (3.267 × mean) as outlined in DOE (2007).

The absolute differences (ΔDIC) of the corrected duplicate CRM (in-bottle) analyses can be investigated to evaluate the precision of the measurement process (Fig. 2.16). The average difference is related to the short term standard deviation, which is an indication of the precision or repeatability of the technique. The chart shows that the measurement precision was in control at all times as all differences were below the upper control limit. Compared to batch 76, batch 81 appeared to be more variable, however no bias was evident.

The precision (repeatability) of the instrument is determined from the standard deviation of the mean DIC value (std_R), estimated from the difference (d) of 50 (k) within-bottle duplicate measurements (Eqn. 2.9):

$$std_R = \left(\frac{\sum_{i=1}^{k} d_i^2}{2\,k} \right)^{1/2} \qquad \text{Equation 2.9.}$$

The precision for the DIC measurements is estimated as 1.5 μmol kg^{-1}, which corresponds to the desired precision of 0.07% for this method (DOE, 2007). The corrected CRM DIC values gave a standard response of the instrument per gram of carbon that is used to determine the sample DIC concentrations. This is achieved by interpolating between the average in-bottle CRM DIC, from the beginning and end of each day, and calculating the corresponding sample DIC.

2.8.2. Total alkalinity

Analysis for TA was carried out by potentiometric titration with hydrochloric acid to the carbonic acid end point (Dickson, 1981) using a VINDTA instrument (Fig. 2.13). The instrument setup comprises a temperature regulated sample delivery system, an open titration cell and an automated burette. The cell and sample tubing are rinsed with sodium chloride solution (0.7 M) and then with a small volume of the sample to be analysed. Seawater is then extracted from the sample bottle, which is held in a thermostat bath at 25°C, until the calibrated pipette is filled and hence the volume of sample can be accurately determined. The sample is then dispensed into the thermostatted titration cell assembled with a glass working electrode, a reference pH electrode, acid injection tube and an earth rod.

A Metrohm (model 719 S, Metrohm, Switzerland) piston burette is used to deliver fixed aliquots of hydrochloric acid (0.15 ml, 0.1 M) into the cell. The electrodes follow the titration by continually measuring the electromotive force (e.m.f) of the solution. When the difference between two successive measurements is less than 0.1 mV the next aliquot of acid is added, up to a total volume of 4.20 ml. The titration curve of e.m.f as a function of acid volume has two points of inflection that correspond to the protonation of firstly carbonate and secondly bicarbonate ions. The acid utilised up to the second point is equivalent to the titration

alkalinity or total alkalinity. TA is determined from a curve fitting approach and a Gran function, which are optimised with best-fit coefficients to calculate the final TA.

At the beginning of each day of sample analysis, the titration cell is flushed with at least two 'test' seawater samples. Samples are run as for DIC analysis, either underway samples or one full CTD station, and a CRM bottle is analysed in duplicate at the beginning and end of each analysis day. The CRM analyses give a standard titration curve that is used to determine the TA of the samples. In addition, the CRM replicate analyses provided an assessment of instrument accuracy and precision each day and over the course of whole analysis period. A correction of 1.0002 is made to each final total alkalinity measurement to account for the dilution of the seawater by the addition of 0.02% saturated mercuric chloride solution.

A total of 53 CRM bottles were analysed for TA in duplicate. As for DIC, individual CRM analyses are plotted sequentially by day of analysis to evaluate the stability of the measurement process for batch 76 (Fig. 2.17a, c, e, g) and batch 81 (Fig. 2.17b, d, f, h). Both charts reveal data points that fall very close to the control limits. These correspond to five and four analyses from batches 76 and 81, respectively (Fig. 2.17a-d). These included the same three flagged bottles from the DIC analyses and further suggest that after an idle period the instrument was still stabilising, or some acid diffuses out of the dispenser or possibly that the bottles were suspect, resulting in outliers in both DIC and TA analyses.

Figure 2.17. (page 93) Control charts of CRM response during TA analysis, showing (a) batch 76 replicates, (b) batch 81 replicates, (c) batch 76 bottle standard deviations, (d) batch 81 bottle standard deviations, (e) batch 76 corrected replicates, (f) batch 81 corrected replicates, (g) batch 76 corrected bottle standard deviations and (h) batch 81 corrected bottle standard deviations. Upper and lower control limits as for Fig. 2.7. Red outlined points (a-d) represent flagged data based on the control limit criteria.

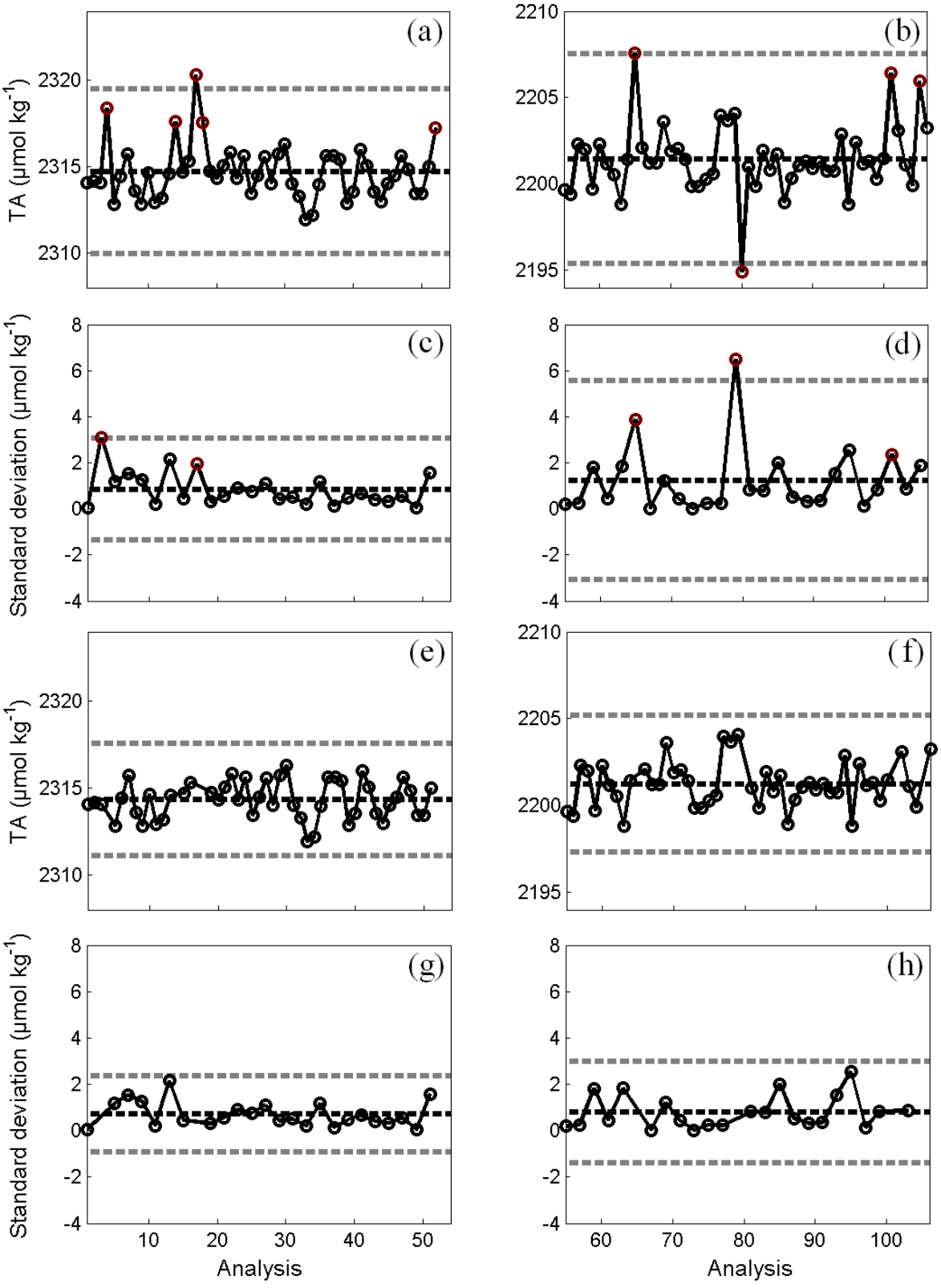
(a)
(b)
(c)
(d)
(e)
(f)
(g)
(h)
TA (µmol kg-1)
Standard deviation (µmol kg-1)
Analysis
2320
2315
2310
2210
2205
2200
2195
8
6
4
2
0
-2
-4
10
20
30
40
50
60
70
80
90
100

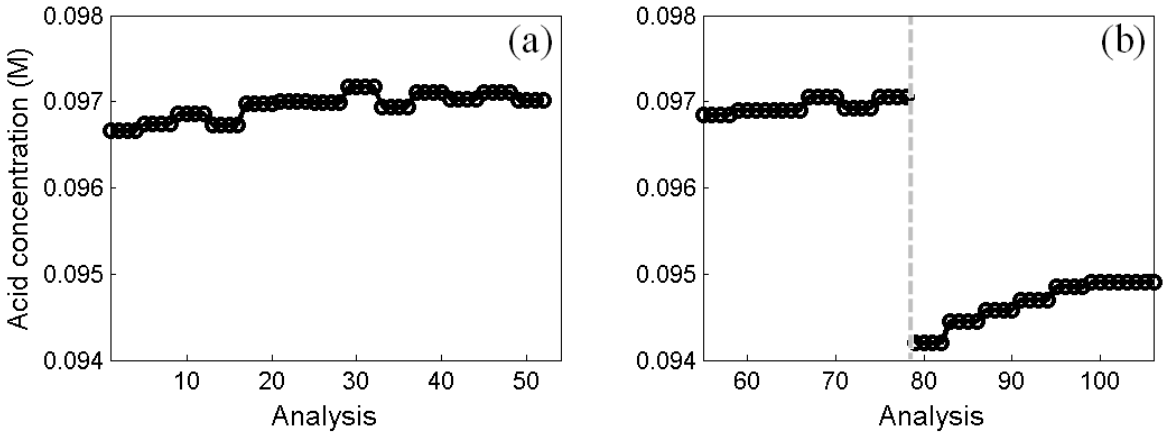

Figure 2.18. Hydrochloric acid concentration factor during the analysis using (a) CRM batch 76 and (b) CRM batch 81. The vertical grey dashed line indicates the change over from acid batch 1 to 2 (day 78-79).

The mean acid concentration factor (Fig 2.18) was calculated for each analysis day, from the two CRM bottles, to replicate the certified alkalinity. A distinct break-point in concentration factor marks the change over to a new batch of hydrochloric acid, upon utilisation of the first batch (Fig. 2.18b). A slight increasing trend can be observed in both sets of acid concentration factors over time. The concentration factors exhibit little variation on a day-to-day basis. Such a trend was observed in alkalinity analyses conducted on the same apparatus in 2004 (Brown, 2008).

These factors were used in the calculation of the 'raw' alkalinities (Fig. 2.17a-b) where no such trend is identified in the control chart. A possible explanation is that throughout the analysis period, the amount of acid decreases with each successive titration, which increases the volume of the headspace in the acid stock bottle. Any evaporation in the stock bottle would result in the acid becoming more concentrated over time. A second explanation could be algal growth and/or dirt within the sample delivery tubing system or pipette. This would result in less sample being dispensed into the cell and hence less acid required, which would imply a more concentrated acid to reach the end point. Finally, any disruptions to the automated sampling procedure, such as pinched tubing, samples running dry, condensation tripping the pipette fill would lead to insufficient sample volume and apparent increasing acid concentrations. Thorough flushing of the system prior to analysis and the use of deionised water reduced the possibility of algal build up. Inspection of laboratory notebooks and

instrument output didn't reveal any hard- or software disruptions that had not already been observed and accounted for.

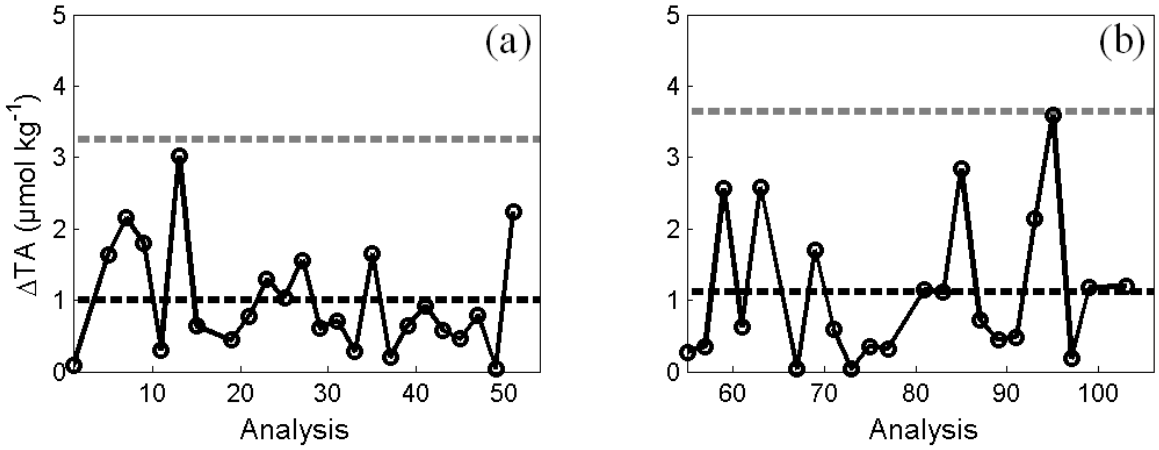

Figure 2.19. Control charts of the corrected replicate TA difference (ΔTA) for (a) batch 76 (b) batch 81. Upper control limit as for Fig. 2.16.

From the minor trends in the acid concentration it is not possible to use a mean acid concentration factor for the calculation of alkalinity. Therefore, the daily mean concentration factor was determined from the 2×2 CRM analyses that gave the certified alkalinity value for the certain CRM batch. As for the DIC analyses, the flagged data originated from one bottle on different days and therefore the data was discarded and the remaining replicate used as the standard. The 'corrected' CRM values can now be used in confidence to evaluate the accuracy and precision of the TA measurements.

The accuracy of the instrument, determined from the maximum difference between the certified TA values and the corrected VINDTA measured TA values is 2.6 μmol kg^{-1}. The control chart of the absolute differences (ΔTA) shows that the measurement precision was in control at all times. Similarly to the DIC analyses, batch 81 measurements appeared to be more variable, however no bias was evident. The precision of the instrument, using Equation 2.4, is estimated as 1.0 μmol kg^{-1}, which is better than the desired precision of 1.5 μmol kg^{-1} for this method (DOE, 2007).

2.9. Carbonate chemistry property-property comparisons

Marine inorganic chemistry data are often normalised to constant salinity to investigate the influence of freshwater. The traditional salinity normalisation involves correction of measured TA, with *in situ* salinity (S), to a reference salinity (S^{ref}) (Friis et al., 2003):

$$TA_S^0 = \frac{TA}{S} \cdot S^{ref} \qquad \text{Equation 2.10.}$$

Typically, the S^{ref} is the mean salinity of the reference data, which is determined as 34 from the average salinity of the WW for all hydrographic stations during JR177 (Tables 2.2 and 2.3). All surface alkalinity data showed a strong salinity dependence (Fig. 2.20a). The data are coloured according to location of collection to observe any latitudinal variations. Linear regression analysis yields the following relationship and associated correlation coefficient ($\underline{r}$):

$$TA = 59.9S + 269 \qquad \underline{r}(160) = 0.81, \underline{p} < 0.01 \qquad \text{Equation 2.11.}$$

The null hypothesis is rejected and the relationship between TA and salinity is statistically significant with a 99% confidence level. Using the traditional technique (Eqn. 2.10), salinity normalised alkalinity (TA_{34}) shows a much reduced salinity dependence, however a slight reversed trend can be observed:

$$TA_{34}^0 = -8.1S + 2578 \qquad \underline{r}(160) = -0.24, \underline{p} < 0.01 \qquad \text{Equation 2.12.}$$

The detectable salinity dependence of the normalised alkalinity (TA^0_{34}) indicated that there is a problem with the traditional technique for this dataset (Fig. 2.20b). The change in sign of the gradient implies that this technique is over-correcting the alkalinity measurements. The correlation coefficient shows that this technique still yields a statistically significant relationship, at 99% confidence, and hence is not a suitable salinity normalisation tool for the data. To improve this correction, a second equation accounts for a non-zero freshwater endmember i.e. a positive alkalinity at zero salinity ($TA_0 > 0$) (Friis et al., 2003):

$$TA_{34} = \left(\frac{TA - TA_0}{S} \right) \cdot 34 + TA_0 \qquad \text{Equation 2.13.}$$

Linear regression analysis of the TA_{34} data shows no salinity dependence (Fig. 2.20c), where $r(160) = -0.02$, $p > 0.01$, and no statistically significant relationship is present between the normalised TA and salinity. Therefore, Eqn. 2.13 is a suitable salinity normalisation technique for the JR177 data set.

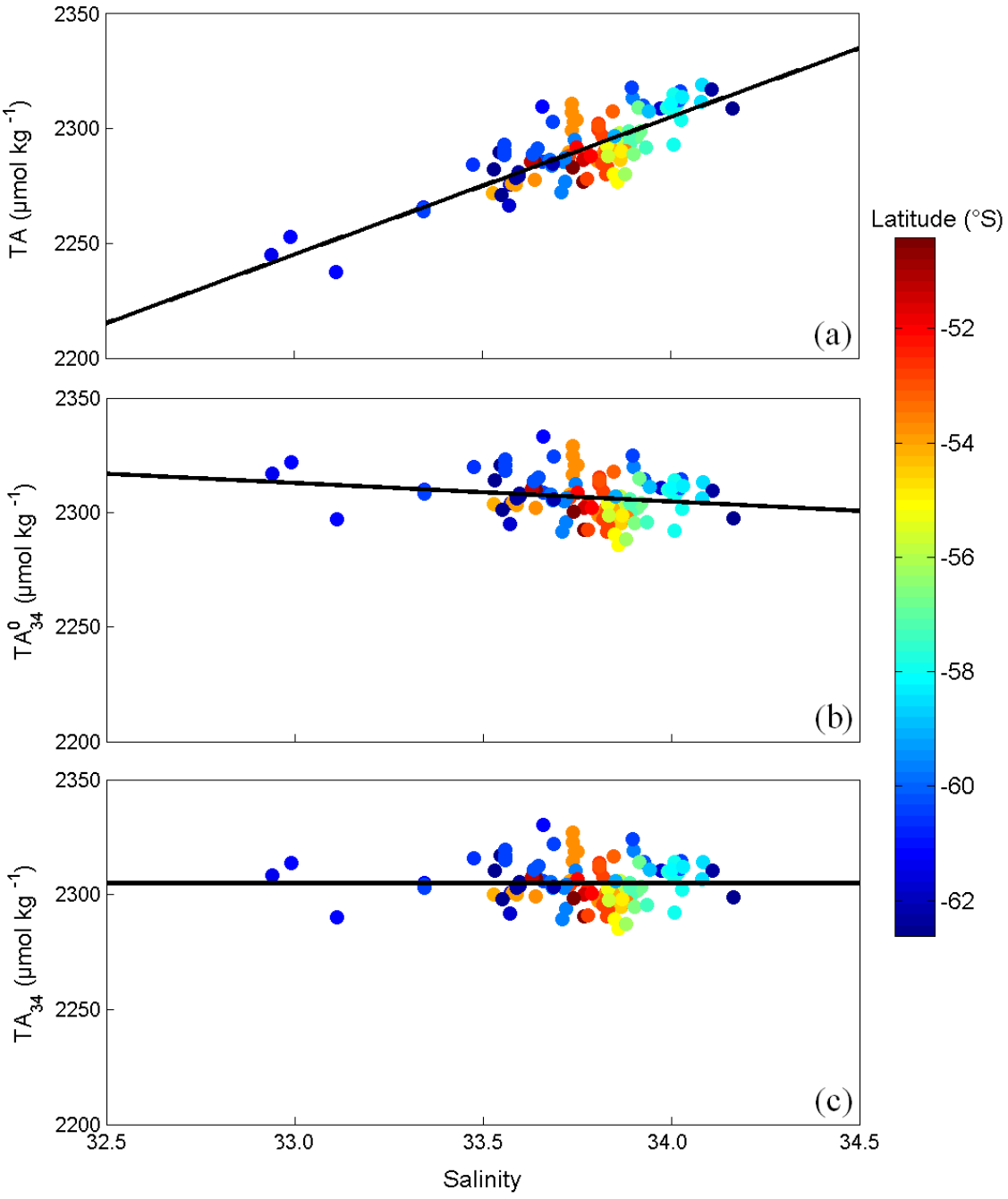

Figure 2.20. The dependence on salinity of (a) alkalinity (TA), (b) normalised alkalinity using the traditional approach (TA^0_{34}) and (c) normalised alkalinity accounting for a non-zero endmember (TA_{34}) for all surface samples collected during cruise JR177.

The TA endmember (TA_0) at zero salinity (Eqn. 2.13) was calculated as 269 µmol kg^{-1}. This relationship takes into account the main processes that affect alkalinity that involve a non-zero endmember, such as sea ice melt, calcium carbonate dissolution and precipitation and upwelling (Friis et al., 2003). This was repeated for the DIC data, where a value of 966 µmol kg^{-1} was determined for DIC_0. DIC and TA values reported in the text are not salinity normalized, unless stated.

A series of de-ionised water samples were analysed to determine an analysis 'blank' for DIC and TA at zero salinity. Average values for $TA_{0\_de\text{-}ionised}$ and $DIC_{0\_de\text{-}ionised}$ of 74 ± 11 and 36 ± 3 µmol kg^{-1} (n = 6), respectively, indicate that the TA_0 and DIC_0 do not result from the analytical technique (discussed further in section 5.3.3).

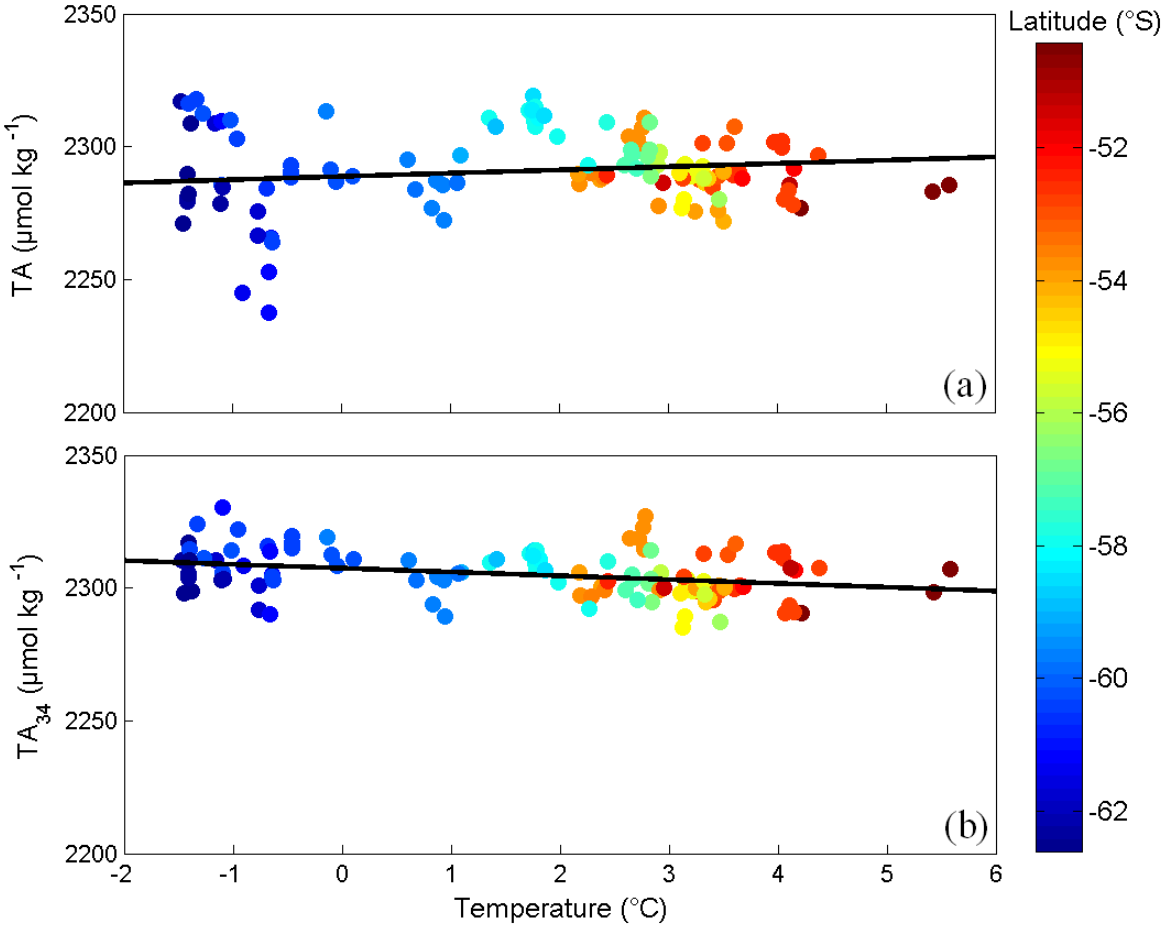

Figure 2.21. The relationship of (a) measured alkalinity (TA) and (b) normalised alkalinity accounting for a non-zero endmember (Eqn. 2.13, TA_{34}) to temperature for all surface samples collected during cruise JR177.

Measured TA showed a slight dependence on temperature (Fig. 2.21a) and when normalised (Eqn. 2.13), the correlation was slightly reversed (Fig. 2.21b). The data show that temperature is not a major variable in determining normalised surface water alkalinity. From the comparison of the two approaches, Equation 2.13 will be used to normalise the inorganic carbon data of JR177 (Chapters 5, 6 and 7).

2.10. Vertical DIC deficits

Depth-integrated DIC deficits were calculated from vertical DIC profiles relative to the concentration of DIC at 100 m depth (Eqn. 2.14). Vertical integration to 100 m depth was selected as mixed layers were shallower than 100 m across the Scotia Sea (Tables 5.3 and 6.2), and winter mixed layers were deeper than 100 m (Tables 5.2 and 6.3) and for consistency with numerous other inorganic carbon studies in the Southern Ocean (Table 6.6). The vertical deficits at depths (z) between the discrete DIC samples were linearly interpolated at 1 m resolution.

$$\Sigma\Delta DIC(z) = \int_0^z \Delta DIC(z)\,\rho(z)\,dz \qquad \text{Equation 2.14.}$$

2.11. Seasonal biogeochemical deficits

The seasonal depletion in DIC, TA and macronutrients was determined from the difference between concentrations in the WW and the average concentration within the summer mixed layer (Jennings et al., 1984). The total seasonal DIC depletion ($\Delta DIC_{seasonal}$) can be expressed as a sum of contributing processes:

$$\Delta DIC_{seasonal} = \Delta DIC_{salinity} + \Delta DIC_{Corg} + \Delta DIC_{CaCO_3} + \Delta DIC_{residual} \qquad \text{Equation 2.15.}$$

Changes in DIC due to changes in salinity are estimated from the difference between the measured and salinity normalised DIC deficit i.e. $\Delta DIC_{seasonal} - (\Delta DIC_{seasonal})_{34}$. Based on the accuracy of the DIC measurements, a composite error of 4.8 μmol kg^{-1} is associated with the salinity term. Modifications in DIC due to processes that change organic carbon, such as photosynthesis and respiration (ΔDIC_{Corg}), have been estimated from salinity normalised nitrate deficits. Different phytoplankton species are likely to have different nutrient uptake ratios. It has been previously reported that utilization of carbon and nitrate per mole of

phosphate is much lower for diatoms than for *Phaeocystis antarctica*, for example (Arrigo et al., 1998). Studies carried out in the Ross Sea showed that carbon:phosphorous (C:P) and carbon:nitrogen (C:N) uptake ratios for diatom dominated blooms were 80.5 and 7.8, respectively (Sweeney et al., 2000). A comparison of carbon to nitrogen and phosphate depletion showed that C:N ratios were more homogeneous than C:P ratios, therefore indicating that N was a better proxy for the biological utilisation of carbon than P (Sweeney et al., 2000).

Table 2.6. Changes in dissolved inorganic carbon (ΔDIC) and alkalinity (ΔTA), on a molar basis, as a result of the formation of organic matter (Corg) through the organic carbon pump and the production of calcium carbonate ($CaCO_3$) through the carbonate pump (Zeebe and Wolf-Gladrow, 2001) (section 1.5.4.1), adapted from Sarmiento and Gruber (2006). Changes in TA due to organic matter production were determined from the nitrogen-carbon stoichiometry of Anderson and Sarmiento (1994).

Parameter	*Production of organic matter (Corg)*	*Production of calcium carbonate ($CaCO_3$)*
ΔDIC	-1.00	-1.00
ΔTA	+0.14	-2.00

As discussed in section 1.5.4.1, the organic carbon and carbonate pumps affect DIC and alkalinity by different proportions (Table 2.6). The residual difference in alkalinity, corrected for salinity and organic matter production, is used as an indicator of calcium carbonate processes based on the 2:1 ratio of changes in TA and DIC due to $CaCO_3$ processes (Table 2.6). The accuracy of the TA data yields a composite error of 3.7 μmol kg^{-1} for the calcium carbonate term. The residual change in DIC accounts for the remaining seasonal change and is the result of processes including CO_2 air-sea exchange, advection and upwelling and the associated error is the sum of that for each of the terms in Equation 2.15.

2.12. Other carbonate chemistry parameters

DIC and TA, complimented with temperature, salinity, pressure and macronutrient concentrations from all discrete samples, were used to calculate the remaining carbonate chemistry parameters, including fCO_2, total pH (pH_T), carbonate ion (CO_3^{2-}) concentration and

aragonite saturation state (Ωaragonite). This was done using the CO2Sys programme (Lewis and Wallace, 1998) with thermodynamic dissociation constants for K_1 and K_2 (Eqns. 1.6 and 1.7) by Mehrbach et al. (1973) and the re-fit by Dickson and Millero (1987). These dissociation constants were selected from results of model comparisons in the literature (Körtzinger et al., 2000; Sarmiento and Gruber 2006, and references cited therein).

2.13. Satellite data

2.13.1. Satellite products used 2006-2009

Satellite data (Table 2.7) have been an essential component in interpreting the seasonal variability in carbonate chemistry as observed by *in situ* data. The superior spatial coverage assisted in hydrographic station selection and allowed the core cruise observations to be put into context. The superior temporal coverage put the cruise observations into a seasonal perspective and allowed interannual variability to be explored (Chapter 7). As with most remotely sensed techniques, satellite data have associated caveats that need consideration.

Table 2.7. Satellite data used during this research.

Sensor	*Parameter*	*Data type and source*	*Coverage*
SeaWiFS	Chlorophyll-a	8 day, 9 km level 3 mapped http://oceancolor.gsfc.nasa.gov	1997-2007
MODIS	Chlorophyll-a	Daily, 4 km level 3 mapped http://oceancolor.gsfc.nasa.gov	2004-2010
SeaWiFS/ MODIS	Chlorophyll-a	8 day, 9 km level 3 mapped http://oceancolor.gsfc.nasa.gov	2004-2007
Merged	Sea surface temperature	Daily, 4 km http://ghrsst-pp.metoffice.com/pages/latest_analysis/ostia.html	2006-2010
Altimeters	Absolute dynamic height	http://www.aviso.oceanobs.com/en/data/products/index.html	2001-2010
QuikSCAT	Wind speed	Twice daily, 0.25° http://podaac.jpl.nasa.gov	1999-2009
Merged	Sea ice	Daily, 4 km http://ghrsst-pp.metoffice.com/pages/latest_analysis/ostia.html	2006-2010

2.13.2. Ocean colour data

Ocean colour satellite data were obtained from NASA using the Sea-viewing Wide Field-of-view Sensor (SeaWiFS) and the MODerate resolution Imaging Spectroradiometer (MODIS). Ocean colour data were downloaded by ftp from http://oceancolor.gsfc.nasa.gov as 8 day, level 3 mapped data (Table 2.7). SeaWiFS derived chlorophyll-a concentrations (Feldman and McClain, 2006b; O'Reilly et al., 1998) had been processed using the standard OC4v5.1 algorithm at 9 km (1/12°) resolution. MODIS derived chlorophyll-a concentrations (Feldman and McClain, 2006a; O'Reilly et al., 1998) were processed using the standard OC3v1.1 algorithm at 4 km (1/24°) resolution.

The SeaWiFS/MODIS merged product is a compound chlorophyll-a concentration as derived by both sensors. Inconsistencies could arise with the use of different sensors, however a previous investigation revealed a consistent agreement between the SeaWiFS and MODIS estimates (Venables, 2007). Therefore, the merged product can be used in confidence and any variability introduced by using data from two sensors is compensated by the increased spatial coverage from swaths of both satellites. SeaWiFS provided chlorophyll-a data until 2007 and MODIS provided chlorophyll-a and sea surface temperature data until 2010. The 8 day composite images were used to determine the time of initiation and termination of the phytoplankton blooms (Chapter 7). The progression of the blooms could be more easily tracked using the 8 day composites than daily images due to the greater spatial coverage for each region whilst maintaining practical temporal resolution.

Satellite chlorophyll-a images may not give a true indication of upper ocean biomass as the chlorophyll-a concentration is derived from the water-leaving irradiance that has penetrated a few meters of the sea surface. Regions of deep mixed layers can often hold high depth integrated biomass (Holm-Hansen et al., 2004a; Holm-Hansen et al., 2005; Whitehouse et al., 2008) and deep chlorophyll-a maxima (DCM) can develop (discussed in Chapters 4 and 6). The Southern Ocean has been previously identified as a region where satellite derived chlorophyll-a estimates differ from *in situ* shipboard measurements (O'Reilly et al., 1998; Moore et al., 1999b; Gregg and Casey, 2004; Korb et al., 2004;). Around South Georgia, this difference was described by a linear relationship (Korb et al., 2004):

$$\left[chl-a\right]_{SeaWiFS} = 0.28\left[chl-a\right]_{in\ situ} + 0.30 \qquad R^2 = 0.61 \qquad \text{Equation 2.16.}$$

This correlation is due, in part, to SeaWiFS underestimating high chlorophyll-a concentrations or the use of 8 day composite images that may cause some loss of resolution in intensity due to short temporal shifts (< 8 days) in chlorophyll-a.

2.13.3. Sea surface temperature

Sea surface temperature (SST) data were supplied from http://ghrsst-pp.metoffice.com/pages/latest_analysis/ostia.html, through the Group for High-Resolution Sea Surface Temperature (GHRSST) (Stark et al., 2007). The main caveat with remotely sensed SST data is that clouds have similar thermal properties and can therefore be difficult to distinguish. Data values that appeared outside the expected range for surface seawater at the specified time of year were searched for and removed, however some may remain, which needs to be considered when interpreting the data.

Satellite derived SST is more precisely a measurement of the skin temperature, the water temperature at the air-sea interface. The thermal skin effect refers to the strong gradient that can exist across the top millimetre of the ocean's surface, relative to the underlying bulk water of the mixed layer. The thermal skin effect influences the solubility of CO_2 at the sea surface, which in turn affects the air-sea flux of CO_2 (Robertson and Watson, 1992; Robinson et al., 1984). Large differences between the skin temperature and that of the bulk water can occur through solar heating during the day and cooling during the night. At high wind speeds, increased turbulence means that the skin and mixed layer temperatures become the same (Donlon and Robinson, 1997). For this research, the mixed layer temperature during winter 2007 is estimated from the satellite derived skin temperature.

2.13.4. Absolute dynamic height

Satellite altimetry data products were produced by Ssalto/Duacs and distributed by Aviso through http://www.aviso.oceanobs.com/en/data/products/index.html, with support from CNES (Rio and Hernandez, 2004) (Table 2.7). The data are a composite from several altimeters: Topex/Poseidon, ERS1/2, Jason-1/2, Envisat and the reference geoid and mean geostrophic currents to create the intercalibrated absolute dynamic topography product. The data then undergo a series of manipulations to produce the final product, mapped absolute dynamic topography.

2.13.5. Wind speed

The SeaWinds microwave scatterometer on QuikSCAT measured the backscatter from the ocean surface in order to derive surface ocean wind vectors. The data were downloaded from http://podaac.jpl.nasa.gov at a resolution of 0.25° latitude at 10 m height (Table 2.7). The specification of QuikSCAT was to measure winds between 3 and 30 m s^{-1} with an associated accuracy of 2 m s^{-1}. Cloud cover does not inhibit microwaves therefore giving complete data coverage from every swath.

2.13.6. Sea ice cover

Daily sea ice concentration data at 4 km resolution from 2006 to 2009 were obtained through the Operational Sea Surface Temperature and Sea Ice Analysis (OSTIA) service, a component of the Group for High-Resolution Sea Surface Temperature (GHRSST) at http://ghrsst-pp.metoffice.com/pages/latest_analysis/ostia.html (Stark et al., 2007). Visual observations of sea ice type and coverage were made from the bridge of RRS *James Clark Ross* as part of the daily position report filed by the Captain during all cruises (Table 2.1).

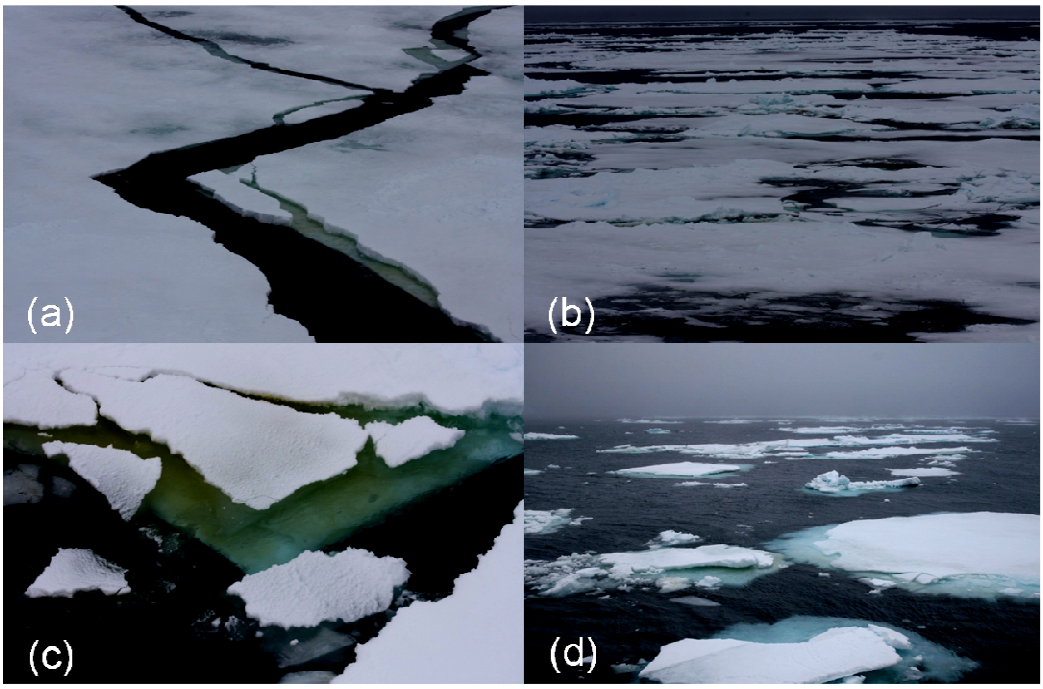

Figure 2.22. Sea ice during JR177 showing (a) consolidated ice pack and leads between stations 12 and 14, (b) smaller ice plates at station 10, (c) a dark layer of sea ice algae between stations 10 and 9 and (d) sporadic ice floes in the meltwaters at station 9.

In addition to the satellite data and shipboard observations, digital photographs were made during cruise JR177 to create a field key to aid interpretation of data in the sea ice region (Fig. 2.22). Each image was selected to capture the contrasting sea ice environments of the Weddell-Scotia Confluence (WSC) in summer 2008. The transition area between open ice-free waters to ice-covered waters is referred to as the marginal ice zone (MIZ), encompassing stations 14, 12, 10 and 9 in the WSC (Fig. 2.22 and Table 2.2) during cruise JR177 (Chapter 5). The 'brown ice' observed between stations 10 and 9 (Fig. 2.22c) is indicative of the presence of diatoms in sea ice (Horner et al., 1992). The ice edge is defined here as the position where consolidated sea ice was first encountered (station 10) on the JR177 transect (Fig. 2.22b). The seasonal ice zone (SIZ) is defined here as the region between the annual maximum and minimum sea ice extent (Chapter 7).

2.14. Winter sea surface data

Sea surface biogeochemical parameters (DIC, TA and macronutrients) during winter were determined from the concentration of each parameter at the depth of the potential temperature minimum (θ_{min}) during summer 2008 (section 2.3.2). This is based on the assumption that the θ_{min} represents the WW, in the remnant of the winter mixed layer, with physical and chemical characteristics that were present at the sea surface during the antecedent winter (2007). This technique has previously been used for seasonal carbon research in the Southern Ocean, assuming that horizontal and vertical mixing processes are minimal (Jennings et al., 1984; Minas and Minas, 1992; Rubin et al., 1998; Pondaven et al., 2000; Ishii et al., 2002; Jouandet et al., 2008).

The timing of mid-winter is defined here as the time of the year when the sea surface temperature was lowest and the mixed layer was deepest, after Shim et al. (2006) and Jouandet et al. (2008). To determine the winter maximum, sea surface temperature (SST) data from GHRSST (section 2.13.3) were used to create a SST climatology from 2006 to 2009 for each hydrographic station occupied on the transect. Daily SST in the research area was lowest in September and, with reference to satellite data (section 2.13.6), this corresponded with the seasonal cover of sea ice. Therefore, based on the θ_{min} during summer 2008, the WW is taken to represent the Antarctic Surface Water (AASW) of September 2007 and the starting day was set to 8 September, based on timings of the summer 2008 transect (Table 7.1). This generated a dataset of AASW parameters during winter 2007 (Chapter 7).

Oxygen utilisation in the Scotia Sea (60-54°S 52°W) in December 2001 suggested that the properties of the winter mixed layer in this region are well preserved by the following summer (Shim et al., 2006). Analysis into the validity of this technique is discussed in section 5.3.7.

2.15. Air-sea CO_2 flux

The flux of CO_2 across the air-sea interface (F, mmol m^{-2} d^{-1}) is proportional to the concentration gradient of fCO_2 (ΔfCO_2) between the sea surface and the overlying air (Liss and Slater, 1974):

$$F = k\, K_0\, \Delta fCO_{2\,(sea-air)} \qquad \text{Equation 2.17.}$$

The solubility of CO_2 in seawater (K_0, mol kg^{-1} atm^{-1}) was calculated using the equation from Weiss (1974). The coefficient of proportionality is the gas transfer velocity (k, m s^{-1}), which parameterises the kinetics of gas exchange. Several empirical relationships have been proposed to relate gas transfer velocities to wind speed. Large differences (up to factor two or three) exist between the relationships, in part due to the gas transfer velocity being dependent on the roughness of the sea surface, which is not governed by instantaneous wind speed alone (Sarmiento and Gruber, 2006).

Three gas transfer velocity formulations are commonly used to derive the CO_2 air-sea flux from wind speeds at 10 m height (U_{10}) and the ΔfCO_2, which will now be discussed. The Liss and Merlivat (1986) parameterisation (hereinafter, LM86) was deduced from wind tunnel experiments using sulphur hexafluoride (SF_6), normalised with lake measurements. Three wind speed regimes were identified: smooth surface (Eqn. 2.18), rough surface (Eqn. 2.19) and breaking waves (Eqn. 2.20) (Liss and Merlivat, 1986):

$$k = 0.17\, U_{10} \left(\frac{Sc}{600}\right)^{-2/3} \qquad U_{10} \le 3.6 \text{ m s}^{-1} \qquad \text{Equation 2.18.}$$

$$k = (U_{10} - 3.4) \cdot 2.8 \left(\frac{Sc}{600}\right)^{-1/2} \qquad 3.6 < U_{10} \le 13.0 \text{ m s}^{-1} \qquad \text{Equation 2.19.}$$

$$k = (U_{10} - 8.4) \cdot 5.9 \left(\frac{Sc}{600}\right)^{-1/2} \qquad 13.0 \text{ m s}^{-1} < U_{10} \qquad \text{Equation 2.20.}$$

The Schmidt number (Sc) is a dimensionless number defined as the ratio of momentum diffusivity, or viscosity (ν), and mass diffusivity (D) (Liss and Merlivat, 1986):

$$Sc = \frac{\nu}{D} \qquad \text{Equation 2.21.}$$

The Schmidt number for CO_2 is dependent on the salinity and temperature and for seawater at 20 °C it is determined as 660 (Liss and Merlivat, 1986). For freshwater at 20 °C, the Schmidt number for CO_2 is 600 (Liss and Merlivat, 1986). The Wanninkhof (1992) parameterisation (hereinafter, W92) uses a quadratic relationship between the gas transfer coefficient and the wind speed, as established from the global inventory of natural and bomb carbon-14 (^{14}C) in the oceans.

Two relationships were suggested, one for short term wind speeds from shipboard anemometers and scatterometers (Eqn. 2.22) and one for long term averages of the wind speed (Eqn. 2.23) (Wanninkhof, 1992) using the Schmidt number for seawater:

$$k = 0.39\, U_{10}^2 \left(\frac{Sc}{660}\right)^{-1/2} \qquad \text{Equation 2.22.}$$

$$k = 0.31\, U_{10}^2 \left(\frac{Sc}{660}\right)^{-1/2} \qquad \text{Equation 2.23.}$$

The Nightingale et al. (2000) parameterisation (hereinafter, N00) was deduced from *in situ* dual tracer measurements, with SF_6 and helium (^3He), at sea. The relationship assumes a second order polynomial relationship between the gas transfer velocity and wind speed (Nightingale et al., 2000) using the Schmidt number for freshwater:

$$k = \left(0.22\, U_{10}^2 + 0.33\, U_{10}\right)\left(\frac{Sc}{600}\right)^{-1/2} \qquad \text{Equation 2.24.}$$

Comparisons of the three commonly used gas transfer velocity formulations showed that the global mean gas transfer velocity determined by the N00 relationship was intermediate between the LM86 relationship, on the low end, and the W92 relationship at the high end (Sarmiento and Gruber, 2006). More recent work, using bomb radiocarbon ($^{14}CO_2$) released during the 1960s bomb tests as a constraint on air-sea CO_2 exchange, stressed the necessity for

the gas transfer velocity formulations to be consistent with the radiocarbon budget (Sweeney et al., 2007). The closest match between the bomb radiocarbon global average gas transfer velocity was achieved by the Nightingale et al. (2000) parameterisation (Fig. 2.23).

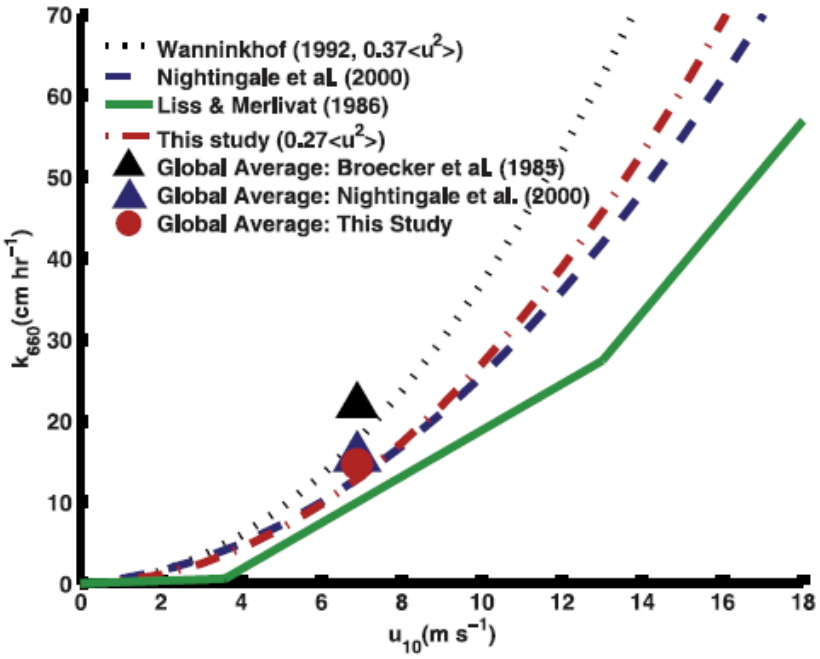

Figure 2.23. Gas transfer velocity (k, cm hr^{-1}) as a function of wind speed (U_{10}, m s^{-1}) for the Wanninkhof (1992) short-term wind relationship (black dotted line), the Sweeney et al. (2007) short-term wind relationship developed from $^{14}CO_2$ inventory (red dash-dot line), the Nightingale et al. (2000) relationship (blue dashed line) and the Liss and Merlivat (1986) short-term wind speed relationship (green line).

In light of these literature reviews, fluxes will be calculated with *in situ* and seasonally averaged wind speeds from QuikSCAT (section 2.13.5) and the Nightingale et al. (2000) relationship. Seasonal wind speeds were calculated by taking the average of the wind speed (measured twice daily) at the position of each ΔfCO_2 value along the transect. A discussion of fluxes using *in situ* and seasonally averaged is presented in Chapter 7 (section 7.9.1).

2.17. Macronutrients

Analyses for macronutrients were carried out by M. J. Whitehouse (BAS) as part of Discovery-2010. Underway samples from the non-toxic seawater and CTD water bottle samples were filtered through a mixed ester membrane (Whatman, pore size 0.45 μm), and the filtrate was analysed colorimetrically for dissolved silicate (SiO_4), phosphate (PO_4), and nitrate (NO_3) with a segmented-flow analyser (Technicon, Whitehouse, 1997). Analyses for nitrate included nitrite (NO_2), which is not considered separately as its concentration had little variation and was typically < 1% of total $NO_3 + NO_2$.

2.18. Iron

Analyses for dissolved iron (dFe) were carried out by M. C. Nielsdóttir (National Oceanography Centre, Southampton) as part of the Discovery-2010 cruises JR161 and JR177. Underway surface water collection for dFe analyses was carried out with a torpedo tow fish positioned at *ca.* 3 m depth whilst steaming at 10-12 knots under ice free conditions, and at 4-5 knots when ice was present. The water was pumped using a peristaltic pump (Watson Marlow) into a clean container and filtered using 0.2 μm cartridge filters (Sartorius, Sartobran 150). Samples for dFe were analysed using an automated Fe(III) flow injection chemiluminescence method (Nielsdóttir et al. 2009).

2.19. Chlorophyll-a

Analyses for chlorophyll-a were carried out by R. E. Korb (BAS) as part of Discovery-2010. Underway samples were collected from the non-toxic seawater supply approximately every hour as the ship was in transit. Underway and CTD samples were filtered through glass fibre filters (Whatman GF/F) under low (< 70 mm Hg) vacuum pressure and immediately frozen and stored at -20 °C until analysis onboard. The samples on the filters were then extracted in acetone (10 ml, 90%) in the dark for 24 hours (Parsons et al., 1984). Fluorescence of the extract was measured before and after acidification with 1.2 M HCl on a TD-700 Turner fluorometer. The instrument was calibrated against commercially prepared chlorophyll-a standards (Sigma).

2.20. Summary

From 2006 to 2009, sea surface pCO_2 data was collected on 14 research cruises in the Scotia Sea, Southern Ocean. This has been possible due to the installation of a new CASIX underway pCO_2 instrument onboard RRS *James Clark Ross* in October 2006. An at-sea pCO_2 instrument intercomparison was carried out during JR177, comparing the new CASIX system to a long running system from UEA (Chapter 3). The concentration of the dissolved inorganic carbon and total alkalinity from the sea surface water and from vertical profiles was measured during summer 2008 (Chapter 4). This was the first deep carbonate chemistry section in the Scotia Sea, which enabled a detailed investigation of the seasonal variability of the marine carbon cycle and its forcing by biological and physical processes (Chapters 5, 6 and 7). These measurements have contributed to alleviating the comparatively sparse surface water pCO_2 data in the Southern Ocean (Takahashi et al., 2009). The outcomes of the methodology demonstrated that the carbonate data collected and analysed as part of this research are of comparable accuracy and precision (Table 2.8) to those described by international guidelines (DOE, 2007).

Table 2.8. Accuracy and precision of numerous parameters as determined from the analyses detailed above or estimated from calculations using other carbonate parameters (Millero, 1995; Millero, 2007). *The accuracy is the composite error of the input parameters.

Instrument	*Parameter*	*Method*	*Unit*	*Accuracy*	*Precision*
LICOR 7000	xCO_2	infrared detection	μmol mol^{-1}	0.40	0.04
LICOR 840	xCO_2	infrared detection	μmol mol^{-1}	1.28	0.23
Pt100/ PRT	temperature	thermostat bath	°C	0.20	0.10
Oceanlogger	temperature	at-sea comparison	°C	0.14	0.02
VINDTA	DIC	coulometry	μmol kg^{-1}	2.4	1.5
VINDTA	TA	potentiometry	μmol kg^{-1}	2.6	1.0
CO2Sys	fCO_2	f(DIC,TA)	μatm	5.7*	-
CO2Sys	pH_T	f(DIC,TA)	-	0.0062*	-

3. An at-sea pCO_2 instrument intercomparison

3.1. Abstract

The performance of a new CASIX (Centre for observation of Air-Sea Interactions and fluXes) underway instrument for the measurement of the partial pressure of carbon dioxide (pCO_2) is described and compared to that of a second established pCO_2 instrument. Two intercomparison experiments were conducted onboard RRS *James Clark Ross* in the Scotia Sea during austral summer 2008. During the first experiment, on 8-10 January, stable atmospheric mixing ratios of CO_2 (xCO_2) permitted a comparison of the xCO_2 measurements in marine air. Both instruments showed considerable agreement for atmospheric xCO_2, with a mean difference of 0.17 ± 0.20 μmol mol^{-1}. The accuracy of both data sets was determined as better than 0.30 μmol mol^{-1} by comparison to data from Jubany station (62.23°S 58.67°W) on the Antarctic Peninsula.

A second intercomparison experiment was carried out during 21-23 January as the sea surface pCO_2 remained stable, providing good conditions for assessing the accuracy and precision of the CASIX seawater pCO_2 measurements. At this time, the difference between the two instruments was largest and hence the accuracy is taken as a 'worst' case scenario. Both instruments displayed near identical trends in the small scale pCO_2 fluctuations indicating similar response times and acute detection. The accuracy of the CASIX seawater pCO_2 measurements, determined from the mean difference in sea surface pCO_2 between the two instruments, is better than 7 μatm. The precision, determined from the standard deviation of the mean pCO_2 value, is 3 μatm.

In contrast, fluctuating sea surface pCO_2 conditions observed during the first experiment presented an opportunity to test the response of both instruments along a pCO_2 gradient. Much larger differences (up to 12 μatm) occurred when the pCO_2 gradient was maximum (over 13 μatm hr^{-1}). This has been attributed to the large spatial variability of surface water pCO_2, which is captured slightly differently by instruments of different designs. The at-sea intercomparison conducted onboard RRS *James Clark Ross* indicates the capability of the

CASIX instrument for underway sea surface pCO_2. Suggestions for modifications to the instrument and the raw data are made to improve the accuracy and stability of the pCO_2 data.

3.2. Introduction

The ocean is one of the largest natural reservoirs of carbon (Fig. 1.8) and the future rates of the oceanic CO_2 uptake are largely unknown (Sarmiento and Gruber, 2006). The significance of the difference in the partial pressure of CO_2 (ΔpCO_2) in oceanic CO_2 uptake has led to numerous international investigations into the spatio-temporal variability of pCO_2 in the global ocean. The Geochemical Ocean Section Study (GEOSECS) in the 1970s established the first collection of inorganic carbon measurements in the global ocean (Craig, 1972; Craig, 1974), which was followed by the Joint Global Ocean Flux Study (JGOFS) in the 1980s and the World Ocean Circulation Experiment (WOCE) in the 1990s (Wallace, 2001). The principle outcome of such research efforts was the generation of extensive databases of carbon parameters, that cover all major ocean basins throughout the different seasons (Key et al., 2004; Takahashi et al., 2009; Key et al., 2010). The continuation of this work is paramount for more accurate estimations of the uptake of carbon dioxide by the ocean.

As part of the UK contribution, the CARBON-OPS project was established to provide a "supply chain" of pCO_2 data, commencing with the collection of automated measurements of surface water pCO_2 in waters frequented by ships of the UK research fleet (Hardman-Mountford et al., 2008). All data are sent in near-real-time to the British Oceanographic Data Centre (www.bodc.ac.uk/carbon-ops/) for processing and quality control and are finally supplied externally for oceanographic research, model validation and policy making. An integral part of this work was the development of autonomous underway pCO_2 instruments, commissioned by the Centre for observation of Air-Sea Interactions and fluXes (CASIX) and carried out by Plymouth Marine Laboratory and Dartcom. For international pCO_2 databases it is essential that the pCO_2 data, collected from different instruments, is comparable and several efforts have been made to address this issue and establish international guidelines for data collection (Körtzinger et al., 1996; Körtzinger et al., 2000; DOE, 2007). In the following chapter, data from two intercomparison experiments that were carried out at sea to test the performance of the new CASIX underway pCO_2 instrument are presented and discussed. The objective of this work is to quantify the accuracy and precision of the CASIX pCO_2 instrument by running a University of East Anglia (UEA) pCO_2 instrument in parallel.

3.3. The pCO_2 instrument intercomparison

The intercomparison experiments were carried out in the Scotia Sea on board RRS *James Clark Ross* during cruise JR177 in January and February 2008 (Table 2.1). Two periods were selected from the 49 day cruise in regions of contrasting hydrological conditions that were about 5° of latitude apart (Fig. 3.1).

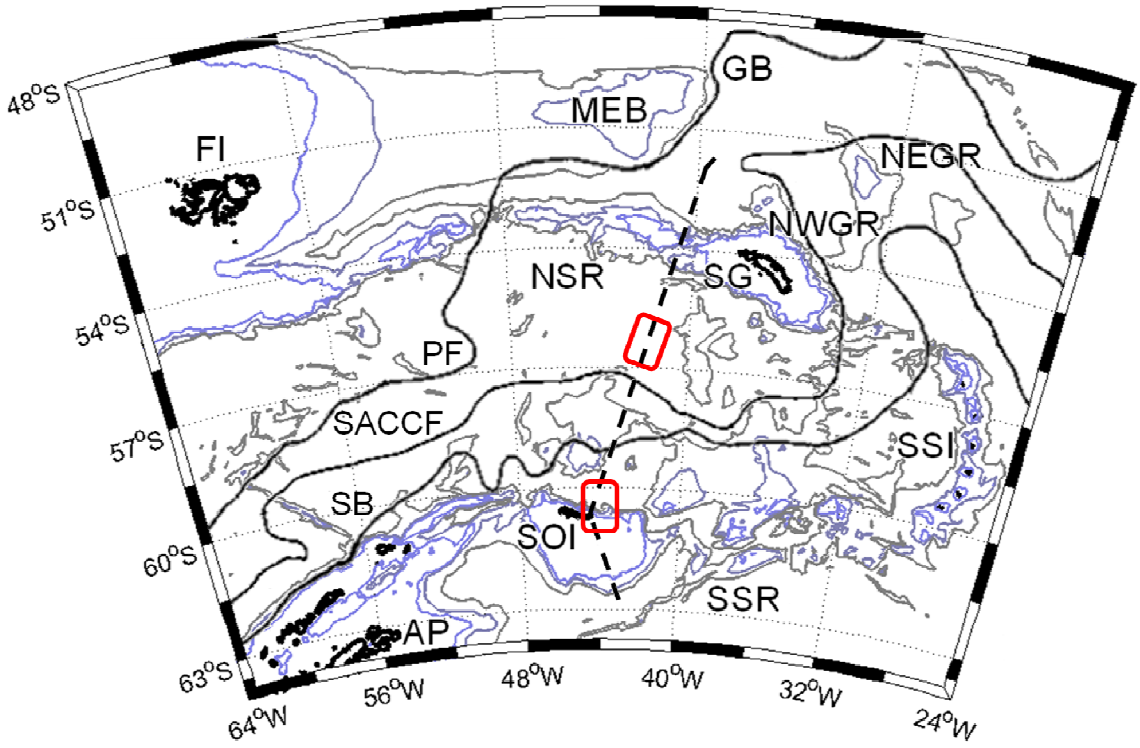

Figure 3.1. A schematic of the Scotia Sea showing the approximate location of the transect (dashed line) during JR177. The locations of the intercomparison experiments are shown (red boxes). Some important topographic features are identified: Antarctic Peninsula (AP), South Orkney Islands (SOI), South Scotia Ridge (SSR), South Sandwich Islands (SSI), North Scotia Ridge (NSR), South Georgia (SG), Northwest Georgia Rise (NWGR), Northeast Georgia Rise (NEGR), Georgia Basin (GB), Maurice Ewing Bank (MEB) and the Falkland Islands (FI). Antarctic Circumpolar Current (ACC) fronts shown schematically, adapted from Meredith et al. (2003a): the Southern Boundary (SB, Orsi et al., 1995), Southern ACC Front (SACCF, Thorpe et al., 2002) and the Polar Front (PF, Moore et al., 1999). Depth contours are at 1000, 2000 and 3000 m (GEBCO, 2001).

During 8-10 January (48 hours), work was carried out on two proximal hydrographic stations close to the sea ice, in the vicinity of the South Orkney Islands (Fig. 3.1). At this time, atmospheric CO_2 mixing ratios (xCO_2) were very stable and provided a good opportunity to compare the instruments response. During this passage the RRS *James Clark Ross* went through sections of fully open water, melting sea ice and waters with sea ice cover. This provided an interesting scenario of fluctuating oceanic conditions across a strong pCO_2 gradient (Fig. 3.2). The second period, 21-23 January (48 hours), was selected as both instruments showed a relatively constant but large difference in stable sea surface pCO_2. Compared to the rest of the cruise data, the second intercomparison period represented a 'worst case' scenario, in that the largest difference between the two instruments was observed for 48 hours in steady sea surface conditions.

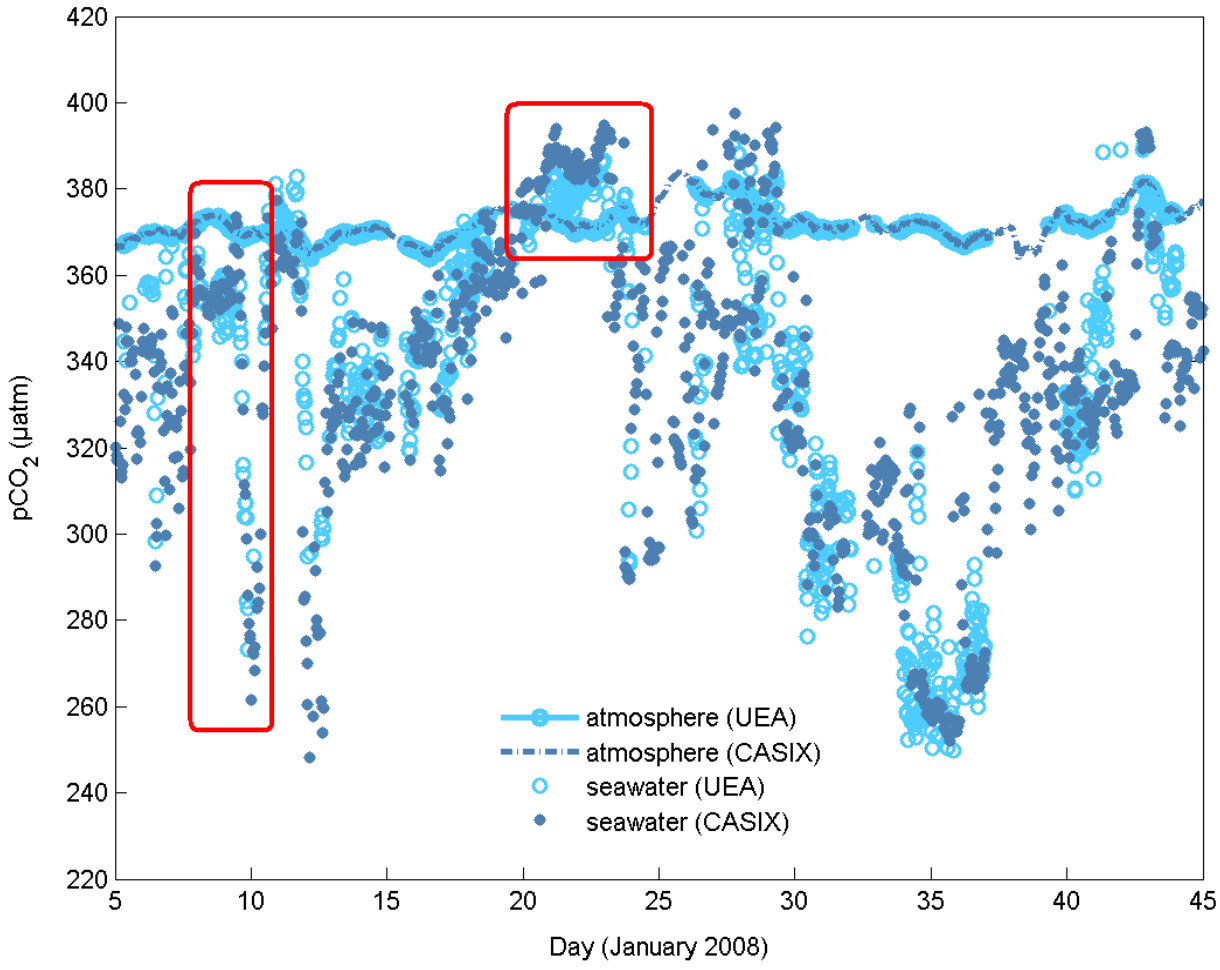

Figure 3.2. The temporal distribution of the partial pressure of CO_2 (pCO_2, µatm) for the atmosphere and surface ocean for the UEA and CASIX pCO_2 instrument during cruise JR177. The two periods selected for the intercomparison experiments are highlighted (red boxes).

3.4. The pCO_2 instruments

Numerous designs of underway pCO_2 instruments have been reported in the literature (e.g., Takahashi, 1961; Weiss, 1981; Poisson et al., 1993; Cooper et al., 1998; Schuster and Watson, 2007). To ensure the acquisition of accurate and comparable datasets, international intercomparison experiments have been conducted (Körtzinger et al.,1996; Körtzinger et al., 2000). In absence of certified references, intercomparisons are the only way to assess the accuracy and precision of underway pCO_2 instruments. Seven pCO_2 instruments were run in parallel with identical seawater supplies and calibration gases on RV *Meteor* in June 1996 (Körtzinger et al., 2000). Sea surface conditions ranged from stable to fluctuating with a range of over 100 μatm. Two systems consistently ran with a difference between 0.0-1.2 μatm and were treated as a 'reference'. An overall uncertainty for the other systems was determined as 5 μatm. Differences up to 10 μatm between well designed and accurately calibrated instruments occasionally occurred, particularly in regions of rapid pCO_2 changes.

The principle of measuring the pCO_2 in seawater is based on the equilibration of CO_2 in a continuous stream of seawater and a headspace, which is sampled to determine the xCO_2 in surface seawater (section 2.5). Different designs of equilibrator discussed in the literature can be grouped into three categories based on the principle design feature: the shower type; the bubble type and the laminar flow type (Körtzinger et al., 1996, and reference cited therein). The UEA and CASIX systems included a bubble type equilibrator, but of different designs, and used a non-dispersive infra-red analyser, a LICOR (LICOR Inc., USA), but of different models. To ensure validity of the experiment, both pCO_2 systems were run under comparable conditions where possible.

Marine boundary air was sampled from the forward bridge on RRS *James Clark Ross* (Fig. 2.2) by two separate, parallel air lines that connected individually to each instrument. Both instruments were located in close proximity in the same laboratory, with the equilibrators being situated side by side and run simultaneously from the same water supply. A consistent, but separate, set of calibration gases of known CO_2 concentrations in artificial air were used for each instrument (section 2.6.1). The principle features and operation of both instruments have been previously described (section 2.5) and are now summarised (Table 3.1).

Table 3.1. The principal features of the University of East Anglia (UEA) and Centre for observation of Air-Sea Interactions and fluXes (CASIX) underway pCO_2 instruments.

Feature	*UEA*	*CASIX*
LICOR gas analyser	7000	840
Calibration gases	250, 350, 450 μmol mol^{-1}	250, 450 μmol mol^{-1}
Drier	Cool box	Peltier condenser
Equilibrator	Bubble type	Bubble type
Vented	Yes	No
Water flow rate	4 L min^{-1}	6 L min^{-1}
Seawater time lag	116 seconds	120 seconds

3.5. Atmospheric xCO_2

3.5.1. Shipboard atmospheric xCO_2

Although atmospheric xCO_2 data are not the immediate focus of this research, they allow an initial inspection of factors that are potential sources of error in the seawater pCO_2 measurements. Following preliminary observations of the raw data signals, the xCO_2 in dry and calibrated marine air is examined to give a suitable indication of the performance of the instruments due to the relative stability of atmospheric CO_2 measurements. Time synchronized atmospheric xCO_2 data from both instruments for the intercomparison periods was about 382 μmol mol^{-1} (Figs. 3.3 and 3.4).

In initial inspection of the CASIX raw xCO_2 in dry marine air from both intercomparison periods revealed variations that close followed variations in ambient pressure. This signal was absent from the UEA data and showed a pressure dependence of the CASIX raw data. This was attributed to internal algorithms of the CASIX LICOR 840 that did not adjust the data to ambient pressure (Eqn. 3.1), creating a more noisy raw data signal in comparison to the UEA LICOR 7000 signal. In addition, the absence of a vent on the CASIX equilibrator could allow conditions of over- and under pressure to be created in the equilibrator headspace. This would add a further degree of noise to the raw data and present a risk of headspace air exchange with laboratory air.

During the first intercomparison experiment (8-10 January) the UEA and CASIX data show similar trends in fine scale fluctuations with a slight decrease after about 18 hours, indicating a good, reliable response of both LICORs (Fig. 3.3). At this time, the average values for atmospheric xCO_2 were 381.90 ± 0.41 μmol mol^{-1} for the UEA instrument and 382.07 ± 0.45 μmol mol^{-1} for the CASIX instrument. This gives an average difference, ΔxCO_2 (CASIX-UEA) of 0.17 ± 0.20 μmol mol^{-1}. Similar fine scale trends were observed in atmospheric xCO_2 during the second intercomparison exercise (Fig. 3.4). Both instruments measured an abrupt increase of about 1 μmol mol^{-1} after the first 24 hours, indicative of a new air mass being sampled. The average values for atmospheric xCO_2 for this second period were 381.79 ± 0.63 and 382.36 ± 0.75 μmol mol^{-1} for the UEA and CASIX instruments, respectively. The average difference was 0.57 ± 0.31 μmol mol^{-1}.

The positive sign of the ΔxCO_2 indicated that on average the CASIX instrument was tending to measure higher relative to the UEA instrument. However, the large, positive standard deviations showed that there is no systematic difference between the two data sets and that the natural variability of xCO_2 in marine boundary air is picked up by both instruments, with either instrument measuring slightly higher than the other at any given time. The increased difference observed during the second experiment is likely to result from the fluctuating xCO_2 and the response time of the individual instruments. In addition, the lower precision of the CASIX LICOR 840 (Table 2.7) is likely to lead to a more 'noisy' xCO_2 profiles compared to that of the UEA LICOR 7000.

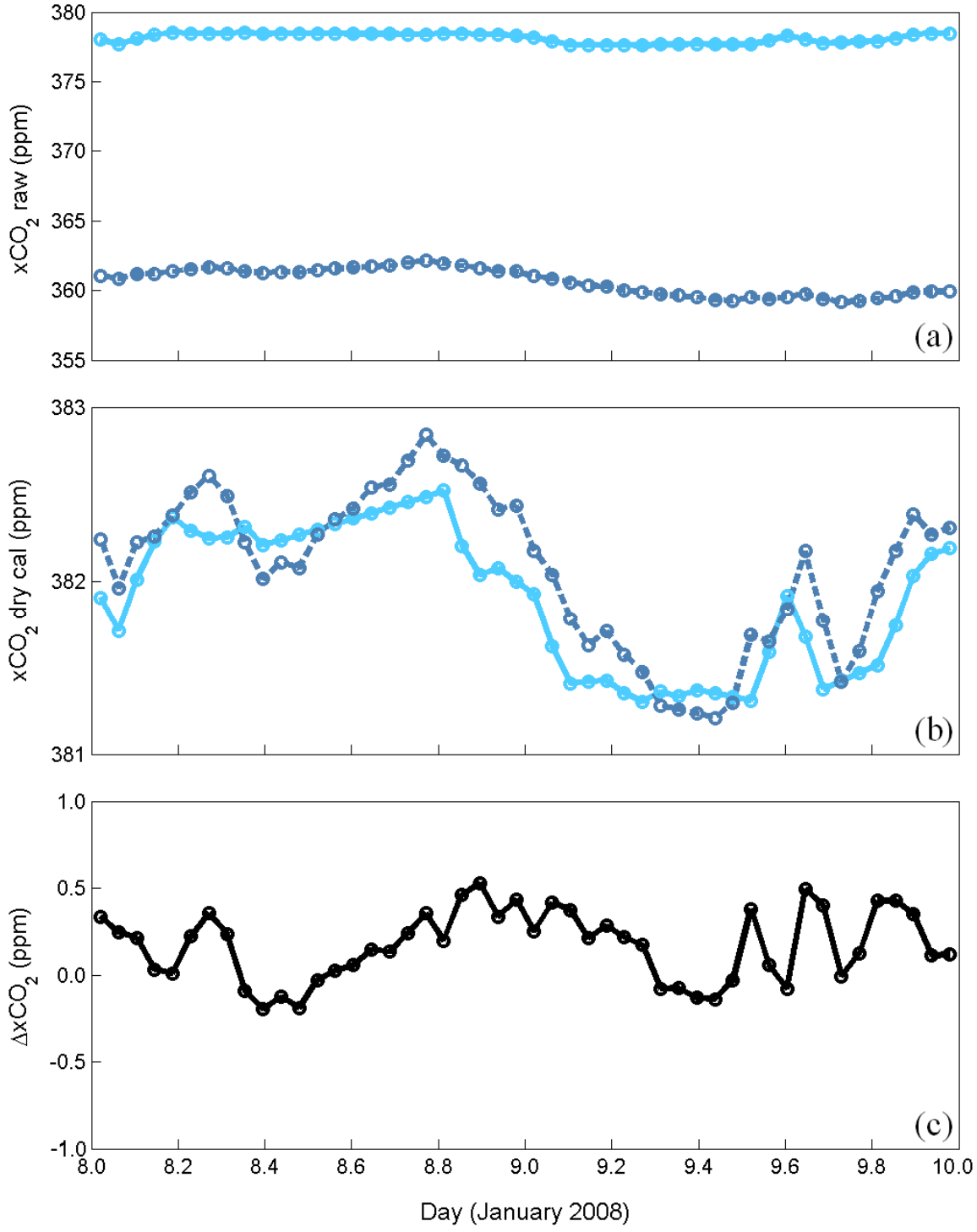

Figure 3.3. Mixing ratios of CO_2 (part per million, ppm, or µmol mol^{-1}) in air (a) raw measurements (xCO_2 raw, µmol mol^{-1}), (b) dry calibrated measurements (xCO_2 dry cal, µmol mol^{-1}) and (c) the difference (CASIX-UEA) in dry calibrated measurements (ΔxCO_2, µmol mol^{-1}) for the UEA (solid line) and CASIX (dashed line) instruments during the first intercomparison period 8-10 January.

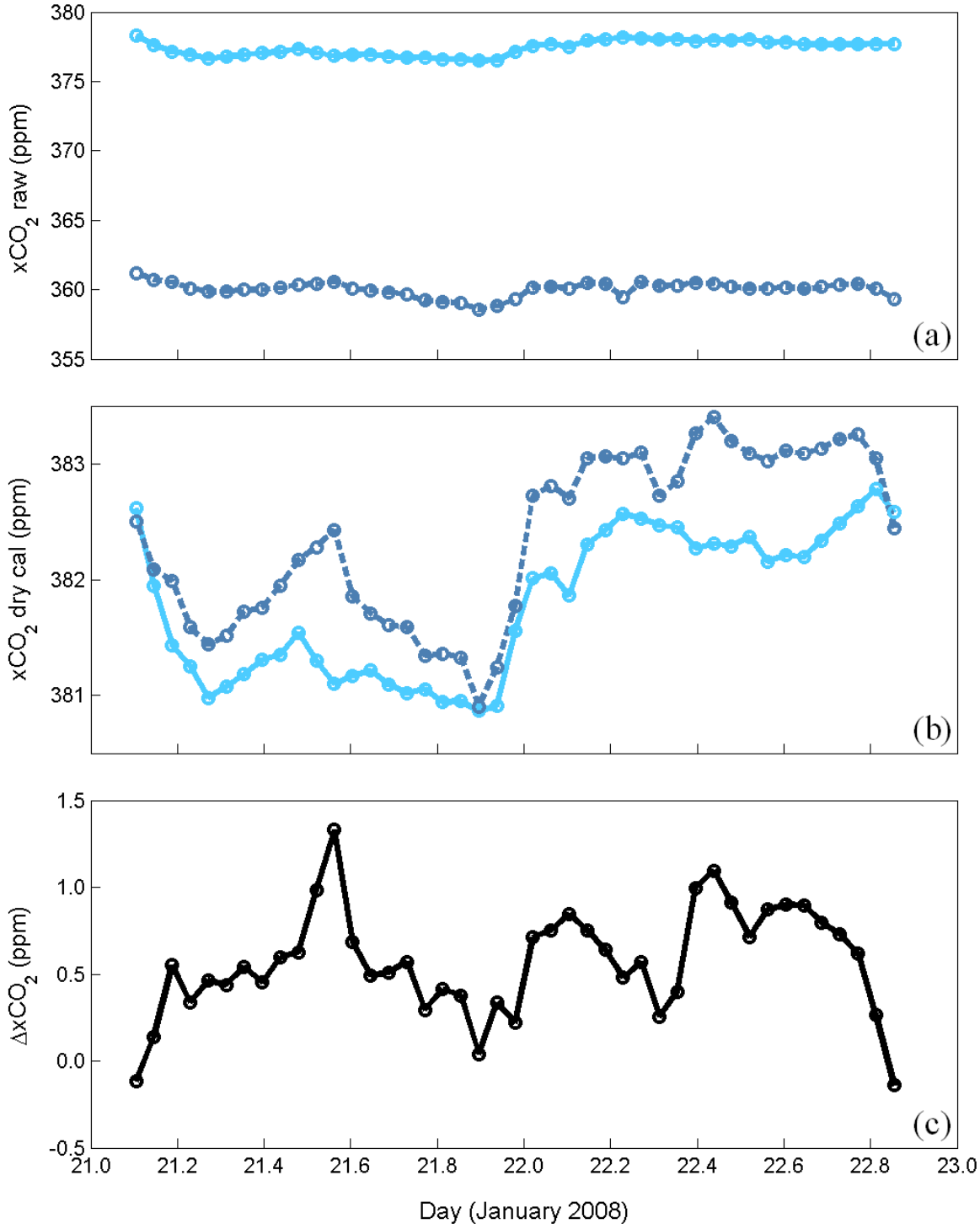

Figure 3.4. Mixing ratios of CO_2 (part per million, ppm, or µmol mol^{-1}) in air (a) raw measurements (xCO_2 raw, µmol mol^{-1}), (b) dry calibrated measurements (xCO_2 dry cal, µmol $mol^{-1}$and (c) the difference (CASIX-UEA) in dry calibrated measurements (ΔxCO_2, µmol mol^{-1}) for the UEA (solid line) and CASIX (dashed line) instruments during the second intercomparison period 21-23 January.

3.5.2. Station atmospheric xCO_2

In order to provide a reference for the atmospheric xCO_2 measurements, several atmospheric stations were located in the wider Scotia Sea region (Fig. 3.5, insert map): Tierra del Fuego (54.87ºS 68.48ºW), Jubany (62.23°S 58.67°W), Palmer (64.77°S 64.05°W) and Halley Bay (75.60°S 25.32°W). From 2006 to 2007, all stations showed analogous trends in atmospheric xCO_2 (Fig. 3.5) and would therefore be suitable references for the instrument intercomparison.

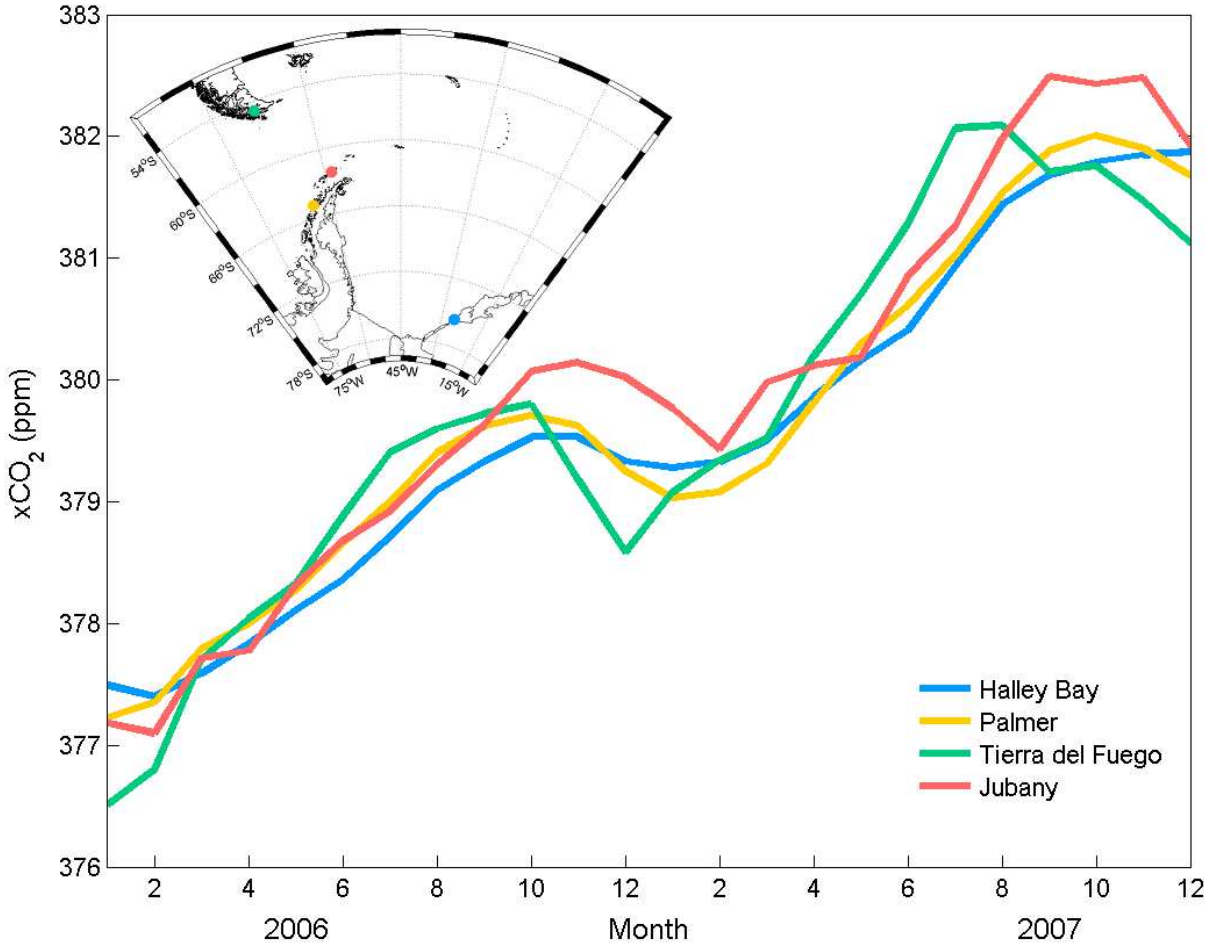

Figure 3.5. Mixing ratios of CO_2 (part per million, ppm, or µmol mol^{-1}) in air (xCO_2, µmol mol^{-1}) during 2006 and 2007 for atmospheric sampling stations in the Scotia Sea region: Halley Bay (blue), Palmer (yellow), Tierra del Fuego (green) and Jubany (red). Insert map shows the location of each of the stations.

Data from Tierra del Fuego showed a more enhanced seasonal signal, which can be ascribed to the effect of photosynthesis on the CO_2 concentrations during austral spring and summer in the more vegetated region. With respect to the location of the RRS *James Clark Ross* during the intercomparison periods (Fig. 3.1), Tierra del Fuego and Jubany stations were selected as the best references for the atmospheric CO_2 measurements. Tierra del Fuego station is situated on the island of Tierra del Fuego, at the southern tip of Argentina (Fig. 3.5, insert map). The sampling station is a ground-based platform at a height of 20 m and samples are taken as flasks and analysed using non-dispersive infra-red (NDIR) for research conducted as part of the NOAA Global Monitoring Division (NOAA/GMD). Measurements are made at weekly intervals, which are then averaged for each month to give monthly means (Thoning et al., 1989). Calibration is done with a series of reference standards with high accuracy and precision, estimated as 0.20 and 0.10 μmol mol^{-1}, respectively (Thoning et al., 1989).

Jubany station is situated on King George Island, in the South Shetland archipelago, north of the Antarctic Peninsula. The sampling station is a ground-based platform at a height of 15 m located within a glaciated, marine type environment under influence of strong westerly winds. Samples are made continuously from an air line and analysed using NDIR for the International Centre for Earth Sciences (CNR-ICES), Italy, and Direcion Nacional del Antartico – Istituto Antartico Argentino (DNA-IAA), Argentina. Hourly data are reported as a mean from xCO_2 measurements made every minute, with an associated accuracy and precision of 0.10 and 0.05 μmol mol^{-1}, respectively (Ciattaglia, 1999). Calibration is done with a series of World Meteorological Organisation gas standards.

3.5.3. Atmospheric xCO_2 back trajectories

To further establish a suitable reference for the shipboard atmospheric xCO_2 measurements, the back trajectories of the sampled air masses from Tierra del Fuego and Jubany stations and the RRS *James Clark Ross* were investigated. To trace the origins of the air sampled during the first intercomparison experiment, 72 hour back trajectory analysis was carried out (Fig. 3.6) using the HYSPLIT (HYbrid Single-Particle Lagrangian Integrated Trajectory) model and NCEP/ NCAR reanalysis data (Draxier and Hess, 1998).

The first intercomparison period was selected for air mass trajectory analysis as the stable atmospheric xCO_2 measurements make this period ideal for reliable atmospheric comparisons (Fig. 3.3b). The 72 hour back trajectories beginning at 00:00 hours on the 9 January revealed

that all sampling platforms were measuring air from the west in the Drake Passage region. By 00:00 hours on 10 January the trajectories had shifted, with Tierra del Fuego station sampling air overlying the Antarctic Peninsula whereas Jubany station and the RRS *James Clark Ross* were measuring air from the northern Scotia Sea (Fig. 3.6). Based on the back trajectories and location of the RRS *James Clark Ross* during the first intercomparison experiment, Jubany station is selected as the most appropriate reference for atmospheric xCO_2 measurements for further data comparisons.

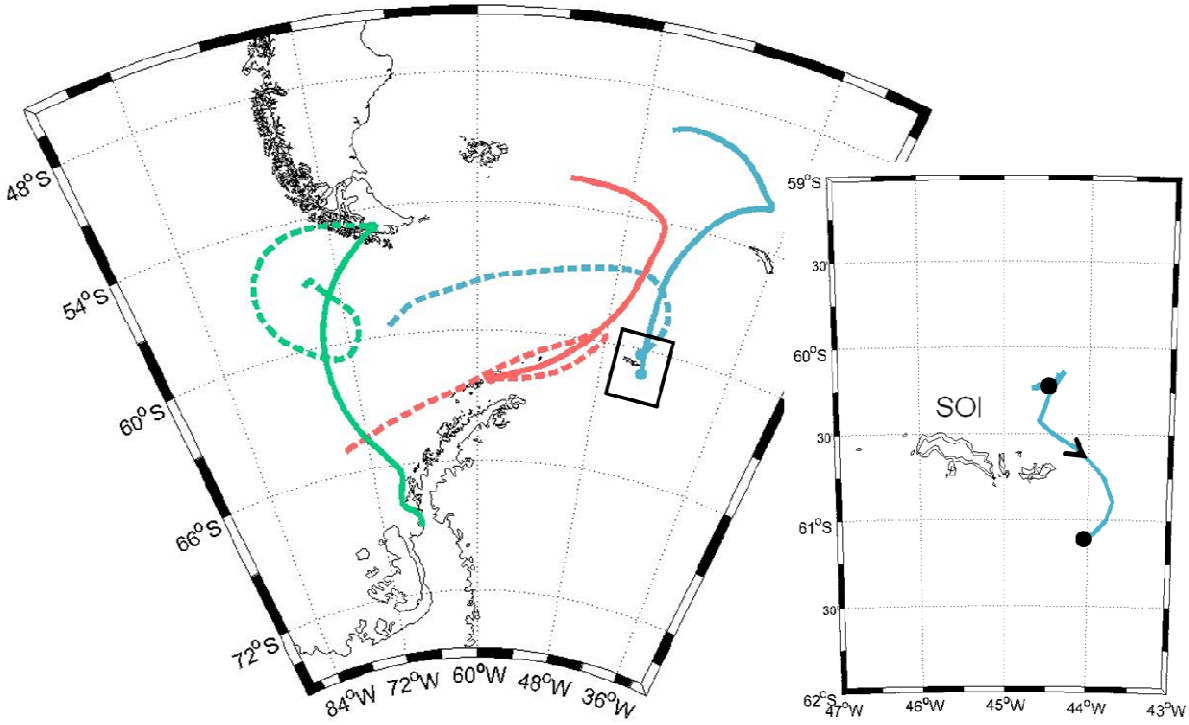

Figure 3.6. HYSPLITT 72 hour back trajectory analysis beginning 00:00 hours on 9 January (dashed lines) and 00:00 hours 10 January (solid lines) 2008 for the RRS *James Clark Ross* (blue), Jubany station (red) and Tierra del Fuego station (green). The box shows an enlargement of the cruise track (Fig. 3.1) around the South Orkney Islands (SOI) during the first intercomparison experiment.

3.5.4. Atmospheric xCO_2 intercomparison

Back trajectories from Jubany station and the RRS *James Clark Ross* show a shift in air mass source from the west to a more northerly direction by the beginning of the 10 January (Fig. 3.6). This can be seen in all three xCO_2 profiles (Fig. 3.7a) as a slight shift in CO_2 content relative to the previous 24 hours. Similar trends were observed during the second experiment,

however the shift in xCO_2, after the first 24 hours, was distinctly larger (Fig. 3.7b). This feature precludes a detailed analysis of atmospheric data as more stable conditions are required to get a realistic accuracy estimate.

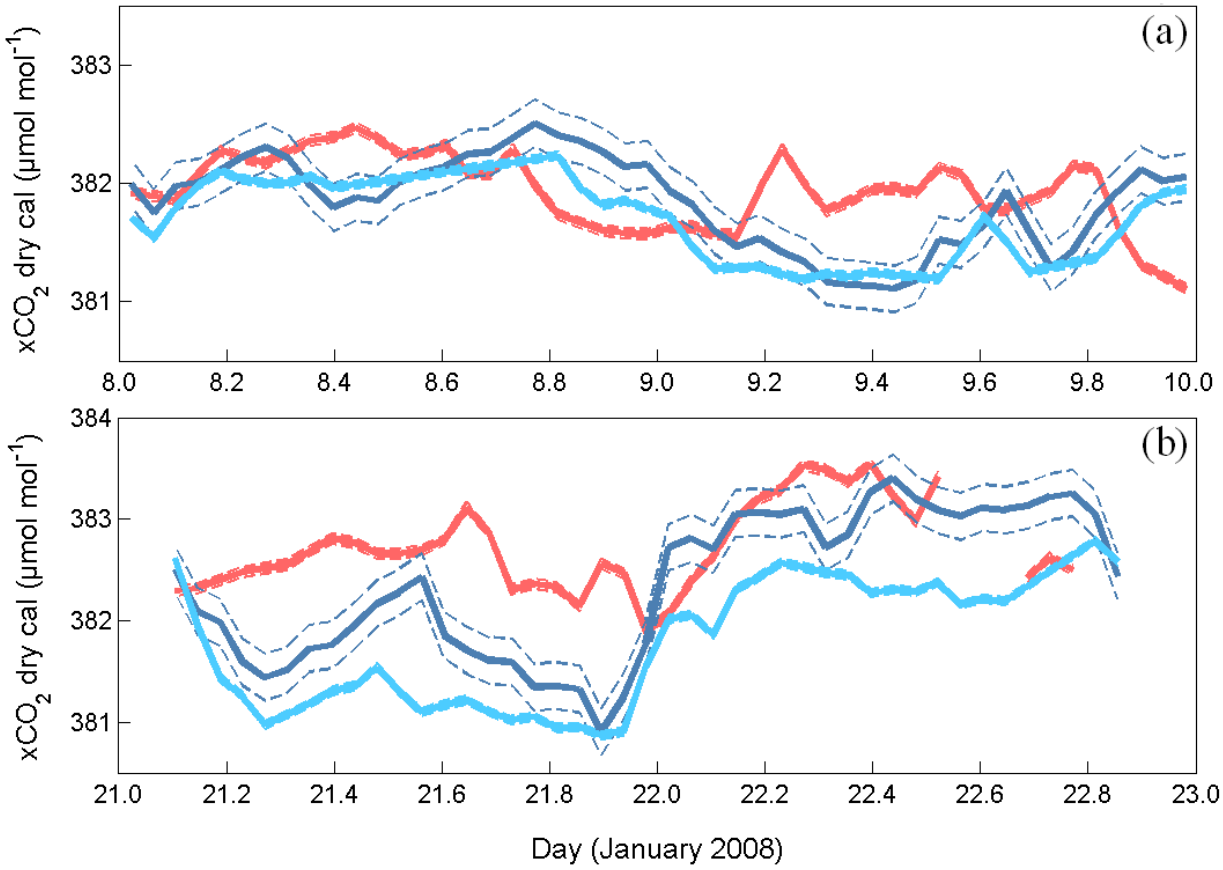

Figure 3.7. Mixing ratios of CO_2 (xCO_2 dry cal, µmol mol^{-1}) in air during (a) 8-10 January and (b) 21-23 January for the UEA (pale blue line) and CASIX (dark blue line) instruments and Jubany station (red line) (Ciattaglia, 1999). The precision of each instrument is represented by the dashed lines: Jubany (0.05 µmol mol^{-1}), UEA (0.04 µmol mol^{-1}) and CASIX (0.23 µmol mol^{-1}).

From the stable atmospheric values during the first intercomparison experiment, average xCO_2 for Jubany was higher than that from both instruments by 0.10-0.30 µmol mol^{-1} (Table 3.2). Therefore, the xCO_2 measurements from both instruments are accurate to within 0.30 µmol mol^{-1}.

Table 3.2. The average CO_2 mixing ratio (xCO_2, μmol mol^{-1}) in dry air from the UEA and CASIX underway pCO_2 instrument is compared to that from Jubany station (Ciattaglia et al., 1999) for the duration of the two intercomparison periods. The values shown are the averages of all data within each intercomparison period with the standard deviation in parentheses.

Year	*Date*	*Jubany xCO_2 μmol mol^{-1}*	*CASIX xCO_2 μmol mol^{-1}*	*UEA xCO_2 μmol mol^{-1}*
2008	8-10 Jan	382.17 (0.37)	382.07 (0.45)	381.90 (0.41)
2008	21-23 Jan	382.71 (0.43)	382.36 (0.75)	381.79 (0.63)

3.6. Seawater pCO_2

The calculation of pCO_2 in seawater requires additional parameters including temperature (in the equilibrator and at the sea surface) and the pressure of the equilibrated air (section 2.5.5). Equilibrator temperature was measured by platinum resistant thermometers in the upper and lower parts of the seawater stream. These were calibrated during the cruise to ensure accurate readings and have an accuracy of 0.2 °C and precision of 0.1 °C (Table 2.7). Comparisons of sea surface and equilibrator temperature for the UEA and CASIX instruments showed that the seawater warmed by 0.74 ± 0.12 °C and 0.78 ± 0.11 °C, respectively. The difference is accounted for by the time lag between seawater at the inlet and reaching the instruments. This was 116 and 120 seconds for the UEA and CASIX instruments, respectively (Table 3.1). Both instruments used ambient pressure as measured by the meteorological unit on the ship. With these variables accounted for, the seawater pCO_2 measurements from both instruments can be compared with the understanding that any differences observed are introduced by either the equilibrator, LICOR or measurement cycle (hard- and software).

Time synchronized seawater pCO_2 data from both instruments is plotted alongside atmospheric pCO_2 for both intercomparison periods (Fig. 3.8). During 8-10 January, both profiles show that surface water pCO_2 was initially at about 360 μatm, which decreased rapidly to just above 260 μatm within the last 12 hours (Fig. 3.8a). This swift reduction of surface water pCO_2 was the result of a phytoplankton bloom at the ice edge as the ship passed ice free water into the ice covered waters over the South Scotia Ridge (Fig. 3.1).

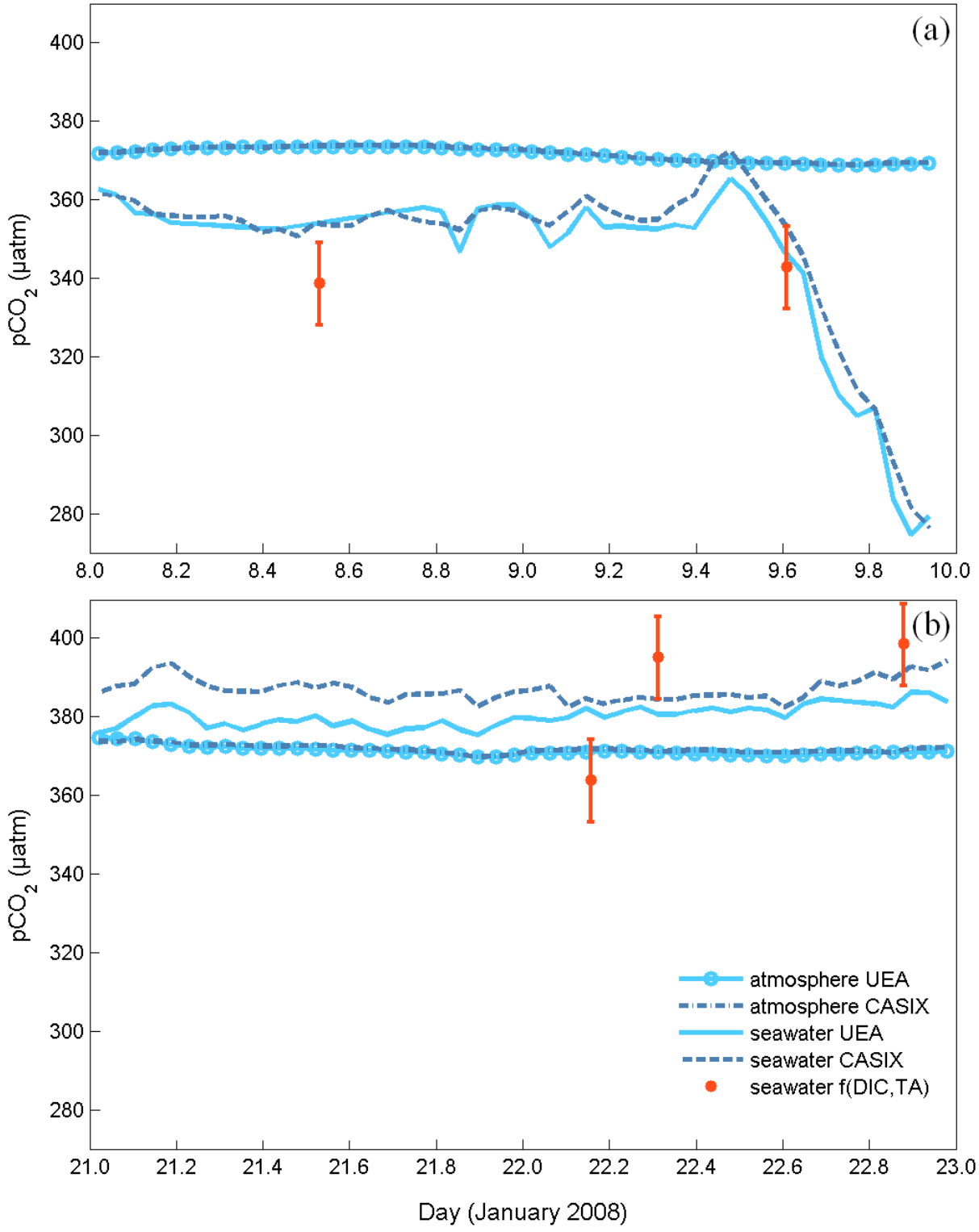

Figure 3.8. Atmospheric and seawater partial pressure of CO_2 (pCO_2, ppm) during (a) 8-10 January and (b) 21-23 January for the UEA (pale blue lines) and CASIX (dark blue lines) instruments. Calculated seawater pCO_2, f(DIC,TA), with error bars representing the accuracy of ± 6 µatm (Table 2.8) (red filled circles).

Upon the rapid decrease in surface water pCO_2, a slight deviation in the profiles was observed (Fig. 3.8a). To investigate this further the rate of change of surface water pCO_2 ($\Delta pCO_2/\Delta t$) was calculated from the UEA data and superimposed to the ΔpCO_2 (CASIX-UEA) profile (Fig. 3.9). For the first 'stable' 36 hours, the hourly averages show a mean difference of 1 ± 2 µatm indicating no systematic difference between the two instruments. Both instruments measured to within 1 µatm of each other even across a slight pCO_2 gradient of about 3 µatm hr^{-1}. During the final 12 hours, the pCO_2 gradient increased up to 13 µatm hr^{-1} , which corresponded to a maximum difference between the instruments of 12 µatm and an average pCO_2 difference of 8 ± 3 µatm. The increased offset under a strong pCO_2 gradient is due to the internal time responses of the different instruments, which is consistent with results from previous at-sea pCO_2 intercomparisons (Körtzinger et al., 1996; Körtzinger et al., 2000).

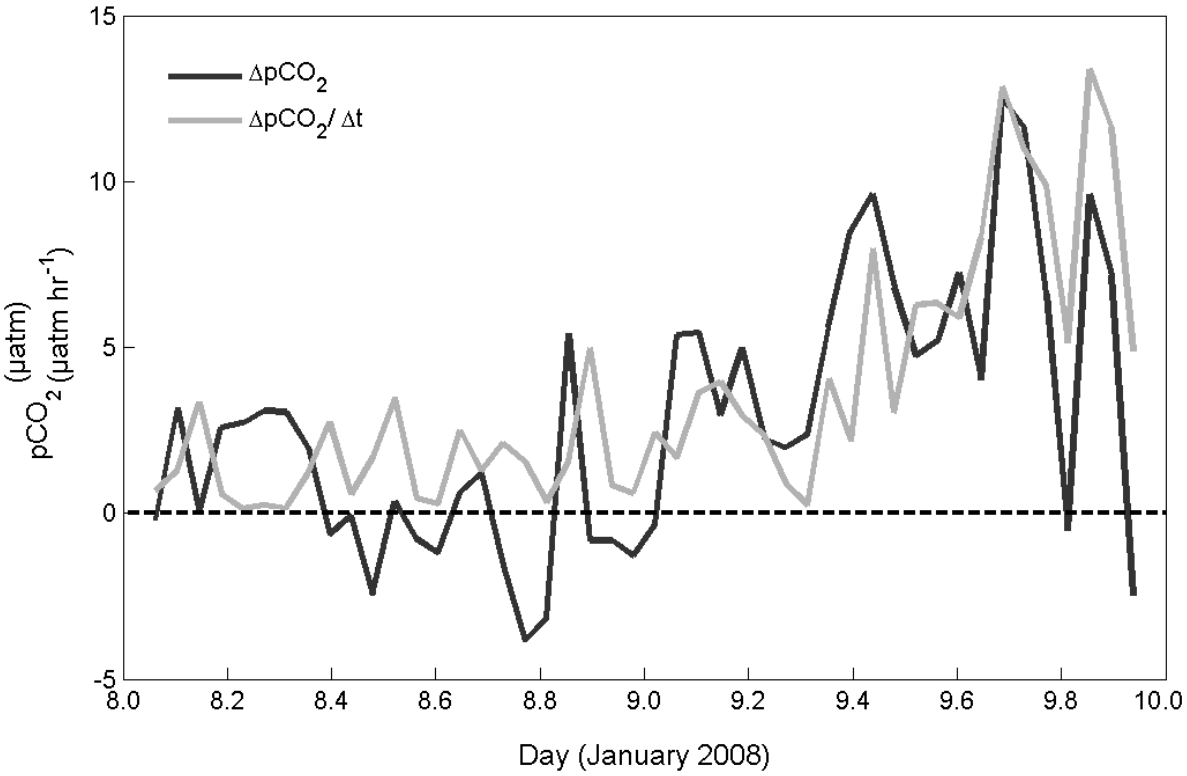

Figure 3.9. The difference in seawater pCO_2 (ΔpCO_2, µatm, black line) between the two instruments (CASIX-UEA) and pCO_2 gradient ($\Delta pCO_2/\Delta t$, µatm hr^{-1}, grey line) during 8-10 January.

The discrete sea water samples collected from the underway supply showed calculated pCO_2 that fell slightly below and above that measured by the instruments, in the stable and strong gradient periods. With no systematic offset between the samples and consideration of the

errors involved the discrete samples (Table 2.7), both instruments are measuring seawater pCO_2 accurately.

During the second intercomparison experiment, sea surface pCO_2 for both instruments was stable for the 48 hour period (Fig. 3.8b). As for the atmospheric xCO_2 data for the first intercomparison experiment, this scenario is good for determining the accuracy and precision of the CASIX measurements. Control charts (Chapter 2) are used to demonstrate whether the instrument measurement is 'in control' and if the data display unbiased, natural variability (DOE, 2007). Upper and lower control limits are determined as ± 3 standard deviations of the mean and they provide an indication of problematic data. For both instruments, the pCO_2 data fall between the upper and lower control limits and display similar natural variability that is independent of each instrument (Fig. 3.10).

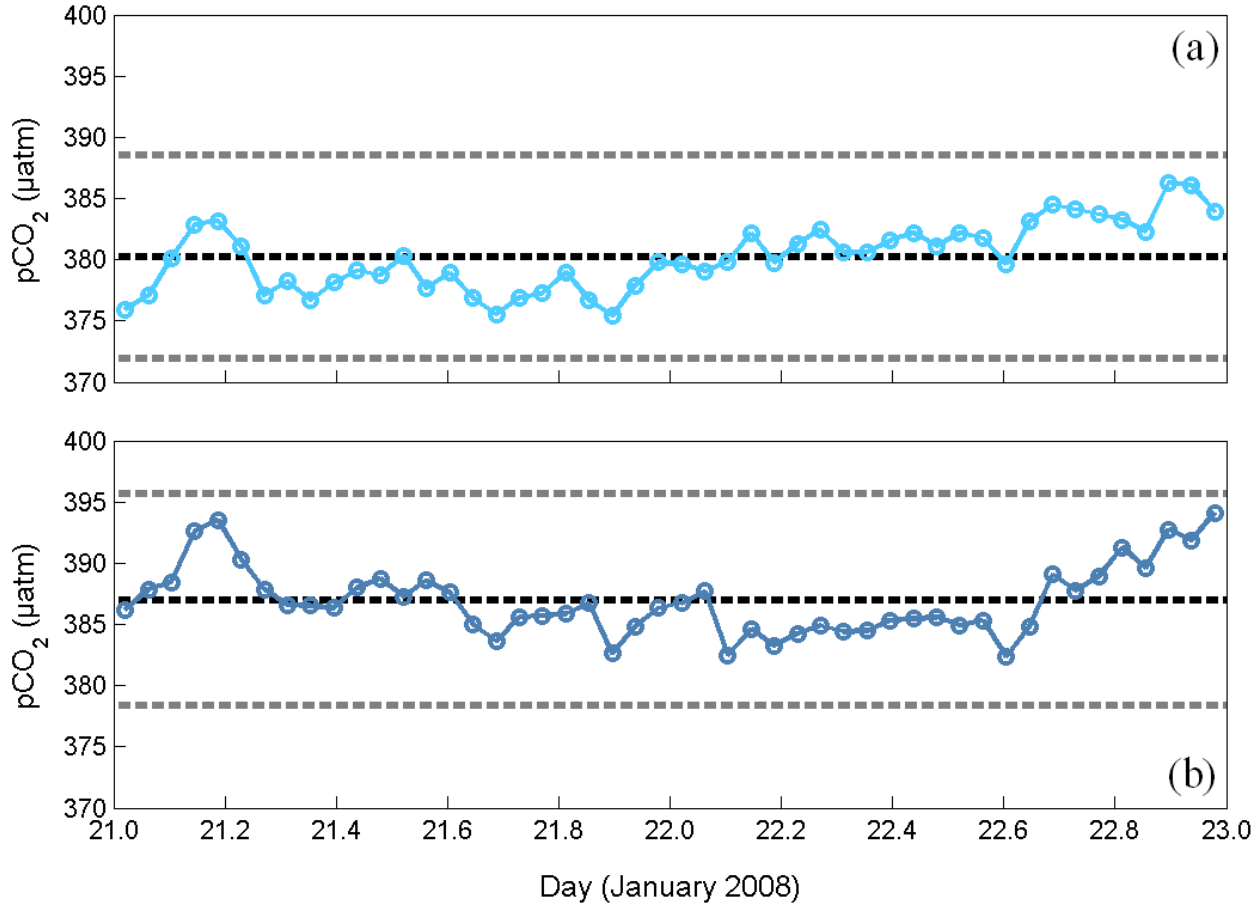

Figure 3.10. Control charts of the seawater partial pressure of CO_2 (pCO_2, µatm) during 21-23 January for (a) the UEA instrument and (b) the CASIX instrument. The black dashed line indicates the mean and grey dashed lines indicate upper and lower control limits (± 3 standard deviations of the mean).

Based on the behaviour of the control charts, the accuracy of the CASIX instrument (Fig. 3.10b), determined as the average offset compared to the UEA instrument (Fig. 3.10a) during 21-23 January, is 7 μatm. The precision of the CASIX seawater pCO_2 measurements (standard deviation) is 3 μatm.

Table 3.3. Details of the accuracy and precision (repeatability) of the mixing ratio of CO_2 (xCO_2, μmol mol^{-1}) and partial pressure of CO_2 (pCO_2, μatm) as determined by investigations of the instruments during the at-sea intercomparison. Adapted from Table 2.7 and updated. *Based on an international at-sea intercomparison (Körtzinger et al., 2000).

Instrument	*Parameter*	*Method*	*Unit*	*Accuracy*	*Precision*
UEA	$xCO_{2\ NOAA}$	infrared detection	μmol mol^{-1}	0.40	0.04
CASIX	$xCO_{2\ NOAA}$	infrared detection	μmol mol^{-1}	1.28	0.23
UEA	$pCO_{2\ seawater}$	infrared detection	μatm	5*	2
CASIX	$pCO_{2\ seawater}$	infrared detection	μatm	7	3

3.7. Conclusion

The at-sea pCO_2 instrument intercomparison conducted onboard RRS *James Clark Ross* summer 2008 indicates the capability of the CASIX instrument for underway sea surface pCO_2 measurements. The results demonstrated that a good agreement of data from different pCO_2 instruments can be achieved at sea. The CASIX instrument was acutely tested and found to be of fast response and suitable accuracy (7 μatm) and precision (3 μatm) for the measurement of underway atmospheric and sea surface pCO_2. Large differences between the two instruments of 12 μatm occurred when along a strong pCO_2 gradient of over 13 μatm hr^{-1}. This has been attributed to the large spatial variability of surface water pCO_2, which was captured differently by each instrument.

Other notable differences between the two xCO_2 and pCO_2 data sets were attributed to the model of LICOR used, equilibrator design and the use of different calibration gases. The use of the LICOR 840 in the CASIX system ultimately affects the final accuracy of the pCO_2 data. In the absence of a vent, the CASIX bubble-type equilibrator was found to operate at a slight

over-pressure compared to ambient conditions. Separate series of gas standards were likely to have introduced a source of error when the raw data sets are calibrated and compared. Suggestions for modifications to the instrument and the raw data are made to improve the accuracy and stability of the pCO_2 data. From this work, recommendations on future use of the CASIX instrument are as follows:

1. A pressure correction (Eqn. 3.1) should be applied to adjust the raw data ($xCO_{2\ raw}$) to pressure of 1 atmosphere (P_0) using the equilibrator pressure (Peq):

$$xCO_{2\ corr} = xCO_{2\ raw} \cdot \frac{P_0}{Peq} \qquad \text{Equation 3.1.}$$

2. Add a vent to the equilibrator to measure at ambient conditions.

3. Change LICOR 840 to a model of increased accuracy, e.g., LICOR 7000.

4. Contemporary carbonate chemistry of the Scotia Sea

4.1. Abstract

Deep carbonate measurements collected across the Scotia Sea during summer 2008 are examined alongside hydrographic data to investigate the distribution of inorganic carbon in relation to the water masses and fronts of the Antarctic Circumpolar Current (ACC). Antarctic Surface Water (AASW) was characterised by distinct summer minima in dissolved inorganic carbon (DIC) and total alkalinity (TA) and was saturated with respect to the calcium carbonate mineral aragonite across the whole Scotia Sea. AASW was further distinguished by a potential temperature (θ) minimum (θ_{min}) at 50-100 m depth, south of 58°S, and at 100-200 m depth, north of 58°S. Upper Circumpolar Deep Water (UCDW) dominated the ACC with a warm core (θ > 1.8 °C) from 500-1000 m depth that extended from 58.0-52.5°S. This water mass was rich in DIC and nitrate. Within the same latitudinal limits, Lower Circumpolar Deep Water (LCDW) occupied the deeper depth range (1000-2000 m) and was distinctly saline, enriched with alkalinity (> 2360 μmol kg^{-1}) and undersaturated with respect to aragonite.

The southward extent of the UCDW core of θ > 1.8 °C and shallower AASW θ_{min} at 58°S marked the location of the Southern ACC Front (SACCF). The terminus of UCDW and shoaling of isohalines at 59°S identified the location of the Southern Boundary (SB) of the ACC and transition into the weakly stratified waters of the Weddell-Scotia Confluence (WSC). In the southern WSC, Warm Deep Water (WDW) was observed flowing out of the northwestern limb of the Weddell Gyre and intruding onto the South Scotia Ridge. The WDW was relatively silicate-rich (> 109 μmol kg^{-1}), with similar carbonate characteristics to LCDW, and is implicated in the thermal erosion of the winter mixed layer (Chapter 5).

Meanders in the SACCF were accompanied by protrusions of cooler, salty water that eroded the UCDW in the northern ACC and in the Georgia Basin (GB). The shoaling isohalines at the SB and the SACCF, in the ACC and GB, provided a mechanism for the DIC-rich UCDW to upwell to the upper ocean. From summer biological carbon uptake to winter DIC enrichment and aragonite undersaturation, these two fronts greatly influence the upper ocean carbonate chemistry of the Scotia Sea on seasonal timescales.

4.2. Introduction

The unbounded flow of the Antarctic Circumpolar Current (ACC) transfers heat, dissolved constituents and plankton around Antarctica and between the three major ocean basins (Rintoul and Sokolov, 2001) and is dynamically linked to the Meridional Overturning Circulation (MOC) through the vertical movement of deep water masses (Naveira Garabato et al., 2002a). The Scotia Sea (Fig. 4.1) is a relatively small but deep ocean basin that forms a transition zone with waters flowing northwards, out of the Weddell Sea, to join the deep currents of the Atlantic (Locarnini et al., 1993; Naveira Garabato et al., 2002a; Meredith at al., 2008). Deep water masses that enter the Scotia Sea in the ACC from Drake Passage undergo intense modification (Whitworth and Nowlin, 1987). The large scale upwelling and formation of deep and intermediate waters in the Southern Ocean implies a close coupling between surface and deep waters. As much of the deep water has been recently ventilated, the distribution of deep waters in the ACC is highly relevant to the marine carbon cycle of the Southern Ocean.

The dominant water mass is Circumpolar Deep Water (CDW), which occupies mid-levels of the ACC beneath the Antarctic Surface Water (AASW) (Reid et al., 1977; Whitworth and Nowlin, 1987). The denser component, Lower Circumpolar Deep Water (LCDW), is distinguished by a salinity maximum, which is derived from North Atlantic Deep Water infiltrating the ACC in the Atlantic sector (Whitworth and Nowlin, 1987). The less dense and older fraction is Upper Circumpolar Deep Water (UCDW), which is characterised by potential temperature (θ_{max}) and nutrient maxima from source waters in the Indian and Pacific oceans (Callahan, 1972). During its passage across the Scotia Sea, CDW becomes cooler and fresher, which has been attributed to interaction with Weddell Sea waters and intense ventilation in the Weddell-Scotia Confluence (WSC), a boundary between the ACC to the north and the Weddell Sea to the south (Whitworth et al., 1994). The broad layer of warm, saline and nutrient-rich CDW shoals to the south with the uplifting isopycnals at the Southern Boundary (SB) (Sievers and Nowlin, 1984; Orsi et al., 1995; Pollard et al., 2002).

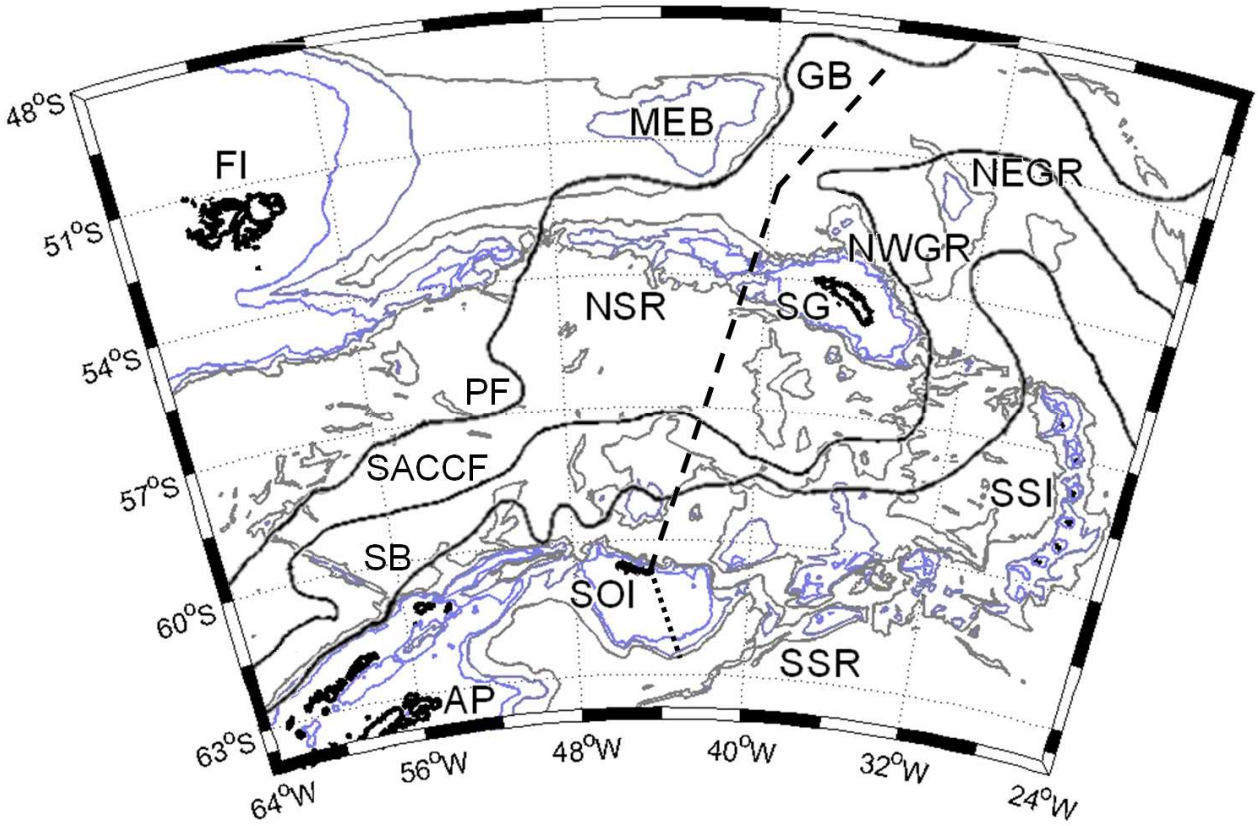

Figure 4.1. A schematic of the Scotia Sea showing the approximate location of the repeat transect (dashed line) and the extended transect (dotted line) from JR177. Some important topographic features are identified: Antarctic Peninsula (AP), South Orkney Islands (SOI), South Scotia Ridge (SSR), South Sandwich Islands (SSI), North Scotia Ridge (NSR), South Georgia (SG), Northwest Georgia Rise (NWGR), Northeast Georgia Rise (NEGR), Georgia Basin (GB), Maurice Ewing Bank (MEB) and the Falkland Islands (FI). Antarctic Circumpolar Current (ACC) fronts shown schematically, adapted from Meredith et al. (2003a): the Southern Boundary (SB, Orsi et al., 1995), Southern ACC Front (SACCF, Thorpe et al., 2002) and the Polar Front (PF, Moore et al., 1999). Depth contours are at 1000, 2000 and 3000 m (GEBCO, 2001).

The SB marks the southern terminus of UCDW, as this water mass outcrops to mix with the AASW where it is transported north and east in the wind-driven Ekman layer. The poleward transport and shoaling of CDW is an important component of the MOC as the northeast component eventually sinks as Antarctic Intermediate Water (AAIW) north of the Polar Front (PF). AAIW formation has been associated with drawing down anthropogenic carbon dioxide (CO_2) into the ocean interior (Caldeira and Duffy, 2000; Sabine et al., 2004). The SB has been

regularly observed as a site of enhanced marine productivity during the spring and summer (Jacques and Panouse, 1991; Comiso et al., 1993; Helbling et al., 1993; Tynan, 1998; Holm-Hansen and Hewes, 2004b; Hewes et al., 2008) with the potential for carbon utilisation through the biological pumps. In contrast, despite an upwelled UCDW providing an iron supply, winter sea ice cover, net remineralisation and unfavourable light conditions allow DIC enrichment in the winter mixed layer (Hoppema et al., 2003), which lowers the pH and saturation state of aragonite in the AASW (McNeil and Matear, 2008). Aragonite undersaturation augments the dissolution of aragonitic exoskeletons of certain marine organisms that contribute to the biological pumps in the Scotia Sea (Feely et al., 2004; Orr et al., 2005; Royal Society, 2005; Fabry et al., 2008).

The Scotia Sea provides a transition zone for recently ventilated deep waters from the Weddell Sea and upwelled CDW within the ACC to flow northwards (Patterson and Sievers, 1980; Orsi et al., 1999; Naveira Garabato et al., 2002a). It is important to gain an insight into the carbonate chemistry distributions across the Scotia Sea, from the sea surface to the deep waters. A 1,400 km transect from the South Orkney Islands to the Polar Front was occupied during spring (November-December) 2006, summer (January-February) 2008 and autumn (March-April) 2009 as part of Scotia Sea FOODWEBS, a component project of the British Antarctic Survey Discovery-2010 programme: http://www.antarctica.ac.uk//bas_research/our_research/previous_research/gsac/discovery_2020.php.

The objective of the project was to understand the seasonal structure and function of different food webs and to infer the effects on the transfer of CO_2 from the atmosphere to the deep ocean. This was to be realised through high frequency surface sampling and deep hydrographic stations. Sea surface fugacity of CO_2 (fCO_2) measurements were made during the three core cruises (section 2.3.2), from a Centre for observation of Air-Sea Interactions and fluXes (CASIX) underway CO_2 system (2006, 2008 and 2009) and a University of East Anglia (UEA) underway CO_2 system (2008) (Chapters 2 and 3). The first deep carbonate measurements of the Scotia Sea were made during summer 2008 and are presented alongside vertical sections of the hydrographic parameters. The distributions of potential temperature and salinity are used to identify the different water masses and locate the hydrographic fronts in the region. The corresponding distributions of the carbonate parameters (Table 4.1) are used

to infer the transport of carbon across the ACC in the context of seasonal processes and future ocean acidification (Chapters 5, 6 and 7).

4.3. Scotia Sea vertical section data

4.3.1. Antarctic Surface Water

As regularly observed, Antarctic Surface Water (AASW) was characterised by a relatively warm, fresh and well mixed surface layer in the upper 200 m (Park et al., 1998; Meredith et al., 2003b). Typical surface temperatures during austral summer were around 1-4 °C, north of 59°S, and between seawater freezing point and -1 °C, south of 59°S (Fig. 4.2). A feature of the AASW was a pronounced sub-surface potential temperature minimum (θ_{min}) of the Winter Water (WW), as a result of the winter mixed layer not being thermally eroded during the summer. The depth of the θ_{min} varied from 50-100 m south of 60°S to 100-200 m in the central ACC. AASW is further distinguished by minima in DIC, alkalinity and macronutrients (Figs. 4.3 and 4.5). This corresponded to relatively high total pH (pH_T) and aragonite saturation states in excess of 1.8 (Fig. 4.4). The transition from the summer mixed layer to the WW was marked by a strong seasonal thermocline and halocline. This was reflected in the distribution of TA and concentration of DIC and carbonate ions as a strong gradient from the base of the summer mixed layer to the WW.

4.3.2. Circumpolar Deep Water

North of 59°S, potential temperature varied from minima ($\theta_{min} \leq 1.0$ °C) in the WW to maxima > 1.5 °C in a core of θ_{max} at 300-800 m depth (Fig. 4.2). This was accompanied by maxima in nitrate and phosphate concentrations (Fig. 4.5), confirming the location of UCDW up to 52.5°S. Silicate concentrations showed a uniform increase with depth across the Scotia Sea and, in contrast to nitrate and phosphate, a strong north south gradient in AASW and UCDW (Fig. 4.6). Concentrations of DIC and alkalinity were wide ranging but showed notable increases with depth (Fig. 4.3). Maximum aragonite saturation states were 1.2 (Fig. 4.4). Beneath the UCDW, salinity increased to a core of S_{max} at 1000-1600 m depth, with similar latitudinal extension (Fig. 4.2). This identified the denser LCDW. Across the Scotia Sea, DIC and TA increased with depth and reached maxima in the AAZ within the LCDW. Concentrations of DIC and alkalinity of 2257-2261 and 2362-2367 μmol kg^{-1}, respectively,

can be attributed to LCDW (Table 4.1). From 55-58°S, LCDW is undersaturated with respect to aragonite below 1500 m (Fig. 4.4).

4.3.3. The ACC fronts

A strong surface temperature gradient was observed in the AASW between stations 21 and 25 (Fig. 4.2). Below 500 m, the UCDW $\theta_{max} \geq 1.8$ °C abruptly decreased at about 58°S near station 25. South of 58°S, the AASW θ_{min} became notably cooler (≤ 0 °C) and shoaled to about 150 m. These features marked the location of the SACCF. Alkalinity showed a deep horizontal gradient across the SACCF boundary. Concentrations of nitrate and phosphate decreased across the SACCF at all depths (Fig. 4.5). In contrast, concentrations of silicate increased as the 80 μmol kg^{-1} contour shoaled from 700 m in the UCDW, over the NSR, to less than 100 m in the AASW. The high concentrations of DIC and alkalinity associated with the LCDW were strongly reduced at depth.

The complete absence of UCDW south of about 59°S (station 21) defined the northern limit of the WSC and the Southern Boundary (SB) of the ACC. The SB separated cold, fresh upper ocean waters to the south (stations 14-21) from the oceanic waters of the ACC (stations 21-53), in the Antarctic Zone (AAZ). The upper ocean (0-400 m) of the WSC was weakly stratified compared to the distinct vertical temperature and salinity characteristics of the CDW in the ACC, supporting early classifications of this sub-region (Patterson and Sievers, 1980).

The Polar Front (PF) is a strong, circumpolar jet that represents the northern limit of the AAZ and the Scotia Sea (Pollard et al., 2002). Sea surface temperature, salinity and contours of dynamic height identified the surface expression of the PF at 49-50°S 40°W during summer 2008 (Chapter 6). However, occupation of the transect did not permit hydrographic stations north of about 52.5°S to be carried out, precluding a vertical identification of the PF at this time.

4.3.4. Warm Deep Water

South of the South Scotia Ridge (SSR), an incursion of warmer and more saline water was observed at 300-800 m depth at station 14 (Fig. 4.2). This is Warm Deep Water (WDW) from the Weddell Gyre and is a cooler, fresher variety of LCDW that was advected into the gyre to the east (Orsi et al., 1993) and is accordingly DIC-rich. The WDW observed at station 14 had an average DIC content of 2260-2261 μmol kg^{-1}, which is very similar to earlier reports of 2266 ± 3 μmol kg^{-1} measured in WDW in the Weddell Gyre during December and January 1993 (Hoppema et al., 1999). In addition, the WDW was comparatively silicate rich, which has been previously observed and attributed to the interaction of WDW with bottom waters overlying sediments in the Weddell Sea (Weiss et al., 1979).

Intrusions of WDW below ice covered AASW can provide sufficient heat to melt the sea ice and enrich the winter mixed layer with CO_2 (Weiss et al., 1979; Takahashi et al., 1993; Hoppema et al., 1999; Stoll et al., 1999; Bakker et al., 2008). The effect of seasonal sea ice melt and potential affects of WDW on the marine carbon cycle of the WSC is discussed in Chapter 5. The WDW observed at station 14 provided further evidence of a pathway for deeper waters with origins in the Weddell Sea to overspill the SSR and mix with the CDW of the ACC (Locarnini et al., 1993; Naveira Garabato et al., 2002a). This observation supports the notion that the WSC is a transition zone between DIC-rich waters flowing out of the Weddell Sea to waters of the ACC (Orsi et al., 1993; Whitworth et al., 1994).

4.3.5. Water masses, fronts and biogeochemistry of the Scotia Sea

A result of the interaction of Weddell Sea and ACC waters is that the CDW outflowing the Scotia Sea in the Georgia Basin (GB) to the north is cooler and fresher compared to the CDW that enters from Drake Passage to the west (Naveira Garabato 2002a). Pathways for CDW to enter the GB are either by flowing over the western NSR in the PF or by passing to the east of the island of South Georgia within the SACCF along the eastern flank of the NSR (Fig. 4.1), before retroflecting to the northeast (Thorpe et al., 2002). The frontal paths are strongly constrained by the bathymetry of the NSR (Smith et al., 2010) (Fig. 1.7). The CDW transported into the GB by the SACCF is slightly cooler and fresher compared to that found at the PF (Naveira Garabato et al., 2002a). Vertical distributions of potential temperature and salinity (Fig. 4.2) in the lower GB (stations 46, 48, 51 and 53) suggest that the CDW was

transported in within the meandering SACCF that loops anticyclonically around South Georgia (Fig. 4.1).

The interaction of CDW with the NSR and SACCF with the eastern NSR has been proposed as a likely mechanism of macronutrient and iron supply to upper waters of the GB (Korb and Whitehouse, 2004; Korb et al., 2008; Whitehouse et al., 2008). Stations over the NSR and lower GB revealed a highly stratified water column, with warm surface waters (> 3.5 °C) overlying the nutrient rich UCDW. These waters supported enhanced phytoplankton biomass, where chlorophyll-a concentrations in the upper 60 m typically exceeded 5 mg m^{-3} (Fig. 4.6). This corresponded to large depletions in DIC, nitrate and phosphate and increases in pH_T and the saturation state of aragonite (Figs. 4.3-4.5). Substantial silicate depletion was observed in the upper water column, north of 56°S where concentrations were reduced to < 1 μmol kg^{-1} in the GB (Fig. 4.6), in accordance with high diatom abundance in summer 2008 (Korb et al., 2010).

The warm, nutrient-rich core of UCDW resided directly below the AASW in the GB (Figs. 4.2 and 4.4) with nitrate concentrations greater than 33 μmol kg^{-1}, in agreement with observations at this location in April-May 2003 (Smith et al., 2010). The upward sloping isohalines and isotherms corresponded to increased macronutrient concentrations, especially silicate, in the sub-surface waters of the GB. These distributions suggest that nutrients are supplied to the surface waters in order to sustain the phytoplankton blooms in this region. The effect of the South Georgia blooms on the marine carbon cycle of the Scotia Sea, and evidence for natural iron fertilisation, is discussed in Chapter 6.

The meandering path of the SACCF was also observed between stations 35 and 37 as cooler and more saline water was entrained at the surface, eroding the thermal structure of the UCDW (Fig. 4.2). Isohalines have stronger slopes at the fronts, which can be seen at stations 21 (SB), 25 (SACCF), 35-37 (SACCF meander) and 51-53 (SACCF meander). These features provided a mechanism for nutrient-rich deep water to enter the euphotic zone with the potential to support high levels of primary production during the growing season. This has been implicated in the elevated phytoplankton biomass and nutrient depletion observed in the AASW at the above named stations during summer 2008 (Figs. 4.5-4.6).

Oppositely, sea ice cover (in the WSC), net remineralisation and enhanced vertical mixing during winter could lead to DIC enrichment of the mixed layer at these locations. The distributions of DIC and TA in the upper 600 m tended to follow the isohalines that shoaled towards stations 21 and 25. Similarly, projections of DIC-rich water from below the AASW were observed at the SACCF meanders at stations 37 and particularly in the GB, stations 48, 51 and 53. This could provide a pathway for DIC-rich sub-surface waters to enter the winter mixed layer. As a result, water of low pH_T and lower saturation states of aragonite can penetrate the AASW along the shoaling isohalines through increased vertical mixing during the winter (Fig. 4.2 and 4.4). The affect of shoaling isohalines and upwelled DIC-rich CDW on sea surface carbonate chemistry from winter to autumn is discussed in Chapter 7.

Table 4.1. Definitions of the principle water masses of the Scotia Sea as distinguished in the vertical distributions of potential temperature and salinity (Fig. 4.1). Macronutrient and carbonate chemistry distributions observed during summer 2008 are added.

	AASW	*UCDW*	*LCDW*	*WDW*
θ (°C)	θ_{min} 100-200 m	$1.6 < \theta_{max} < 3.2$ 500 m	$0.2 < \theta < 1.9$	$0.2 < \theta_{max} < 0.6$ 500 m
Salinity (*S*)		$34.00 < S < 34.71$	$S_{max} > 34.73$ 1000-1500 m	$S_{max} < 34.69$ 800 m
References		Callahan (1972) Naveira Garabato et al. (2002a)	Reid et al. (1977) Whitworth and Nowlin (1987)	Orsi et al. (1993) Orsi et al. (1995)
Nitrate (μmol kg^{-1})	13.8-36.4	31.2-36.1	33.5-33.6	31.1-31.5
Silicate (μmol kg^{-1})	0.0-100.6	49.7-94.2	100.8-109.4	109.8-117.0
DIC (μmol kg^{-1})	2084-2252	2239-2263	2257-2261	2260-2261
TA (μmol kg^{-1})	2237-2350	2329-2356	2362-2367	2352-2357
Ωaragonite	1.0-2.3	≤ 1.2	≤ 1.0	1.1

4.3.6. Deep chlorophyll-a maxima

In the central Scotia Sea, chlorophyll-a profiles at stations 30 and 33 revealed deep chlorophyll-a maxima (DCM) at 60-80 m depth (Fig. 4.6), a feature not uncommon to this region (Holm-Hansen et al., 2004a; Holm-Hansen et al., 2005). Despite the high macronutrient concentrations (Fig. 4.5), the water column above the DCM had the lowest concentration of chlorophyll-a observed in summer 2008. These characteristics exemplify high-nutrient low-chlorophyll (HNLC) conditions. The location of the DCM coincided with a deepening of the 2200 μmol kg^{-1} contour of DIC from about 50 m across the WSC and southern AAZ to 200 m close to South Georgia (Fig. 4.3). This suggests that despite surface HNLC conditions, some biological carbon uptake in the mid-Scotia Sea could result in the presence of DCM. This has implications in using satellites that only 'see' the surface as tools to distinguish HNLC waters, which may lead to an underestimation of the biological utilisation of DIC during the summer (Chapter 6).

4.3.7. Vertical section profiles

Figure 4.2. (page 140) Vertical distribution of potential temperature (θ) and salinity across the Scotia Sea in summer 2008. Hydrographic station positions (triangles) are shown. Principle water masses are identified, based on the definitions of Naveira Garabato et al. (2002a) and Meredith et al. (2003b): Antarctic Surface Water (AASW), Upper Circumpolar Deep Water (UCDW), Lower Circumpolar Deep Water (LCDW) and Warm Deep Water (WDW). The location of the Southern Boundary (SB) and Southern Antarctic Circumpolar Current Front (SACCF) are indicated, according to the definitions of Orsi et al. (1995). Key bathymetric features are the South Scotia Ridge (SSR), South Orkney Islands (SOI), the North Scotia Ridge (NSR) and the Georgia Basin (GB). The latitudinal limits of the Weddell-Scotia Confluence (WSC) and the Antarctic zone (AAZ) are shown.

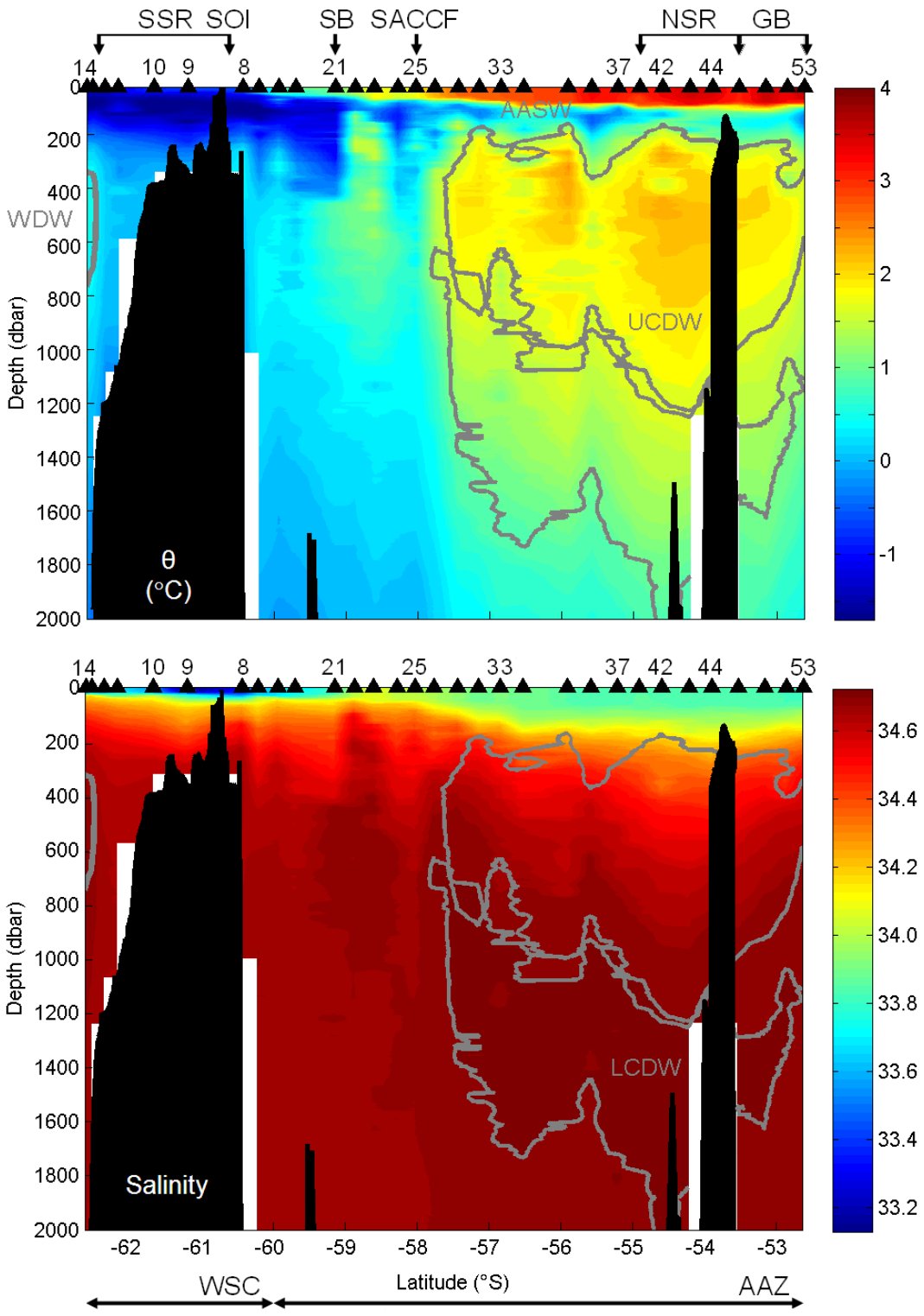
SSR SOI
SB SACCF
NSR GB
14 10 9 8 21 25 33 37 42 44 53
AASW
WDW
UCDW
LCDW
θ
(°C)
Salinity
Depth (dbar)
0 200 400 600 800 1000 1200 1400 1600 1800 2000
4 3 2 1 0 -1
34.6 34.4 34.2 34.0 33.8 33.6 33.4 33.2
-62 -61 -60 -59 -58 -57 -56 -55 -54 -53
WSC
Latitude (°S)
AAZ

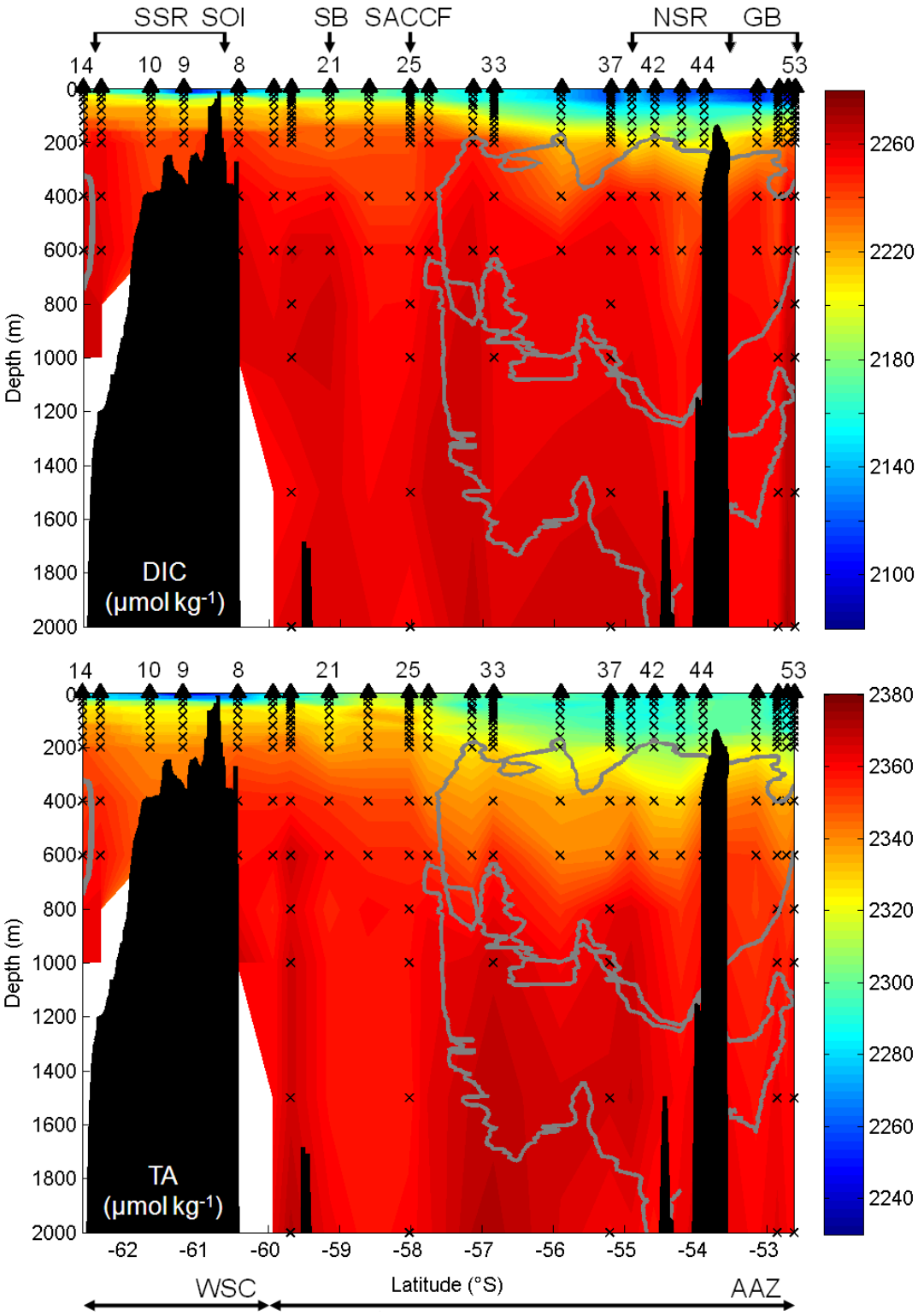

Figure 4.3. Vertical distribution of dissolved inorganic carbon (DIC, µmol kg^{-1}) and total alkalinity (TA, µmol kg^{-1}) across the Scotia Sea in summer 2008. Sample locations (crosses) and hydrographic station positions (triangles) are shown. Water masses, fronts, bathymetric features and hydrographic regions as in Fig. 4.2.

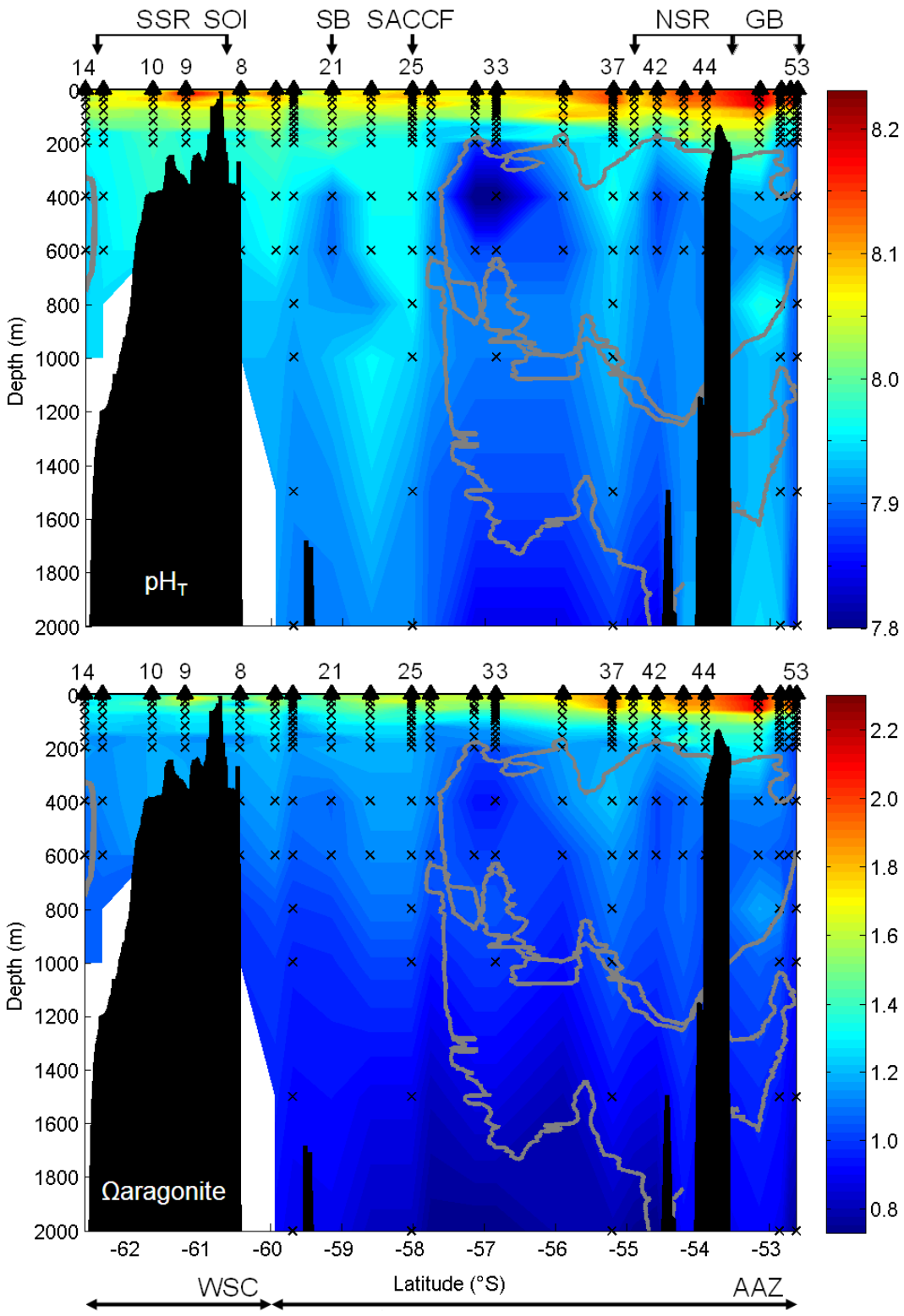

Figure 4.4. Vertical distribution of total pH (pH_T) and aragonite saturation state (Ωaragonite) across the Scotia Sea in summer 2008. Sample locations (crosses) and hydrographic station positions (triangles) are shown. Water masses, fronts, bathymetric features and hydrographic regions as in Fig. 4.2.

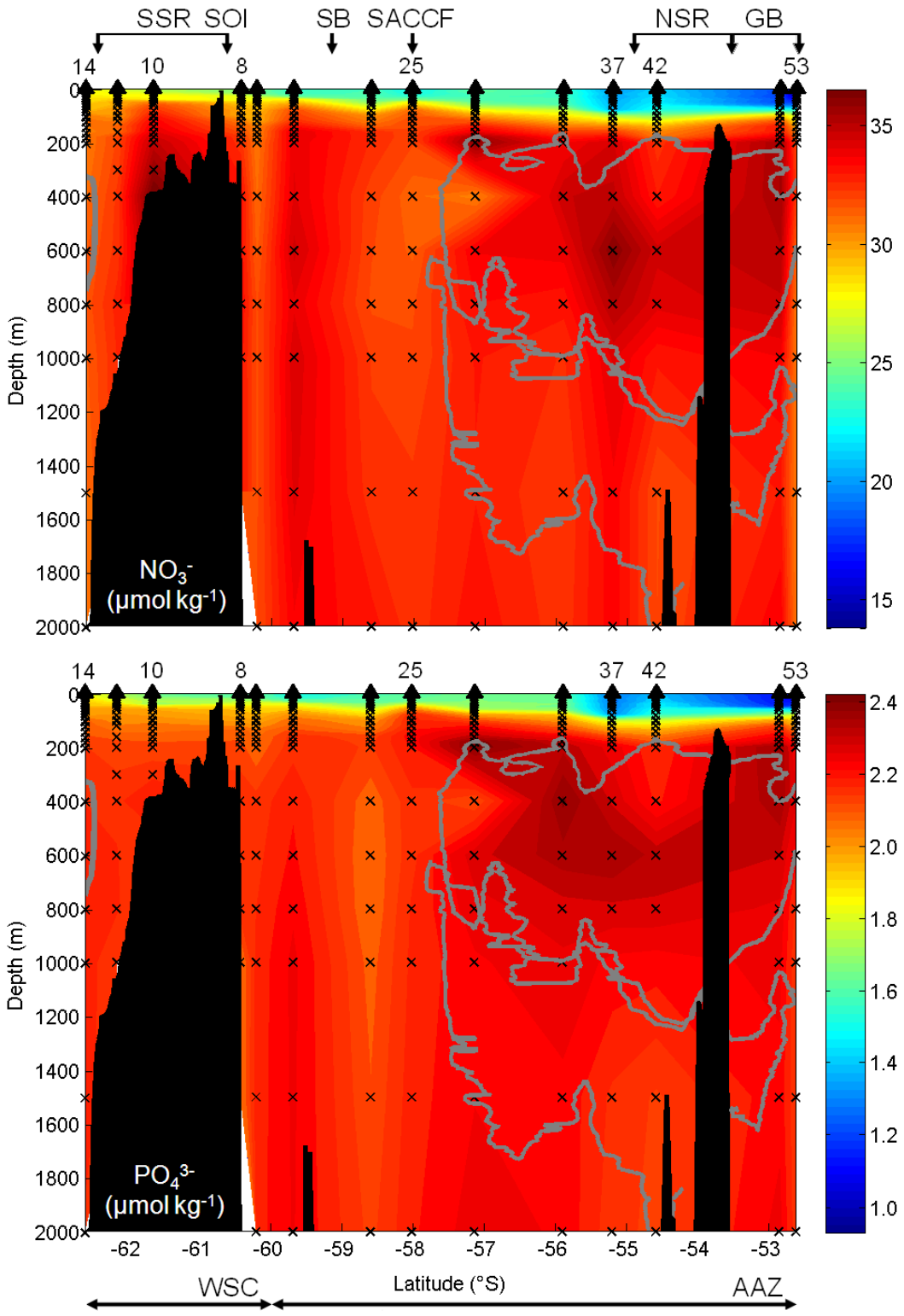

Figure 4.5. Vertical distribution of nitrate (NO_3^-, µmol kg^{-1}) and phosphate (PO_4^{3-}, µmol kg^{-1}) across the Scotia Sea in summer 2008. Sample locations (crosses) and hydrographic station positions (triangles) are shown. Water masses, fronts, bathymetric features and hydrographic regions as in Fig. 4.2.

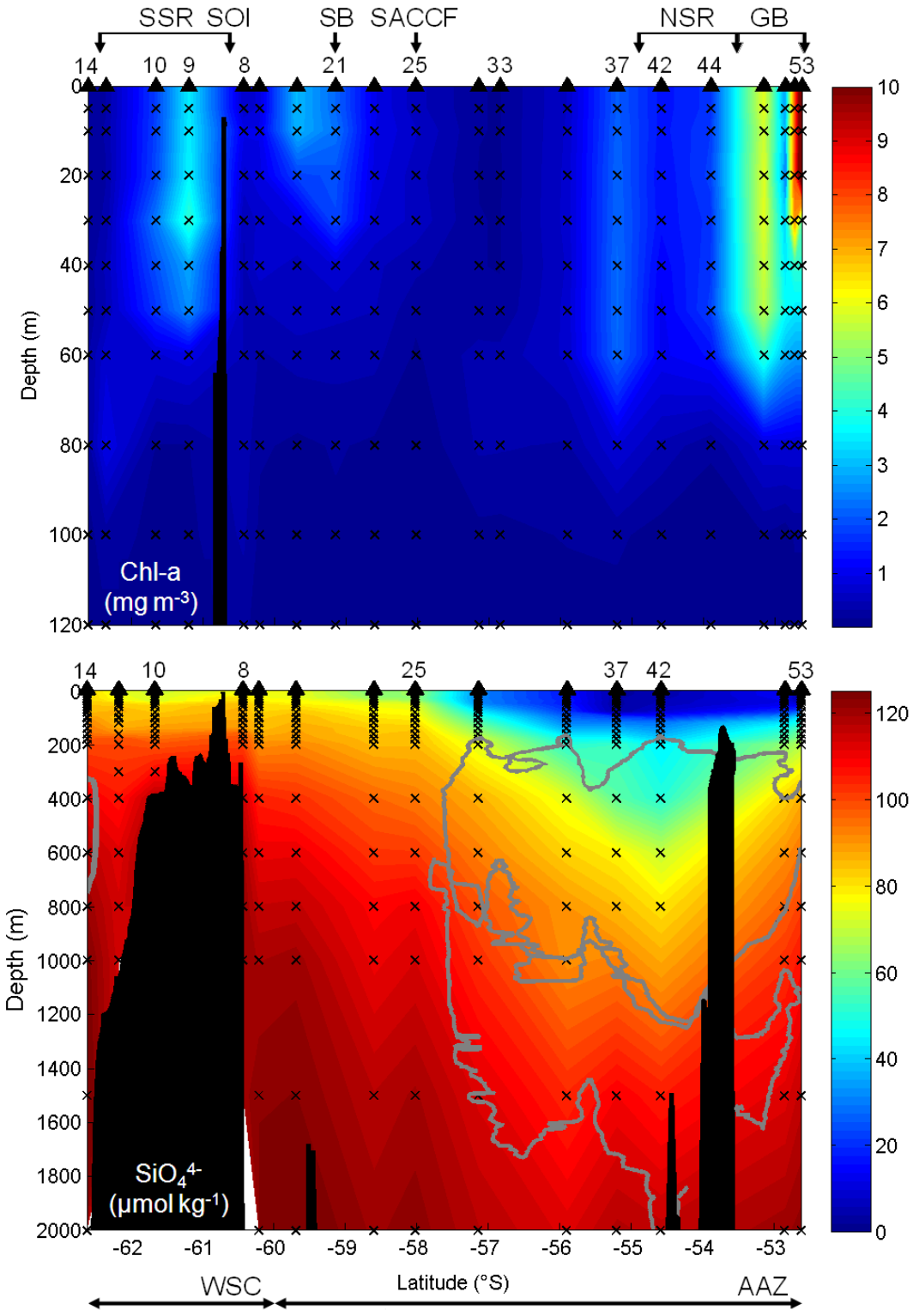

Figure 4.6. Vertical distribution of chlorophyll-a (chl-a, mg m^{-3}) and silicate (SiO_4^{4-}, µmol kg^{-1}) across the Scotia Sea in summer 2008. Sample locations (crosses) and hydrographic station positions (triangles) are shown. Water masses, fronts, bathymetric features and hydrographic regions as in Fig. 4.2.

4.4. Conclusion

Deep vertical sections of hydrographic and carbonate parameters across the Scotia Sea during summer 2008 are presented and discussed. The major water masses and fronts were identified. The corresponding distributions of carbonate chemistry parameters inform on the processes that affect the distribution of carbon across the ACC. AASW was characterised by distinct minima for all parameters and was saturated with respect to aragonite across the Scotia Sea. Warm UCDW was rich in DIC and nitrate and had a large range in silicate concentrations due to the latitudinal gradient present at this depth range. Salty LCDW was distinctly enriched with alkalinity and was undersaturated with respect to aragonite. WDW was observed in the southern WSC and was found to be relatively silicate-rich, with similar characteristics to LCDW.

At depth, the ACC transports high concentrations of DIC, nitrate, phosphate and alkalinity within the CDW around the Southern Ocean. The sloping isohalines at the SB and the SACCF provide a mechanism for CDW to reach the upper ocean. During the summer, the upwelled CDW at the SB mixed with AASW and was transported north and east in the wind-driven Ekman layer where it became notably warmer and fresher. The nutrient-rich water enhanced phytoplankton activity at upwelling sites of the SB, SACCF and SACCF meanders in the central ACC and the GB. This was accompanied by a reduction in DIC and macronutrients. In contrast, the absence of photosynthetic activity during winter would lead to DIC enrichment in the winter mixed layer through increased vertical mixing of the AASW into the DIC-rich sub-surface water. This would lead to low pH_T waters entering the upper ocean and a reduction in the saturation state of aragonite in the winter AASW. This suggests the potential for large seasonal (winter-summer) variability in sea surface carbonate chemistry, which has implications for calcareous organisms and the onset of ocean acidification in the Scotia Sea.

The hydrographic data presented in Chapter 4 can be summarised schematically (Fig. 4.7) to provide a basis for interpretation of the marine carbon cycle during summer in the Weddell-Scotia Confluence (Chapter 5), the Antarctic Zone (Chapter 6) and from a seasonal perspective across the whole Scotia Sea (Chapter 7).

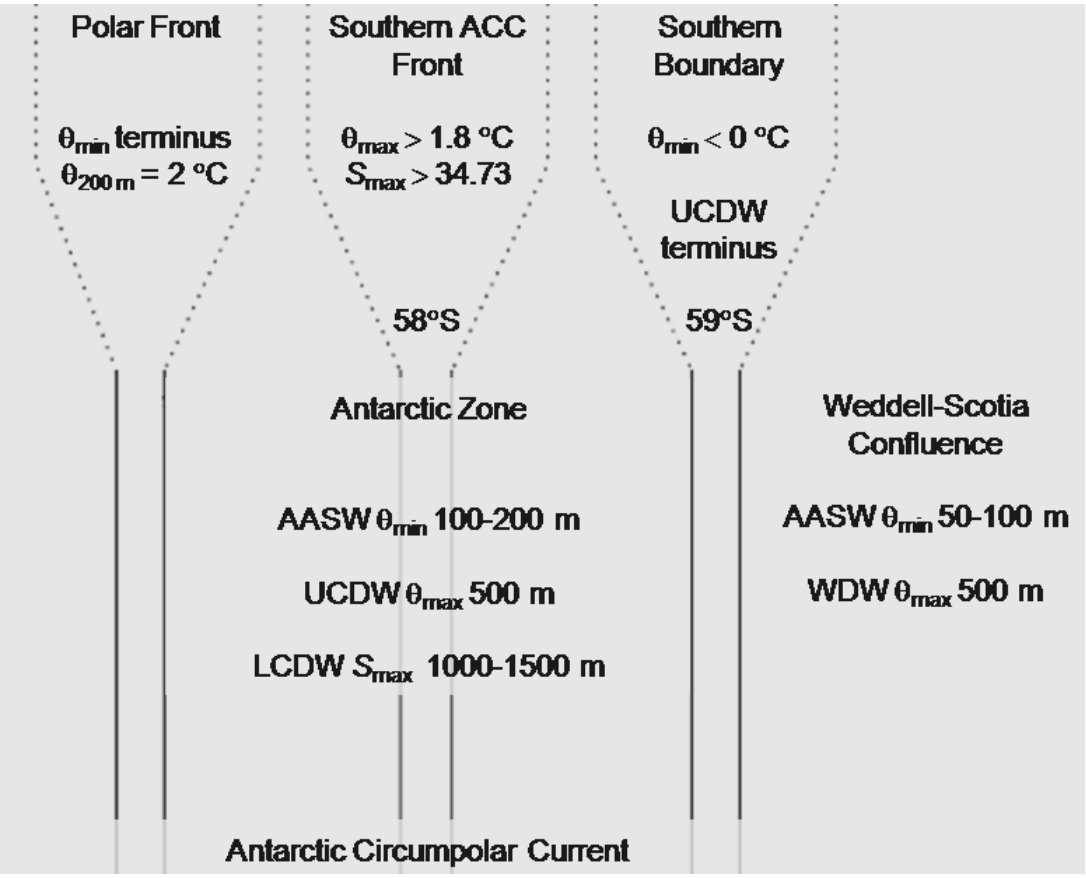

Figure 4.7. Schematic of the fronts and zones of the Scotia Sea based on the vertical distributions of potential temperature (θ, °C) and salinity (*S*) during summer 2008, adapted from Pollard et al. (2002). Frontal boundaries based on definitions from Orsi et al. (1995) and Belkin and Gordon (1996). Antarctic Surface Water (AASW), Upper Circumpolar Deep Water (UCDW), Lower Circumpolar Deep Water (LCDW) and Warm Deep Water (WDW) characteristics from Reid et al. (1977), Whitworth and Nowlin (1987), Naveira Garabato et al. (2002a) and Meredith et al. (2003b). Antarctic Zone and Weddell-Scotia Confluence as described in Whitworth et al. (1994) and Pollard et al. (2002).

5. Rapid changes in surface water carbonate chemistry during Antarctic sea ice melt

5.1. Abstract

The effect of sea ice melt on the carbonate chemistry of surface waters in the Weddell-Scotia Confluence, Southern Ocean, was investigated during January 2008. Contrasting concentrations of dissolved inorganic carbon (DIC), total alkalinity (TA) and the fugacity of carbon dioxide (fCO_2) were observed at and around the receding sea ice edge. The precipitation of carbonates such as ikaite ($CaCO_3.6H_2O$) in sea ice brine has the net effect of decreasing DIC and TA and increasing the fCO_2 in the brine. Deficits in DIC up to 12 ± 3 μmol kg^{-1} in the marginal ice zone (MIZ) are consistent with the release of DIC-poor brines to surface waters during sea ice melt. Biological utilisation of carbon was the dominant process and accounted for 41 ± 1 μmol kg^{-1} of the summer DIC deficit. The data suggest that the combined effects of biological carbon uptake and the precipitation of carbonates created substantial CO_2 undersaturation of 95 μatm in the MIZ during summer sea ice melt. Further work is required to improve the understanding of ikaite chemistry in Antarctic sea ice and its importance for the sea ice carbon pump.

This chapter by Jones, E.M., Bakker, D.C.E., Venables, H.J., Whitehouse, M.J., Korb, R.E. and Watson, A.J. has been published in the 8th International Carbon Dioxide Conference Tellus B special issue.

5.2. Introduction

The Southern Ocean greatly influences the climate system through the biological and physical pumps that facilitate the uptake of atmospheric carbon dioxide (CO_2) and transport of carbon to the deep ocean (Heinze et al., 1991). Marginal ice zones (MIZ) form the boundary from dense sea ice cover to the open ocean and show large spatial and temporal variability in sea surface CO_2 (Bakker et al., 1997; Gibson and Trull, 1999; Hoppema et al., 1999; Hoppema et al., 2000; Alvarez et al., 2002; Bellerby et al., 2004; Shim et al., 2006). The significance of sea ice regions in the oceanic carbon cycle has been demonstrated by a dramatic revision of the Southern Ocean (50-62°S) CO_2 sink estimate, from -0.34 Pg C yr^{-1} to -0.06 Pg C yr^{-1} in the reference years 1995 and 2000, respectively (Takahashi et al., 2009). This trend has been governed by increased data coverage that highlights the dominance of winter CO_2 release, as a result of upwelling and respiration, over CO_2 uptake upon seasonal sea ice melt.

The eastward-flowing Antarctic Circumpolar Current (ACC) transports heat and dissolved constituents around the Antarctic continent (Rintoul and Sokolov, 2001). The dominant water mass in the ACC is Circumpolar Deep Water (CDW), a broad layer of warm, saline and nutrient-rich water, which shoals to the south with the uplifting isopycnals at the Southern Boundary (SB) (Sievers and Nowlin, 1984; Orsi et al., 1995; Pollard et al., 2002).

The Weddell Sea is dominated by a cyclonic gyre, bounded to the west and south by the Antarctic continent but, open to the north and east for interaction with waters of the ACC. CDW is advected into the eastern side of the gyre and can be identified by maxima in temperature, salinity and nutrients within the gyre (Deacon, 1979; Whitworth and Nowlin, 1987; Gouretski and Danilov, 1993; Schroder and Fahrbach, 1999). A substantial part of the ocean is ventilated in the Weddell Gyre as a result of the formation of deep and bottom waters due to strong atmosphere-ice-ocean interactions (Gill, 1973; Carmack and Foster, 1975). Early studies largely regarded this region as a source of CO_2 due to the upwelling of the CO_2-rich deep water (Deacon, 1979; Weiss et al., 1979; Takahashi et al., 1993). Since then, several investigations into the carbonate chemistry of the Weddell Gyre have shown this area to be a net sink for atmospheric CO_2 (Hoppema et al., 1995; Hoppema et al., 1999; Stoll et al., 1999; Hoppema et al., 2000; Stoll et al., 2002; Bakker et al., 2008).

In the western Atlantic sector of the Southern Ocean, the SB lies just north of the Weddell-Scotia Confluence, which extends from the Antarctic Peninsula to about 20°W (Patterson and Sievers, 1980; Whitworth et al., 1994), separating the Weddell Sea to the south from the ACC in the Scotia Sea to the north (Orsi et al., 1995). The Weddell-Scotia Confluence provides a transition zone where the recently ventilated waters flow out of the Weddell Sea and into the Scotia Sea (Patterson and Sievers, 1980; Orsi et al., 1999; Naveira Garabato et al., 2002a). Therefore, it is important to improve the understanding of the ocean carbonate chemistry of the Weddell-Scotia Confluence and its contribution to the Southern Ocean carbon cycle.

Increased biomass and productivity are regularly observed in MIZs (Smith and Nelson, 1986; Moore et al., 1999b; Kang et al., 2001; Korb et al., 2005) due to factors including water-column stability (Smith and Nelson, 1985; Holm-Hansen and Mitchell, 1991; Sakshaug et al., 1991; Lancelot et al., 1993), seeding by ice algae (Smith and Nelson, 1985; Ackley and Sullivan, 1994) and the release of bioavailable iron (de Baar et al., 1990; Martin, 1990; Sedwick and DiTullio, 1997). Additional supplies of iron into surface waters of the Weddell-Scotia Confluence could originate from upwelling within the ACC (Hoppema et al., 2003; Blain et al., 2007) and advection from waters flowing out from the tip of the Antarctic Peninsula (Nolting et al., 1991; Sanudo-Wilhelmy et al., 2002; Dulaiova et al., 2009). These processes have been implicated in the enhanced productivity and ecological diversity associated with the Weddell-Scotia Confluence (Jacques and Panouse, 1991; Comiso et al., 1993; Helbling et al., 1993; Tynan, 1998; Holm-Hansen and Hewes, 2004; Hewes et al., 2008).

Field and laboratory studies have shown that ikaite, a hydrous calcium carbonate mineral ($CaCO_3.6H_2O$), precipitates out within brines during sea ice formation (Marion, 2001; Papadimitriou et al., 2004; Delille et al., 2007; Papadimitriou et al., 2007; Rysgaard et al., 2007; Dieckmann et al., 2008):

$$Ca^{2+}(aq) + 2HCO_3^-(aq) + 5H_2O(l) \leftrightarrow CaCO_3.6H_2O(s) + CO_2(aq) \qquad \text{Equation 5.1.}$$

The net effect of ikaite precipitation in brine is to reduce the concentration of DIC and total alkalinity (TA), whilst increasing the fCO_2 (Eqn. 5.1). Any brine rejected during winter or released during ice melt transfers these inorganic carbon characteristics to the underlying water. One implication of these processes is that during sea ice growth, the winter mixed layer

becomes isolated from the atmosphere (Klatt et al., 2002), allowing levels of fCO_2 to reach supersaturation beneath the sea ice. During sea ice melt in spring and summer, any remaining $CaCO_3$ minerals within the ice are thought to be released into the water column where they re-enter the carbon cycle through dissolution. According to Eqn. 5.1, this would increase TA and DIC and reduce fCO_2 of the water.

The activity of ice algae also leads to changes in the carbonate system of the brine and the water at the ice-sea interface (Gleitz et al., 1995; Gleitz et al., 1996; Gibson and Trull, 1999; Krembs and Engel, 2001; Meiners et al., 2009). During summer, increased light levels promote photosynthesis, reducing DIC and the fCO_2 of the brine. As the ice melts, these carbonate characteristics are transferred to the surrounding water, becoming superimposed on effects from carbonate mineral chemistry.

The sea ice carbonate chemistry processes have been described as a 'sea ice CO_2 pump', assuming dissolution of ikaite in the summer promotes atmospheric CO_2 uptake and that DIC- and TA-poor, but CO_2-rich brines are transported out of the surface waters during the winter (Rysgaard et al., 2007). The MIZs of the Southern Ocean are of great interest due to the effects of enhanced biological activity and, more recently, calcium carbonate chemistry on the oceanic carbon cycle. However, few data exist to investigate and quantify the carbonate chemistry processes in melting polar sea ice and to infer the implications of the sea ice carbon pump for the global carbon cycle. In this paper, we present direct measurements of fCO_2, DIC and TA from waters at and around the receding ice edge. The distribution of upper ocean carbonate chemistry in the Weddell-Scotia Confluence during austral summer is evaluated within the context of physical and biological controls, including (1) the influence of sea ice cover; (2) the effect of recent sea ice melt and an ice edge bloom; (3) the influence of the Southern Boundary.

5.3. Methods

5.3.1. Underway and station sampling

Data were collected in the Weddell-Scotia Confluence during cruise JR177 on the RRS *James Clark Ross* in January 2008 (Fig. 5.1). The ship reached the South Orkney Islands on 8 January 2008 and made two transects in the Weddell-Scotia Confluence, southward and northward, passing the ice edge overlying the South Orkney shelf at station 5 (Table 5.1, Fig.

5.2). The southward transect ended in the sea ice at station 1 (62.61°S 43.24°W), over the break of the South Orkney shelf on 11 January. Between stations 1 and 6 the ship sailed through waters with partial sea ice cover, melting sea ice and areas of open water. The ship left the MIZ on 13 January and continued northward to the Southern Boundary (SB) at station 13 (59.14°S 43.69°W) on 17 January.

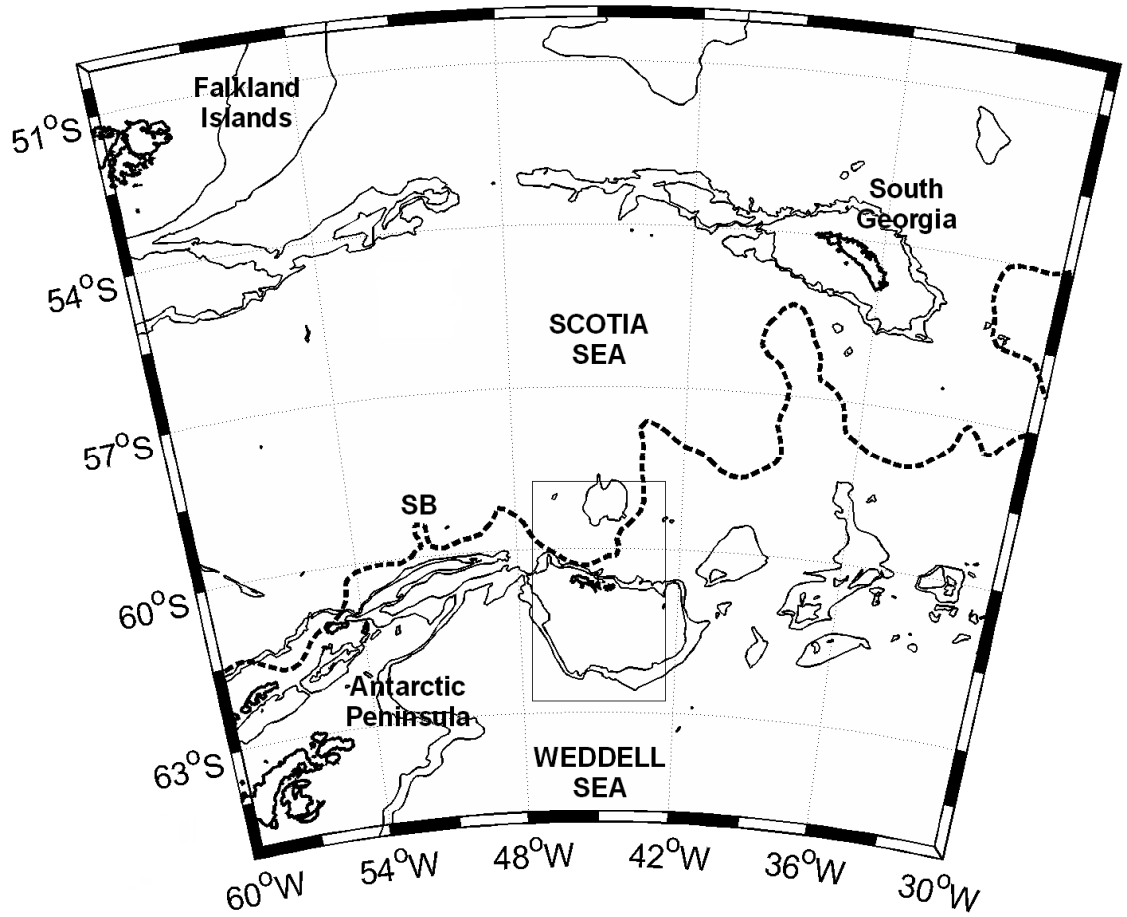

Figure 5.1. Map of the Weddell-Scotia Confluence region. The boxed area shows the research site, see Fig. 5.2 for further details. The dashed line represents the Southern Boundary (SB) at the time of sampling with the dynamic height for the front selected after comparison with the hydrographic section. The absolute dynamic height topography data were produced by Ssalto/Duacs and distributed by Aviso (http://www.aviso.oceanobs.com) with support from the Centre National d'Etudes Spatiales (CNES). Depth contours are at 1000 and 2000 m (GEBCO, 2001).

Table 5.1. Station number, classification, date, location (°S °W) and bottom depth (m) for all hydrographic stations in the Weddell-Scotia Confluence.

Station	*Classification*	*Date* *2008*	*Latitude* *°S*	*Longitude* *°W*	*Bottom depth* *m*
9	Open water	8 Jan	60.208	44.408	5543
8	Open water	9 Jan	60.431	44.593	999
6	Meltwater	10 Jan	61.198	44.408	319
5	Ice edge	10 Jan	61.665	44.053	570
3	Sea ice	11 Jan	62.355	43.529	1238
1	Sea ice	11 Jan	62.608	43.234	3075
10	Open water	13 Jan	59.936	44.239	4784
11	Open water	15 Jan	59.689	44.054	4172
13	Southern Boundary	17 Jan	59.144	43.694	3611

Continuous measurements of temperature and salinity in surface water were made using seawater from the non-toxic underway supply (bow intake 6.5 m below the surface). High resolution, vertical profiles of potential temperature and salinity were obtained during the downcast using a conductivity, temperature, depth (CTD) sensor (Seabird SBE9+). An offset in sea surface temperature (0.37 °C) was detected between the ship's oceanlogger temperature sensor and the CTD surface temperature (section 2.4.6), which has been applied to the underway temperature dataset. All salinity values are reported on the practical salinity scale.

The summer mixed layer depth (MLD) is defined here as the depth where the potential density exceeds that measured at 10 m by 0.05 kg m^{-3} (Brainerd and Gregg, 1995). This definition was selected to provide a depth that is located between the active mixing layer and the seasonal mixed layer. Mixed layer depths were calculated from 2 dbar profiles of the potential temperature and salinity from the CTD deployment at each station. The winter mixed layer, marking the remnant of the Winter Water (WW), is defined here as the depth of the potential temperature minimum (θ_{min}). For all stations, the WW layer was identified by a well defined θ_{min} at depths in the range of 60 - 100 m.

5.3.2. Fugacity of CO_2 in surface seawater and the atmosphere

Quasi-continuous measurements of the fugacity of CO_2 (fCO_2) in surface water were made using an underway fCO_2 system and seawater from the underway supply (Schuster and Watson, 2007). Atmospheric samples were taken from an air inlet located forward at 15 m height on the ship's bridge. Mixing ratios of CO_2 and moisture in the equilibrator headspace and the outside air were determined by circulation through a non-dispersive infra-red analyser (LICOR 7000). The LICOR was calibrated using three secondary gas standards of known CO_2 concentrations of 249.1 ± 0.2, 356.5 ± 0.2 and 457.4 ± 0.2 μmol CO_2 mol^{-1} in an air mixture (21% O_2, 79% N_2). All gases underwent pre- and post-cruise calibration against certified, high precision, primary standards from the National Oceanic and Atmospheric Administration (NOAA). Samples from the equilibrator headspace and marine air were partially dried by being passing through an electric cool box at about 2 °C, prior to analysis in the LICOR. The fCO_2 for equilibrated water samples and the air was computed from the partly dried mixing ratios and ambient barometric pressure and then corrected for seawater vapour pressure (assuming saturation at the sea surface) (section 2.5.5).

Two platinum resistant thermometers positioned in the upper and lower part of the seawater stream determined the temperature of the water in the equilibrator. Warming of the seawater between the intake and the equilibrator was on average 0.8 °C (σ = 0.1 °C; n = 250). Sea surface fCO_2 data were corrected to sea surface temperature to account for this warming (Takahashi et al., 1993). The difference in fCO_2 between the seawater and overlying air (ΔfCO_2(w-a)) was calculated continuously during the cruise. The time lag between sampling and the seawater reaching the equilibrator was 116 seconds, which has been corrected for. Sea surface fCO_2 from the underway supply was co-located to the CTD casts by interpolation to the time of the 5 m sample from the upcast of the CTD. Gaps in the data are due to the seawater supply being turned off in thick ice cover or contamination from the ship exhaust gases. The accuracy of the marine air fCO_2 data was determined as 0.6 μatm from comparisons with atmospheric data from Jubany Station, South Shetland Islands (62.23°S 58.67°W) (Ciattaglia et al., 1999). The precision of the fCO_2 data is 2.0 μatm (Table 3.3).

5.3.3. Carbonate system

Underway samples for sea surface dissolved inorganic carbon (DIC) and total alkalinity (TA) analysis were collected from the underway seawater supply. Vertical profile samples were taken from the 24 × 10 L Niskin bottles mounted onto the CTD rosette at 5, 10, 30, 50, 80, 120, 160 and 200 m depth on the upcast of the CTD. Seawater (250 or 500 ml) was collected in borosilicate glass bottles and a small volume was extracted to create a head space. Saturated aqueous mercuric chloride was immediately added (0.02% vol/vol) and the bottle was sealed, shaken and stored in a dark location at ambient temperature for shipment to the UK.

The DIC concentration was determined by coulometric analysis (Johnson et al., 1987) and TA analyses were carried out by potentiometric titration with hydrochloric acid (Dickson, 1981) using a VINDTA instrument from April to May 2008. Duplicate analyses were made for each 500 ml bottle. Two bottles of certified reference material (CRM) from batches 76 or 81 (DOE, 2007) were analysed in duplicate per CTD cast and per 10 samples from the underway supply. DIC and TA values were corrected to account for the dilution of the seawater by the addition of mercuric chloride solution. The accuracy for the DIC and alkalinity measurements is determined as 2 μmol kg^{-1} (n = 96) from the average difference between certified and calculated values for each CRM analysis. The precision for the DIC and alkalinity measurements is estimated as better than 2 μmol kg^{-1} (n = 96) based on the average difference between duplicate CRM bottle analyses. DIC and TA from all sea surface samples were used to calculate fCO_2, f(DIC,TA), using the CO2Sys programme (Lewis and Wallace, 1998) with thermodynamic dissociation constants for K_1 and K_2 by Mehrbach et al. (1973) and the re-fit by Dickson and Millero (1987).

All surface alkalinity samples showed strong salinity dependence with a positive intercept of 269 μmol kg^{-1} (TA_0) at zero salinity. To correct for dilution or concentration effects, TA data were normalised to salinity 34.3, the average salinity of the WW for all stations in the Weddell-Scotia Confluence, using Eqn. 5.2 to account for the non-zero end-member (Friis et al., 2003):

$$TA_{34.3} = \left(\frac{TA - TA_0}{S} \right) \cdot 34.3 + TA_0 \qquad \text{Equation 5.2.}$$

This was repeated for the DIC data, where a value of 966 μmol kg^{-1} was determined for DIC_0. A series of de-ionised water samples were analysed to determine a 'blank' for DIC and TA at zero salinity. Average values for $TA_{0\_de\text{-}ionised}$ and $DIC_{0\_de\text{-}ionised}$ of 74 ± 11 and 36 ± 3 μmol kg^{-1} (n = 6), respectively, indicate that the TA_0 and DIC_0 determined for the Weddell-Scotia Confluence samples do not result from the analytical technique but from natural sources, which could include dissolution of carbonate minerals during the analysis and bacterial degradation. DIC and TA measurements reported in the text are not salinity normalized unless stated.

5.3.4. Macronutrients

Underway samples from the underway seawater supply and CTD water bottle samples were filtered through a mixed ester membrane (Whatman, pore size 0.45 μm), and the filtrate was analysed colorimetrically for dissolved silicate (SiO_4^{4-}), phosphate (PO_4^{3-}), and nitrate (NO_3^-) with a segmented-flow analyser (Technicon, Whitehouse, 1997). Analyses for nitrate included nitrite (NO_2), which is not considered separately as its concentration had little variation and was typically < 1% of total $NO_3 + NO_2$. Nutrient data were normalised to salinity 34.3 using a direct normalisation procedure by multiplication with 34.3 and division by the *in situ* salinity. Nutrient concentrations reported in the text are not salinity normalized unless stated.

5.3.5. Chlorophyll-a

Underway samples for sea surface chlorophyll-a were collected from the non-toxic seawater supply approximately every hour as the ship was in transit. Water samples were filtered through glass fibre filters (Whatman GF/F) under low (< 70 mm Hg) vacuum pressure and immediately frozen and stored at -20 °C until analysis onboard. The samples on the filters were then extracted in acetone (10 ml, 90%) in the dark for 24 hours (Parsons et al., 1984). Fluorescence of the extract was measured before and after acidification with 1.2 M HCl on a TD-700 Turner fluorometer. The instrument was calibrated against commercially prepared chlorophyll-a standards (Sigma).

5.3.6. Sea ice

Visual observations of sea ice coverage were made from the vessel's bridge as part of the daily position report filed by the Captain. The observations included primary ice types present, the sea ice coverage and meteorological conditions and were supported by digital photographs taken at each station (Fig. 2.22). Daily sea ice concentration data at 4 km resolution were obtained through the Operational SST and Sea Ice Analysis (OSTIA) service, a component of the Group for High-Resolution Sea Surface Temperature (GHRSST) at http://ghrsst-pp.metoffice.com/pages/latest_analysis/ostia.html (Stark et al., 2007). The transition area between open ice-free waters to ice-covered waters is referred to as the marginal ice zone (MIZ), encompassing stations 1, 3, 5 and 6 during the present study. The ice edge is defined here as the position where consolidated sea ice was first encountered (station 5) on the southern transect.

5.3.7. Seasonal biogeochemical deficits

The seasonal depletion in DIC, alkalinity and nutrients was determined for each station from the difference between the average concentration in the summer mixed layer and the concentration at the depth of the θ_{min}, in the WW (Jennings et al., 1984). The biogeochemical properties of the WW have previously been used as proxies for conditions present in Southern Ocean surface waters during the preceding winter (e.g., Minas and Minas, 1992; Ishii et al., 1998; Rubin et al., 1998; Pondaven et al., 2000; Ishii et al., 2002).

The validity of this method for the Weddell-Scotia Confluence data is discussed below. For the sea ice stations (1-6), values for the θ_{min} were between -1.60 and -1.70 °C (Table 5.2). Satellite derived sea ice cover indicated that the break-up of the sea ice (last day when ice cover was ≥ 90%) occurred in early December, 4 weeks prior to sampling. Therefore, top-down warming was very recent and any erosion of the winter mixed layer was attributed to vertical mixing of warmer waters below the thermocline. To estimate any bottom-up influences, the value of the θ_{min} was compared to the temperature at the base of the thermocline, assuming an end member winter mixed layer temperature of -1.70 °C and that the specific heat capacity of seawater was constant. For the range of θ_{min} values, mixing from deeper waters from winter to summer is estimated at 4-7%. This could lead to a slight over

estimation in winter DIC and TA as highlighted during a comparable seasonal study in the Indian sector of the Southern Ocean (Jouandet et al., 2008).

The total DIC deficit ($\Delta DIC_{deficit}$) can be expressed as a sum of contributing processes, represented by the following:

$$\Delta DIC_{deficit} = \Delta DIC_{salinity} + \Delta DIC_{Corg} + \Delta DIC_{CaCO_3} + \Delta DIC_{residual} \quad \text{Equation 5.3}$$

Deficits in DIC due to salinity changes are determined from the difference between the measured and salinity normalised DIC deficit. A composite error of 2 μmol kg^{-1} is associated with the $\Delta DIC_{salinity}$ term. Modifications in DIC due to abundance of organic matter through photosynthesis and respiration (ΔDIC_{Corg}) have been estimated from normalised nitrate deficits (Sweeney et al., 2000), assuming a carbon to nitrogen uptake ratio of 117:16 moles (Anderson and Sarmiento, 1994). Comparisons to phosphate utilization by Redfield stoichiometry (Redfield et al., 1963) indicate uncertainties in ΔDIC_{Corg} of 1 to 9 μmol kg^{-1}. The deficit in alkalinity, corrected for salinity and organic matter effects, indicates carbonate mineral (ikaite) precipitation or dissolution based on 2:1 changes in TA and DIC (Zeebe and Wolf-Gladrow, 2001). A composite error of 3 μmol kg^{-1} accompanies the carbonate term. The residual term accounts for the remaining seasonal deficit as a result of processes including CO_2 air-sea exchange, surface advection and slight vertical mixing (see above). The associated error is the sum of that for each term in Eqn. 5.3.

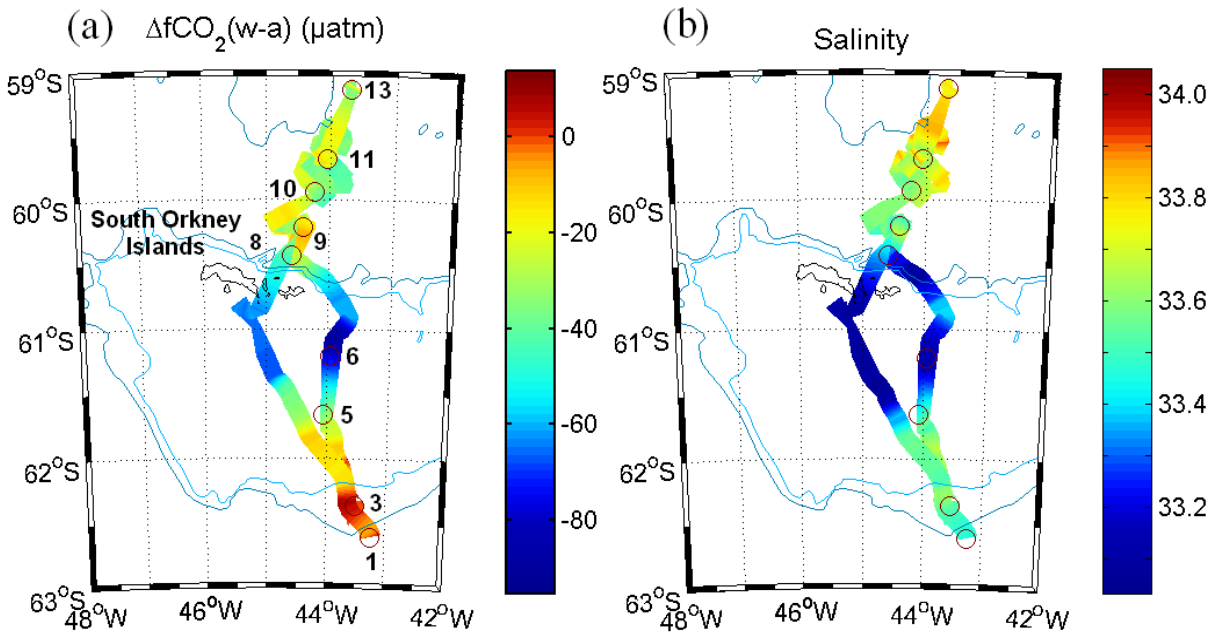

Figure. 5.2. The research area showing (a) Δ*f*CO_2(water-air) (µatm) and (b) sea surface salinity along the two transects and the station locations. The marginal ice zone (MIZ), south of the South Orkney Islands, includes stations 1, 3, 5 and 6. Depth contours are at 1000 and 2000 m (GEBCO, 2001).

5.4.1. Hydrography

Surface waters (0-20 dbar) showed a strong northward gradient in potential temperature from about -1.4 °C beneath the sea ice to greater than 1.0 °C at about 59°S (Fig. 5.3b). Surface salinity showed a similar trend, increasing from values close to 33.5 beneath the sea ice to values above 33.8 at 59°S (Fig. 5.3a). A notable exception to this trend was the distinct reduction in salinity in the region of substantial sea ice melt to the south of the South Orkney Islands, at and around station 6 (Table 5.3, Fig. 5.2b).

A distinct WW layer could be observed for all stations, with an average potential temperature minimum (θ_{min}) of -1.55 ± 0.12 °C and a winter mixed layer depth of 79 ± 15 m (*n* = 9, Table 5.2). Potential temperature of the WW predominantly followed the increasing northward trend of summer mixed layer potential temperature. In comparison, WW salinity was much more variable, from the most saline WW beneath the sea ice decreasing to the freshest water in the

region of substantial ice melt. North of the MIZ, WW salinity increased from values close to 34.2 over the South Orkney shelf up to about 34.3 at 59°S.

Table 5.2. Winter mixed layer depth (WMLD, m), temperature (°C), salinity, silicate (SiO_4, μmol kg^{-1}), phosphate (PO_4, μmol kg^{-1}), nitrate (NO_3, μmol kg^{-1}), dissolved inorganic carbon (DIC, μmol kg^{-1}) and total alkalinity (TA, μmol kg^{-1}) of the winter mixed layer (representing the WW) for all stations in the Weddell-Scotia Confluence from 62.61°S (station 1) to 59.14°S (station 13). The absolute value for each station is shown measured from 1 bottle at the depth of the potential temperature minimum (θ_{min}). Stations 6 and 13 have interpolated nutrient concentrations from proximal stations 8 and 11, respectively.

Station	*WMLD*	θ_{min}	*Salinity*	SiO_4	PO_4	NO_3	*DIC*	*TA*
	m	℃		*μmol kg^{-1}*	*μmol kg^{-1}*	*μmol kg^{-1}*	*μmol kg^{-1}*	*μmol kg^{-1}*
1	61	-1.65	34.33	82.8	1.96	28.3	2224	2328
3	57	-1.60	34.28	84.6	1.97	29.6	2224	2332
5	69	-1.70	34.24	80.3	1.94	31.0	2222	2325
6	67	-1.63	34.14	78.0	1.81	29.5	2214	2325
8	71	-1.56	34.24	84.4	1.93	29.0	2218	2326
9	87	-1.56	34.20	80.8	1.94	28.8	2213	2326
10	91	-1.46	34.30	84.4	2.02	28.8	2220	2333
11	97	-1.35	34.30	83.5	2.02	31.2	2223	2332
13	93	-1.39	34.25	83.2	1.99	31.6	2222	2330

5.4.2. Macronutrients

Surface silicate (hereinafter SiO_4) concentrations were generally high (≥ 70 μmol kg^{-1}) throughout the Weddell-Scotia Confluence (Table 5.3). The SiO_4 concentration showed a slight decreasing gradient for stations 1-6 in the MIZ and a more homogenous distribution north of the MIZ (stations 8-13). Surface nitrate (hereinafter NO_3) and phosphate (hereinafter PO_4) concentrations showed general decreasing northward trends with average values of 24.3 and 1.56 μmol kg^{-1}, respectively. Compared to sea ice stations 1, 3 and 5, large depletion of all three macronutrients had occurred in the region of extensive ice melt at station 6. Average WW concentrations for SiO_4, NO_3 and PO_4 were 82.4, 30.1 and 1.95 μmol kg^{-1}, respectively, with lower values at station 6 (Table 5.2). Concentrations of NO_3 and PO_4 are similar to WW values measured further north in the Scotia Sea and higher concentrations of SiO_4 are

consistent with the major gradient that exists for this macronutrient in this region (Whitehouse et al., 2008).

Table 5.3. Mixed layer depth (MLD, m), temperature (°C), salinity, silicate (SiO_4, μmol kg^{-1}), phosphate (PO_4, μmol kg^{-1}) and nitrate (NO_3, μmol kg^{-1}) of the summer mixed layer for all stations in the Weddell-Scotia Confluence from 62.61°S (station 1) to 59.14°S (station 13). The mean value for each station is shown (from values measured at *n* bottle depths up to the MLD) with the standard deviation (for stations where $n > 2$) and the difference (for stations where $n = 2$) in brackets. Stations 6 and 13 have interpolated nutrient concentrations from proximal stations 8 and 11, respectively.

Station	*n*	*MLD*	*Temperature*	*Salinity*	*SiO_4*	*PO_4*	*NO_3*
		m	*℃*		*μmol kg^{-1}*	*μmol kg^{-1}*	*μmol kg^{-1}*
1	2	23	-1.40 (0.02)	33.54 (0.02)	80.5 (0.2)	1.82 (0.00)	27.1 (0.2)
3	2	25	-1.41 (0.00)	33.60 (0.00)	71.7 (0.2)	1.73 (0.01)	26.4 (0.1)
5	2	19	-0.76 (0.00)	33.57 (0.00)	69.5 (0.1)	1.62 (0.00)	25.6 (0.2)
6	2	17	-0.65 (0.02)	33.23 (0.23)	66.0 (0.1)	1.42 (0.01)	23.4 (0.2)
8	2	23	-0.63 (0.01)	33.35 (0.00)	73.4 (0.3)	1.58 (0.01)	24.4 (0.5)
9	3	29	-0.01 (0.11)	33.64 (0.01)	74.3 (0.2)	1.60 (0.01)	24.1 (0.2)
10	3	33	0.64 (0.06)	33.70 (0.02)	74.9 (0.1)	1.44 (0.03)	23.2 (0.1)
11	2	17	0.94 (0.01)	33.71 (0.00)	73.0 (0.2)	1.48 (0.02)	22.8 (0.2)
13	2	29	1.09 (0.01)	33.85 (0.00)	71.0 (0.3)	1.34 (0.01)	22.4 (0.0)

5.4.3. Chlorophyll-a and phytoplankton species distribution

Chlorophyll-a concentrations ([chl-a]) varied between 1.85 and 2.84 mg m^{-3} (Fig. 5.3f) in the open waters of the Weddell-Scotia Confluence, south of 59°S to about 60°S (stations 10-13). A summer maximum in chlorophyll-a of 3.51 mg m^{-3} was observed in the melt waters at and around station 6, signifying the presence of a phytoplankton bloom (defined here as [chl-a] ≥ 2.0 mg m^{-3}). Chlorophyll-a concentrations sharply decreased to a minimum of 0.21 mg m^{-3} beneath the sea ice at station 1. For the MIZ (stations 1-6), the phytoplankton community was dominated by naked, heterotrophic dinoflagellates with diatoms accounting for between 21 and 46% of the total cell abundance (Korb et al., 2010). North of the South Orkney Islands to 59°S (stations 8-13) the community consisted of a mixture of dinoflagellates and cryptophytes, with less than 20% diatoms (Korb et al., 2010).

Table 5.4. Dissolved inorganic carbon (DIC, μmol kg^{-1}), total alkalinity (TA, μmol kg^{-1}), salinity normalised DIC ($DIC_{34.4}$, μmol kg^{-1}) and salinity normalised TA ($TA_{34.3}$, μmol kg^{-1}) of the summer mixed layer and surface water $fCO_{2\ measured}$ (μatm), $fCO_{2\ calculated}$ (as f(DIC,TA), μatm) and chlorophyll-a (chl-a, mg m^{-3}) for all stations in the Weddell-Scotia Confluence from 62.61°S (station 1) to 59.14°S (station 13). The mean value for DIC, $DIC_{34.3}$, TA and $TA_{34.3}$ is shown (from values measured at *n* bottle depths up to the depth of the mixed layer) with the standard deviation (for stations where $n > 2$) and the difference (for stations where $n = 2$) in brackets.

Station	*n*	*DIC*	*TA*	$DIC_{34.3}$	$TA_{34.3}$	$fCO_{2\ measured}$	$fCO_{2\ calculated}$	*Chl-a*
		μmol kg^{-1}		*μmol kg^{-1}*		*μatm*		*mg m^{-3}*
1	2	2169 (7)	2286 (7)	2196 (6)	2332 (7)	377	357	0.21
3	2	2166 (1)	2280 (2)	2191 (1)	2322 (2)	375	359	0.24
5	2	2159 (1)	2273 (5)	2185 (1)	2316 (5)	336	378	1.14
6	2	2105 (2)	2252 (28)	2142 (7)	2315 (15)	294	314	3.51
8	2	2140 (0)	2265 (1)	2173 (0)	2321 (1)	345	343	0.96
9	3	2156 (3)	2289 (2)	2180 (3)	2328 (2)	352	339	0.60
10	3	2152 (7)	2293 (8)	2174 (7)	2329 (8)	340	355	1.85
11	2	2169 (1)	2290 (14)	2190 (1)	2325 (14)	334	406	2.84
13	2	2161 (8)	2299 (4)	2177 (8)	2326 (4)	332	346	2.06

Figure 5.3. (page 162) The latitudinal distribution of sea surface (a) salinity, (b) temperature (SST, °C), (c) $fCO_{2\ measured}$ (lines, μatm) and $fCO_{2\ calculated}$ (crosses, μatm), (d) dissolved inorganic carbon (DIC, μmol kg^{-1}), (e) total alkalinity (TA, μmol kg^{-1}), and (f) chlorophyll-a (chl-a, mg m^{-3}) for the southward (solid line, filled circles) and northward (dashed line, open circles) transects across the Weddell-Scotia Confluence. The data show values for station and underway samples. Calculated seawater fCO_2 , f(DIC,TA), has an accuracy of ± 6 μatm (Table 2.8).

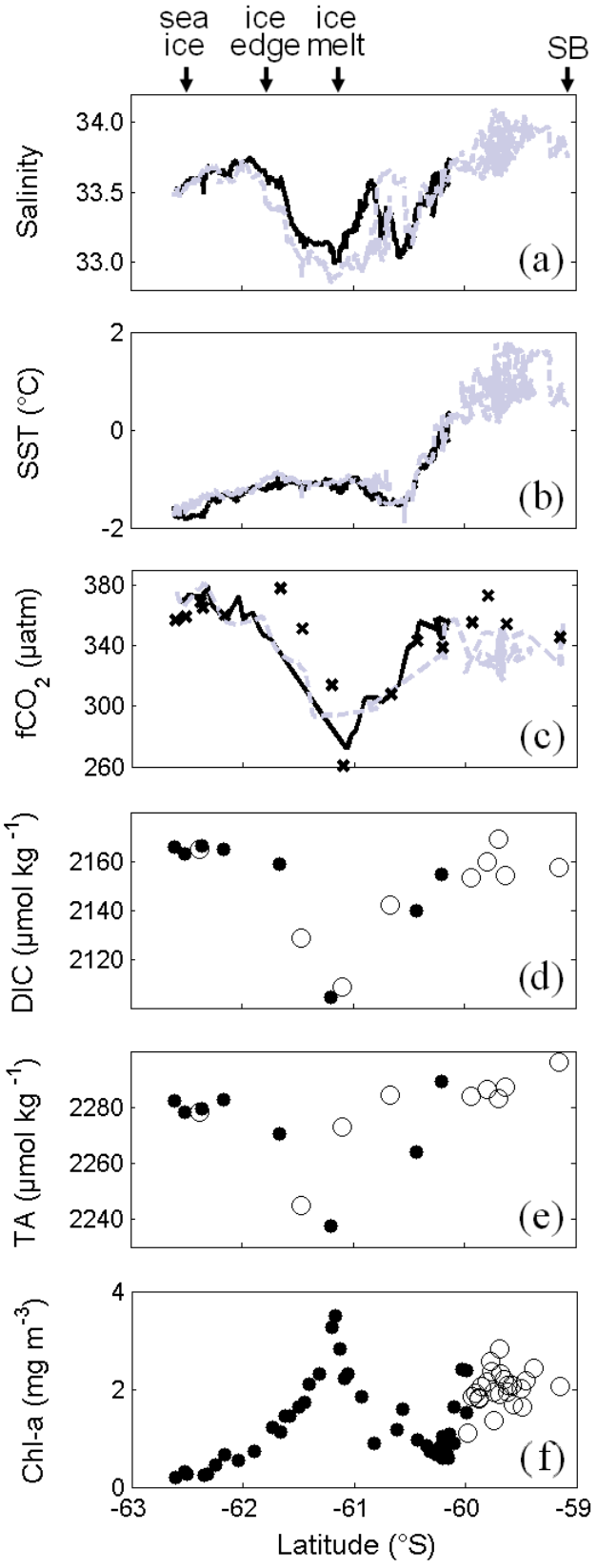
sea ice
ice edge
ice melt
SB
Salinity
34.0
33.5
33.0
(a)
SST (°C)
2
0
-2
(b)
fCO2 (µatm)
380
340
300
260
(c)
DIC (µmol kg-1)
2160
2140
2120
(d)
TA (µmol kg-1)
2280
2260
2240
(e)
Chl-a (mg m-3)
4
2
0
(f)
-63
-62
-61
-60
-59
Latitude (°S)

5.4.4. Carbonate chemistry

Contrasting concentrations of fCO_2, DIC and TA were observed at and around the sea ice edge and within the frontal waters of the SB (Fig. 5.3c-e). The fCO_2 varied from supersaturation with ΔfCO_2 of 14 µatm in waters beneath the sea ice to strong undersaturation with ΔfCO_2 of -95 µatm in the region of substantial ice melt (Fig. 5.2). Calculated fCO_2 generally showed a close agreement to measured fCO_2, apart from a positive offset due to higher calculated fCO_2 values from the ice edge to the meltwater region (Fig. 5.3c).

The concentration of sea surface DIC showed similar patterns and predominantly followed the trend of the fCO_2 observations (Fig. 5.3d). The highest concentration of DIC, TA and the highest value of fCO_2 were measured beneath the sea ice close to station 1 (Table 5.4). Relative to all other MIZ stations, DIC, TA and fCO_2 reached distinct summer minima in the region of extensive ice melt (Fig. 5.3). Sea surface normalised DIC ($DIC_{34.3}$) predominantly followed the trend in DIC concentrations, decreasing from values greater than 2190 µmol kg^{-1} beneath the sea ice to values around 2180 µmol kg^{-1} at the SB (Table 5.4). An exception to this gradual decreasing trend was at station 6, where a substantial reduction in $DIC_{34.3}$ of up to 40 µmol kg^{-1} was observed, relative to the average $DIC_{34.3}$ in the summer mixed layer at all other stations. Sea surface normalised TA ($TA_{34.3}$) showed a similar variation, with the highest values of about 2332 µmol kg^{-1} in the area of greater sea ice coverage and the lowest values in the region of extensive sea ice melt (stations 5 and 6).

Across the Weddell-Scotia Confluence, WW DIC was relatively homogenous with average concentrations of about 2220 µmol kg^{-1} (Table 5.2). Alkalinity showed more variation, with distinct low values at MIZ stations in and near the area of greatest sea ice melt. There was an overall northward increase in $TA_{34.3}$ of the WW.

5.5. Sea surface carbonate chemistry during summer ice melt

The processes affecting carbonate chemistry in waters at and around the ice edge will be investigated by comparing surface water fCO_2, DIC and TA measured at the contrasting sites in the MIZ. To the south of the South Orkney Islands (stations 1-3), the sea surface was characterised by large plates of consolidated sea ice as well as regions where the ice pack had begun to break up (Fig. 2.22). Macronutrient concentrations were the highest (Table 5.3) and

chlorophyll-a reached the lowest concentration of 0.21 mg m^{-3} (Table 5.4) for whole Weddell-Scotia Confluence. Surface temperatures in excess of the freezing point of seawater and reduced salinity, compared to station 5 at the ice edge, indicate that slight sea ice melt had occurred (Fig. 5.4). Effects of sea ice melt were most pronounced at station 6 (Fig. 5.2b), where the site was largely open water with sporadic ice floes. Substantial sea ice melt had stabilized the upper water column by forming a warm and shallow meltwater lens at the surface (Fig. 5.4), which supported elevated chlorophyll-a (Fig. 5.3f). This corresponded to a rapid reduction in sea surface DIC by 53 μmol kg^{-1} and fCO_2 by 55 μatm, compared to all other stations, driving a strong CO_2 undersaturation of 74 μatm at station 6 (Fig. 5.2a).

Figure 5.4. (page 165) Vertical profiles of upper water column (a, d, g) potential temperature (θ, solid line, °C) and salinity (dashed line), (b, e, h) dissolved inorganic carbon (DIC, black solid line, μmol kg^{-1}), total alkalinity (TA, black dashed line, μmol kg^{-1}), salinity normalised DIC (grey solid line, μmol kg^{-1}), salinity normalised TA (grey dashed line, μmol kg^{-1}) and (c, f, i) nitrate (NO_3, solid line, μmol kg^{-1}), phosphate (PO_4, dashed line, μmol kg^{-1}) and silicate

(SiO_4, dot-dash line, µmol kg^{-1}), in meltwaters (station 6), at the ice edge (station 5) and beneath the sea ice (station 11).

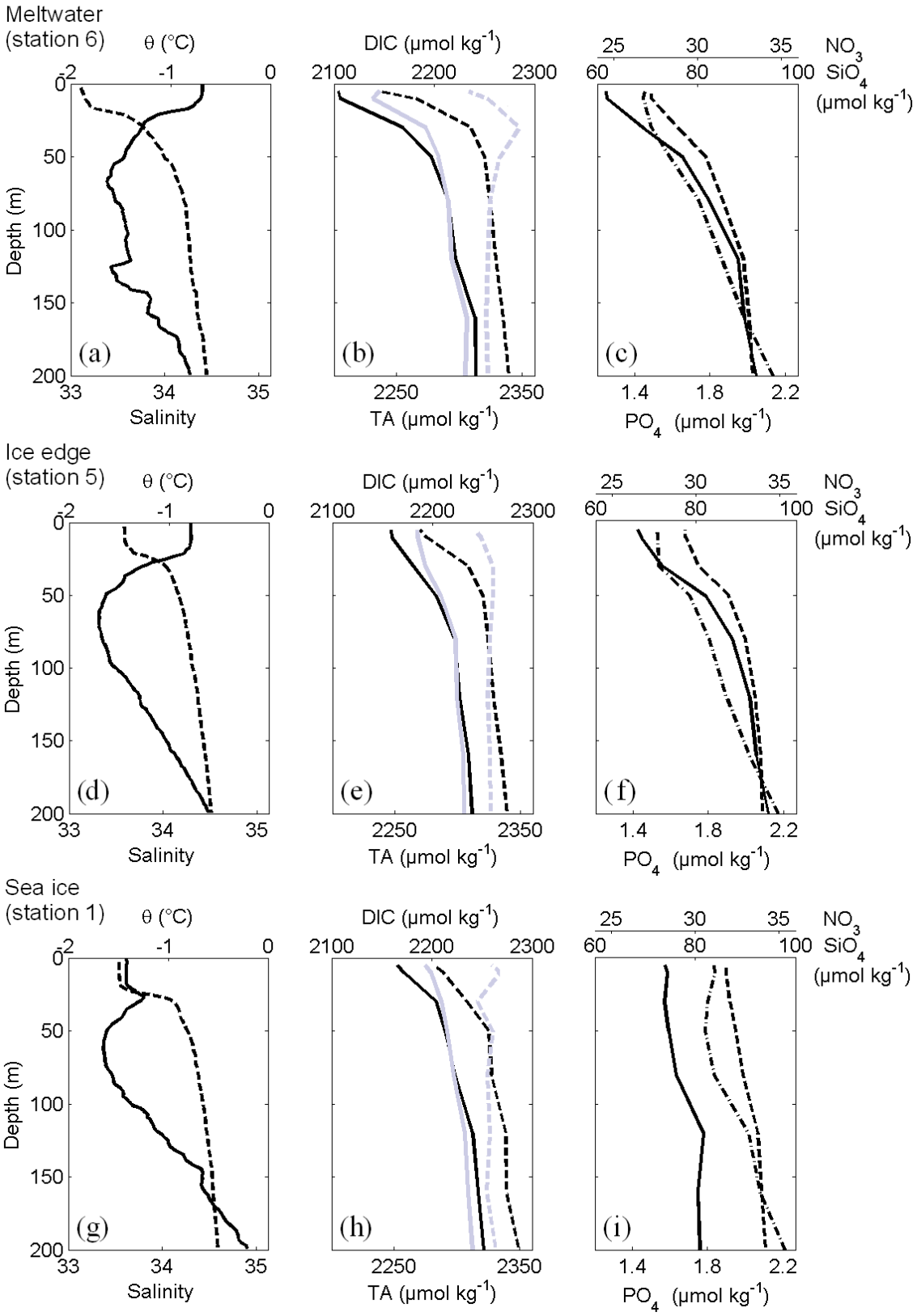

Melting sea ice forms shallow mixed layers with favourable light conditions that promote the development of phytoplankton blooms in the meltwaters (Smith and Nelson, 1986; Lancelot et al., 1993). Blooms associated with the receding ice edge have been previously observed in the MIZ of the Weddell-Scotia Confluence region (Buma et al., 1992; Lancelot et al., 1993; Kang et al., 2001; Korb et al., 2005). The bloom in the meltwaters at station 6 could be partially sustained by natural iron enrichment from melting sea ice (Löscher et al., 1997; Lannuzel et al., 2007; Lannuzel et al., 2008), vertical mixing over shallow topography (Table 5.1), upwelling in the ACC (Hoppema et al., 2003; Blain et al., 2007) or advection from the Antarctic Peninsula region (Nolting et al., 1991; Sanudo-Wilhelmy et al., 2002; Dulaiova et al., 2009). Recent evidence strongly suggests that iron is advected into the Scotia Sea from the South Shetland Islands and the Antarctic Peninsula, supporting phytoplankton growth in this downstream region (Ardelan et al., 2010). It has been inferred that it is the interaction between iron and light that limits the initiation and maintenance of blooms in the MIZ (Korb et al., 2005, and references therein).

In addition, diatoms in sea ice can act as an inoculum and seed the formation of phytoplankton blooms when released upon sea ice melt (Smith and Nelson, 1985; Ackley and Sullivan, 1994). Diatom activity reduces the concentrations of macronutrients and DIC in the sea ice brine. These chemical signatures are transferred to the surrounding water as the sea ice melts. It is likely that a combination of these processes stimulated the formation and growth of the bloom in the meltwaters of the Weddell-Scotia Confluence and contributed to the reductions in DIC and macronutrient concentrations within the shallow mixed layer (Figs. 5.3 and 5.4).

Changes in concentrations of macronutrients were compared to $DIC_{34.3}$ to investigate whether biological utilization of nutrients had occurred (Fig. 5.5a-c). Nitrate and phosphate showed similar decreasing concentrations with decreasing $DIC_{34.3}$, which suggests nutrient depletion as a result of phytoplankton growth. The C:N ratio of 112:16 is very similar to that determined from phytoplankton decomposition analyses, C:N:P of 106:16:1 (Redfield et al., 1963), and to that calculated by examination of spatial changes in nutrient concentrations, C:N:P of 117:16:1 (Anderson and Sarmiento, 1994). The ratio of the change in $DIC_{34.3}$ with respect to phosphate (48) is much smaller than that predicted by either nutrient utilization ratio. The decreasing concentration of silicate indicates the activity of the diatoms observed in this region (Korb et al., 2010). Despite the bloom being dominated by naked dinoflagellates, with little photosynthetic ability, it is predicted that the few diatoms present would account for the

majority of the photosynthetic activity and carbon utilisation. Based on the $DIC_{34.3}$, $TA_{34.3}$ and nutrient deficits, photosynthesis had reduced nutrients and DIC by approximate Redfield ratios. Deviations from predicted nutrient depletion ratios may be due to other processes, including sea ice carbonate chemistry, which will now be investigated.

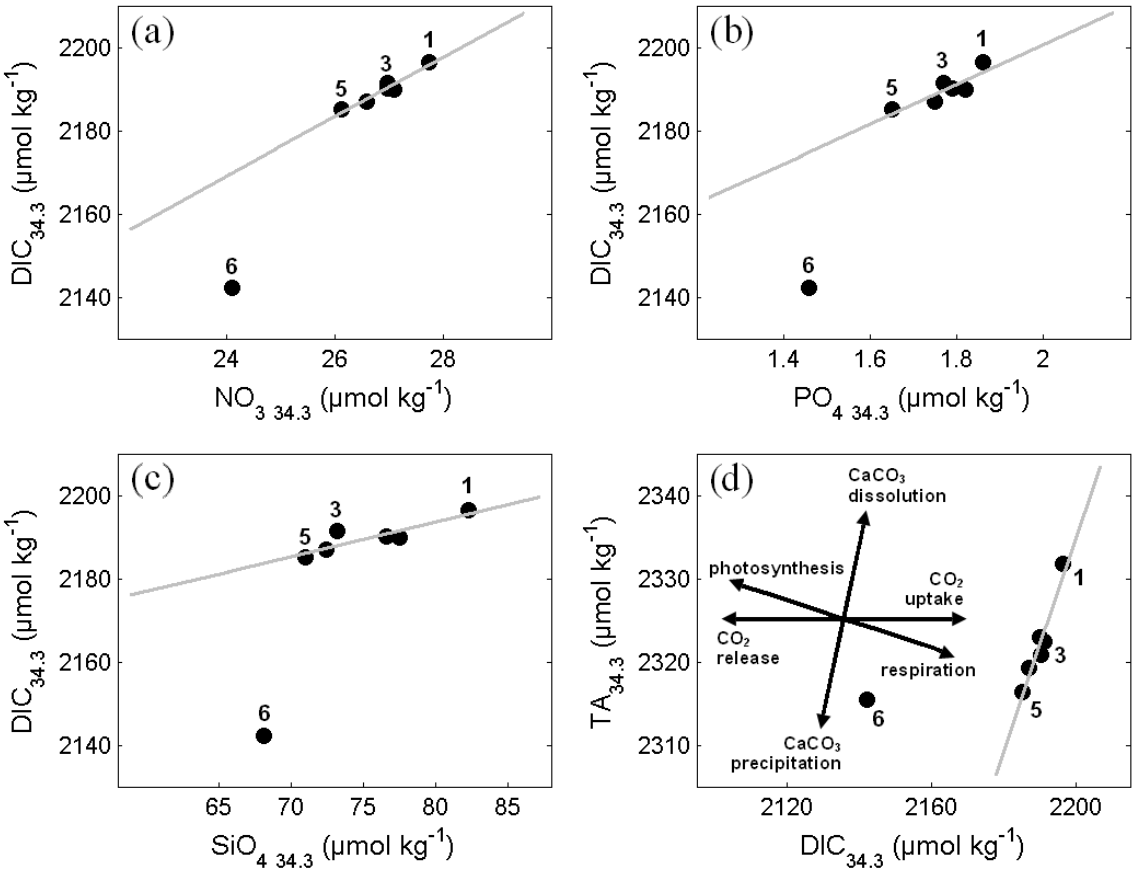

Figure 5.5. Average summer mixed layer (stations 1, 3, 5 and 6) and underway salinity normalised DIC ($DIC_{34.3}$, µmol kg^{-1}) as a function of salinity normalised (a) nitrate ($NO_{3\ 34.3}$, µmol kg^{-1}), (b) phosphate ($PO_{4\ 34.3}$, µmol kg^{-1}), (c) silicate ($SiO_{4\ 34.3}$, µmol kg^{-1}) and (d) salinity normalised total alkalinity ($TA_{34.3}$, µmol kg^{-1}) as a function of $DIC_{34.3}$ (µmol kg^{-1}). The theoretical trends (d, insert) show the variation of $DIC_{34.3}$ and $TA_{34.3}$ with respect to certain biogeochemical processes, adapted from Zeebe and Wolf-Gladrow (2001). The trend lines represent the best fit from linear regression, excluding station 6.

A relationship between $\Delta DIC_{34.3}$ and $\Delta TA_{34.3}$ of 1:2 is indicative of ikaite ($CaCO_3.6H_2O$) precipitation (Eqn. 5.1). Values of $DIC_{34.3}$ and $TA_{34.3}$ for the MIZ stations (1-6) group together in a decreasing trend close to 1:2, with the exception of station 6 (Fig. 5.5d). During sea ice formation and growth, precipitation of ikaite creates DIC- and TA-poor and fCO_2-rich brines. Any brine remaining in channels and pockets within the sea ice matrix is released into the underlying water during sea ice melt, which would have the net effect of reducing $TA_{34.3}$ and $DIC_{34.3}$ (2:1) at the surface. Using salinity as a proxy for ice melt (Fig. 5.2b), in conjunction with *in situ* and satellite observations, sea ice melt was evident to some degree at all stations in the MIZ during summer 2008. We put forward the hypothesis that ikaite precipitation had occurred in the sea ice brines of the Weddell-Scotia Confluence during the preceding winter and the resultant DIC- and TA-poor brines were released into the underlying water as the ice melted, transferring the inorganic carbon characteristics into the summer mixed layer. The absence of calcifying phytoplankton in this region (Korb et al., 2010) supports the proposed mechanism of the observed depletion in DIC and TA at the sea surface.

An outlier to the principle trend is station 6 in the meltwaters supporting a phytoplankton bloom. Although not numerically dominant within the bloom, diatoms had rapidly reduced $DIC_{34.3}$ by 35 μmol kg^{-1} at the sea surface, compared to ice edge station 5. Based on the $DIC_{34.3}$ and nutrient distributions for the MIZ stations (Fig. 5.5), biological carbon uptake had further reduced the DIC signature from the released brine, driving a strong undersaturation in fCO_2 at the sea surface.

A notable feature in sea surface fCO_2 was the higher calculated fCO_2 values along the strong fCO_2 gradient that existed from the ice edge to the meltwater region (Fig. 5.3c). This suggests that samples from this location had either enriched DIC or depleted TA, or both, upon analysis. DIC increases occur from dissolution of carbonates, CO_2 uptake and remineralisation of organic matter (Fig. 5.5d). Alkalinity deficits result from carbonate mineral precipitation and remineralisation of organic matter. With respect to the high DIC_0 (section 5.3.3), it is proposed that there is an additional source of DIC in the sea ice, such as bacterial degradation or the presence of labile organic matter. In the region of very recent ice melt, prior to biological assimilation, the 'extra' DIC would contribute to the observed fCO_2 offset.

5.6. Seasonal changes in carbonate chemistry

The depth of the winter mixed layer and temperature of the WW increased northwards from waters beneath sea ice to waters proximal to the ACC at 59°S (Table 5.2). Away from the region of greatest sea ice melt, WW salinity and concentrations of macronutrients, DIC and TA had little variation. North of the MIZ, the phytoplankton community was made up of cryptophytes and naked dinoflagellates (Korb et al., 2010), with the cryptophytes accounting for the elevated concentrations of chlorophyll-a north of the South Orkney Islands (Fig. 5.3f). This corresponded to the undersaturation in sea surface fCO_2 observed approaching the SB (north of station 10) and supports the idea of the frontal waters as an area of high productivity. In contrast, WW values of DIC and $DIC_{34.3}$ are relatively constant for nearly all stations and hence processes that affect DIC concentrations, either at the surface during the winter or through advection and slight vertical mixing in the winter mixed layer during the summer (section 5.3.7), act uniformly across the Weddell-Scotia Confluence.

The seasonal change in carbonate chemistry can be explored by comparing $DIC_{34.3}$ and $TA_{34.3}$ at depth intervals from the surface to below the winter mixed layer (Fig. 5.6). Trends in $DIC_{34.3}$ and $TA_{34.3}$ in the summer mixed layer for stations located in the MIZ were explained previously (section 5.5). Stations north of the MIZ, showed comparatively reduced DIC in the summer mixed layer at a narrow range of $TA_{34.3}$ of less than 10 μmol kg^{-1}. With the exception of station 11, surface $TA_{34.3}$ and $DIC_{34.3}$ for stations north of the MIZ tended to follow a 2:1 trend, but from a different starting point compared to the MIZ stations (Fig. 5.6a). As WW $DIC_{34.3}$ and $TA_{34.3}$ for all stations are quite similar (Fig. 5.6c), the greater $DIC_{34.3}$ deficit observed north of the MIZ is attributed to the greater photosynthetic activity that had occurred in the northern Weddell-Scotia Confluence, compared to the MIZ, by the summer.

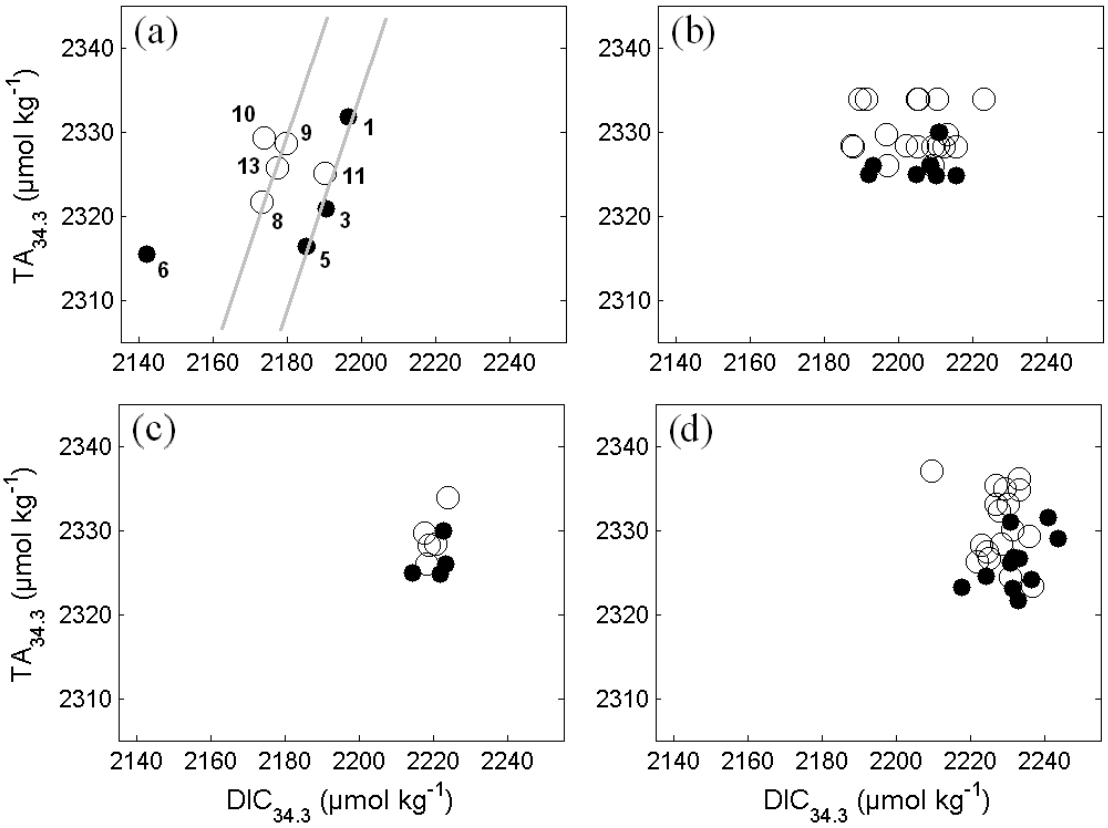

Figure 5.6. Salinity normalised total alkalinity ($TA_{34.3}$, µmol kg^{-1}) as a function of salinity normalised dissolved inorganic carbon ($DIC_{34.3}$, µmol kg^{-1}) for all marginal ice zone (MIZ) stations (stations 1-6, filled circles) and stations north of the MIZ (stations 8-13, open circles) within (a) the summer mixed layer, (b) the transition between the summer and winter mixed layers, (c) the Winter Water at the θ_{min} and (d) below the θ_{min} to 200 m depth. The grey lines (a) are hypothetical trend lines with a 2:1 slope.

Below the summer mixed layer, there was a gradual increase in $DIC_{34.3}$ and $TA_{34.3}$ throughout the water column for all stations (Fig. 5.6b). Values of $TA_{34.3}$ remained relatively constant compared to $DIC_{34.3}$ at all depths. This pattern indicates the influence of biological carbon uptake on summer DIC concentrations (Fig. 5.5d) across the Weddell-Scotia Confluence.

Similarly to surface biogeochemical distributions, the principal exception to the WW trends was station 6, where salinity and the concentrations of macronutrients and DIC were the lowest observed for the whole Weddell-Scotia Confluence (Table 5.2). Vertical profiles at station 6 show a deflection below the winter mixed layer, at about 130 m, of relatively cold, fresh water (Fig. 5.4a). This corresponds to reduced DIC and macronutrient concentrations

compared to station 5 (Fig. 5.4d-f). This could be a result of the deep penetration of brines where biological activity has amplified the reduction in DIC. As station 6 is located over shallow topography, the interaction of water masses and bathymetry (Table 5.1) could enhance vertical mixing and potentially erode the winter mixed layer from below. These results highlight the potential for overestimation of hydrographic and biogeochemical parameters in the WW, however this effect is estimated to be small (section 5.3.7).

To further investigate the processes that affect the sea surface carbonate chemistry across the Weddell-Scotia Confluence during the summer, the seasonal depletion of inorganic carbon was determined for all stations, as detailed in section 5.3.7 (Table 5.5).

Table 5.5. The inorganic carbon budget for all stations from 62.61°S (station 1) to 59.14°S (station 13) as determined by Eqn. 5.3.

Station	$\Delta DIC_{deficit}$ $\mu mol\ kg^{-1}$	$\Delta DIC_{salinity}$ $\mu mol\ kg^{-1}$	ΔDIC_{Corg} $\mu mol\ kg^{-1}$	ΔDIC_{CaCO_3} $\mu mol\ kg^{-1}$	$\Delta DIC_{residual}$ $\mu mol\ kg^{-1}$
1	-54 ± 2	-28 ± 2	-4 ± 6	2 ± 3	-24 ± 7
3	-57 ± 2	-24 ± 2	-19 ± 5	-7 ± 3	-7 ± 6
5	-63 ± 2	-24 ± 2	-36 ± 2	-8 ± 3	5 ± 5
6	-109 ± 2	-31 ± 2	-41 ± 1	-12 ± 3	-25 ± 4
8	-80 ± 2	-32 ± 2	-29 ± 8	-6 ± 3	-13 ± 9
9	-61 ± 2	-20 ± 2	-31 ± 5	-4 ± 3	-6 ± 6
10	-67 ± 2	-21 ± 2	-59 ± 6	-6 ± 3	19 ± 7
11	-54 ± 2	-21 ± 2	-59 ± 1	-8 ± 3	34 ± 4
13	-60 ± 2	-14 ± 2	-66 ± 9	-8 ± 3	28 ± 10

Changes in salinity as a result of freshwater input accounted for between 14 and 32 ± 2 μmol kg^{-1} of the seasonal change for all stations (Table 5.5), highlighting the influence of sea ice melt on the carbonate chemistry of the Southern Ocean. The seasonal depletion in DIC due to the photosynthetic production of organic carbon showed a general northward increase, with prominent utilisation of DIC at and around the receding ice edge and at the SB. This is in agreement with previous accounts of enhanced biological activity at these locations (Comiso et al., 1993; Helbling et al., 1993; Holm-Hansen and Hewes, 2004; Hewes et al., 2008). Surface waters for the whole region showed $TA_{34.3}$ and $DIC_{34.3}$ deficits characteristic of ikaite precipitation (Figs. 5.5d and 5.6). For most stations this was strongly correlated to salinity,

which suggests that continual sea ice melt and release of DIC- and TA-poor brines into the surface acts to rapidly change the carbonate chemistry of the Weddell-Scotia Confluence during summer sea ice melt. This was exemplified where the greatest extent of sea ice melt had occurred and an ice edge bloom had developed. Upper ocean distributions of DIC and TA showed a general decrease from waters beneath sea ice to the region of substantial sea ice melt and enhanced biological activity (Fig. 5.3). This culminated with the largest DIC deficits due to photosynthetic production of organic carbon and carbonate processes of 41 ± 1 and 12 ± 3 μmol kg^{-1}, respectively, and was accompanied by a strong drawdown of CO_2 (Fig. 5.2a). Following the same hypothesis, carbonate minerals in melting Nordic sea ice have been proposed to enhance the uptake of CO_2 during summer sea ice melt (Rysgaard et al., 2009).

The residual DIC changes are the result of other processes not previously assessed, such as CO_2 exchange. Large, positive residuals north of the MIZ (Table 5.5) and ΔfCO_2 of about -30 μatm (Fig. 5.2a) suggest a sustained input of DIC through CO_2 uptake from the atmosphere. Based on *in situ* fCO_2, ΔfCO_2 and DIC measurements and Revelle factors between 13 and 15 (Revelle and Suess, 1957), atmospheric CO_2 uptake would act to increase DIC by 15-16 μmol kg^{-1} at stations 11 and 13. This could, in part, account for the residual DIC concentrations at the SB where longer duration, but lower magnitude, CO_2 uptake from the atmosphere is likely to occur in comparison with the larger, more transient sink of the MIZ. The large residuals could also imply limitations to the seasonal deficit technique, as previously discussed (section 5.3.7).

5.7. Comparison to a surface water CO_2 climatology

The CO_2 sink of -0.06 Pg C yr^{-1}, between 62-52°S in the reference year 2000, is a result of an average ΔfCO_2 of -5 μatm, ranging from -15 μatm in January to 12 μatm in September (Takahashi et al., 2009). Data from the Weddell-Scotia Confluence (62.6-59.1°S) show that the region was dominated by CO_2 undersaturation at the sea surface, with an average ΔfCO_2 of -25 μatm (range from -95 to 14 μatm, Fig. 5.2a) during summer 2008. The potential CO_2 source of 14 μatm observed beneath the sea ice cover near station 1 is very similar to the ΔfCO_2 maximum from the climatology (12 μatm). The strong undersaturation of fCO_2 in the region of substantial sea ice melt far exceeded that of the climatology, by up to 80 μatm. In reference to the climatological ΔfCO_2 maximum of about 12 μatm, it is hypothesised that the

Weddell-Scotia Confluence is a region of CO_2 uptake of greater than 0.06 Pg C yr^{-1}. However, investigations into the function of Antarctic sea ice as a permeable 'barrier' to CO_2 exchange may require these estimates to be re-evaluated (Semiletov et al., 2004; Nomura et al., 2006).

5.8. Conclusion

The precipitation of carbonates such as ikaite in sea ice has the net effect of decreasing DIC and alkalinity and increasing the fCO_2 in the sea ice brine. Deficits in salinity normalised DIC and alkalinity observed in the summer mixed layer of the Weddell-Scotia Confluence are consistent with the release of brines from melting sea ice, where ikaite precipitation has taken place. Across the marginal ice zone, ikaite precipitation accounted for up 12 ± 3 μmol kg^{-1}, or 13%, of the summer DIC deficit and was strongly correlated to the amount of sea ice melt that had taken place. Photosynthetic production of organic carbon had the largest effect on summer DIC concentrations, resulting in deficits of 41 ± 1 μmol kg^{-1} at the receding ice edge and 66 ± 9 μmol kg^{-1} at the Southern Boundary. The effects of biological carbon uptake became superimposed on those of the sea ice carbonate chemistry, rapidly reducing fCO_2 compared to waters beneath the sea ice. These processes created substantial CO_2 undersaturation of 95 μatm in the marginal ice zone during the summer.

The 'sea ice CO_2 pump' hypothesis suggests that the dissolution of calcium carbonate minerals in meltwater during the summer promotes CO_2 uptake from the atmosphere. The carbonate chemistry data for the marginal ice zone of the Weddell-Scotia Confluence suggest that it is the transfer of DIC- and TA-poor brines into the surface water during ice melt, in the presence of phytoplankton blooms, that drive a strong sink for CO_2 during the summer. Further work should be directed at improving the understanding of sea ice carbonate chemistry and its role in the sea ice carbon pump of the polar oceans.

6. South Georgia: extensive island blooms and substantial biological carbon uptake

6.1. Abstract

The influence of the island mass effect of South Georgia on the marine carbon cycle of the Scotia Sea was investigated during January and February 2008. South Georgia (54-55°S 36-38°W) is located on the North Scotia Ridge, between the Polar Front to the north and the Southern Antarctic Circumpolar Current Front (SACCF) to the south. Surface waters upstream (south) of the island were characterised by high-nutrient low-chlorophyll (HNLC) conditions, with chlorophyll-a concentrations less than 0.2 mg m^{-3}. The fugacity of carbon dioxide (fCO_2) was slightly supersaturated and this region represented a CO_2 source of 2.6 ± 0.9 mmol m^{-2} day^{-1} during summer 2008.

An extensive diatom bloom with chlorophyll-a concentrations greater than 11.0 mg m^{-3} developed in the Georgia Basin (GB), downstream of South Georgia, in November 2007 and persisted for three months. The seasonal depletion in DIC was 98 ± 5 μmol kg^{-1} and the ΔfCO_2(sea-air) was -96 ± 35μatm in the core of the bloom. These conditions created a strong sink for atmospheric CO_2 of -15.1 ± 5.7 mmol m^{-2} day^{-1}, which corresponded to a total biological carbon uptake of 1.3 ± 0.5 Tg C (1 Tg = 10^{12} g) during summer 2008. The deficit of DIC in the upper 100 m downstream (4.6 ± 0.8 mol m^{-2}) of South Georgia was over twice that of the upstream (2.2 ± 0.3 mol m^{-2}) HNLC waters. The DIC deficit in HNLC waters suggested that this region is more productive than indicated by satellite observations. In comparison to the island blooms of Kerguelen and Crozet, the South Georgia bloom is likely to be naturally iron fertilised. The DIC deficit of the South Georgia bloom in summer 2008 firmly established the bloom as the strongest region to date for biological carbon uptake in non-ice covered waters of the Southern Ocean.

6.2. Introduction

In contrast to the high-nutrient low-chlorophyll (HNLC) waters of much of the Southern Ocean, enhanced phytoplankton concentrations are regularly observed downstream of bathymetric features (Moore and Abbot, 2000; Blain et al., 2001; Holm-Hansen et al., 2005; Pollard et al., 2007; Sokolov and Rintoul, 2007). The blooms associated with the sub-Antarctic islands of Crozet (45.5-47.0°S 49.0-53.0°E) and Kerguelen (48.5-49.7°S 68.5-70.5°E) are sustained through natural iron fertilisation (Bucciarelli et al., 2001; Blain et al., 2007; Planquette et al., 2007) and create regions of substantial biological carbon uptake (Bakker et al., 2007; Jouandet et al., 2008). Similarly to Crozet and Kerguelen, large diatom-dominated phytoplankton blooms are recurrent features downstream of the island of South Georgia where chlorophyll-a concentrations often exceed 10 mg m^{-3} for four months or more (Korb and Whitehouse, 2004; Korb et al., 2004; Korb et al., 2010).

In order to sustain the vast blooms downstream of South Georgia, a supply of iron is required (Holeton et al., 2005), alleviating the otherwise high-nutrient low-chlorophyll conditions (section 1.4.4.1). Possible sources include the North Scotia Ridge (NSR), the Northwest Georgia Rise (NWGR), South Georgia and the interaction of the Southern Antarctic Circumpolar Current Front (SACCF) with surrounding bathymetric features (Ward et al., 2002; Meredith et al., 2003a; Meredith et al., 2003b; Korb et al., 2008; Whitehouse et al., 2008) (Fig. 6.1). In addition to iron, silicate could limit diatom growth in the northern AAZ due to the decreasing northward concentration gradient in this macronutrient that exists across the Scotia Sea (Boyd, 2002; Whitehouse et al., 2008). The South Georgia bloom is considered to be a region of important CO_2 uptake (Schlitzer, 2002; Takahashi et al., 2009) in the Southern Ocean however this remains unquantified.

This research investigates the effect of the South Georgia bloom on the marine carbon cycle of the Scotia Sea, with respect to seasonal changes in dissolved inorganic carbon (DIC) and air-sea CO_2 exchange. It is hypothesised that higher biological carbon uptake and a stronger CO_2 sink will exist in the bloom waters (downstream), compared to HNLC waters (upstream) in the central Antarctic Circumpolar Current (ACC) (Fig. 6.2). The results will be compared to similar carbon work carried out for the sub-Antarctic islands of Crozet and Kerguelen, both in the Indian sector of the Southern Ocean (Bakker et al., 2007; Jouandet et al., 2008).

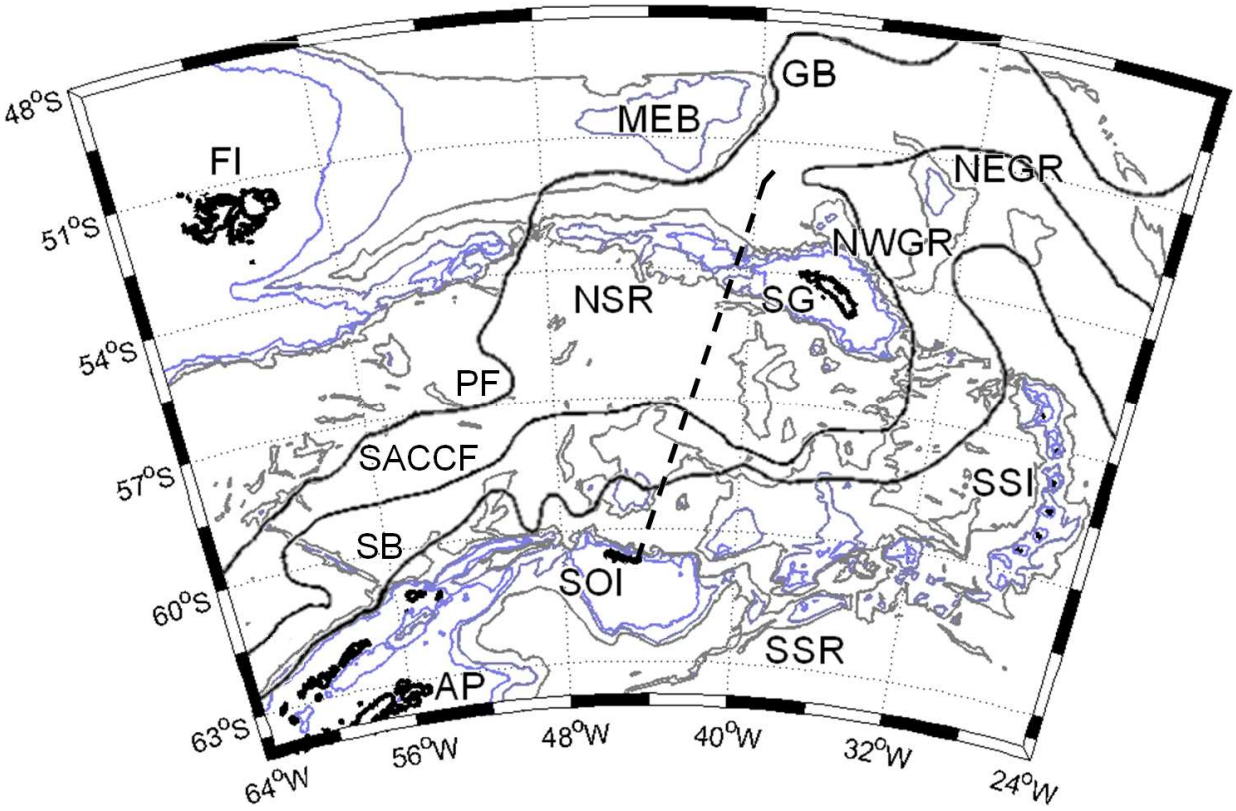

Figure 6.1. A schematic of the Scotia Sea showing the approximate location of the JR177 transect (see Fig. 6.3 for more detail) across the Antarctic Zone (dashed line). Some important topographic features are identified: Antarctic Peninsula (AP), South Scotia Ridge (SSR), South Orkney Islands (SOI), South Sandwich Islands (SSI), North Scotia Ridge (NSR), South Georgia (SG), Northwest Georgia Rise (NWGR), Northeast Georgia Rise (NEGR), Georgia Basin (GB), Maurice Ewing Bank (MEB) and the Falkland Islands (FI). Antarctic Circumpolar Current (ACC) fronts shown schematically, adapted from Meredith et al. (2003a): the Southern Boundary (SB, Orsi et al., 1995), Southern ACC Front (SACCF, Thorpe et al., 2002) and the Polar Front (PF, Moore et al., 1999). Depth contours are at 1000, 2000 and 3000 m (GEBCO, 2001).

The ship entered the Antarctic Zone (AAZ) and the Antarctic Circumpolar Current (ACC) on 17 January 2008 after crossing the Southern Boundary (SB) at 59°S (Fig. 6.1). From here, a northward transect was made, which encompassed the SACCF at 58°S and reached the most northerly point in the Georgia Basin (GB) at station 53 (52.63°S 39.10°W) on 4 February (Fig. 6.3, Table 6.1). Satellite derived chlorophyll-a revealed an area of ocean in the central ACC that supported low levels of chlorophyll-a ([chl-a] ≤ 0.2 mg m^{-3}) throughout the cruise. In relation to concentrations of nitrate and phosphate, this region was defined as having high-

nutrient low-chlorophyll (HNLC) conditions, forming an unproductive band from 57.5°S to 56.0°S (Fig. 6.2).

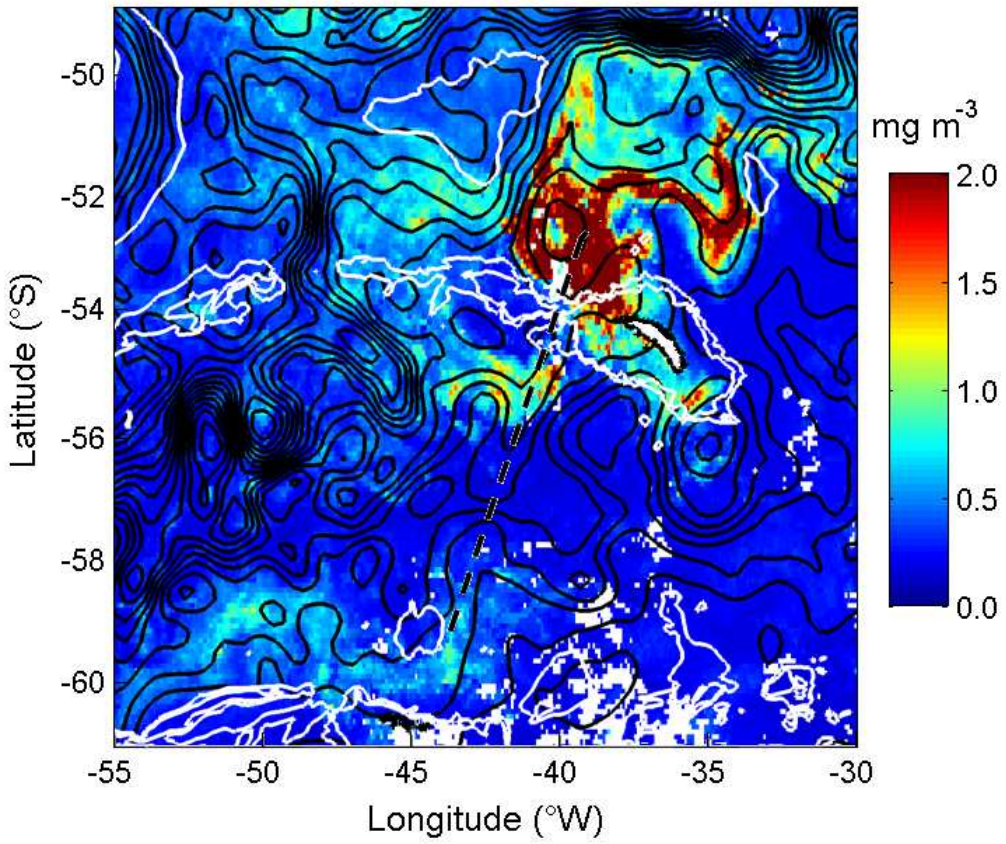

Figure 6.2. A cruise composite (1 January – 17 February 2008) of MODIS chlorophyll-a (mg m^{-3}) and contours of dynamic height (dyn cm). The approximate location of the transect (see Fig. 6.3 for more detail) across the Antarctic Zone (AAZ) is shown (dashed line). Depth contours are at 1000 and 2000 m (GEBCO, 2001).

In contrast, a huge phytoplankton bloom was identified downstream, of South Georgia in the GB, referred to here as the South Georgia bloom. A smaller bloom was identified to the south of the NSR at about 55°S and is referred to as the ACC bloom. Thus, four sub-regions along the transect are identified: HNLC (stations 30 and 33), ACC bloom (station 37), NSR (stations 43, 44, 46 and 48) and the South Georgia bloom (stations 51 and 53) in the GB, where HNLC and GB stations represent the principle unproductive and productive regions, respectfully, with a continuum of productivity in between. The SB and SACCF were identified using vertical profiles of hydrographic data (Chapter 4) and sea surface dynamic height (Fig. 6.2).

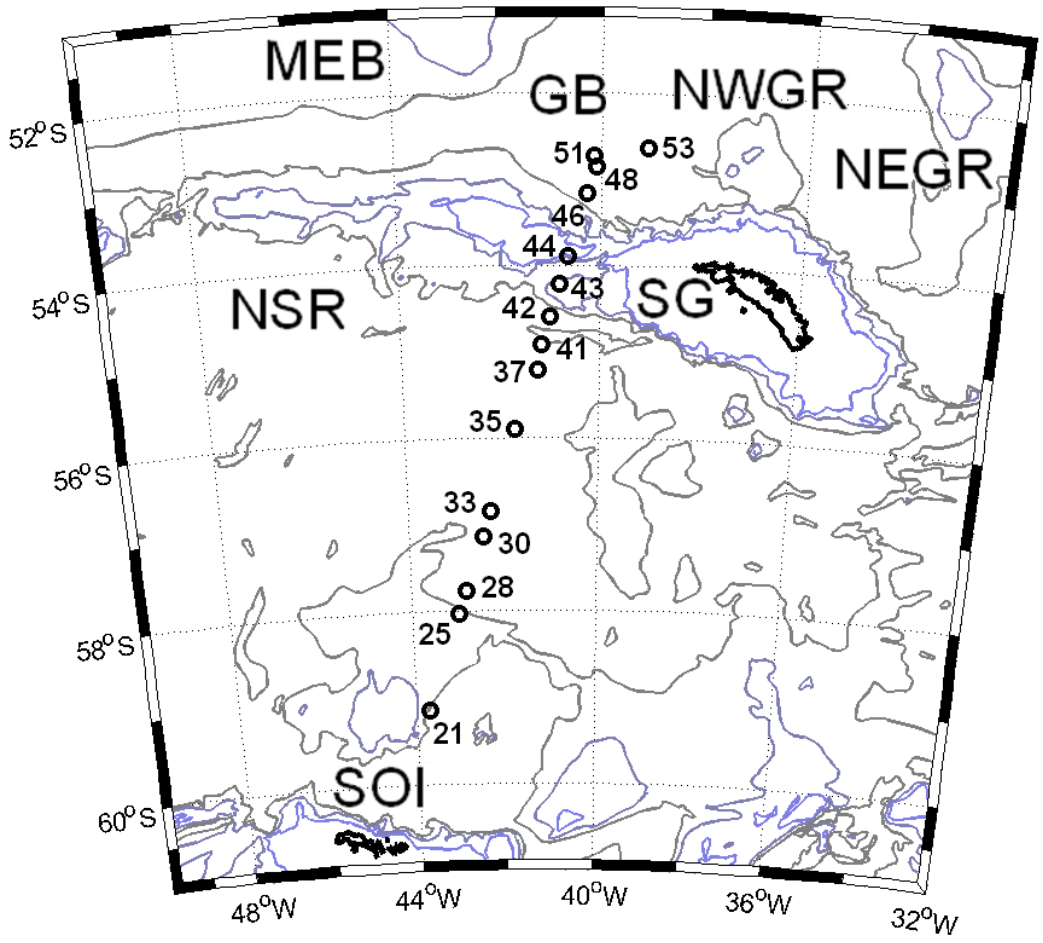

Figure 6.3. A schematic of the Antarctic Zone (AAZ) of the Scotia Sea showing the location of the hydrographic stations (Table 6.1). Topographic features and bathymetry as in Figure 6.1.

Table 6.1. Station number, classification, date, location (°S, °W) and bottom depth (m) for all hydrographic stations in the Antarctic Zone (AAZ). Abbreviations used: Southern Boundary (SB), Southern Antarctic Circumpolar Current Front (SACCF), Antarctic Circumpolar Current (ACC), high-nutrient low-chlorophyll (HNLC), North Scotia Ridge (NSR), South Georgia (SG).

Station	*Region*	*Date 2008*	*Latitude °S*	*Longitude °W*	*Bottom depth m*	*Sub-region*
21	SB	17 Jan	59.144	43.694	3611	
25	SACCF	19 Jan	58.023	42.985	2831	
28	SACCF	20 Jan	57.758	42.801	2904	
30	HNLC	22 Jan	57.140	42.433	3700	HNLC
33	HNLC	22 Jan	56.843	42.257	4248	HNLC
35	ACC	23 Jan	55.902	41.720	3595	
37	ACC	25 Jan	55.207	41.246	3246	ACC bloom
41	ACC	28 Jan	54.913	41.173	3442	
42	ACC	29 Jan	54.591	40.997	3301	
43	NSR	29 Jan	54.216	40.813	2461	NSR
44	NSR	29 Jan	53.897	40.645	1233	NSR
46	NSR	30 Jan	53.155	40.276	4052	NSR
48	GB	01 Feb	52.857	40.097	3811	NSR
51	GB	02 Feb	52.727	40.147	405	SG bloom
53	GB	04 Feb	52.627	39.102	3750	SG bloom

6.3. Hydrography

Surface waters showed a strong northward gradient in temperature from about 1.09 °C at the SB (station 21) to 4.02 °C in the GB at stations 51 and 53 (Fig. 6.4a). Surface salinity showed an opposing trend, decreasing from values greater than 34 in the south (stations 21, 23 and 25) to values close to 33.8 in the NSR-GB region. With the exception of waters in the GB, there was a general deepening of the MLD across the AAZ, with the deepest mixed layers around 70 m to the south of the NSR (Table 6.2). A distinct Winter Water (WW) layer could be observed in the Antarctic Surface Water (AASW) across the AAZ (Fig. 4.2), with an average potential temperature minimum (θ_{min}) of -0.02 ± 0.47 °C and a winter mixed layer depth of 113 ± 22 m (n = 16, Table 6.3). The value of the θ_{min} increased northwards, until station 44 over the NSR, where it steadily decreased by over 0.80 °C, reaching -0.29 °C at station 53. This corresponded to an increase in the salinity of the WW from station 44 to 53, deviating from the otherwise northward decrease.

6.4. Circulation

Maps of sea surface dynamic height can inform on the location, structure and variability of the ACC fronts (Sokolov and Rintoul, 2007). Upon inspection of sea surface dynamic height, the transect was parallel to the contours until about 58°S where the contours tightened and intercepted the transect, marking the surface expression of the SACCF (Fig. 6.2). Further north, the contour patterns indicate that stations 35-37, at about 55.5°S, are located close to a meander in the SACCF to the east and an encroaching meander of the Polar Front (PF) to the west. Comparing MODIS chlorophyll-a and sea surface dynamic height shows a strong link to the bathymetry of the region (Figs. 6.1). A diversion in the dynamic height contours is apparent at about 55°S 40°W, southwest of South Georgia. This has been previously observed by diverging drifter trajectories at this location (Korb et al., 2008). Waters flowing to the east in the SACCF followed NSR and retroflected behind South Georgia passing either directly into the GB or first via circulation around the NWGR (Meredith et al., 2003a; Thorpe et al., 2002). The anticyclonic circulation near the NWGR is shown by a de-linearity and spacing out of the contours. Currents flowing to the northwest are strongly governed by the bathymetry (Arhan et al., 2002; Smith et al., 2010), as the contours tighten close to Maurice Ewing Bank (MEB), identifying the location of the PF, before spreading out into the cyclonic circulation of

the GB. The observations of sea surface dynamic height in the vicinity of the NSR supported modelled flow patterns (Trathan et al., 1997) for this region (Fig. 1.7).

6.5. Macronutrients

Near-surface (0-50 m) silicate (hereinafter SiO_4) concentrations showed a strong northward gradient, decreasing by 70 μmol kg^{-1} from the SB to the GB (Table 6.2). The distributions of near-surface nitrate (hereinafter NO_3) and phosphate (hereinafter PO_4) had a more variable decrease across the AAZ. Distinct depletion of all three macronutrients was observed in regions of elevated chlorophyll-a in the northern ACC, over the NSR and in the GB (Fig. 6.2). Average WW concentrations for silicate, nitrate and phosphate were 47.9, 28.9 and 1.96 μmol kg^{-1}, respectively (n = 16, Table 6.3). These values are similar to winter and pre-bloom surface values measured previously in this region (Whitehouse et al., 2008).

6.6. Iron

Moderate concentrations of dissolved iron (dFe), 0.20-0.40 nM, were observed in the vicinity of the SACCF up to 57°S (Fig. 6.4e). The lowest concentrations, < 0.01 nM, were observed over the NSR. High concentrations (≥ 0.50 nM) were observed between the NSR and the GB, reaching a summer time maximum for dFe of 1.17 nM in the lower GB.

Figure 6.4. (page 182) The latitudinal distribution of sea surface (a) salinity (red line) and temperature (SST, °C, blue line), (b) fugacity of CO_2 (fCO_2, μatm), (c) dissolved inorganic carbon (DIC, μmol kg^{-1}), (d) total alkalinity (TA, μmol kg^{-1}, solid line), (e) iron (nM) and (f) chlorophyll-a (chl-a, mg m^{-3}) across the Antarctic Zone during summer 2008. The approximate location of the Southern Boundary (SB), Southern ACC Front (SACCF), high-nutrient low-chlorophyll (HNLC) waters, the North Scotia Ridge (NSR) and the Georgia Basin (GB) are indicated.

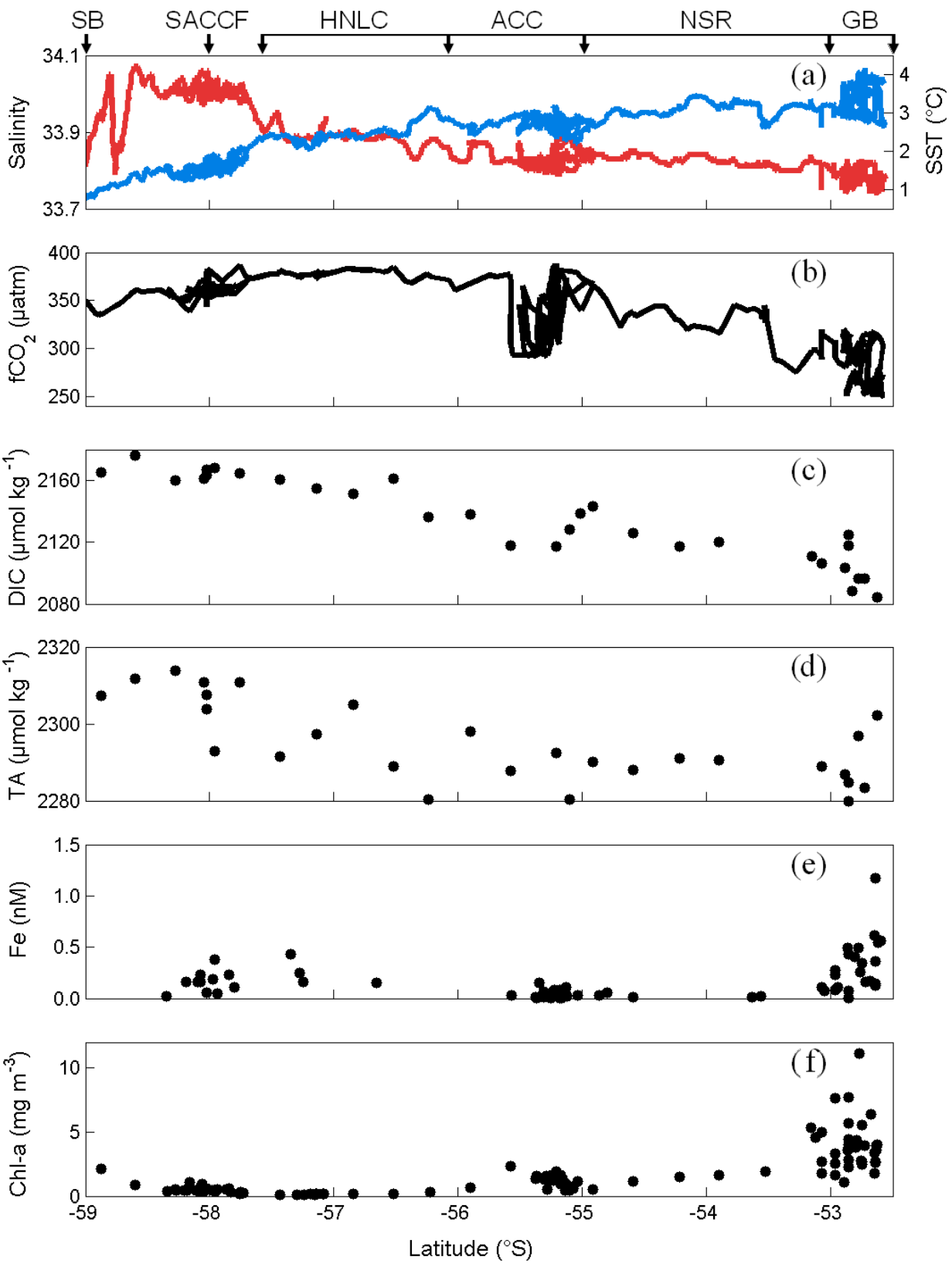
SB
SACCF
HNLC
ACC
NSR
GB
(a)
Salinity
SST (°C)
34.1
33.9
33.7
4
3
2
1
(b)
fCO2 (µatm)
400
350
300
250
(c)
DIC (µmol kg-1)
2160
2120
2080
(d)
TA (µmol kg-1)
2320
2300
2280
(e)
Fe (nM)
1.5
1.0
0.5
0.0
(f)
Chl-a (mg m-3)
10
5
0
-59
-58
-57
-56
-55
-54
-53
Latitude (°S)

Table 6.2. Mixed layer depth (MLD, m), temperature (°C), salinity, silicate (SiO_4, μmol kg^{-1}), phosphate (PO_4, μmol kg^{-1}) and nitrate (NO_3, μmol kg^{-1}) of the summer mixed layer for all stations in the AAZ from 59.14°S (station 21) to 52.63°S (station 53). The mean value for each station is shown (from values measured at *n* bottle depths up to the MLD) with the standard deviation (for stations where $n > 2$) and the difference (for stations where $n = 2$) in brackets. Stations 21, 28, 33, 41, 43, 44, 46 and 51 have interpolated nutrient concentrations from proximal stations with the same classification. The summer mixed layer depth (MLD) is defined as the depth where the potential density exceeds that measured at 10 m by 0.05 kg m^{-3} (Brainerd and Gregg, 1995).

Station	*n*	*MLD*	*Temperature*	*Salinity*	*SiO_4*	*PO_4*	*NO_3*
		m	*℃*		*μmol kg^{-1}*	*μmol kg^{-1}*	*μmol kg^{-1}*
21	2	29	1.09 (0.01)	33.85 (0.00)	71.0 (0.3)	1.34 (0.01)	22.4 (0.0)
23	2	53	1.82 (0.10)	34.08 (0.00)	60.5 (0.3)	1.56 (0.01)	23.1 (0.1)
25	5	47	1.68 (0.18)	34.01 (0.00)	63.7 (0.9)	1.63 (0.07)	22.5 (1.1)
28	3	47	2.43 (0.01)	33.99 (0.00)	46.9 (0.8)	1.50 (0.02)	24.0 (0.5)
30	4	55	2.62 (0.06)	33.89 (0.00)	30.4 (0.3)	1.64 (0.01)	23.5 (0.3)
33	6	57	2.56 (0.53)	34.33 (0.01)	34.3 (0.3)	1.49 (0.01)	24.8 (0.2)
35	4	67	2.91 (0.01)	33.87 (0.00)	16.5 (0.2)	1.61(0.01)	23.0 (0.1)
37	7	61	3.18 (0.07)	33.83 (0.00)	3.5 (0.2)	1.26 (0.02)	19.7 (0.3)
41	4	71	3.04 (0.08)	33.87 (0.00)	12.5 (0.3)	1.33 (0.01)	22.8 (0.1)
42	3	63	3.36 (0.01)	33.87 (0.00)	4.6 (0.5)	1.39 (0.01)	20.8 (0.1)
43	3	65	3.47 (0.07)	33.84 (0.00)	3.2 (1.0)	1.69 (0.04)	19.2 (0.5)
44	3	65	3.46 (0.08)	33.84 (0.00)	3.7 (0.7)	1.18 (0.04)	19.2 (0.4)
46	3	69	3.59 (0.02)	33.85 (0.00)	19.5 (0.8)	0.64 (0.03)	14.6 (0.1)
48	6	67	3.30 (0.08)	33.82 (0.01)	12.8 (0.9)	1.12 (0.02)	17.6 (0.1)
51	3	33	3.96 (0.21)	33.83 (0.00)	6.3 (1.0)	0.97 (0.10)	15.3 (0.8)
53	3	21	4.02 (0.04)	33.81 (0.00)	0.0 (0.0)	0.93 (0.04)	13.6 (0.2)

Table 6.3. Winter mixed layer depth (WMLD, m), temperature (°C), salinity, silicate (SiO_4, μmol kg^{-1}), phosphate (PO_4, μmol kg^{-1}), nitrate (NO_3, μmol kg^{-1}), dissolved inorganic carbon (DIC, μmol kg^{-1}) and total alkalinity (TA, μmol kg^{-1}) of the winter mixed layer (representing the WW) for all stations in the AAZ from 59.14°S (station 21) to 52.63°S (station 53). The absolute value for each station is shown measured from 1 bottle at the depth of the potential temperature minimum (θ_{min}). Stations 21, 28, 33, 41, 43, 44, 46 and 51 have interpolated nutrient concentrations from proximal stations with the same classification.

Station	*WMLD*	*θ_{min}*	*Salinity*	*SiO_4*	*PO_4*	*NO_3*	*DIC*	*TA*
	m	*℃*		*μmol kg^{-1}*	*μmol kg^{-1}*	*μmol kg^{-1}*	*μmol kg^{-1}*	*μmol kg^{-1}*
21	93	-1.39	34.25	83.2	1.99	31.6	2222	2330
23	99	-0.35	34.33	79.3	1.99	29.9	2224	2331
25	77	-0.28	34.24	73.1	2.01	28.2	2205	2325
28	101	-0.16	34.20	63.7	2.06	31.7	2208	2321
30	101	-0.22	34.07	59.5	2.07	29.1	2191	2307
33	101	0.11	34.05	52.1	1.97	30.0	2191	2305
35	99	0.14	33.95	29.4	2.03	28.6	2185	2301
37	97	-0.18	33.95	28.7	1.87	27.5	2165	2296
41	125	0.32	34.01	27.0	1.83	28.4	2175	2293
42	107	0.12	33.95	31.3	1.94	28.8	2178	2294
43	167	0.49	34.04	33.5	2.20	28.8	2175	2303
44	133	0.53	34.00	27.1	1.66	26.4	2171	2299
46	135	0.37	34.03	45.9	1.76	28.9	2185	2301
48	119	0.37	34.02	42.0	2.08	30.8	2194	2297
51	121	0.17	34.01	51.7	1.94	27.8	2193	2289
53	131	-0.29	34.05	47.8	1.93	26.9	2190	2287

6.7. Satellite and shipboard chlorophyll-a

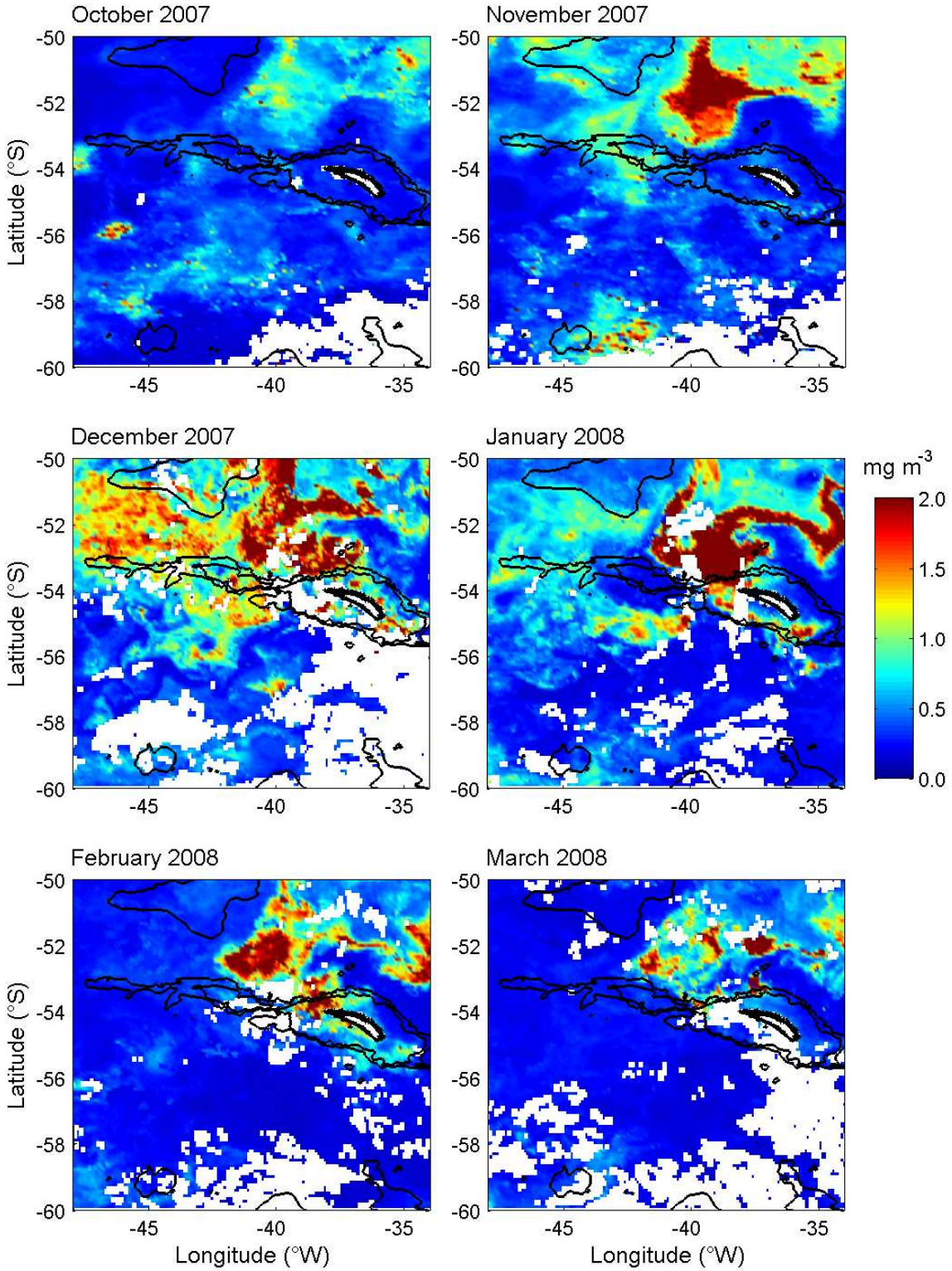

Figure 6.5. Monthly composites of MODIS chlorophyll-a (mg m^{-3}) for the Scotia Sea during summer (December 2007-February 2008) and early autumn (March 2008). Depth contours are at 1000 and 2000 m (GEBCO, 2001).

MODIS provided large-scale coverage of the surface chlorophyll-a concentrations of the Scotia Sea, before, during and after JR177 in austral summer 2008 (Fig. 6.5). Low chlorophyll-a concentrations (< 0.20 mg m^{-3}) persisted for much of the AAZ from October to March. This was confirmed by shipboard observations, where chlorophyll-a concentrations were 0.16 mg m^{-3} between stations 30 and 33 on 22 January. Satellite images from October to December 2007 showed the development of extensive phytoplankton blooms over the NSR and in the GB. The surface expression of the bloom over the NSR had largely dispersed to the northwest and northeast by January 2008, leaving an intense patch to the south of the NSR in the ACC.

In contrast, the South Georgia bloom reached maximum intensity by January 2008 and gradually extended to the north and east, along the contours of the SACCF and PF (Fig. 6.2) before declining in March. The RRS *James Clark Ross* reached the GB in early February, shortly after the maximum extent of the bloom. Shipboard observations revealed a summer chlorophyll-a maximum of 11.14 mg m^{-3} in the lower GB. From inspection of satellite chlorophyll-a, the duration of the South Georgia bloom was estimated at 90 ± 14 days, concurring with estimates for summer bloom duration of 82-122 days by Ward et al. (2002). The uncertainty was determined subjectively, based on the presence of a smaller bloom for part of October 2007 and February 2008.

The vertical distribution of chlorophyll-a up to 120 m showed that concentrations were typically lower than 1 mg m^{-3} throughout the upper water column from 59°S to 55°S, representing a true HNLC belt at the surface in the ACC (Fig. 4.6). An exception to this, were subsurface peaks of chlorophyll-a at about 70 m, close to 55°S, between stations 30 and 33. Enhanced concentrations were observed in the near surface waters of the phytoplankton patches in the ACC, over the NSR and in the GB.

6.8. Phytoplankton species distribution

Two main phytoplankton clusters were identified in the southern and northern regions of the AAZ (Korb et al., 2010). From the SB to the SACCF, the species composition was dominated by naked, heterotrophic dinoflagellates with very few diatoms. In waters north of the SACCF to the NSR and the GB, the community shifted to one dominated by diatoms, with the greatest

abundance to the northwest of South Georgia. Diatom dominated phytoplankton communities have consistently been found around South Georgia during austral summer (Korb et al., 2008).

Table 6.4. Dissolved inorganic carbon (DIC, μmol kg^{-1}), total alkalinity (TA, μmol kg^{-1}), salinity normalised DIC (DIC_{34}, μmol kg^{-1}) and salinity normalised TA (TA_{34}, μmol kg^{-1}) of the summer mixed layer and surface water fCO_2 (μatm) and chlorophyll-a (chl-a, mg m^{-3}) for all stations in the AAZ from 59.14°S (station 21) to 52.63°S (station 53). The mean value for DIC, DIC_{34}, TA and TA_{34} is shown (from values measured at *n* bottle depths up to the depth of the mixed layer) with the standard deviation (for stations where $n > 2$) and the difference (for stations where $n = 2$) in brackets.

Station	*n*	*DIC*	*TA*	DIC_{34}	TA_{34}	fCO_2	*Chl-a*
		μmol kg^{-1}	*μmol* kg^{-1}	*μmol* kg^{-1}	*μmol* kg^{-1}	*μatm*	*mg* m^{-3}
21	2	2161 (8)	2299 (4)	2177 (8)	2326 (4)	332	2.06
23	2	2176 (0)	2315 (8)	2184 (0)	2328 (8)	360	0.86
25	5	2166 (7)	2311 (2)	2177 (7)	2328 (2)	345	0.62
28	3	2166 (2)	2309 (1)	2177 (2)	2327 (1)	386	0.16
30	4	2155 (1)	2295 (4)	2158 (1)	2301 (4)	379	0.16
33	6	2159 (5)	2298 (4)	2162 (5)	2303 (4)	382	0.16
35	4	2142 (4)	2295 (3)	2147 (4)	2303 (3)	371	0.63
37	7	2120 (7)	2293 (2)	2126 (7)	2303 (2)	320	1.93
41	4	2144 (1)	2290 (0)	2148 (1)	2298 (0)	348	0.49
42	3	2125 (2)	2288 (1)	2129 (2)	2296 (1)	335	1.18
43	3	2121 (6)	2292 (2)	2126 (6)	2302 (2)	320	1.51
44	3	2127 (7)	2297 (6)	2133 (7)	2307 (6)	319	1.62
46	3	2109 (2)	2298 (0)	2114 (2)	2307 (0)	298	5.37
48	6	2124 (2)	2288 (2)	2130 (2)	2298 (2)	297	2.28
51	3	2098 (2)	2277 (6)	2104 (2)	2287 (6)	289	7.68
53	3	2090 (6)	2301 (1)	2097 (6)	2313 (1)	255	11.14

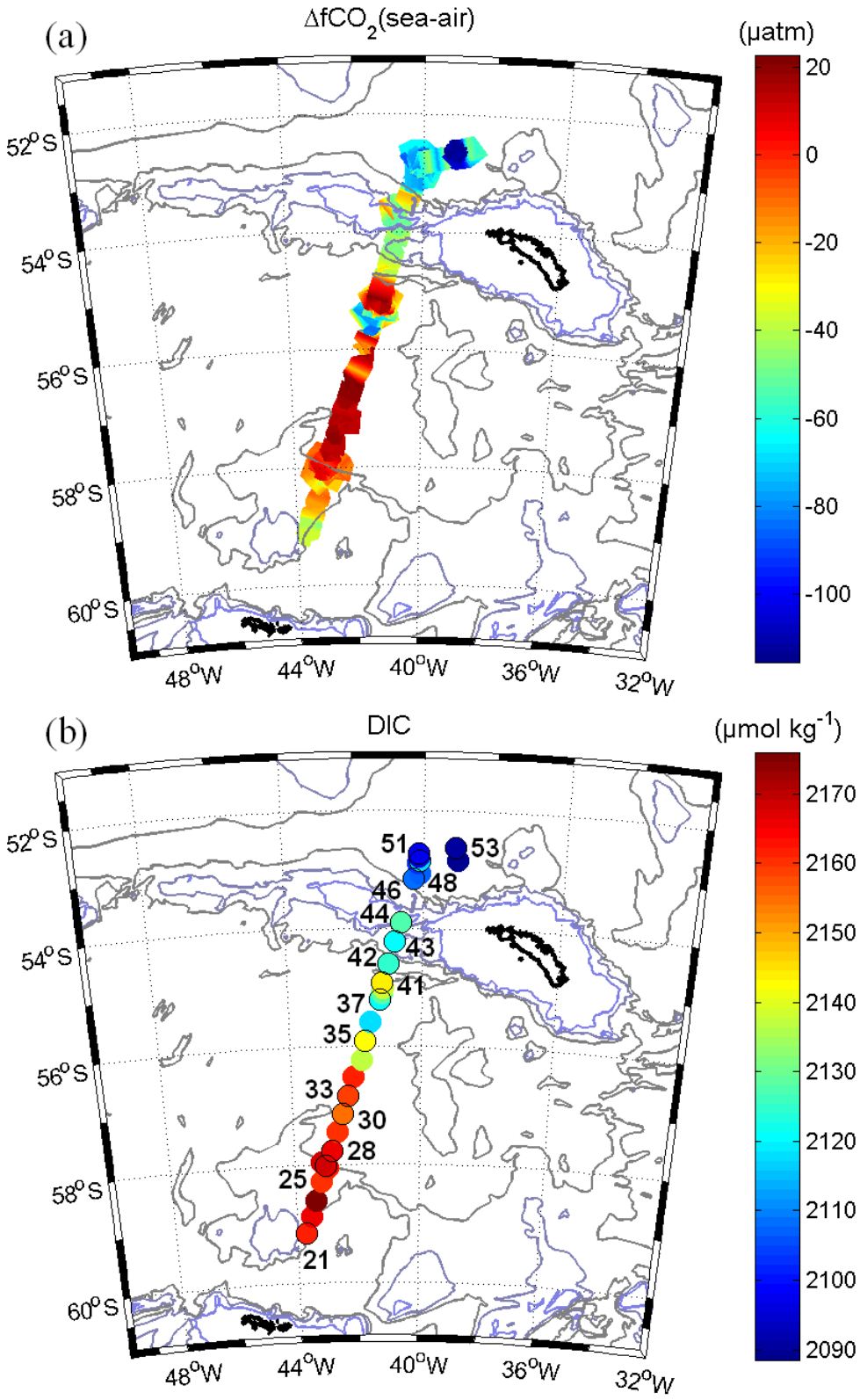

Figure 6.6. Maps of the (a) Δ*f*CO_2 (µatm) and (b) dissolved inorganic carbon (DIC, µmol kg^{-1}) along the transect. The location of the hydrographic stations (Table 6.1) are shown (b). Bathymetry as in Figure 6.1.

6.9. The carbon dioxide system

From 58°S to 56°S, sea surface fCO_2 concentrations formed a band of moderate supersaturation near station 33, where ΔfCO_2 was about 20 μatm (Fig. 6.6). Waters of the GB had strong levels of undersaturation with a summer minimum of ΔfCO_2 reaching -121 μatm, between stations 51 and 53. The concentration of sea surface DIC predominantly followed the trend of fCO_2, decreasing by nearly 100 μmol kg^{-1} across the AAZ (Fig. 6.4c). The distribution of sea surface alkalinity showed a general decreasing trend to the north with large variability close to the SB and in the GB (Fig. 6.4d). Concentrations of DIC and alkalinity reached summer maxima of 2176 and 2314 μmol kg^{-1}, respectively, close to the SACCF.

Sea surface normalised DIC (DIC_{34}) followed the trend in DIC concentrations (Table 6.4). Upon normalisation, the variation in TA (TA_{34}) across the AAZ was largely reduced. Exceptions were stations 21 to 28 near the SACCF and stations 51 and 53 in the GB. WW DIC (Table 6.3) showed a northward decrease of up to 50 μmol kg^{-1}, up to the NSR. From the NSR and into the GB, DIC increased to values close to 2190 μmol kg^{-1} at stations 51 and 53. WW TA also showed a strong northward gradient, decreasing from values close to 2330 μmol kg^{-1} at the SB to less than 2290 μmol kg^{-1} in the GB. The higher DIC concentration at the more southerly stations is consistent with the previously observed latitudinal gradient in DIC (Bakker et al., 1999; Jabaud-Jan et al., 2004; Shim et al., 2006; Jouandet et al., 2008).

6.10. DIC deficits and air-sea CO_2 fluxes

The DIC deficit increased from 2.2 ± 0.3 mol m^{-2} in the HNLC waters (upstream) to 4.6 ± 0.8 mol m^{-2} in the core of the bloom (downstream) in the GB (Table 6.5). Summation of the DIC deficit in each of the four sub-regions (HNLC, ACC, NSR and GB) provides a total DIC deficit of 9.7 ± 0.9 Tg C for the AAZ of the Scotia Sea during summer 2008.

Fluxes at atmospheric pressure with seasonally averaged wind speeds from QuikSCAT (section 2.15) were calculated using the Nightingale et al. (2000) relationship for short term winds. Seasonal wind speed averages were calculated by taking an average of the wind speed (measured twice daily) at the position of each ΔfCO_2 value along the transect. The use of seasonal winds gave more representative CO_2 fluxes on seasonal timescales and hence present

a more realistic picture of CO_2 exchange for the duration of the bloom (90 days). A discussion of fluxes using *in situ* and seasonally averaged is presented in Chapter 7 (section 7.10.1).

During summer 2008, the upstream HNLC waters represented an oceanic source of CO_2 2.6 ± 0.9 mmol m^{-2} day^{-1} (Table 6.5). The ACC bloom region 2° north of the HNLC waters was a strong sink for atmospheric CO_2 of -10.3 ± 0.0 mmol m^{-2} day^{-1}. The strongest summer CO_2 uptake of -15.1 ± 5.7 mmol m^{-2} day^{-1} occurred in the GB.

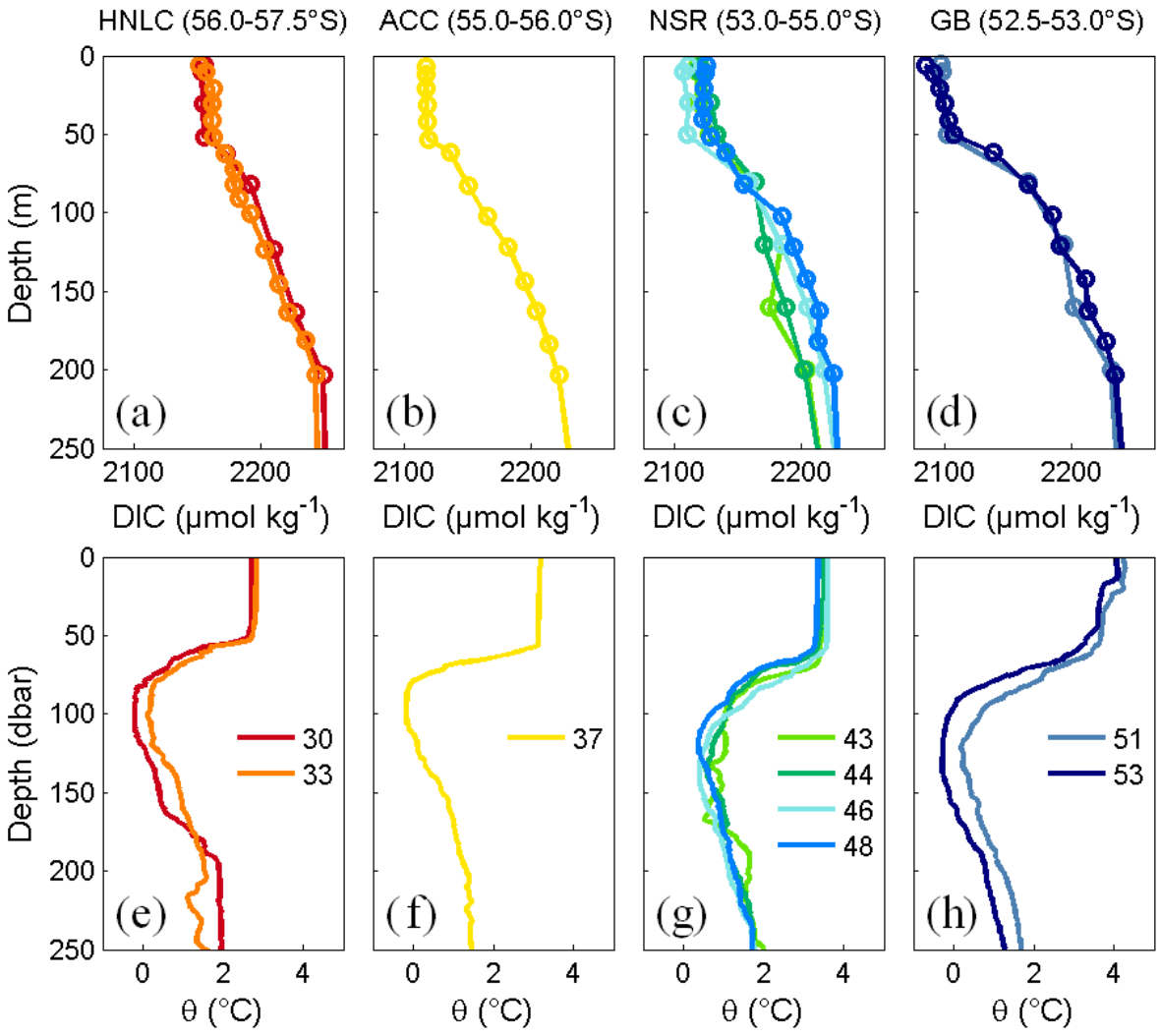

Figure 6.7. Vertical profiles of upper water column (a, b, c, d) dissolved inorganic carbon (DIC, µmol kg^{-1}) and (e, f, g, h) potential temperature (θ, °C) for HNLC stations 30 and 33 (a and e), ACC station 37 (b and f), North Scotia Ridge (NSR) stations 43, 44, 46 and 48 (c and g) and Georgia Basin (GB) stations 51 and 53 (d and h).

Table 6.5. The coverage (km^2), duration (days), mixed layer depth (MLD, m), depth integrated chlorophyll-a ($[chl\text{-}a]_{100\ m}$) over 100 m (mg m^{-2}), dissolved inorganic carbon in the summer mixed layer (DIC_{summer}, μmol kg^{-1}), DIC in the Winter Water (DIC_{winter}, μmol kg^{-1}), seasonal change in DIC (ΔDIC, μmol kg^{-1}), DIC deficit integrated over 100 m (mol m^{-2}), total DIC deficit (Tg C), ΔfCO_2(sea-air) (μatm), CO_2 flux (mmol m^{-2} d^{-1}) , CO_2 flux (mol m^{-2}) and total flux (Tg C) for the high-nutrient low-chlorophyll (HNLC) stations 30 and 33 (n = 2), Antarctic Circumpolar Current (ACC) station 37 (n = 1), North Scotia Ridge stations 43, 44, 46 and 48 (n = 4) and the Georgia Basin (GB) stations 51 and 53 (n = 2). The mean value is presented from all data in each region with the standard deviation in parentheses. Fluxes were calculated using seasonally averaged QuikSCAT winds, by taking an average of the wind speed (measured twice daily) at the position of each ΔfCO_2 value, and the Nightingale et al. (2000) relationship. Tg C is 10^{12} g C.

	HNLC	*ACC*	*NSR*	*GB*	*Total*
Latitude	-58.0/-55.5	-55.5/-54.5	-54.5/-53.5	-53.5/-51.5	
Longitude	-45.0/-37.0	-44.0/-40.0	-40.0/-35.0	-42.0/-37.0	
Area (10^3 km^2)	124	28	36	80	268
Time (days)	90 (14)	90 (14)	90 (14)	90 (14)	
MLD (m)	56 (2)	61 (0)	67 (2)	27 (12)	
$[chl\text{-}a]_{100\ m}$ (mg m^{-2})	11.6 (0.5)	84.9 (0.0)	123.9 (69.8)	215.0 (29.2)	
DIC_{summer} (μmol kg^{-1})	2157 (5)	2120 (0)	2120 (8)	2094 (8)	
DIC_{winter} (μmol kg^{-1})	2191 (0)	2165 (0)	2181 (10)	2192 (3)	
ΔDIC (μmol kg^{-1})	-34 (5)	-45 (0)	-61 (15)	-98 (5)	
DIC deficit (mol m^{-2})	2.2 (0.3)	2.4 (0.0)	2.8 (0.3)	4.6 (0.8)	
Total DIC deficit (Tg C)	3.2 (0.4)	0.8 (0.0)	1.2 (0.1)	4.4 (0.8)	9.7 (0.9)
ΔfCO_2 (μatm)	16 (5)	-61 (0)	-59 (12)	-96 (35)	
CO_2 flux (mmol m^{-2} d^{-1})	2.6 (0.9)	-10.3 (0.0)	-9.2 (1.8)	-15.1 (5.7)	
CO_2 flux (mol m^{-2})	0.23 (0.1)	-0.9 (0.1)	-0.8 (0.2)	-1.4 (0.6)	
Total CO_2 flux (Tg C)	0.3 (0.1)	-0.3 (0.0)	-0.4 (0.1)	-1.3 (0.5)	-1.7 (0.5)

6.11. HNLC waters upstream of South Georgia

Satellite measurements of chlorophyll-a have greatly improved the understanding of phytoplankton dynamics by enhancing the spatial and temporal coverage of data that already existed from shipboard surveys (Korb et al., 2004). Monthly MODIS composite images from October 2007 to March 2008 indicated low phytoplankton activity at stations 30 and 33 in the central ACC (Figs. 6.2 and 6.4f). However, shipboard data collected along this part of the transect in January 2008 revealed deep chlorophyll-a maxima (DCM) at both stations at about 70 m (Fig. 4.6). This is not an uncommon occurrence in open waters of the ACC (Holm-Hansen, 2004a; Holm-Hansen et al., 2005; Whitehouse et al., 2008). Depth integrated chlorophyll-a to 100 m at these stations was 11.6 ± 0.5 mg m^{-2}, showing that these stations held a small standing stock of phytoplankton (Table 6.5). Compared to the Winter Water, all three macronutrients had been reduced in the upper water column, with depletions in silicate of 20-30 μmol kg^{-1} (Tables 6.2 and 6.3). This is consistent with observations of increased diatom abundance north of the SB (Korb et al., 2010). The presence of phytoplankton in this region had reduced summer DIC concentrations by 34 ± 5 μmol kg^{-1} and created a sizable DIC deficit of 2.2 mol m^{-2} by January (Table 6.5). Sea surface fCO_2 did not reflect this modest phytoplankton activity as surface water warming counteracted the biological carbon uptake (Fig. 6.6a).

However, based on surface distributions of fCO_2, DIC, macronutrients and chlorophyll-a this region represented unproductive waters compared to the northern ACC, NSR and the GB. The standing stocks of chlorophyll-a were the lowest observed for the whole AAZ. Henceforth, the relatively unproductive site in the central ACC was classified as HNLC waters (stations 30 and 33) and the most productive sites in the core of the South Georgia bloom (stations 51 and 53), with a continuum of phytoplankton activity in between, especially in the northern ACC (station 37) and over the NSR (stations 43, 44, 46 and 48). Low, but persistent, phytoplankton activity in moderate mixed layer depths of 55-57 m appeared unproductive by satellite detection (Fig. 6.2). It has been suggested that satellite chlorophyll-a concentrations underestimate sea surface chlorophyll-a and marine productivity in this region (Schlitzer, 2002; Korb and Whitehouse, 2004).

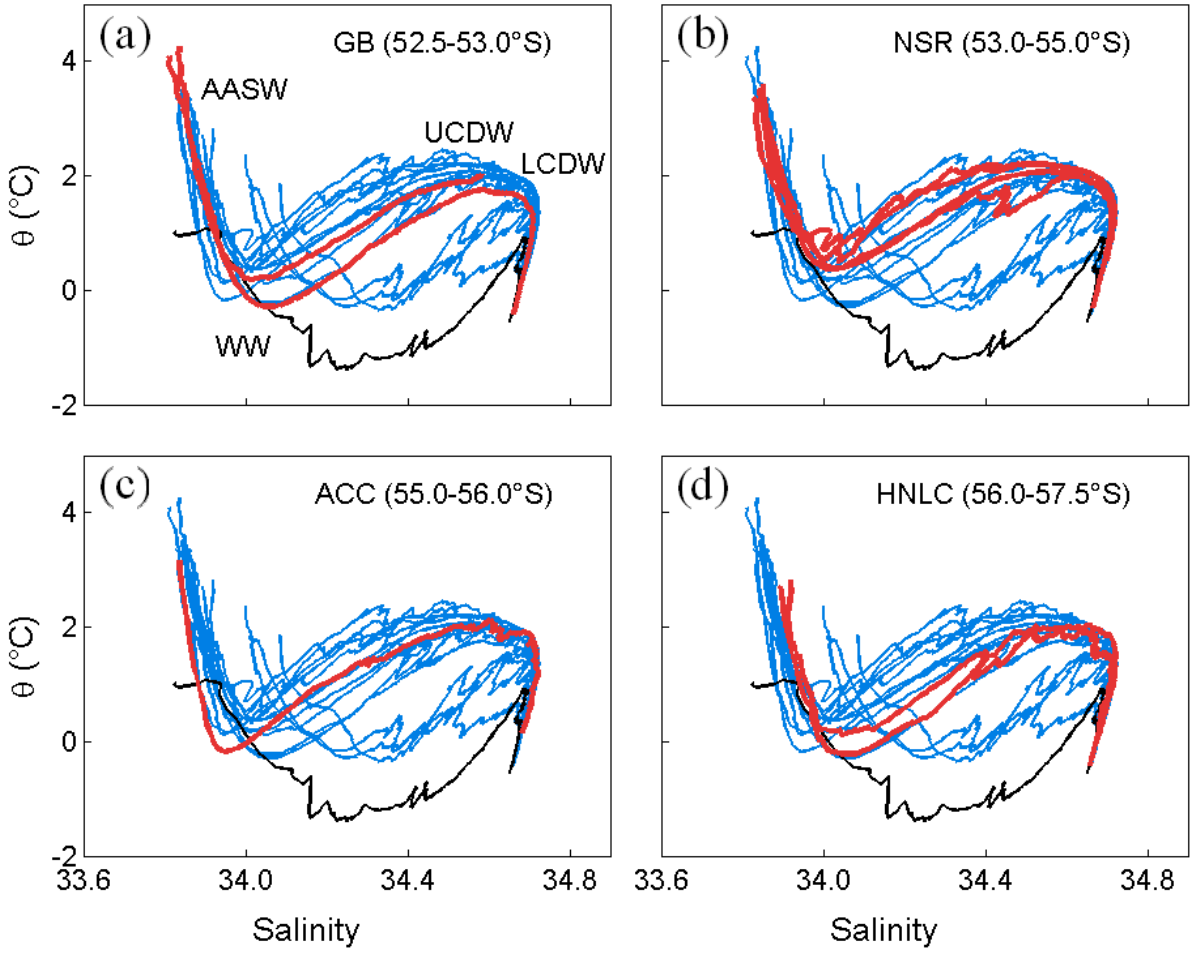

Figure 6.8. Potential temperature (θ, °C) as a function of salinity for the 16 hydrographic stations in the Antarctic Zone (blue). Highlighted profiles (red) indicate station groups (a) Georgia Basin (GB) stations 51 and 53, (b)North Scotia Ridge (NSR) stations 43, 44, 46 and 48, (c) ACC station 37 and (d) HNLC stations 30 and 33. The temperature-salinity profile for the Southern Boundary (station 21) is highlighted in black to indicate the transition into waters of the Weddell-Scotia Confluence. Identified water masses (a) are Antarctic Surface Water (AASW), Upper Circumpolar Deep Water (UCDW), Lower Circumpolar Deep Water (LCDW) and Winter Water (WW) after Meredith et al. (2003b) and Naveira Garabato et al. (2002a).

6.12. Phytoplankton blooms of the ACC

In contrast to the HNLC waters, satellite and shipboard surface chlorophyll-a concentrations identified elevated phytoplankton biomass in the northern ACC on 25 January (station 37) (Figs. 6.2 and 6.4f). Chlorophyll-a concentrations approached bloom conditions at 1.93 mg m^{-3} with a subsequent decrease in all three macronutrients, most notably silicate by over 30 μmol kg^{-1} compared to the HNLC stations (Table 6.2). This was accompanied by a reduction in mixed layer DIC by over 30 μmol kg^{-1} and surface water fCO_2 by nearly 60 μatm (Table 6.4), despite an increase in sea surface temperature of up to 0.59 °C (Table 6.2). These conditions created a patch of CO_2 undersaturation (Fig. 6.6a) and a strong sink of atmospheric CO_2 of -10.3 ± 0.0 mmol m^{-2} day^{-1} (Table 6.5).

Station 37 is located just south of the NSR, with a meander in the SACCF to the east and detrainment from a PF jet approaching from the west (Fig. 6.2). The influence of the SACCF can be seen in the potential temperature-salinity profile as compared to waters over the NSR, cooler, more saline water mixed within the UCDW, below the θ_{min} (Fig. 6.8c). The close proximity to frontal waters on either side could provide a source of nutrients and iron to the surface and influence the carbonate characteristics at this location, through biological utilization of DIC and/ or advection. It is hypothesised that this enhancement of production was due to localised iron enrichment, from either atmospheric or oceanic origin, where concentrations of dFe were 0.05 nM (Fig. 6.4e). Potential source regions of aeolian iron-rich dust are the arid and semi-arid areas of Patagonia, South America (Fung et al., 2000). Comparisons of aerosol optical depth, chlorophyll-a and simulated dust deposition revealed a strong correlation between aeolian derived iron and phytoplankton productivity in surface waters of the ACC (40-60°S) downwind from Patagonia (Erickson et al., 2003). However, atmospheric inputs are estimated to be small in the Southern Ocean (Jickells et al., 2005), although few data currently exist in this region. Oceanic sources are most likely and include advection (Nolting et al., 1991; Johnson et al., 1999; Sanudo-Wilhelmy et al., 2002; Dulaiova et al., 2009; Ardelan et al., 2010) and mesoscale frontal dynamics (Naveira Garabato et al., 2002b; Strass et al., 2002).

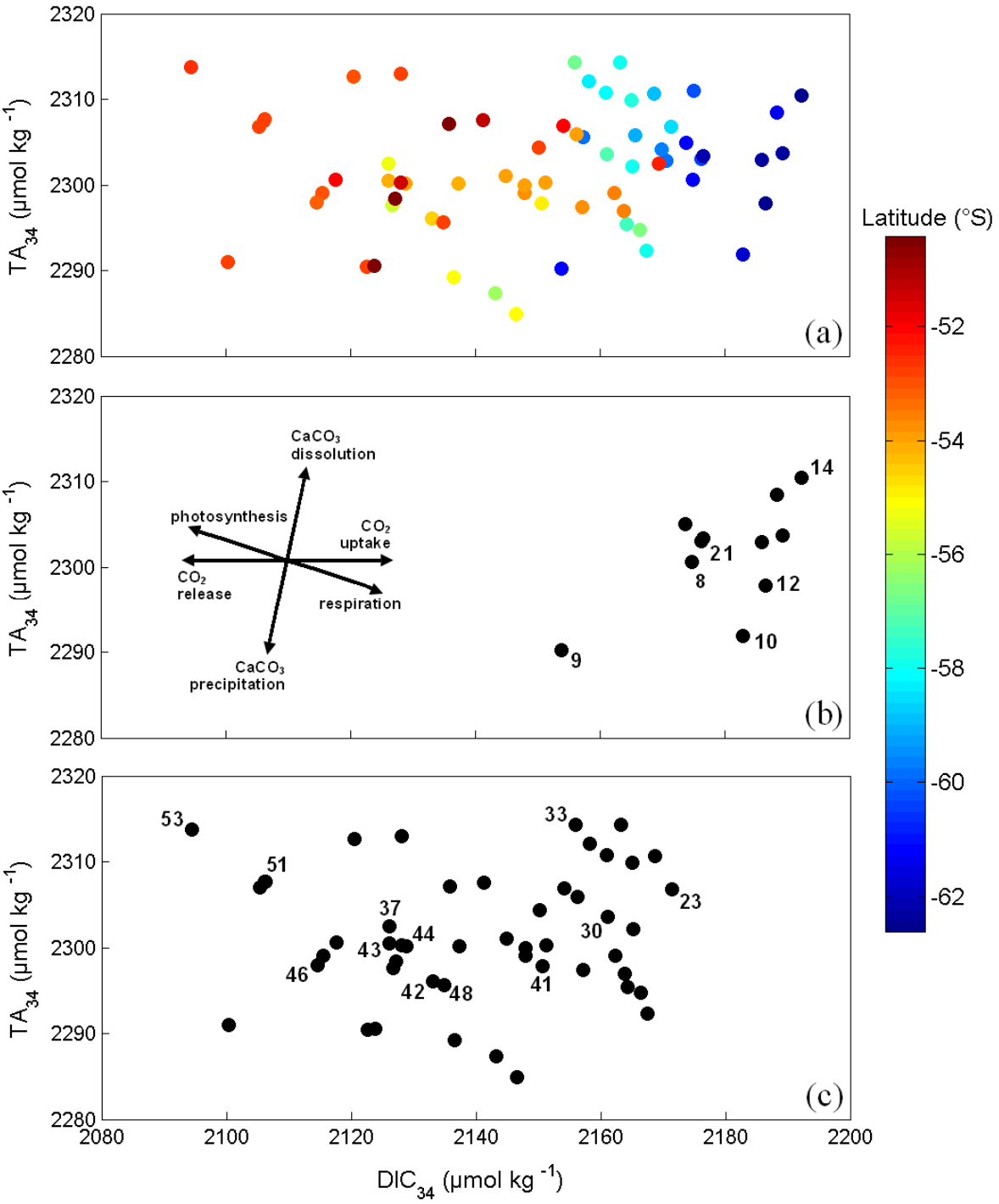

Figure 6.9. Hydrographic station (5 m sample) and underway sea surface normalised alkalinity (TA_{34}, µmol kg^{-1}) as a function of sea surface normalised dissolved inorganic carbon (DIC_{34}, µmol kg^{-1}) collected during cruise JR177 for (a) all samples, coloured according to latitude, (b) samples in the Weddell-Scotia Confluence and (c) samples from the Antarctic Zone. Key hydrographic stations are identified. The theoretical trends (b, insert) show the variation of DIC_{34} and TA_{34} with respect to certain biogeochemical processes, adapted from Zeebe and Wolf-Gladrow (2001).

6.13. The South Georgia bloom

The marine carbon cycle varied considerably upstream, in the HNLC waters, and downstream of South Georgia, in the GB, during summer 2008 (Figs. 6.4-6.7). Extensive phytoplankton blooms covered the GB and biological carbon uptake reduced DIC and fCO_2, creating a substantial sink for atmospheric CO_2 (Table 6.5). Inspection of temperature-salinity profiles (Fig. 6.8) indicated the presence of the same water masses at HNLC stations (30 and 33) and at South Georgia bloom stations (51 and 53), with comparable winter mixed layer characteristics (Table 6.3). Stations 30 and 33 were therefore selected as suitable unproductive sites in order to investigate the effects of the South Georgia bloom on the marine carbon cycle of the Scotia Sea.

The circulation features of the PF and SACCF in the vicinity of the NSR are governed by the bathymetry and in turn greatly influence the structure of the phytoplankton bloom in the GB (Figs. 6.1 and 6.2). The South Georgia bloom was initiated in October 2007 and reached maximum intensity in January 2008 (Fig. 6.5). The most intense patch of chlorophyll-a was confined to the GB where shipboard measurements indicated a summer maximum of 11.14 mg m^{-3} (Table 6.4), which is of comparable magnitude to South Georgia blooms in austral summer 2000, 2002, 2003, 2005 (Holm-Hansen et al., 2004b; Korb et al., 2004; Korb et al., 2008). Bloom duration (90 days) is likely to influenced by, among other factors, water column stability, which is largely controlled by circulation features of the GB and the long residence time of water at this location (Brandon et al., 2000; Meredith et al., 2005). Warm sea surface temperatures (Fig. 6.4a) and shallow mixed layers (Table 6.2) increased the water column stability in the GB and promoted phytoplankton activity.

Previous studies in the South Georgia bloom during three austral summers (2002, 2003 and 2005) found that the euphotic depths were equal to or deeper than the MLD, indicating that light is not usually limiting for phytoplankton growth in this region during the summer (Korb et al., 2008). Chlorophyll-a concentrations were high in the upper water column across the GB (Fig. 4.6), with a high standing stock of chlorophyll-a of 215.0 ± 29 mg m^{-2} in the top 100 m (Table 6.5). Comparable phytoplankton stocks of 295.0 ± 50 mg m^{-2} were measured in the upper 100 m of the GB in summer 2003 (Korb et al., 2005). Silicate had become completely exhausted in the mixed layer (Table 6.2), consistent with the presence of a diatom dominated bloom (Korb et al., 2010).

A distinct latitudinal trend can be observed for salinity normalised DIC (DIC_{34}), where concentrations were highest in the south (Fig. 6.9a). The lowest DIC_{34} values occurred at around 53°S, downstream of South Georgia in the GB. The distribution in TA_{34} shows that a range of values were observed at all latitudes in contrasting regions. Data collected in the Weddell-Scotia Confluence (WSC) are included for comparison (Fig. 6.9b) and are discussed in Chapter 5.

Summer biological carbon uptake in the South Georgia bloom had reduced winter DIC by 98 ± 5 μmol kg^{-1}, representing a factor three increase in the seasonal DIC depletion compared to the HNLC waters (Table 6.5). This was accompanied by substantial CO_2 undersaturation of 96 ± 35 μatm (Fig. 6.6a). Comparisons of DIC deficits and air-sea CO_2 fluxes in upstream and downstream waters gives a further indication of the effect of South Georgia bloom on the marine carbon cycle of the Scotia Sea. Although the HNLC region was an oceanic CO_2 source of 2.6 ± 0.9 mmol m^{-2} day^{-1}, a DIC deficit of 2.2 ± 0.3 mol m^{-2} existed in the upper 100 m through modest biological activity (section 6.11). The DIC deficit increased two-fold to 4.6 ± 0.8 mol m^{-2} in waters downstream of South Georgia, creating the largest summertime CO_2 sink of -15.1 ± 5.7 mmol m^{-2} day^{-1}. Air-sea exchange resupplied the summer mixed layer with 1.4 ± 0.6 mol m^{-2} of atmospheric CO_2 in the core of the South Georgia bloom over the 90 day duration. This corresponded to 30% of the DIC deficit that had been created during the summer. This resupply of DIC is higher than the 23-24% determined for the bloom downstream of the Crozet islands (Bakker et al., 2007), highlighting the strength of the South Georgia bloom in atmospheric CO_2 uptake.

Previous shipboard campaigns (Korb et al., 2008; Whitehouse et al., 2008) and satellite chlorophyll-a data (Korb et al., 2004) indicated that the South Georgia bloom is a recurrent feature and hence, based on this research, a total of 1.3 ± 0.5 Tg C is transferred from the atmosphere to the ocean each summer. However, the DIC deficit observed in early February (Table 6.1) is likely to persist after decay of the bloom, which was determined to occur in March from inspection of satellite derived chlorophyll-a concentrations (Fig. 6.5). Further oceanic uptake of atmospheric CO_2 would take place in the ensuing DIC deficit, thereby enhancing the seasonal biological carbon uptake (determined above) downstream of South Georgia.

Elevated concentrations of dFe, up to 1.17 nM, in surface waters of the bloom, compared to the rest of the AAZ, provided further evidence for natural iron fertilisation downstream of South Georgia (Fig. 6.4e). As surface waters were depleted in silicate, continuation of the diatom bloom was only possible by nutrient replenishment or a shift in community structure to non-siliceous species. If seeding by iron and/ or silicate is a key factor then sources included upwelled waters of the ACC flowing over the NSR, interaction of the SACCF with other bathymetric features and run-off from South Georgia (Korb and Whitehouse, 2004; Korb et al., 2004; Ward et al., 2002; Whitehouse et al., 2008).

Bathymetric features such as the NWGR have been implicated in enhanced meandering and eddy shedding of the SACCF, advecting nutrients across the frontal boundary and retaining circulating waters in the GB for several months (Thorpe et al., 2002). The long residence times of water over the GB would allow iron to be supplied to the upper ocean prior to the growing season. The spatial and temporal dynamics of the bloom indicated that iron enrichment from Patagonian dust deposition is not a major control on enhanced biological productivity downstream of South Georgia (Meskhidze et al., 2007) and the oceanic iron sources and dominant. However, the limited data in this region highlight the importance of detailed iron measurements in the vicinity of South Georgia (ongoing investigation).

6.14. Southern Ocean blooms and CO_2 uptake

6.14.1. Island blooms

The impact of Southern Ocean island blooms on the marine carbon cycle can be examined by comparing waters within the bloom and waters remote from it (Bakker et al., 2007; Jouandet et al., 2008; section 6.13). Enhanced marine productivity and biological carbon uptake has been observed downstream of the sub-Antarctic islands of Crozet (45.5-47.0°S 49.0-53.0°E) and Kerguelen (48.5-49.7°S 68.5-70.5°E) during austral spring and summer (Bakker et al., 2007; Jouandet et al., 2008) (Fig. 6.10).

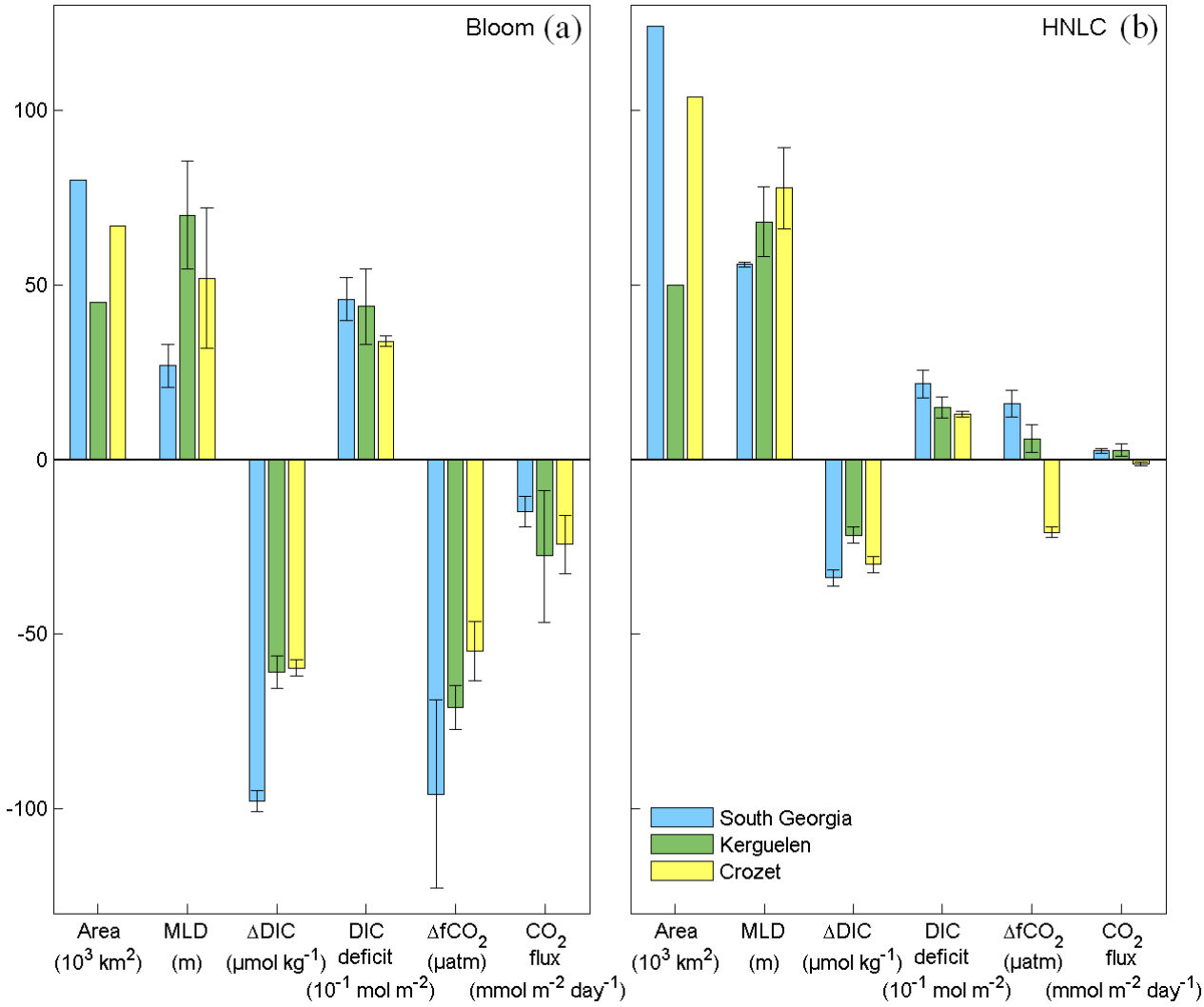

Figure 6.10. Area (km^2), mixed layer depth (MLD, m), seasonal change in dissolved inorganic carbon (ΔDIC, μmol kg^{-1}), DIC deficit (mol m^{-2}), Δ*f*CO_2(sea-air) (μatm) and the CO_2 flux (mmol m^{-2} d^{-1}) for (a) core bloom and (b) high-nutrient low-chlorophyll (HNLC) regions at South Georgia (this research), Kerguelen Island (Jouandet et al., 2008) and the Crozet islands (Bakker et al., 2007). DIC deficit is the average summer deficit in DIC for the upper 100 m (South Georgia and Crozet) and relative to the temperature minimum (Kerguelen).

The contrasting upstream, HNLC waters for the three islands showed summer depletion in DIC, which has been attributed to low but persistent marine productivity in sub-surface waters (Bakker et al., 2007; section 6.11). This highlighted the limitation of using satellite derived surface chlorophyll-a alone as an indicator for productivity and associated biological carbon uptake. Despite summer reductions in DIC, sea surface *f*CO_2 was close to the atmospheric

value for each of the unproductive sites and HNLC waters upstream of South Georgia and Kerguelen were slight sources of CO_2 of 2.6-2.7 mmol m^{-2} day^{-1} (Fig. 6.10b).

Compared to the blooms associated with Crozet and Kerguelen, biological carbon uptake in the South Georgia bloom utilised up to 40 μmol kg^{-1} more DIC during the summer, creating the largest DIC deficit of 4.6 ± 0.8 mol m^{-2} (Fig. 6.10a). The DIC deficit appeared to increase with decreasing latitude. Subsequently, the fCO_2 undersaturation in the South Georgia bloom is greater by 76 and 40% compared to Crozet and Kerguelen blooms, respectively.

The spatial and temporal characteristics of the South Georgia bloom is similar to that observed at Kerguelen (Blain et al., 2007) and evidence suggests that it is also sustained by an iron supply, which becomes rapidly exhausted by the resident diatom community (Korb et al., 2008; Korb et al., 2010). With the greatest spatial coverage (80,000 km^2), combined with long duration (90 ± 14 days), the South Georgia bloom created the largest summer DIC deficit of 4.4 ± 0.8 Tg C, in comparison to the blooms of Kerguelen (2.4 ± 1.0 Tg C) and Crozet (2.7 ± 0.1 Tg C), and subsequently removed 1.3 ± 0.5 Tg C from the atmosphere.

6.14.2. A Southern Ocean perspective

In the context of other blooms in the Southern Ocean, only the Ross Sea (Bates et al., 1998; Sweeney et al., 2000) had a greater seasonal DIC deficit compared to South Georgia to date (Table 6.6). It must be noted, however, that DIC deficits determined at the height of the growing season (January-February) are expected to be larger than those measured at the beginning (October) and at the end (March). Data in Table 6.6 and timeseries studies (Sweeney et al., 2000) show this to be largely true.

Table 6.6. (page 201) The location, year, month, mixed layer depth (MLD, m), ΔfCO_2(sea-air) (μatm) and DIC deficit (mol m^{-2}) for a selection of phytoplankton blooms in the Southern Ocean. Method for determination of DIC deficit: [1]DIC deficit in the upper 100 m, [2]DIC deficit relative to the temperature minimum, [3]DIC deficit in the summer mixed layer, [4]net community production, [5]from nitrate deficits relative to the temperature minimum. No data is represented by -.

Location	*Year*	*Month*	*MLD*	ΔfCO_2	*DIC deficit*	*Reference*
			m	*µatm*	*mol* m^{-2}	
Weddell Sea	1972	Jan	60/110	-	1.7[5]	Jennings et al. (1984)
(60°S 0°W)						
Pacific sector	1992	Feb-Mar	-	-	2.5[4]	Minas and Minas (1992)
(48-62°S 65°E)						
Polar Front	1992	Nov	80	-21	1.4[4]	Bakker et al. (1997)
(47-60°S 6°W)						
Seasonal ice zone	1993	Feb-Mar	40/60	-	0.9/3.7[3]	Ishii et al. (1998)
(63-69°S 30-150°E)						
Casey Bay	1993	Feb	-	-	1.7/2.8[3]	Ishii et al. (1998)
(69°S 40°E)						
Prydz Bay	1993	Feb-Mar	5	-250	1.3/4.0[3]	Ishii et al. (1998)
(70°S 70-80°E)						Gibson and Trull (1999)
Pacific sector	1994	Sept-Mar	25/65	-1/-18	0.8-2.8[4]	Rubin et al. (1998)
(67-70°S 110-170°E)	1995					
Ross Sea	1994	Oct-Feb	10/80	-80/-150	1.2/10.8[1]	Bates et al. (1998)
(74-78°S 163-187°E)	1995					Sweeney et al. (2000)
Marginal ice zone	1994	Dec-Jan	10/20	-35	0.3/2.5[2]	Ishii et al. (2002)
(64-65°S 140°W)	1995					
Scotia Sea	2001	Dec	30/70	-8/-13	1.0/1.2[4]	Shim et al. (2006)
(57-60°S 52°W)						
Weddell Sea	2003	Jan	-	-	2.0[2]	Geibert et al. (2010)
(54-66°S 17-23°E)						
Crozet islands	2004	Nov-Dec	22/85	-55	3.4[1]	Bakker et al. (2007)
(45-47°S 49-53°E)						
Kerguelen Island	2005	Jan-Feb	70	-71	4.4[2]	Jouandet et al. (2008)
(50-52°S 70-74°E)						
Weddell Sea	2005	Mar	-	-	1.1/2.3[2]	Hoppema et al. (2007)
(63-70°S 16-46°W)						
South Georgia	2008	Feb	27	-96	4.6[1]	this research
(52-54°S 38-42°W)						

6.15. Conclusion

The impact of the South Georgia phytoplankton bloom on the marine carbon cycle of the Scotia Sea has been investigated during summer 2008. Shipboard and satellite surface chlorophyll-a concentrations were used to determine the location of stations within the core of the bloom and stations that represented HNLC waters. Data collected during cruise JR177 illustrated some of the limitations of using satellite chlorophyll-a as an indicator of marine productivity. The 'unproductive' HNLC stations held a small standing stock of chlorophyll-a and had a summer DIC deficit of 2.2 ± 0.3 mol m^{-2}. This suggests that HNLC waters of the ACC are more productive than perceived, as suggested by Bakker et al. (2007).

Extensive diatom blooms covered the GB by summer and are closely constrained by the bathymetry of the region. DIC deficits in the upper 100 m doubled from 2.2 ± 0.3 mol m^{-2} upstream to 4.6 ± 0.8 mol m^{-2} downstream of the South Georgia. The substantial biological carbon uptake created an oceanic sink for atmospheric CO_2 of 15.1 ± 5.7 mmol m^{-2} d^{-1}, corresponding to a total transfer of 1.3 ± 0.5 Tg C from the atmosphere to the upper ocean during summer 2008.

Sea surface distributions of iron across the AAZ provided evidence for natural iron fertilisation downstream of South Georgia. This scenario is very similar to the naturally iron fertilised blooms of the sub-Antarctic islands of Kerguelen and Crozet. Despite smaller *in situ* CO_2 sinks due to slighter wind speeds, the South Georgia bloom was the strongest island bloom, ascribed to the largest bloom extent of 80,000 km^2 and long duration of 90 days. Across the entire bloom, the summertime DIC deficit in the upper ocean was 4.4 ± 0.8 Tg C, which superseded the blooms of Kerguelen (2.4 ± 1.0 Tg C) and Crozet (2.7 ± 0.1 Tg C).

For a total DIC deficit of 9.7 ± 0.9 Tg C along the Scotia Sea transect from 58.0-51.5°S, CO_2 uptake resupplied the upper ocean with 1.7 ± 0.5 Tg C. This emphasized the significance of the South Georgia bloom in the marine carbon cycle of this region, which accounted for 76% of the total uptake of atmospheric CO_2 in the Scotia Sea during summer 2008. In a Southern Ocean context, the summertime DIC deficit of the South Georgia bloom is the largest reported to date in non-ice covered waters of the Southern Ocean. A thorough investigation of natural iron enrichment is essential to fully understand the controls on phytoplankton biomass and biological carbon uptake in the complex environment of the Scotia Sea.

7. Seasonal variability in sea ice, blooms and carbonate chemistry: the role of the Scotia Sea in CO_2 uptake and ocean acidification

7.1. Abstract

Seasonal variations in the marine carbon cycle were investigated during austral spring 2006, summer 2008 and autumn 2009 along a 1,400 km transect in the Scotia Sea. Sea surface conditions present during the winter (2007) were inferred from parameters measured at the depth of the potential temperature minimum, within the Winter Water, during the summer (2008) occupation of the transect. The transect traversed through archetypal Southern Ocean environments: sea ice, hydrographic fronts, high-nutrient low-chlorophyll (HNLC) waters, waters of the Antarctic Circumpolar Current (ACC) and intense phytoplankton blooms downstream of islands and over submarine ridges. The first full seasonal cycle of sea surface fCO_2 for the Scotia Sea is presented. The marine carbon cycle of the Southern Ocean in autumn is particularly unknown (Stoll et al., 1999) and the autumn data collected during this research help to address this issue. The novel seasonal fCO_2 data allowed an assessment of the controls on the transition from winter CO_2 source to summer CO_2 sink and provided an insight into how the annual marine carbon cycle of the Southern Ocean might respond to future climate change.

Satellite derived chlorophyll-a and sea ice cover were used alongside *in situ* physical and biogeochemical observations to examine the processes that govern the seasonal variations in the marine carbon cycle. Maximum sea ice cover extended from 63° to 57°S during winter 2007 and thus defined the seasonal ice zone (SIZ) of the Scotia Sea. A strong correlation was observed between sea ice, ice edge phytoplankton blooms and subsequent undersaturation in sea surface fugacity of CO_2 (fCO_2). Moderate sea ice advance in winter and retreat by early spring set up conditions most favourable for phytoplankton blooms in the SIZ, transferring 1.01 ± 0.72 Tg C from the atmosphere to the ocean during the three month lifetime of a bloom in spring and summer 2006-2007. Oppositely, the weaker bloom that followed the 'icy' winter of 2007 removed less than 0.01 ± 0.17 Tg C from the atmosphere with termination of the bloom after one month. Prior to bloom development, the SIZ acted as a potential strong CO_2

source region due to the supersaturation of fCO_2 beneath the sea ice. During the spring thaw, initial break-up of the sea ice allowed strong CO_2 outgassing of up to 6.0 ± 2.7 mmol m^{-2} d^{-1}. The Southern ACC Front and the Southern Boundary became transient CO_2 sinks with the SIZ blooms that 'tracked' the southward retreating sea ice.

The HNLC waters were a steady CO_2 source of over 2.0-2.3 mmol m^{-2} d^{-1}, due to seasonal warming from summer to autumn. Downstream of the island of South Georgia, extensive phytoplankton blooms developed each year and extended across the Georgia Basin (GB), reaching maximum strength in summer. This corresponded to substantial fCO_2 undersaturation and created the strongest seasonal sink for atmospheric CO_2 in the Scotia Sea of 12.0 ± 4.2 mmol m^{-2} d^{-1} during summer. The effect of the Scotia Sea blooms dominated the summertime air-sea CO_2 flux to create a net CO_2 sink of 5.7 ± 1.4 mmol m^{-2} d^{-1}.

By the winter, the Scotia Sea was transformed into a CO_2 source of 2.9 ± 1.0 mmol m^{-2} d^{-1} due to increased vertical mixing and upwelling, bringing Circumpolar Deep Water rich in dissolved inorganic carbon to the surface. Concomitant low pH and carbonate ion concentrations, particularly south of 59°S and in the GB make these regions vulnerable to wintertime aragonite undersaturation, possibly by 2030-2040. Below the thermocline in the GB, the water column was undersaturated with respect to aragonite, presenting conditions of early ocean acidification to calcifyers south of the Polar Front.

The Scotia Sea from 62.6° to 49.5°S is a strong sink for atmospheric CO_2 of 6.2 ± 2.1 mmol CO_2 m^{-2} d^{-1} using seasonally averaged wind speeds and the Nightingale et al. (2000) parameterisation. The South Georgia bloom is a predictable element of this CO_2 sink, transferring an average of 1.01 ± 0.41 Tg C from the atmosphere to the upper ocean each summer. The large inter-annual variability in the SIZ appears to impose constraints on the CO_2 sink. Future climate change is likely to affect the sea ice-CO_2 relationship and the annual sinks of the SIZ could diminish. These observations emphasize the need to address seasonal variability in assessing the contribution of the Southern Ocean to the oceanic control of atmospheric CO_2. The mosaic patterns in sea surface carbonate chemistry of the Scotia Sea create a natural mesocosm to infer the effects of seasonal variability on the distributions of air-sea CO_2 fluxes, pH and aragonite undersaturation for the contemporary and future Southern Ocean.

7.2. Introduction

The Southern Ocean is a complex region of physical, chemical and biological processes that have a large influence on the global marine carbon cycle but, compared to other ocean basins, remains relatively undersampled (Takahashi et al., 2009). The Scotia Sea, between the Weddell Sea to the south and the Polar Front (PF) to the north, epitomises the diverse environments of the Southern Ocean with the seasonal advance and retreat of sea ice, meandering hydrographic fronts, high-nutrient low-chlorophyll (HNLC) waters and waters of the Antarctic Circumpolar Current (ACC) in open ocean regimes, downstream of islands and over submarine ridges. The region is recognised as being important for the mixing of the deep water masses in the ACC (Naveira Garabato et al., 2002a) and as supporting valuable fisheries (Atkinson et al., 2001).

In contrast to the low productivity waters of the ACC entering the Scotia Sea from Drake Passage, areas of high productivity are regularly observed in spring and summer at the receding ice edge (Smith and Nelson, 1986; Kang et al., 2001; Korb et al., 2005), in frontal regions (Jacques and Panouse, 1991; Comiso et al., 1993; Helbling et al., 1993; Tynan, 1998; Holm-Hansen and Hewes, 2004; Hewes et al., 2008) and downstream of bathymetric features (Moore and Abbot, 2000; Blain et al., 2001; Holm-Hansen et al., 2005; Pollard et al., 2007; Sokolov and Rintoul, 2007). Through the action of the biological carbon pumps, substantial carbon uptake in surface waters occurred across the Scotia Sea (Chapter 4), particularly in the marginal ice zone (Chapter 5) and downstream of South Georgia (Chapter 6) in summer 2008. Sea ice cover, vertical mixing and upwelling of Circumpolar Deep Water present contrasting conditions in the upper ocean (Chapter 4) during winter, generating large seasonal changes in sea surface pH and aragonite saturation. Aragonite undersaturation poses considerable threats to calcifying species, such as pteropods, which are the major aragonite producers in the Southern Ocean (Honjo, 2004; Hunt and Hosie, 2006). Aragonite undersaturation in seawater augments the dissolution of aragonite concretions and reduces the ability of marine organisms to secrete aragonite during the construction of exoskeletons (Feely et al., 2004; Orr et al., 2005; Fabry et al., 2008).

With numerous crossings from October to May each year by RRS *James Clark Ross*, the Scotia Sea is an ideal 'mesocosm' to examine the contemporary marine carbon cycle across characteristic Southern Ocean regimes. This research investigates the seasonal cycling of inorganic carbon, air-sea CO_2 fluxes, pH and aragonite saturation, in waters with sea ice cover, HNLC conditions, extensive phytoplankton blooms and the frontal waters of the Southern Boundary (SB), the Southern ACC Front (SACCF) and the PF (Fig. 7.1). The Scotia Sea is established as a 'mosaic' of carbonate chemistry and the contribution to the Southern Ocean carbon cycle is determined and projections of future ocean acidification are made.

The 1,400 km transect across the Scotia Sea extended from 61.0°S at the South Orkney Islands to 49.5°S at the northern limit of the Antarctic Circumpolar Current (ACC) and the Antarctic Zone (AAZ). The transect was initiated by RRS *James Clark Ross* during the spring cruise JR161 (Table 7.1) in October-November 2006 from the South Orkney Islands (Fig. 7.1). The transect was repeated, and extended south to 62.6°S in the Weddell-Scotia Confluence (WSC) in January-February 2008, during the summer cruise JR177. The final occupation of the transect was conducted in March-April 2009, during the autumn cruise JR200.

Table 7.1. The core seasonal cruises of the Scotia Sea. Data from each season is presented in colour, as specified in the colour code, to enable easy identification in the Figures. Start and end dates refer to the initial and final sea surface datum. *Winter start and end dates are based on summer JR177 station dates, back-dated to winter 2007, as no cruise took place.

Season	*Cruise*	*Year*	*Colour code*	*Start date*	*End date*	*Hydrographic stations*
Spring	JR161	2006	Green	20 Oct	01 Dec	59
Winter	-	2007	Blue	08 Sept*	04 Oct*	24
Summer	JR177	2008	Yellow	02 Jan	17 Feb	59
Autumn	JR200	2009	Red	11 Mar	17 Apr	50

The lowest sea surface temperatures and deepest mixed layers occurred annually in September (section 2.14). Carbonate parameters measured from samples collected in the Winter Water (WW), at the depth of the potential temperature minimum, during summer 2008 were used as proxies for the preceding winter i.e. sea surface conditions along the transect during September (winter) 2007. The dates of the JR177 WW samples were used to derive 'start' and

'end' dates for the winter season: the first station (5, Table 2.2) on 8 January corresponded to the first WW data on 8 September 2007 and the final station (53, Table 2.3) on 4 February 2008 corresponded to the final WW data on 4 October 2007. The winter data completed the seasonal data set for Scotia Sea from 2006 to 2009. Each cruise is used to 'represent' conditions typical to a given season, specified here as winter (June, July, August), spring (September, October, November), summer (December, January, February) and autumn (March, April, May).

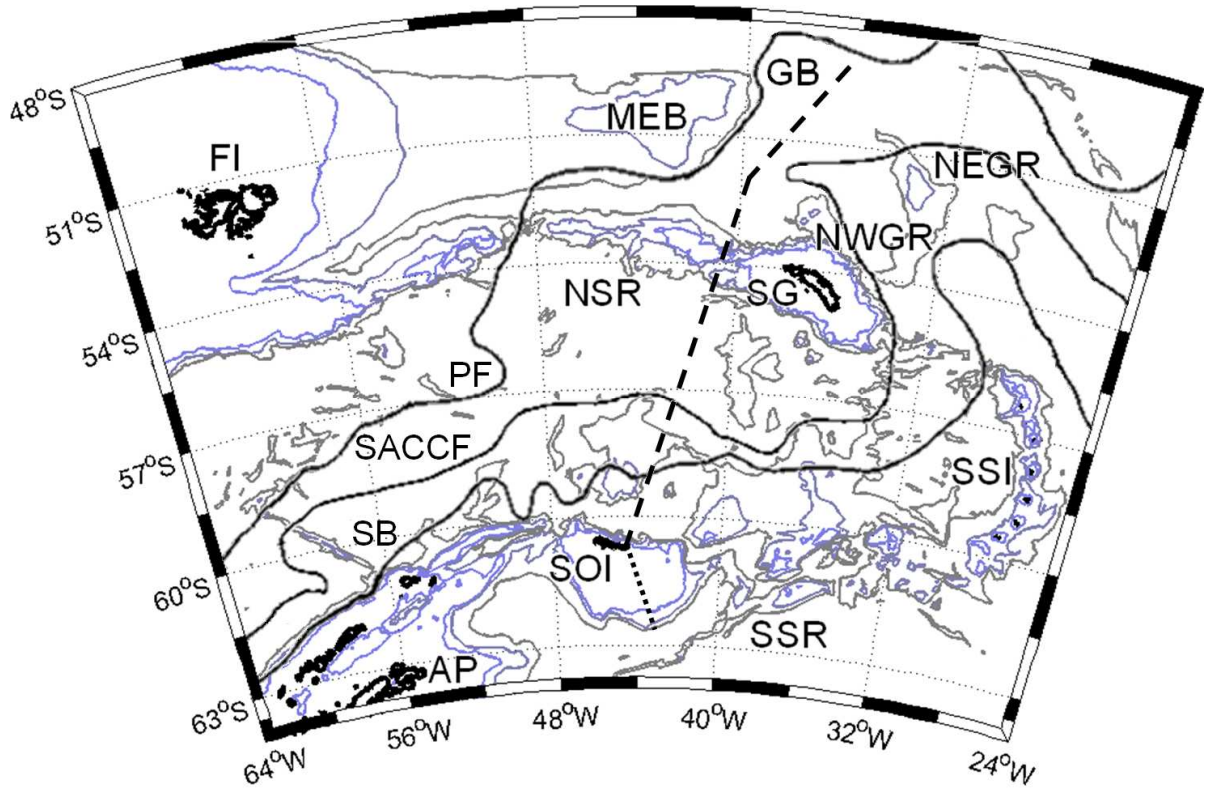

Figure 7.1. A schematic of the Scotia Sea showing the approximate location of the repeat transect (dashed line) and the extended transect (dotted line) from JR177. Some important topographic features are identified: Antarctic Peninsula (AP), South Orkney Islands (SOI), South Scotia Ridge (SSR), South Sandwich Islands (SSI), North Scotia Ridge (NSR), South Georgia (SG), Northwest Georgia Rise (NWGR), Northeast Georgia Rise (NEGR), Georgia Basin (GB), Maurice Ewing Bank (MEB) and the Falkland Islands (FI). Antarctic Circumpolar Current (ACC) fronts shown schematically, adapted from Meredith et al. (2003a): the Southern Boundary (SB, Orsi et al., 1995), Southern ACC Front (SACCF, Thorpe et al., 2002) and the Polar Front (PF, Moore et al., 1999). Depth contours are at 1000, 2000 and 3000 m (GEBCO, 2001).

Each cruise began from the Falkland Islands, where the ship sailed south in the direction of the South Orkney Islands to begin the northward transect, eventually passing to the northwest of South Georgia, up to the PF before returning back to the Falkland Islands (Fig. 7.1). During the seasonal cruises the ship sailed through ice covered waters, regions of substantial sea ice melt, frontal systems, open ocean regimes and intense phytoplankton blooms. Yearly composites of satellite chlorophyll-a (section 7.6.1) revealed an area of ocean in the central ACC that supported low levels of chlorophyll-a, < 0.2 mg m^{-3}, for most of the year. In relation to concentrations of nitrate and phosphate, this region is defined as having HNLC conditions, forming an unproductive band from 57.5°S to 56.0°S along the transect throughout the research period. In contrast, a large area of elevated chlorophyll-a was identified that persisted for up to eight months and extended across most of the Georgia Basin (GB) each year. This annual biological event is referred to as the South Georgia bloom (Chapter 6), forming a productive region north of the North Scotia Ridge (NSR) at 53.0-50.5°S along the transect.

The SB, SACCF and the PF were identified using vertical profiles of hydrographic data (Chapter 4) and sea surface dynamic height (Chapter 6) during summer cruise JR177. The SB was crossed at about 59°S and marks the transition from the WSC into waters of the ACC and the AAZ. The PF marks the northern limit of the AAZ, which is taken here as the northern limit of the Scotia Sea. Eight sub-regions of the Scotia Sea have thus been distinguished, defined by latitude along the transect: the Weddell-Scotia Confluence (62.6-59.5°S), the Southern Boundary (59.5-58.5°S), the Southern ACC Front (58.5-57.5°S), high-nutrient low-chlorophyll waters (57.5-56.0°S), the ACC (56.0-55.0°S), the North Scotia Ridge (55.0-53.0°S), the Georgia Basin (53.0-50.5°S) and the Polar Front (50.5-49.5°S). The data for each parameter in each region are commonly expressed as a mean, with accompanying standard deviation, of all the data within the specified latitudinal limits.

7.3. Hydrography

7.3.1. Winter 2007

The vertical location of the fronts was determined from potential temperature (θ) and salinity (*S*) profiles from the summer occupation of the transect (Chapter 4). Hydrographic properties of the WW layer are used as a proxy of surface conditions during the preceding winter. The WW properties are taken from the depth of the potential temperature minimum (θ_{min}), which

showed a northward gradient (Fig. 7.2b). The average θ_{min}, south of 59°S, was -1.55 ± 0.12 °C (n = 9), compared to the warmer, but more variable, average of 0.05 ± 0.31 °C (n = 10), north of 59°S to 50°S. Exceptions to this general trend were waters north of the NSR, where the value of the θ_{min} decreased to -0.29 °C in the central GB. Satellite SST data (section 2.13.3) showed the same general trend, with average winter SST of -1.77 ± 0.02 °C (n = 9), south of 59°S, and -0.93 ± 0.71 °C (n = 10), north of 59°S. The higher *in situ* temperatures of the WW compared to satellite derived sea surface temperature are likely to be due to bottom-up warming slightly eroding the θ_{min} along the thermocline, as discussed previously (section 5.3.7). Salinity decreased northwards, from the most saline waters, representing seasonal maxima of > 34.3, in the southern WSC to comparatively fresh waters (S < 33.9) north of 58°S (Fig. 7.2c). Across the Scotia Sea, a seasonal deepening of the mixed layer is indicative of increased vertical mixing in winter, up to depths of 130 m in the vicinity of South Georgia (Fig. 7.2f).

7.3.2. Spring 2006

Surface waters showed a strong northward gradient in sea surface temperature across the Scotia Sea with abrupt increases at the SACCF, the NSR and the PF (Fig. 7.2b). Close to the South Orkney Islands sea surface salinity had a large range from about 33.7 to over 34.1 (Fig. 7.2c). Salinity showed a general northward decrease with an abrupt freshening to the north of 58.5°S. Across the WSC and up to the SACCF, mixed layer depths ranged between 40 m and 80 m (Fig. 7.2f). The deepest mixed layers (> 120 m) were observed in the central ACC at about 55°S.

7.3.3. Summer 2008

Surface waters continued to warm from winter with a strong northward gradient and abrupt increases in temperature at the SB, the GB and the PF (Fig. 7.2b). Across the WSC, surface salinity showed a general northward increase (Fig. 7.2c). A notable exception to this trend was a sharp reduction in salinity to a seasonal minimum of < 33.4 over the South Scotia Ridge (SSR). Across the AAZ, salinity gradually decreased to 33.6 in the central part of the GB, where maximum seasonal freshening had occurred. Mixed layer depths ranged from about 20 m, south of 60°S and in the GB, to the deepest mixed layers close to 70 m over the NSR (Fig. 7.2f).

7.3.4. Autumn 2009

The warmest sea surface temperatures occurred during autumn, retaining a strong northward gradient from 0.5-1.0 °C over the SSR to over 7.0 °C close to the PF at 50°S (Fig. 7.2b). Surface salinity was largely non-trending and variable up to 57°S where it abruptly decreased (Fig. 7.2c). A seasonal minimum in sea surface salinity was observed across the AAZ before increasing in the GB. Mixed layer depths were very variable, ranging between 40 m and 80 m across the Scotia Sea (Fig. 7.2f). Although no distinct latitudinal trend was observed, the shallowest and deepest mixed layers were measured near the SB and the PF, respectively.

Figure 7.2. (page 211) The latitudinal distribution of sea surface (a) ΔfCO_2(sea-air) (μatm), (b) temperature (°C), (c) salinity, (d) iron (nM), (e) chlorophyll-a (chl-a, mg m^{-3}) and (f) mixed layer depth (MLD, m) during winter 2007 (blue), spring 2006 (green), summer 2008 (yellow) and autumn 2009 (red). The approximate location of the South Orkney Islands (SOI), Southern Boundary (SB), Southern ACC Front (SACCF), high-nutrient low-chlorophyll (HNLC) waters, the North Scotia Ridge (NSR), the Georgia Basin (GB) and the Polar Front (PF) are indicated. The latitudinal limits of the Weddell-Scotia Confluence (WSC) and the Antarctic zone (AAZ) are shown.

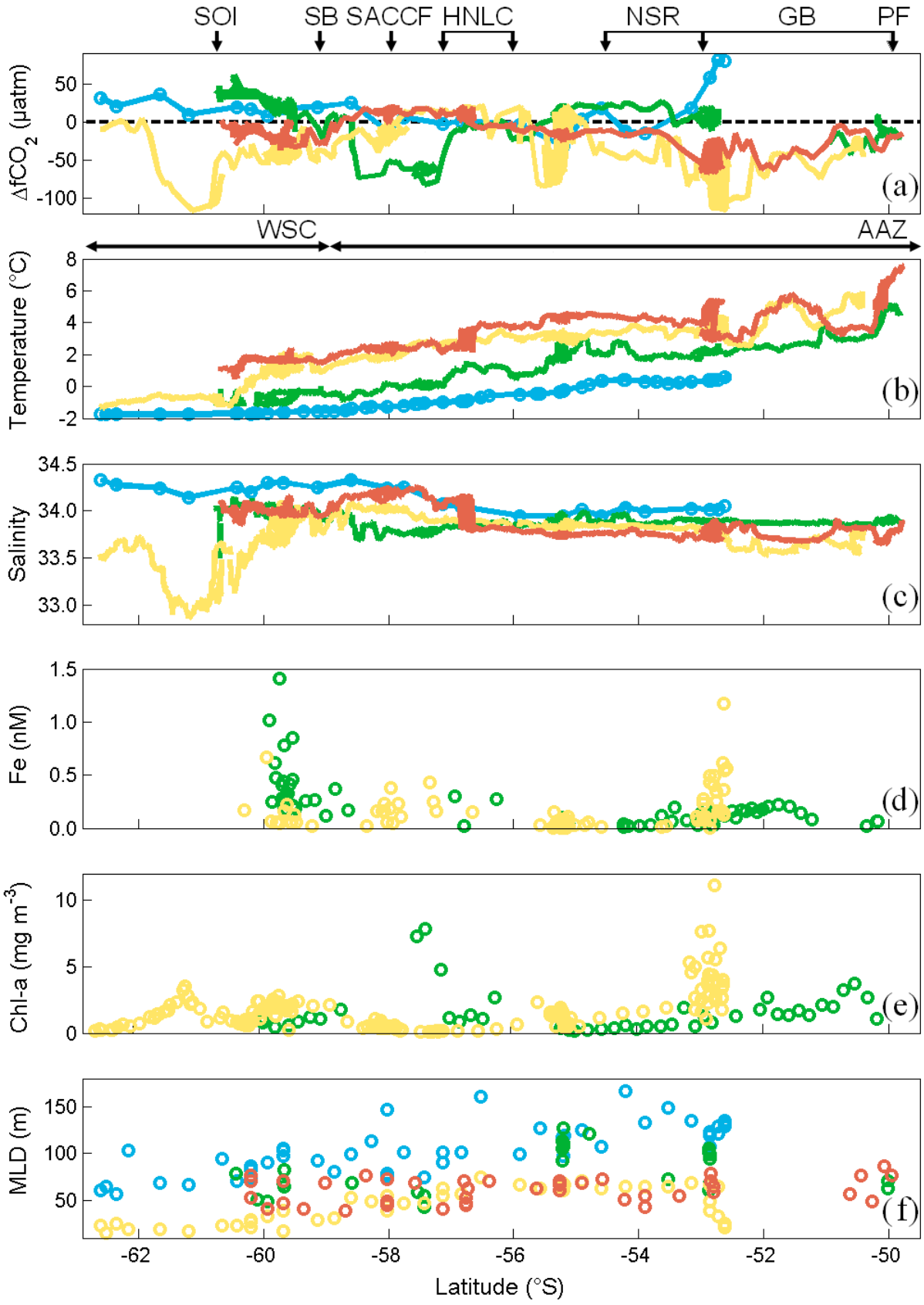
SOI
SB
SACCF
HNLC
NSR
GB
PF
ΔfCO2 (µatm)
50
0
-50
-100
(a)
WSC
AAZ
Temperature (°C)
8
6
4
2
0
-2
(b)
Salinity
34.5
34.0
33.5
33.0
(c)
Fe (nM)
1.5
1.0
0.5
0.0
(d)
Chl-a (mg m-3)
10
5
0
(e)
MLD (m)
150
100
50
(f)
-62
-60
-58
-56
-54
-52
-50
Latitude (°S)

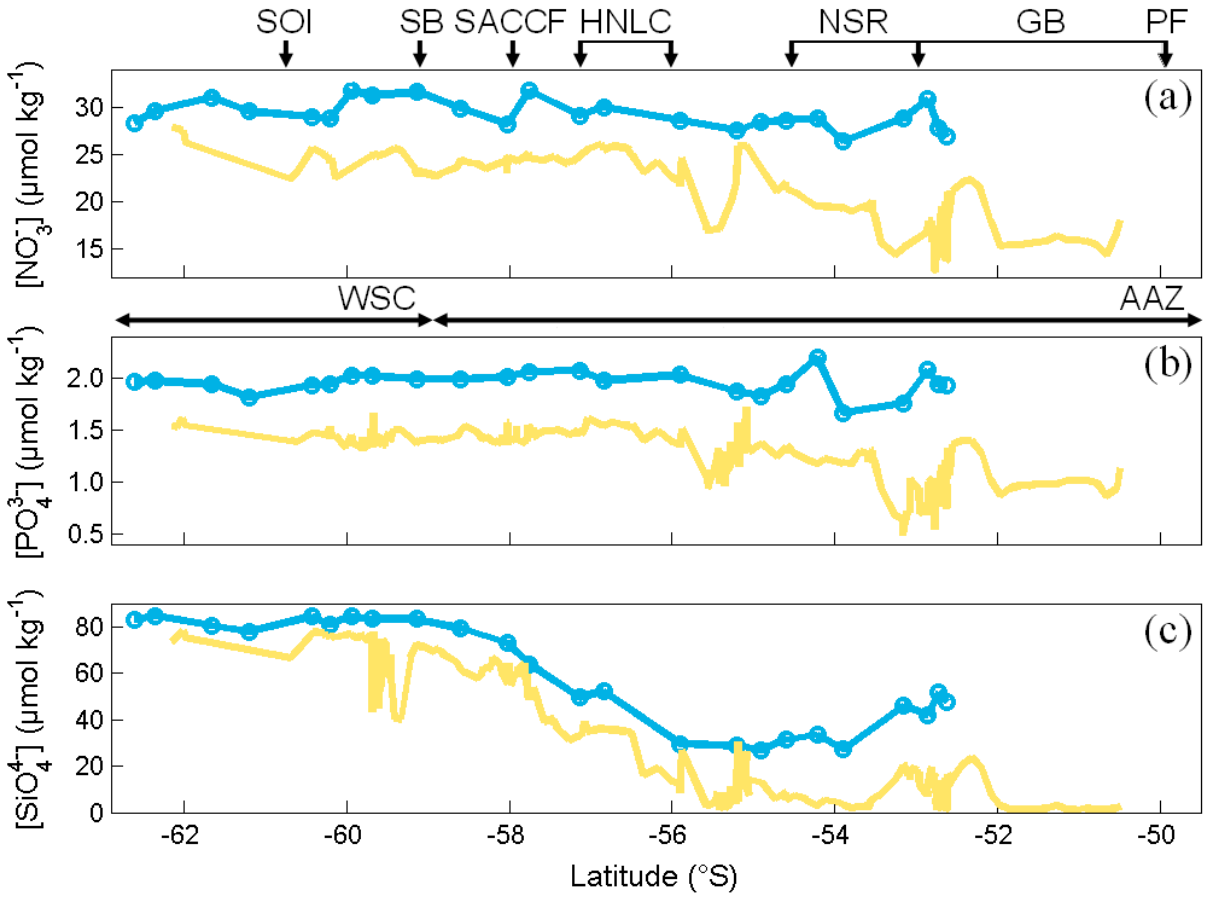

Figure 7.3. The latitudinal distribution of sea surface concentrations of (a) nitrate ($[NO_3^-]$, µmol kg^{-1}), (b) phosphate ($[PO_4^{3-}]$, µmol kg^{-1}) and (c) silicate ($[SiO_4^{4-}]$, µmol kg^{-1}) during winter 2007 (blue), spring 2006 (green), summer 2008 (yellow) and autumn 2009 (red). The approximate locations of bathymetry, fronts and hydrographic regions as in Figure 7.2.

7.4. Macronutrients

7.4.1. Winter 2007

Nitrate concentrations $[NO_3^-]$ displayed large variability across the Scotia Sea (Fig. 7.3a). Elevated concentrations (≥ 30 µmol kg^{-1}) were measured near the SB, the SACCF and at the NSR-GB boundary (53°S). In contrast, phosphate concentrations ($[PO_4^{3-}]$) were relatively homogenous at about 2.0 µmol kg^{-1} with localised increases over the NSR and in the lower GB (Fig. 7.3b). Silicate concentrations $[SiO_4^{4-}]$ across the WSC were 82.4 ± 2.3 µmol kg^{-1}, which decreased sharply across the SB to form a decreasing gradient reaching about 30 µmol kg^{-1} at 55°S (Fig. 7.3c). Similarly to $[NO_3^-]$ and $[PO_4^{3-}]$, $[SiO_4^{4-}]$ increased over the NSR and into the

central GB. These values are similar to winter values previously measured in the Scotia Sea (Whitehouse et al., 2008).

7.4.2. Summer 2008

Sea surface [NO_3^-] decreased across the Scotia Sea from 24-26 μmol kg^{-1} in the WSC to about 12 μmol kg^{-1} at the NSR-GB boundary (Fig. 7.3a). The [PO_4^{3-}] followed a similar trend, decreasing from 1.3-1.6 μmol kg^{-1} in the WSC to a 0.5 μmol kg^{-1} over the NSR (Fig. 7.3b). Similarly, [SiO_4^{4-}] decreased from high concentrations of 70-80 μmol kg^{-1} in the WSC to less than 1 μmol kg^{-1} in the GB (Fig. 7.3c). The concentration of all macronutrients reached seasonal minima in the NSR and GB regions.

7.5. Iron

7.5.1. Spring 2006

Surface concentrations of dissolved iron (dFe) showed a springtime maximum of 1.41 nM between 60°S to the SB at 59°S (Fig. 7.2d). Moderate concentrations of iron of 0.20-0.30 nM were observed at 57°S and in the lower GB at 53-52°S. The lowest concentrations, < 0.02 nM, were observed over the NSR.

7.5.2. Summer 2008

Elevated concentrations of iron, up to 0.67 nM, were observed between the South Orkney Islands and the SB (Fig. 7.2d). Concentrations remained moderately high at 0.20-0.40 nM in the vicinity of the SACCF up to 57°S. The lowest concentrations, < 0.01 nM, were observed over the NSR. High concentrations, > 0.50 nM, were observed north of 53°S reaching a summer time maximum of 1.17 nM in the lower GB.

7.6. Chlorophyll-a

7.6.1. Annual satellite chlorophyll-a

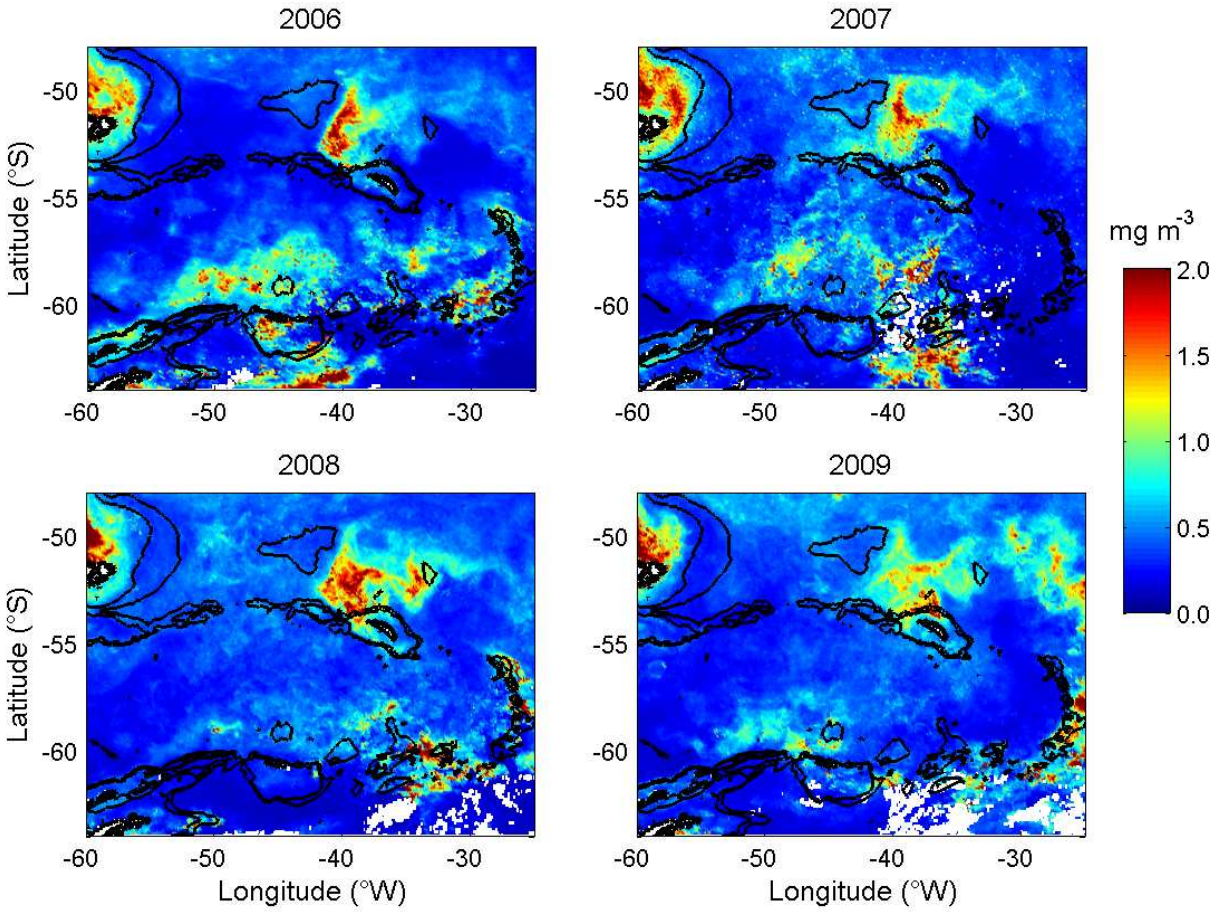

Figure 7.4. Yearly (January-December) composites of satellite chlorophyll-a (mg m^{-3}) for the Scotia Sea during 2006 (SeaWiFS/MODIS merged product), 2007 (SeaWiFS), 2008 (MODIS) and 2009 (MODIS). Depth contours are at 1000 and 2000 m (GEBCO, 2001) and for subsequent satellite images.

The SeaWiFS and MODIS satellites provided large-scale coverage of surface chlorophyll-a concentrations (section 2.13.2) in the Scotia Sea from 2006 to 2009 (Fig. 7.4). The satellite images revealed that the phytoplankton bloom to the northwest of South Georgia is a distinct biological feature, occurring on an annual basis with similar magnitude and duration. The core of the bloom (chlorophyll-a ≥ 2 mg m^{-3}) is largely confined within the GB, constrained by the NSR to the south, the MEB to the northwest, the Northeast Georgia Rise (NEGR) to the east and the Northwest Georgia Rise (NWGR) to the southeast (Fig. 7.1). Analysis of satellite chlorophyll-a during austral summer 2008 revealed a strong correlation to sea surface dynamic

height, illustrating the effect of the PF and SACCF on chlorophyll-a distributions in this region (Chapter 6). The surface expression of the PF was identified by a tightening of the contours of dynamic height along the eastern edge of MEB, before spreading out into the cyclonic circulation of the GB (Fig. 6.2). Similarly, the SACCF was identified following the edge of the NSR to the east, entering the GB behind South Georgia.

The satellite composite (2006-2009) images revealed the influence of the fronts on the structure of the South Georgia bloom as detrainment of elevated chlorophyll-a is observed to the north, along the PF at about 50°S, and to the east along the main path of the SACCF, looping around the NEGR (Fig. 7.4). This was most distinct in 2009, where a large portion of the bloom had been transported out of the GB along the meandering path of the PF and mixed with waters of the SACCF.

Elevated chlorophyll-a is also regularly observed south of about 57°S in the ACC, extending west-east across large parts of the Scotia Sea in some years. This is most pronounced downstream of the Antarctic Peninsula, over the SSR and within the waters of the SACCF and SB. These biological features show considerable inter-annual variability with large blooms across the ACC during 2006 and 2007 compared to the smaller blooms in the vicinity of the SB during 2008 and 2009. Other areas of enhanced chlorophyll-a are the shallow waters overlying the Falkland Island shelf and to the east in the waters around the South Sandwich Islands, in close proximity to the SB.

7.6.2. Seasonal satellite and shipboard chlorophyll-a

During summer 2005-2006 a bloom covered much of the GB, with advection within the PF and the SACCF to the east (Fig. 7.5). A second bloom developed in the ACC, within the SACCF and the SB, downstream of the Antarctic Peninsula. By autumn 2006, the ACC bloom had largely disappeared except for a small patch at about 60°S 50°W. The South Georgia bloom became concentrated to the east and west of the GB with little frontal advection. Much of the ACC maintained HNLC conditions. Sea ice and cloud cover obscured most of the sea surface from space during the winter months. By spring, a bloom developed at about 59°S that covered a large part of the AAZ with chlorophyll-a concentrations of at least 2.0 mg m^{-3}. Shipboard chlorophyll-a confirmed moderate concentrations of 0.5-1.0 mg m^{-3} north of the South Orkney Islands, which increased to about 1.8 mg m^{-3} at the SB and up to 7.9 mg m^{-3}

close to the SACCF during November 2006 (Fig. 7.2e). Satellite data indicated that waters downstream of South Georgia had low levels of chlorophyll-a (< 0.5 mg m^{-3}). However, shipboard chlorophyll-a measurements displayed a gradual increase over the NSR and across the GB to about 3.7 mg m^{-3} at the PF. The northern AAZ retained HNLC conditions, as suggested by both satellite and shipboard concentrations, of less than 0.2 mg m^{-3}.

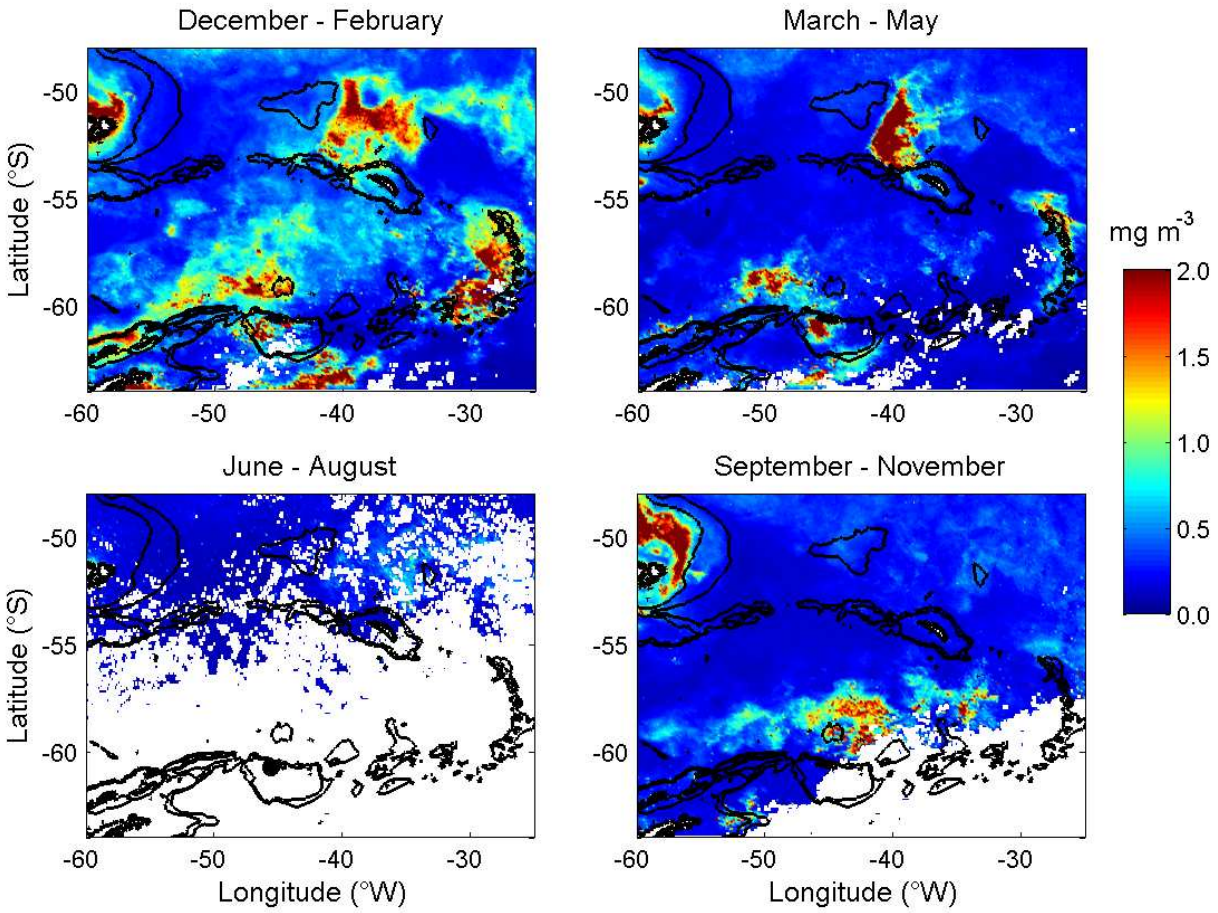

Figure 7.5. Seasonal composites of satellite chlorophyll-a (SeaWiFS/MODIS merged product) for the Scotia Sea during summer (December 2005-February 2006), autumn (March-May 2006), winter (June-August 2006) and spring (September-November 2006).

During summer 2006-2007 an intense bloom had developed in the GB, which became incorporated in the mesoscale features of the cyclonic circulation of the GB and the PF and SACCF (Fig. 7.6). The ACC bloom, from the preceding spring, peaked and persisted throughout the summer with latitudinal coverage from 54-60°S. Similarly, the South Georgia bloom maintained intensity, but less surface coverage compared to summer 2005-2006. Both blooms had substantially weakened by Autumn 2007. The Scotia Sea had persistent HNLC

conditions, in contrast to 2006 where the comparatively larger summer bloom had endured through to the autumn. As before, sea ice and cloud cover obscured most of the sea surface from space during the winter months. During spring 2007, a bloom had developed in the GB with plumes of enhanced chlorophyll-a following the frontal boundaries. By the end of the spring, a few localised patches of elevated chlorophyll-a were observed in the ACC.

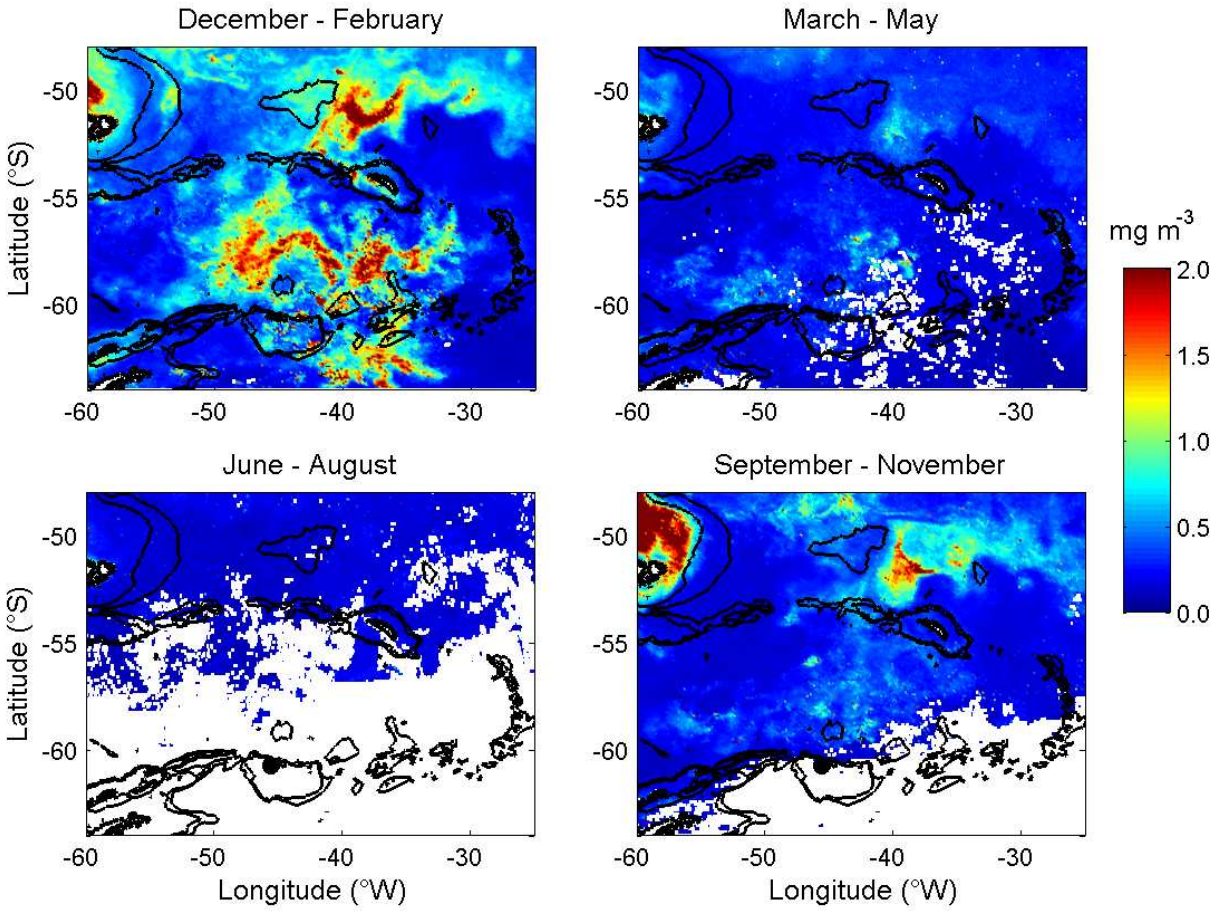

Figure 7.6. Seasonal composites of satellite chlorophyll-a (SeaWiFS) for the Scotia Sea during summer (December 2006-February 2007), autumn (March-May 2007), winter (June-August 2007) and spring (September-November 2007).

Low chlorophyll-a concentrations (< 0.2 mg m^{-3}) persisted for much of the WSC and the AAZ during summer 2007-2008 and autumn 2008 (Fig. 7.7). Shipboard chlorophyll-a measurements detected elevated concentrations up to 3.5 mg m^{-3} in waters overlying the SSR (Fig. 7.2e) that were obscured by cloud in the satellite image. The South Georgia bloom became initiated in summer and intensified to cover most of the GB. Shipboard observations revealed chlorophyll-a concentrations of 11.1 mg m^{-3} in the lower GB. The bloom gradually

extended to the north and east of the GB, along the contours of the PF and the SACCF. During autumn, most of the ACC had HNLC conditions. The remnants of the larger summer bloom downstream of South Georgia persisted until the onset of winter. In the following spring, a bloom developed at about 59°S that extended from 50 to 30°W along the contours and meanders of the SACCF. The South Georgia bloom also became seeded at this time.

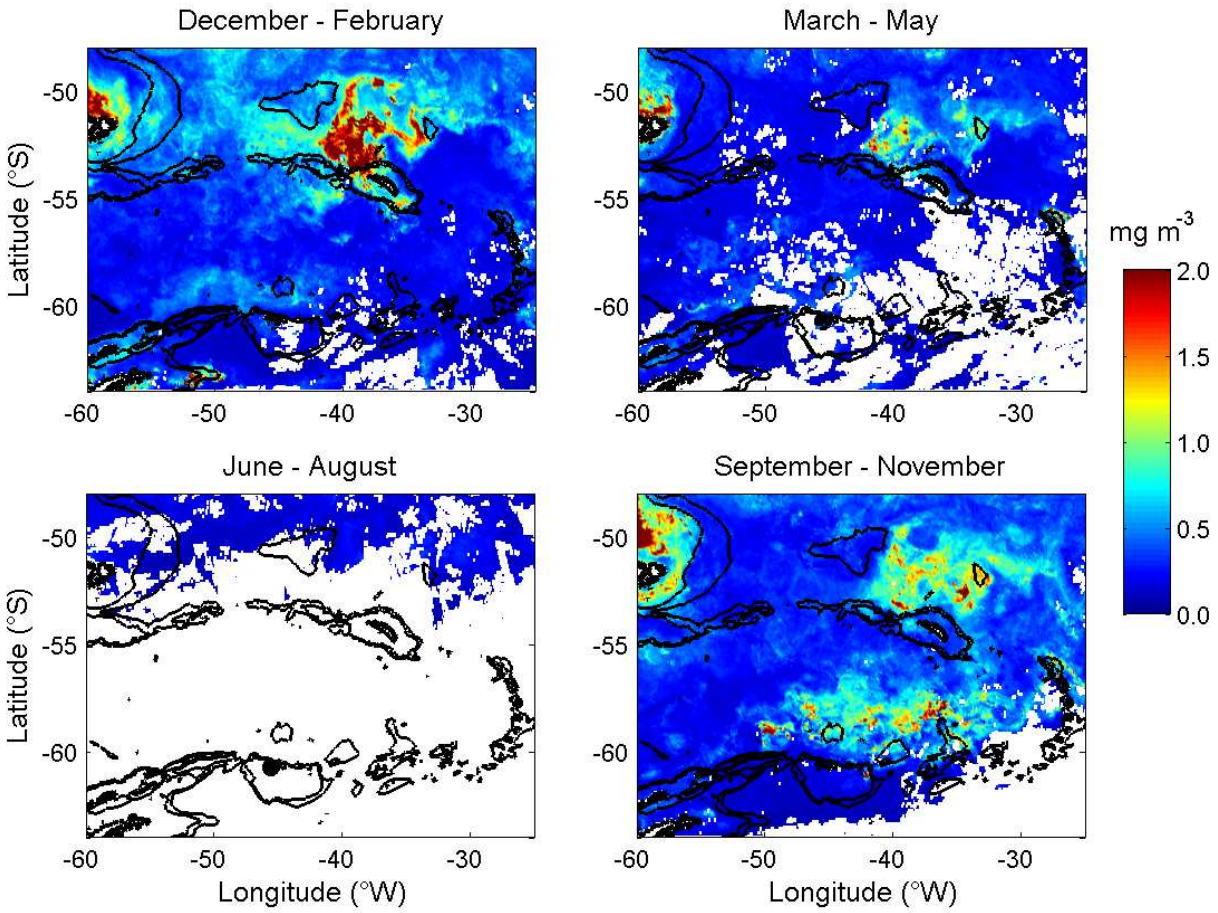

Figure 7.7. Seasonal composites of satellite chlorophyll-a (MODIS) for the Scotia Sea during summer (December 2007-February 2008), autumn (March-May 2008), winter (June-August 2008) and spring (September-November 2008).

The seasonal patterns in satellite chlorophyll-a during 2009 (Fig. 7.8) were very similar to those of 2008. HNLC conditions persisted across the northern part of the AAZ during the previous spring and summer. The slightly weaker South Georgia bloom that had developed in spring 2008 had increased in magnitude and spatial coverage, developing an intense patch over the northern shelf of the NSR. The ACC blooms during previous spring had dispersed and left a patchy chlorophyll-a distribution across the AAZ. Similarly to autumn 2006 and

2008, the remnants of the larger summer South Georgia bloom persisted throughout the autumn, especially over the NSR. The ACC waters of the AAZ had returned to typical HNLC conditions. By the following spring, substantial detrainment of the South Georgia bloom to the north and east within the PF and SACCF was detectable. Areas of elevated chlorophyll-a persisted in sporadic patches in the southern ACC.

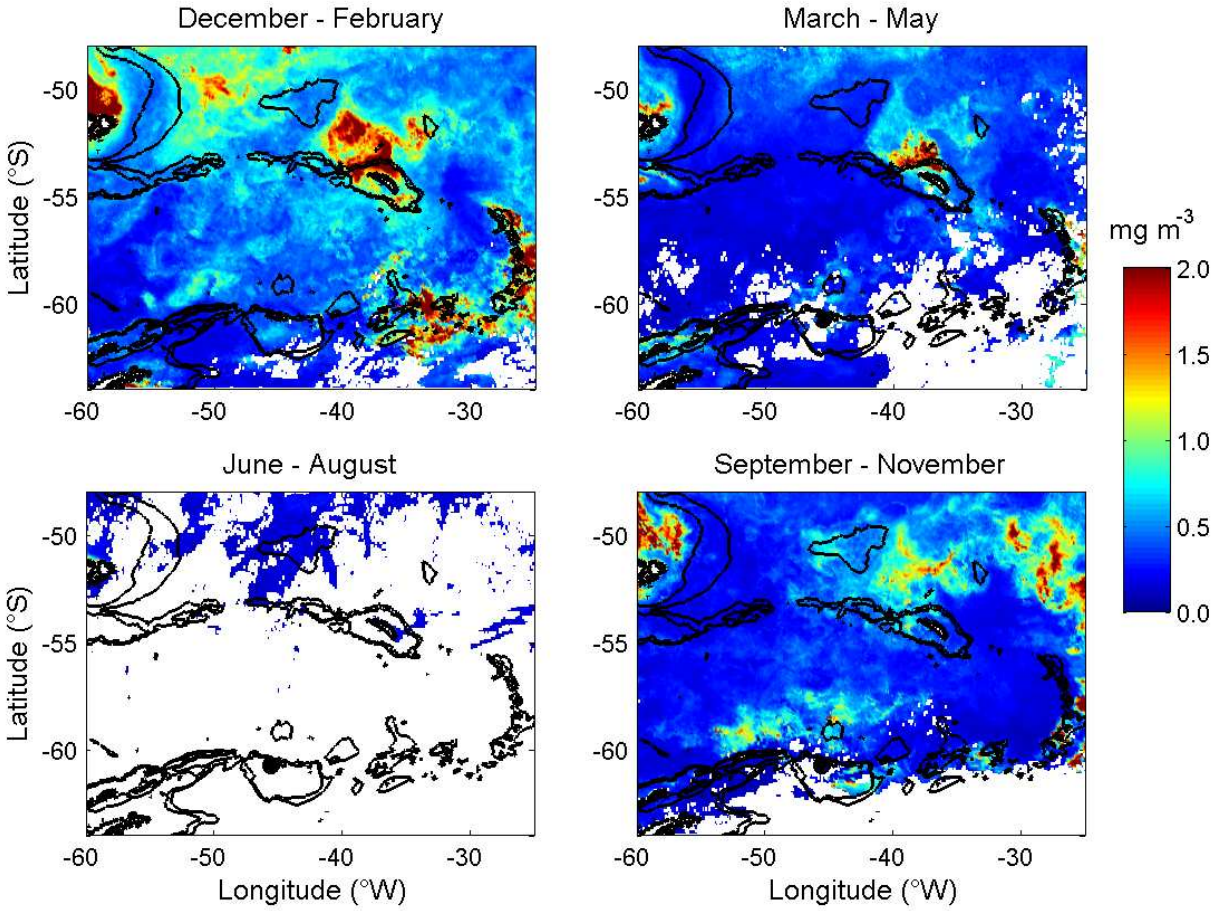

Figure 7.8. Seasonal composites of satellite chlorophyll-a (MODIS) for the Scotia Sea during summer (December 2008-February 2009), autumn (March-May 2009), winter (June-August 2009) and spring (September-November 2009).

The seasonal coverage and duration during each year, from 2006 to 2009, of the major blooms of the Scotia Sea are summarised in Tables 7.2 and 7.3.

Table 7.2. The seasonal coverage (km^2) and duration (days) of the ACC blooms from 2006 to 2009. A phytoplankton bloom is defined here as surface chlorophyll-a concentrations exceeding 2 mg m^{-3}. No bloom was detected during the winter months June, July and August throughout the 2006-2009 research period. Each seasonal bloom is ranked in terms of area and duration (where a rank 1 is for both the largest area and longest duration). The relative 'strength' of each seasonal bloom is determined as a product of area and duration ranking. The four strongest blooms are highlighted in bold.

Season	*Year*	*Latitude*	*Longitude*	*Area*		*Duration*		*Rank product*
		°S	*°W*	*10^3 km^2*	*Rank*	*days*	*Rank*	*10^3 km^2 days*
Summer	2005/2006	-59.5/-58.5	-49.5/-44.5	32	4	89	1	**4**
Autumn	2006	-59.5/-58.3	-51.5/-48.0	27	5	52	5	25
Spring	2006	-59.5/-57.5	-46.0/-40.5	70	2	45	6	**12**
Summer	2006/2007	-60.5/-57.5	-47.5/-36.0	220	1	87	2	**2**
Autumn	2007	-59.0/-59.5	-43.0/-42.0	3	8	8	11	88
Spring	2007	-58.0/-57.5	-45.0/-44.5	2	9	32	7	63
Summer	2007/2008	-59.5/-59.0	-44.0/-43.5	2	9	31	8	72
Autumn	2008	-58.5/-58.0	-44.0/-43.5	2	9	12	10	90
Spring	2008	-58.5/-58.0	-48.0/-36.0	39	3	71	3	**9**
Summer	2008/2009	-58.5/-58.0	-37.0/-35.0	7	7	70	4	28
Autumn	2009	-59.5/-59.0	-45.0/-44.5	2	9	23	9	81
Spring	2009	-58.5/-58.0	-53.0/-49.0	13	6	45	6	36

Table 7.3. The seasonal coverage (km^2) and duration (days) of the South Georgia bloom from 2006 to 2009. A phytoplankton bloom is defined here as surface chlorophyll-a concentrations exceeding 2 mg m^{-3}.No bloom was detected during the winter months June, July and August throughout the 2006-2009 research period. Area and duration rankings as for Table 7.2.

Season	*Year*	*Latitude*	*Longitude*	*Area*		*Duration*		*Rank product*
		°S	*°W*	*10^3 km^2*	*Rank*	*days*	*Rank*	*10^3 km^2 days*
Summer	2005/2006	-52.0/-50.0	-40.5/-35.0	85	2	87	3	**6**
Autumn	2006	-53.0/-50.2	-41.5/-38.5	64	4	45	8	32
Spring	2006	-51.0/-50.5	-38.7/-38.0	3	12	29	11	132
Summer	2006/2007	-51.5/-50.0	-40.0/-35.5	52	5	86	4	**20**
Autumn	2007	-52.0/-51.0	-40.5/-39.5	8	11	9	12	132
Spring	2007	-52.0/-50.3	-40.0/-37.5	33	6	61	7	42
Summer	2007/2008	-53.5/-51.5	-42.0/-37.0	80	3	90	1	**3**
Autumn	2008	-52.5/-51.7	-41.5/-39.5	12	9	74	5	45
Spring	2008	-53.0/-52.0	-35.5/-34.0	11	10	70	6	60
Summer	2008/2009	-53.5/-51.2	-41.0/-36.0	87	1	89	2	**2**
Autumn	2009	-53.5/-52.5	-40.0/-36.5	26	7	36	10	70
Spring	2009	-52.0/-51.0	-40.0/-38.0	15	8	38	9	72

7.7. Sea ice

7.7.1. Sea ice: seasonal patterns and inter-annual variability

Satellite derived sea ice cover from 2006 to 2009 (section 2.13.6) showed the seasonal advance and retreat of the sea ice across the Scotia Sea (Figs. 7.9-7.11). Sea ice extent is defined here as the area enclosed by the ocean-ice edges, after Gloersen and Campbell (1991). During winter (June-August) and early spring (September-October), sea ice extended across the WSC and the southern part of the AAZ, up to the SACCF at about 58°S. By the end of

spring (November), sea ice was absent in the AAZ and had ≥ 70% coverage across the WSC. During summer (December-February), the whole Scotia Sea was ice free until the end of Autumn (May) where sea ice began to extend into the southern WSC and advance into the AAZ by the following winter.

From 2006-2009, inter-annual variability in the timing of the sea ice advance and retreat and maximum coverage was observed. The maximum extent of the sea ice, defined here as the northward limit of the sea ice cover where ice is present for the whole month, occurred in September 2007 (Fig. 7.10). At this time, sea ice extended from the southern WSC and into the southern part of the AAZ at 57°S (Table 7.4). This defines the latitudinal limits of the seasonal ice zone (SIZ) of the Scotia Sea for the 2006 to 2009 research period. During summer 2007-2008, partial sea ice cover (≤ 40%) was present over the southern WSC (Fig. 7.10). By February 2008, the whole Scotia Sea became ice free, which was 2-3 months later than in 2006-2007 (Fig. 7.9) and 2008-2009 (Fig. 7.11). Sea ice advance began at least 1-2 months early in 2008 (April) and had reached ≥ 80% coverage in the WSC by the end of May. This resulted in 2007-2008 being a relatively 'icy' period (Fig. 7.10). Oppositely, sea ice was only present in the WSC (up to 60°S) for the following winter-spring (2008) and had completely retreated by November. This led to 2008-2009 being a relatively ice free period (Fig. 7.11).

Figure 7.9. (page 223) Monthly averages of satellite derived sea ice cover (%) for the Scotia Sea from June 2006 to May 2007.

Figure 7.10. (page 224) Monthly averages of satellite derived sea ice cover (%) for the Scotia Sea from June 2007 to May 2008.

Figure 7.11. (page 225) Monthly averages of satellite derived sea ice cover (%) for the Scotia Sea from June 2008 to May 2009.

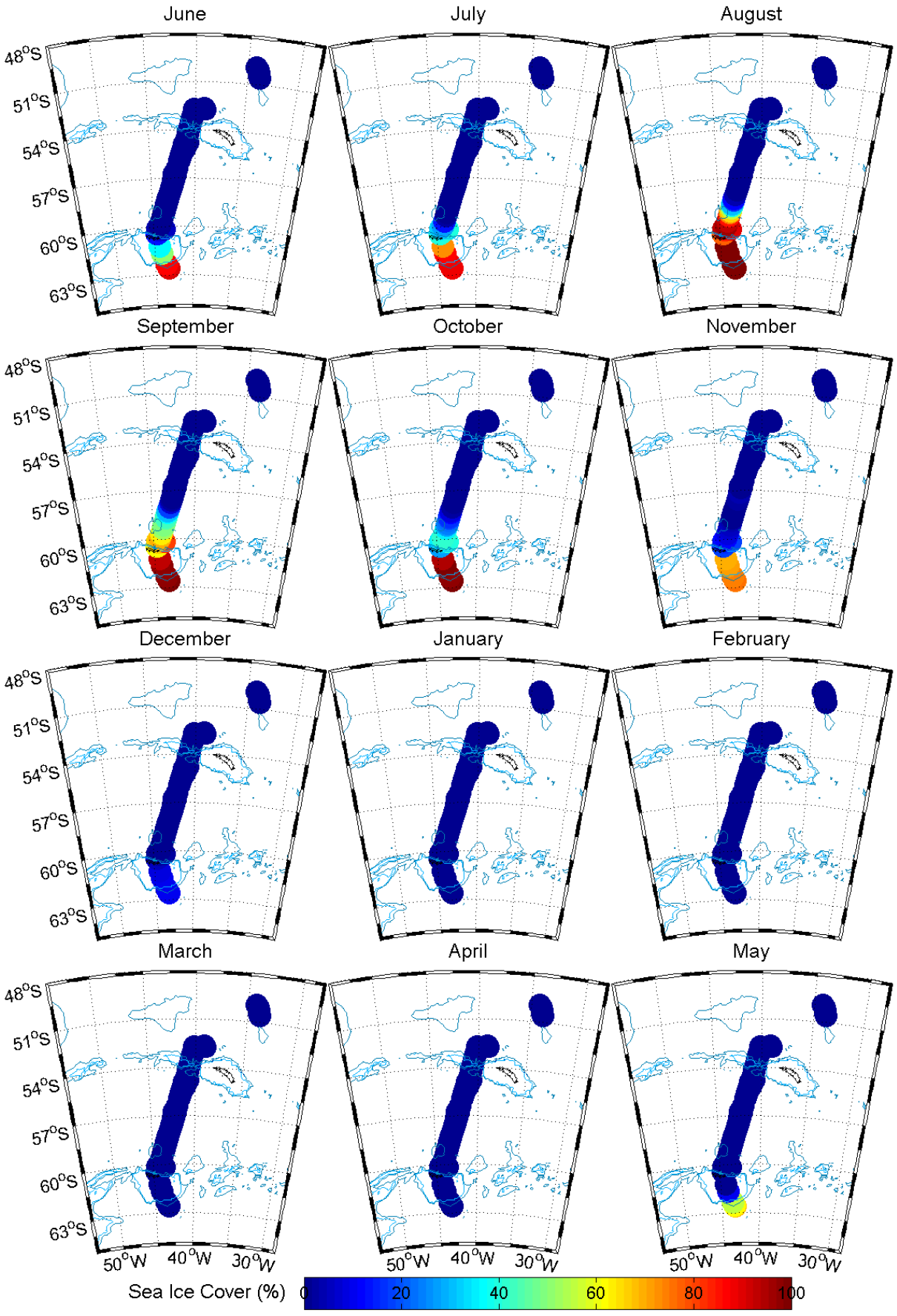
June
July
August
September
October
November
December
January
February
March
April
May
48°S
51°S
54°S
57°S
60°S
63°S
50°W
40°W
30°W
Sea Ice Cover (%)
0
20
40
60
80
100

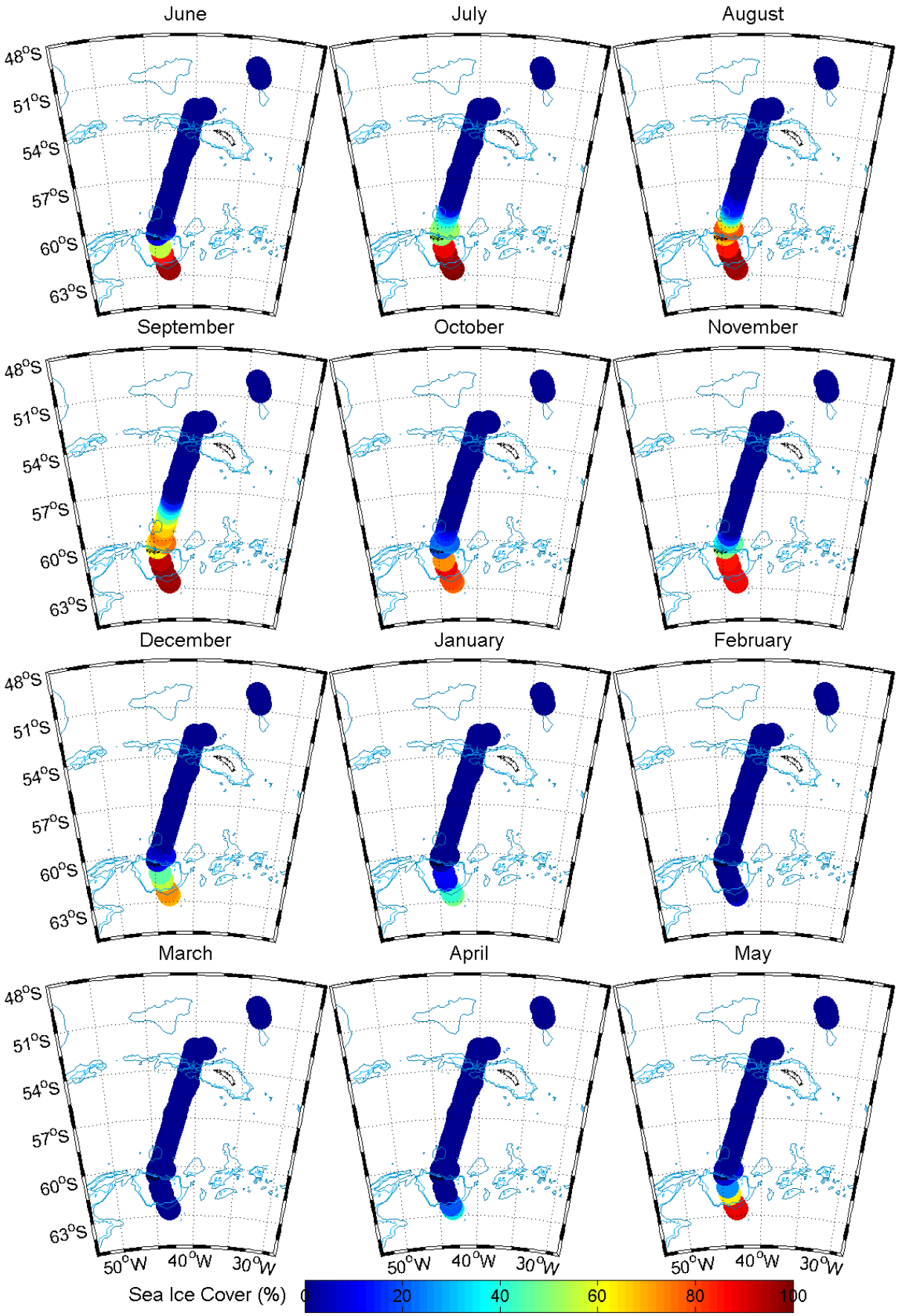
June
July
August
September
October
November
December
January
February
March
April
May
48°S
51°S
54°S
57°S
60°S
63°S
50°W
40°W
30°W
Sea Ice Cover (%)
0
20
40
60
80
100

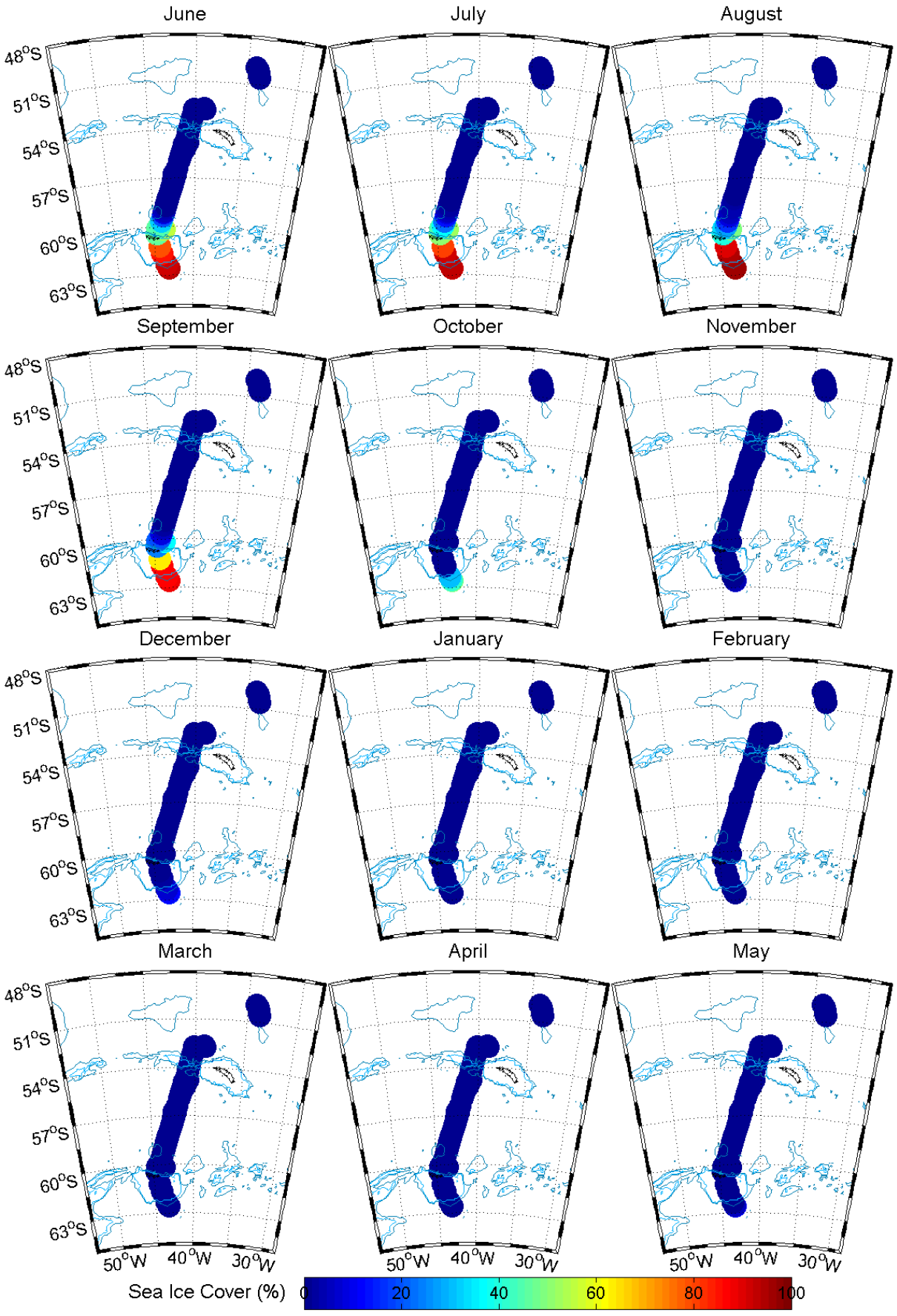
June
July
August
September
October
November
December
January
February
March
April
May
48°S
51°S
54°S
57°S
60°S
63°S
50°W
40°W
30°W
Sea Ice Cover (%)
0
20
40
60
80
100

Table 7.4. Summary of the seasonal advance and retreat of the sea ice and the initiation, duration and termination of the principle phytoplankton blooms of the Scotia Sea from 2006 to 2009. No data is represented by -. Abbreviations: SIZ, seasonal ice zone; GB, Georgia Basin. Bloom rank products as determined in Tables 7.2 and 7.3, where a ranking of 1 indicates the strongest bloom in terms of coverage and duration.

Season	*Sea ice*	*SIZ bloom*	*South Georgia bloom*
Summer 2005 - Autumn 2006	-	Dec 05 – May 06 63-58°S, 60-40°W bloom rank: 4	Dec 05 – May 06 covered most of GB bloom rank: 6
Winter 2006 - Autumn 2007	maximum extent Aug 06 extent to 58°S Jan 07 – Apr 07 ice free	Oct 06 – Feb 07 63-57°S, 50-30°W bloom rank: 2	Dec 06 – Feb 07 covered part of GB bloom rank: 20
Winter 2007 - Autumn 2008	maximum extent Sept 07 extent to 57°S Feb 08 – Mar 08 ice free	Sept 07 – Oct 07 60-58°S, 45-40°W bloom rank: 63	Sept 07 – Apr 08 covered most of GB bloom rank: 3
Winter 2008 - Autumn 2009	maximum extent Jul 08 extent to 60°S Jan 09 – May 09 ice free	Sept 08 – Feb 09 60-58°S, 50-30°W bloom rank: 9	Oct 08 – May 09 covered most of GB bloom rank: 2

From satellite data from 2006-2009, the general seasonal trends in sea ice and sea surface chlorophyll-a for the Scotia Sea are summarised as follows (Table 7.4):

- Winter: maximum sea ice cover up to 57°S (limit of the SIZ), no blooms
- Spring: ice retreat in the AAZ, initiation of SIZ blooms and sometimes the South Georgia bloom
- Summer: minimum sea ice cover, decaying SIZ blooms, strong South Georgia bloom (based on ranks, the strongest South Georgia blooms all occurred in the summer)
- Autumn: ice advance in the WSC, SIZ blooms usually absent, decaying South Georgia bloom

7.8. Atmospheric CO_2

The average CO_2 mixing ratio (xCO_2) in dry air from the CASIX underway pCO_2 instrument is compared to that from Jubany station (Ciattaglia et al., 1999) for the duration of the seasonal cruises (Table 7.5). Jubany station (62.23°S 58.67°W) is situated on King George Island, in the South Shetland archipelago, north of the Antarctic Peninsula and was previously selected as the most appropriate station for atmospheric xCO_2 comparisons (section 3.5). A large variation in atmospheric pressure was measured during each cruise, with generally higher pressures during summer. This will affect the ΔfCO_2, and in turn the air-sea flux of CO_2, but with similar pressure variations throughout the year the effects on the data will not be seasonally biased. Intermittent periods of both calm, high pressure and storms are frequent features of Southern Ocean atmospheric and oceanic research.

Table 7.5. Seasonal cruise details, sampling period and atmospheric mixing ratio of CO_2 (xCO_2) from the shipboard instrument and Jubany station. Atmospheric xCO_2 values are an average of all data within the cruise period with the standard deviation in parentheses. No data is represented by -.

Season	*Cruise*	*Year*	*Period*	*Shipboard xCO_2 $\mu mol\ mol^{-1}$*	*Jubany xCO_2 $\mu mol\ mol^{-1}$*
Spring	JR161	2006	20 Oct – 1 Dec	380.4 (0.7)	380.2 (0.4)
Winter	-	2007	8 Sept – 4 Oct	-	382.6 (0.5)
Summer	JR177	2008	2 Jan – 17 Feb	382.4 (0.5)	382.2 (0.6)
Autumn	JR200	2009	11 Mar – 17 Apr	385.3 (0.6)	383.9 (0.2)

7.9. Sea surface fCO_2

7.9.1. Seasonal data

The distribution of surface water fCO_2 along the transect was inferred from the quasi-continuous underway measurements of fCO_2 during spring, summer and autumn (Fig. 7.2a). Surface water fCO_2 during the winter was calculated from dissolved inorganic carbon (DIC) and total alkalinity (TA) in the Winter Water during summer 2008, using the CO2Sys programme (section 2.12). With respect to atmospheric CO_2 concentrations determined from

shipboard measurements for spring 2006, summer 2008 and autumn 2009 and Jubany station measurements for winter 2007 (Table 7.5), the difference in fCO_2 between the sea surface and overlying air (ΔfCO_2(sea-air)) was determined for each season (Fig. 7.12).

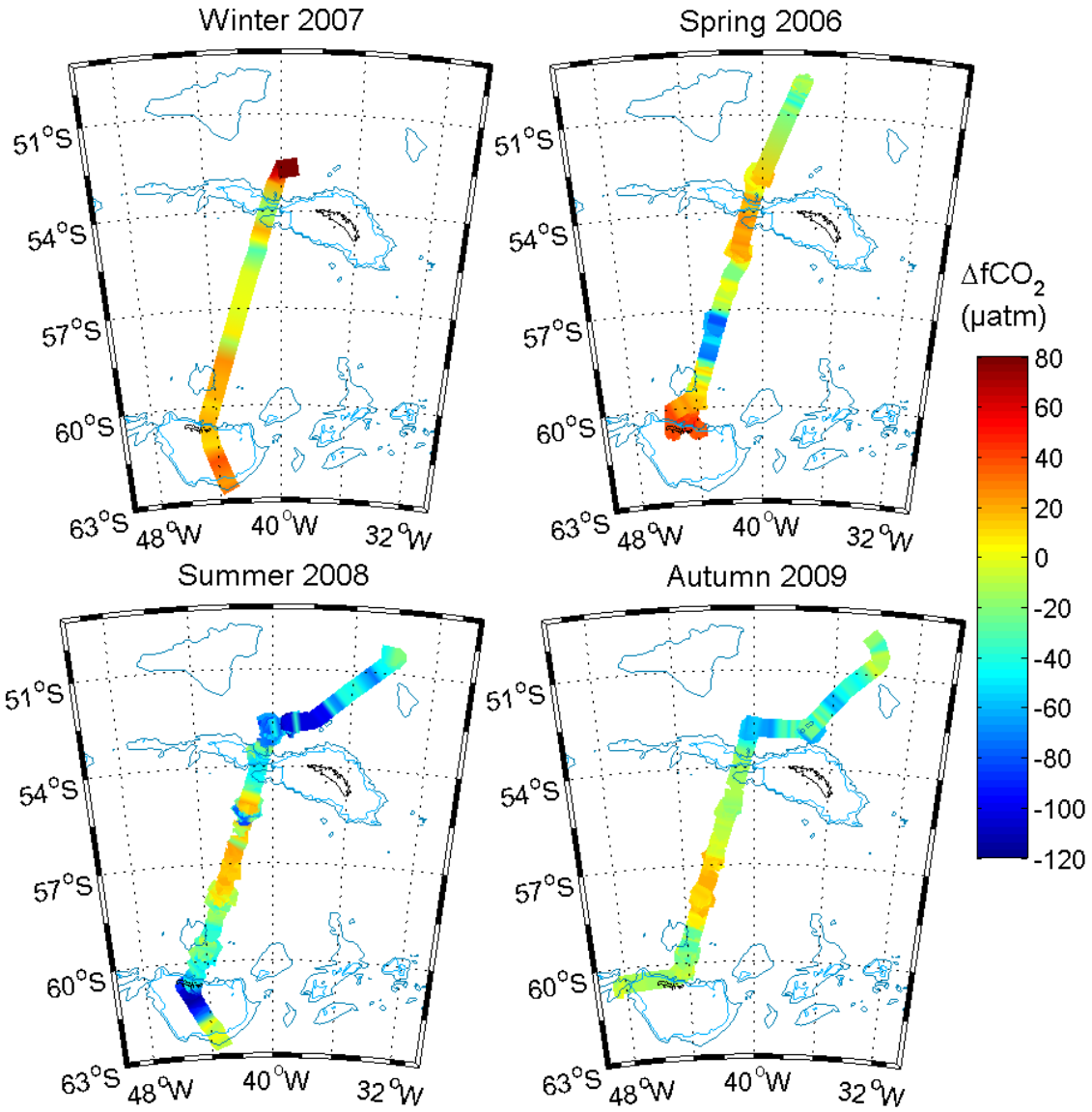

Figure 7.12. Distribution in ΔfCO_2(sea-air) (µatm) across the Scotia Sea from spring 2006, winter 2007, summer 2008 and autumn 2009. Winter ΔfCO_2 is determined from the difference in fCO_2(sea), calculated from DIC and TA values in the Winter Water during summer 2008 (f(DIC,TA)), and fCO_2(air) as measured at Jubany station during September 2007. Bathymetry as for Figure 7.4.

7.9.2. Winter 2007

South of the SACCF, at about 58°S, the sea surface was supersaturated with respect to atmospheric CO_2 with an average ΔfCO_2 of 21 ± 9 µatm (n = 10) (Fig. 7.12). North of the SACCF, surface water fCO_2 was on average undersaturated as ΔfCO_2 decreased to -5 ± 14 µatm (n = 10). An exception to this general trend was in the GB, where the sea surface reached an annual maximum of CO_2 saturation of 60 ± 30 µatm (n = 4) (Fig. 7.2a).

7.9.3. Spring 2006

During spring, waters in the vicinity of the South Orkney Islands had strong CO_2 supersaturation of over 60 µatm (Fig. 7.12). North of 60°S, surface seawater reached equilibrium concentrations in the region of the SB at about 59°S. The level of CO_2 saturation continued to decrease across the SACCF, reaching strong undersaturation, as low as -82 µatm, between 58°S and 57°S (Fig. 7.2a). For the remainder of the transect, surface waters were close to saturation levels with respect to atmospheric CO_2.

7.9.4. Summer 2008

Surface water fCO_2 rapidly decreased from near-saturation in the southern WSC to strong undersaturation (ΔfCO_2 less than -100 µatm) over SSR at about 61°S (Figs. 7.2a and 7.12). The level of undersaturation weakened, to about -50 µatm, close to the South Orkney Islands and continued to be reduced across the SB, reaching equilibrium concentrations in the vicinity of the SACCF. From 58°S to 56°S, the sea surface formed a band of moderate supersaturation, where ΔfCO_2 was about 20 µatm. Waters of the GB had strong levels of undersaturation with an annual minimum of ΔfCO_2 at nearly -120 µatm.

7.9.5. Autumn 2009

From 61°S to 59°S, the sea surface had moderate CO_2 saturation with ΔfCO_2 of -36 µatm just south of the SB (Fig. 7.2a). North of the SB, fCO_2 increased by up to 50 µatm to levels of variable supersaturation across the SACCF. Over the NSR, ΔfCO_2 rapidly decreased to strong undersaturation of -68 µatm, close to 53°S (Fig. 7.12). For the remainder of the transect, ΔfCO_2 was more variable but remained at undersaturation in the GB, increasing to more saturation levels on approach to the PF.

7.10. Air-sea CO_2 flux

7.10.1. Seasonal air-sea CO_2 fluxes and winds

Fluxes at atmospheric pressure with wind speeds from QuikSCAT (section 2.15) and *in situ* fCO_2 measurements were calculated using the Nightingale (Nightingale et al., 2000) relationship for short term winds (Fig. 7.13). The effect of the wind speed product used, i.e. *in situ* winds measured at the time of sampling (Fig. 7.13b) or seasonal wind speed averages (Fig. 7.13c) can be seen on the magnitude of the fluxes, in either direction, although the trends remained largely unaltered. Seasonal wind speed averages were calculated by taking an average of the wind speed (measured twice daily) at the position of each ΔfCO_2 value along the transect for each season.

Using *in situ* winds represented a 'snap-shot' of the CO_2 fluxes, which captured intense fluxes that resulted from extreme wind events (annual range 1.2-17.3 m s^{-1}) that occurred during the period of data collection. Using seasonal winds (annual range 7.9-10.4 m s^{-1}) the CO_2 fluxes were more representative of each season and hence presented a more realistic picture of annual CO_2 exchange when using a single cruise to represent a whole season. A discussion of fluxes using *in situ* winds will be carried out initially to present a qualitative analysis of the natural range of CO_2 uptake and release that occurred at the time of the seasonal sampling. Fluxes calculated using seasonal winds will be used to provide a quantitative analysis of the annual CO_2 flux of the Scotia Sea (Tables 7.6 and 7.9).

Figure 7.13. (page 231) The latitudinal distribution of (a) ΔfCO_2(sea-air) (μatm), (b) CO_2 flux (mmol m^{-2} d^{-1}) using *in situ* QuikSCAT winds and (c) CO_2 flux (mmol m^{-2} d^{-1}) using seasonally averaged QuikSCAT winds during winter (blue), spring (green), summer (yellow) and autumn (red). The approximate locations of bathymetry, fronts and hydrographic regions as in Figure 7.2. The latitudinal limits of the seasonal ice zone (SIZ) are now shown (section 7.7.1).

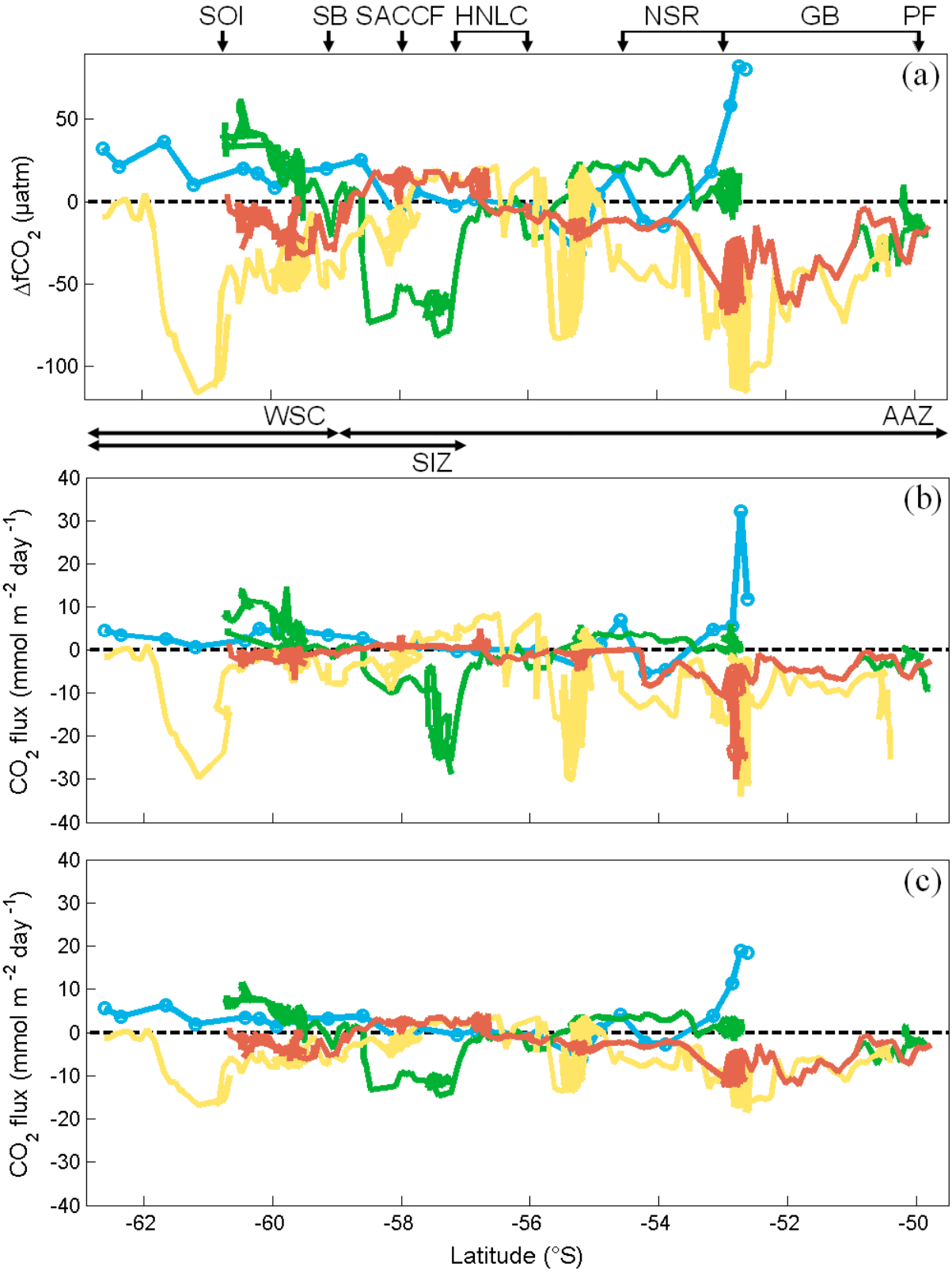
SOI
SB
SACCF
HNLC
NSR
GB
PF
(a)
ΔfCO2 (µatm)
50
0
-50
-100
WSC
AAZ
SIZ
(b)
CO2 flux (mmol m-2 day-1)
40
30
20
10
0
-10
-20
-30
-40
(c)
CO2 flux (mmol m-2 day-1)
-62
-60
-58
-56
-54
-52
-50
Latitude (°S)

7.10.2. Winter 2007

Across the SIZ the upper ocean was a potential moderate source of CO_2 of 5.0 mmol m^{-2} d^{-1}, which was largely inhibited due to sea ice cover (Fig. 7.13b). North of the SACCF, the sea surface had negligible CO_2 uptake or release beyond the SIZ. A small sink of 5.5 mmol m^{-2} d^{-1} was created over the NSR with the occurrence of very high *in situ* wind speeds (> 15 m s^{-1}). The situation swiftly shifted with high winds and an annual maximum of ΔfCO_2 (Fig. 7.13a) creating a strong CO_2 source of 32.2 mmol m^{-2} d^{-1} in the lower GB.

Table 7.6. Average air-sea flux of CO_2 (mmol m^{-2} d^{-1}) for the eight hydrographic regions along the transect using the Nightingale et al. (2000) relationship with *in situ* atmospheric pressure and seasonally averaged winds from QuikSCAT (Fig. 7.13c). As no field campaign was conducted during the winter, ΔfCO_2sea-air is determined from DIC and TA measured in the Winter Water during summer 2008 (fCO_2sea as f(DIC,TA)) and fCO_2air based on Jubany data (Chapter 3). The standard deviation, of the mean of all data, in each region is in parentheses. Negative fluxes indicate oceanic uptake of CO_2. No data is represented by -.

Season	*WSC*	*SB*	*SACCF*	*HNLC*	*ACC*	*NSR*	*GB*	*PF*
Winter	0	0	0	-0.1	-3.4	0.7	16.2	-
	(0.0)	(0.0)	(0.0)	(0.5)	(3.8)	(3.3)	(4.1)	-
Spring	6.0	-1.1	-11.6	-9.2	2.2	2.7	0.6	-2.3
	(2.7)	(2.9)	(1.2)	(4.1)	(1.2)	(1.3)	(1.5)	(1.2)
Summer	-6.2	-4.6	-1.2	2.3	-5.0	-6.9	-12.0	-4.5
	(3.8)	(1.7)	(1.7)	(1.0)	(4.7)	(3.5)	(4.2)	(1.2)
Autumn	-2.4	-3.0	1.9	2.0	-3.0	-3.4	-9.6	-4.4
	(1.5)	(2.9)	(0.8)	(1.6)	(0.8)	(1.6)	(2.3)	(2.1)

7.10.3. Spring 2006

High *in situ* wind speeds (> 10 m s^{-1}) and a large positive ΔfCO_2 over the South Orkney Islands (Fig. 7.13a) created a strong CO_2 source of up to 14.0 mmol m^{-2} d^{-1} (Fig. 7.13b). Equilibrium concentrations of surface water CO_2 at the SB and lower *in situ* wind speeds allowed negligible exchange of CO_2 between the ocean and atmosphere. In contrast, waters north of the SACCF presented conditions of strong CO_2 undersaturation and this region represented the strongest *in situ* CO_2 sink during spring 2006 of -28.7 mmol m^{-2} d^{-1}. The rest

of the AAZ varied between small source and sink areas, with enhanced CO_2 uptake of nearly 10.0 mmol m^{-2} d^{-1} at the PF.

7.10.4. Summer 2008

In the presence of high *in situ* wind speeds (≥10 m s^{-1}), the large undersaturation in the WSC promoted strong CO_2 uptake in the order of -29.8 mmol m^{-2} d^{-1} (Fig. 7.13b). Across the remainder of the SIZ, increased *in situ* wind speeds and ΔfCO_2 culminated in the release of up to 8.8 mmol m^{-2} d^{-1} of CO_2 in the HNLC waters. Substantial CO_2 sinks of 30.2 and 34.0 mmol m^{-2} d^{-1} were found to the south of the NSR and in the lower GB, respectively, representing the greatest annual CO_2 uptake along the transect.

7.10.5. Autumn 2009

The combination of high *in situ* wind speeds (≥ 10 m s^{-1}) and small ΔfCO_2 followed by low, steady *in situ* winds (≤ 4 m s^{-1}) and large ΔfCO_2 presented a situation of negligible air-sea CO_2 flux across the SIZ in autumn (Fig. 7.13b). The largest autumnal flux was in the HNLC region, as a temporal peak in wind speeds allowed the slightly CO_2 supersaturated seawater to outgas at a rate of 4.9 mmol m^{-2} d^{-1}. The remnant of the summer CO_2 sink persisted at -29.9 mmol m^{-2} d^{-1} in the lower GB. The degree of CO_2 uptake decreased in line with the increasing ΔfCO_2 up to the PF.

7.11. Carbonate chemistry

7.11.1. Seasonal carbonate chemistry measurements

During summer 2008, underway fCO_2 measurements and surface water DIC and TA measurements were made. Total pH (pH_T), carbonate ion concentration ($[CO_3^{2-}]$) and aragonite saturation (Ωaragonite) were calculated from the DIC and TA measurements using the CO_2Sys programme (section 2.12). Sea surface fCO_2, pH_T, $[CO_3^{2-}]$ and Ωaragonite during winter 2007 were determined from measurements of DIC and TA in the Winter Water during the summer 2008.

7.11.2. Winter 2007

Winter DIC had little variation across the WSC and up to the SACCF, with an average concentration of 2221 ± 3 μmol kg^{-1} (*n* = 10) (Fig. 7.14a). Concentrations decreased to the north, reaching a minimum concentration of 2165 μmol kg^{-1} at 55°S. Over the NSR, DIC increased to 2190 μmol kg^{-1} in the lower GB. Alkalinity had a strong northward gradient across the whole Scotia Sea, decreasing from values of 2329 ± 3 μmol kg^{-1}, south of the SACCF, to a winter minimum of 2287 μmol kg^{-1} in the GB (Fig. 7.14b). Winter surface pH_T, $[CO_3^{2-}]$ and Ωaragonite all showed similar, increasing trends from the southern WSC to 55°S (Fig. 7.14c-e). All three parameters peaked at about 55°S, with values for pH_T, $[CO_3^{2-}]$ and Ωaragonite of 8.09, 98 μmol kg^{-1} and 1.5, respectively. Over the NSR and into the GB, pH_T decreased to 7.98 where $[CO_3^{2-}]$ were reduced by nearly 20 μmol kg^{-1} and Ωaragonite fell below 1.2.

7.11.3. Summer2008

The concentration of DIC predominantly followed the trend of ΔfCO_2 (Figs. 7.2a and 7.14a). The distribution of sea surface measured and salinity normalised TA was more variable, with large differences in the SIZ (Fig. 7.14b). In the southern WSC, DIC and alkalinity declined rapidly, which has been previously described (Chapter 5). Concentrations of DIC and alkalinity reached summer maxima of 2176 and 2314 μmol kg^{-1}, respectively, close to the SACCF. Across the remainder of the AAZ, DIC decreased by nearly 100 μmol kg^{-1}, to a seasonal minimum of 2084 μmol kg^{-1} in the GB. The $[CO_3^{2-}]$ increased from 87 μmol kg^{-1} in the south to 153 μmol kg^{-1} in the GB (Fig. 7.14c). The distribution of pH_T was quite variable but showed a northward increase to 8.23 in the GB (Fig. 7.14d). The Ωaragonite traced the distribution of $[CO_3^{2-}]$ from saturation states of 1.3 in the south to 2.3 in the north (Fig. 7.13e).

Figure 7.14. (page 235) The latitudinal distribution of (a) dissolved inorganic carbon (DIC, μmol kg^{-1}, solid line) and salinity normalised DIC (dashed line), (b) total alkalinity (TA, μmol kg^{-1}, solid line) and salinity normalised TA (dashed line), (c) carbonate ion concentration ($[CO_3^{2-}]$, μmol kg^{-1}), (d) total pH (pH_T) and (e) aragonite saturation state (Ωaragonite) during winter (blue) and summer (yellow). The approximate locations of bathymetry, fronts and hydrographic regions as in Figure 7.13.

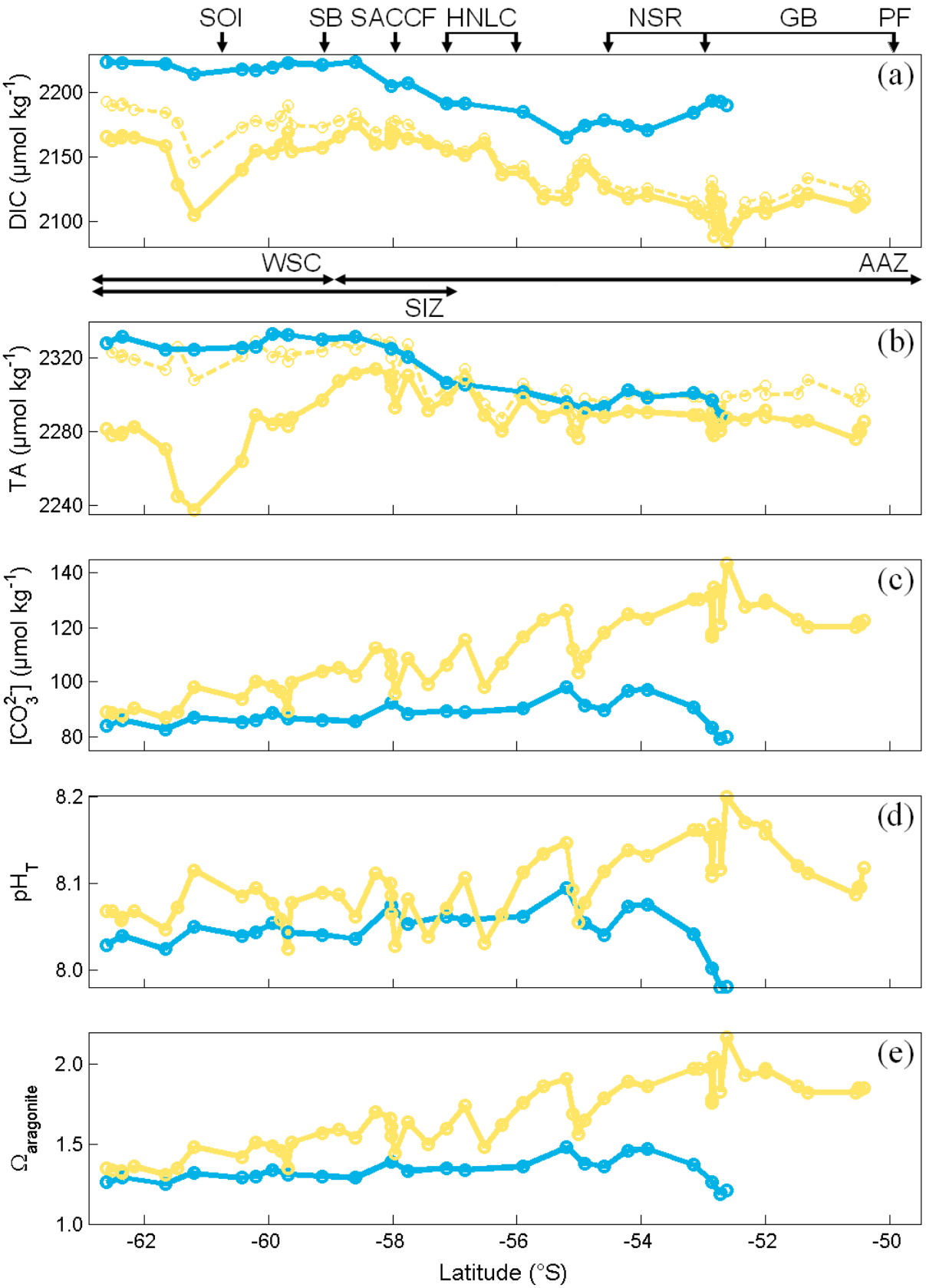
SOI
SB
SACCF
HNLC
NSR
GB
PF
(a)
DIC (µmol kg-1)
2200
2150
2100
WSC
AAZ
SIZ
(b)
TA (µmol kg-1)
2320
2280
2240
(c)
[CO32-] (µmol kg-1)
140
120
100
80
(d)
pHT
8.2
8.1
8.0
(e)
Ωaragonite
2.0
1.5
1.0
-62
-60
-58
-56
-54
-52
-50
Latitude (°S)

7.11.4. Seasonal amplitudes

From the latitudinal distribution of the sea surface carbonate parameters during winter 2007 and summer 2008 (Fig. 7.14), seasonal amplitudes were determined as the differences between winter (maxima) and summer (minima) (Fig. 7.15). Across the WSC, the seasonal cycles in DIC and TA were dictated by the large reduction in summer concentrations to the south of the South Orkney Islands (Fig. 7.14a-b). Similarly, the substantial summer DIC deficit in the GB (section 6.13) compared to high winter DIC values resulted in an amplified seasonal signal (Fig. 7.15a).

Largely following the winter and summer trends in TA, the amplitudes in pH_T, $[CO_3^{2-}]$ and Ωaragonite showed a northward decrease and strong decline over the NSR and into the GB (Fig. 7.15c-e). This was the result of two distinct seasonal features: 1. persistent low pH_T, $[CO_3^{2-}]$ and Ωaragonite values south of 59°S during winter and summer and 2. very low pH_T, $[CO_3^{2-}]$ and Ωaragonite values in the GB during winter, which can be observed in the vertical profiles through the summer and winter mixed layers on the Antarctic Surface Water (AASW) (Fig. 4.4).

Figure 7.15. (page 237) The latitudinal distribution of the seasonal differences (winter - summer) of (a) dissolved inorganic carbon (DIC, red solid line) and normalised DIC (grey dashed line) (μmol kg^{-1}), (b) total alkalinity (TA, red solid line) and normalised TA (grey dashed line) (μmol kg^{-1}), (c) carbonate ion concentration ($[CO_3^{2-}]$, μmol kg^{-1}), (d) total pH (pH_T), and (e) aragonite saturation state (Ωaragonite). The approximate locations of bathymetry, fronts and hydrographic regions as in Figure 7.13.

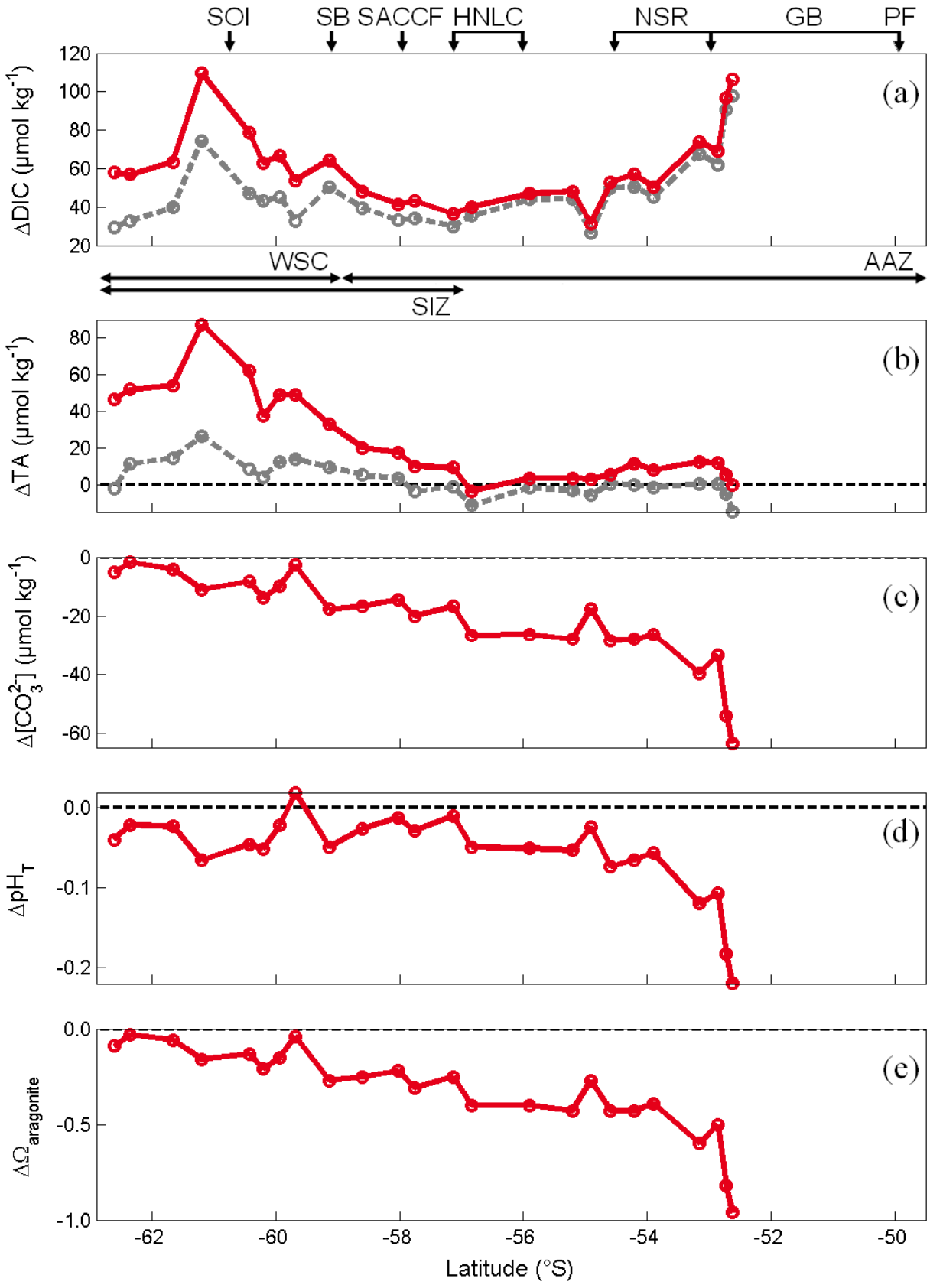
SOI
SB
SACCF
HNLC
NSR
GB
PF
ΔDIC (µmol kg-1)
(a)
WSC
AAZ
SIZ
ΔTA (µmol kg-1)
(b)
Δ[CO32-] (µmol kg-1)
(c)
ΔpHT
(d)
ΔΩaragonite
(e)
Latitude (°S)

Tables 7.7 and 7.8. (pages 239 and 240) Averages of sea surface (5 m) temperature (SST, °C), salinity, mixed layer depth (MLD, m), nitrate (NO_3^-, μmol kg^{-1}), phosphate (PO_4^{3-}, μmol kg^{-1}), silicate (SiO_4^{4-}, μmol kg^{-1}), dissolved iron (dFe, nM), chlorophyll-a (chl-a, mg m^{-3}), fCO_2 (μatm), dissolved inorganic carbon (DIC, μmol kg^{-1}) and total alkalinity (TA, μmol kg^{-1}) for the eight sub-regions of the Scotia Sea, as defined by latitude along the transect: the Weddell-Scotia Confluence (62.6-59.5°S), the Southern Boundary (59.5-58.5°S), the Southern ACC Front (58.5-57.5°S), high-nutrient low-chlorophyll waters (57.5-56.0°S), the ACC (56.0-55.0°S), the North Scotia Ridge (55.0-53.0°S), the Georgia Basin (53.0-50.5°S) and the Polar Front (50.5-49.5°S). The data represent the seasonal averages of all measurements made within each sub-region during winter (Wi), spring (Sp), summer (Su) and autumn (Au). The standard deviation, of the mean of all data, for each parameter in each region is in parentheses. Winter fCO_2 values were calculated from DIC and TA measurements in the Winter Water during summer 2008.

Region	*SST*	*Salinity*	*MLD*	NO_3^-	PO_4^{3-}	SiO_4^{4-}	*dFe*	*Chl-a*	fCO_2	*DIC*	*TA*
Season	*℃*		*m*	*μmol kg^{-1}*	*μmol kg^{-1}*	*μmol kg^{-1}*	*nM*	*mg m^{-3}*	*μatm*	*μmol kg^{-1}*	*μmol kg^{-1}*
WSC											
Wi	-1.43 (0.40)	34.26 (0.06)	82 (17)	30.1 (1.2)	1.96 (0.06)	82.1 (2.3)	-	-	392 (9)	2221 (3)	2329 (3)
Sp	-1.30 (0.18)	33.99 (0.08)	66 (14)	-	-	-	0.48 (0.33)	0.8 (0.2)	398 (13)	-	-
Su	0.44 (0.87)	33.63 (0.23)	23 (7)	24.5 (1.8)	1.61 (0.17)	71.8 (5.4)	0.16 (0.19)	1.5 (0.8)	324 (26)	2156 (17)	2280 (19)
Au	1.49 (0.33)	34.01 (0.05)	58 (14)	-	-	-	-	-	367 (7)	-	-
SB											
Wi	-0.87 (0.74)	34.29 (0.05)	91 (9)	30.7 (1.2)	1.99 (0.00)	81.3 (2.8)	-	-	394 (4)	2223 (2)	2331 (1)
Sp	-0.93 (0.14)	33.95 (0.06)	69 (0)	-	-	-	0.23 (0.09)	1.2 (0.4)	357 (17)	-	-
Su	1.36 (0.33)	33.92 (0.09)	38 (13)	22.5 (0.5)	1.58 (0.26)	63.8 (6.1)	0.04 (0.03)	1.9 (0.5)	334 (12)	2166 (9)	2305 (8)
Au	1.77 (0.25)	34.03 (0.09)	50 (17)	-	-	-	-	-	367 (16)	-	-
SACCF											
Wi	-0.22 (0.09)	34.24 (0.00)	103 (29)	30.0 (2.5)	2.03 (0.04)	68.4 (6.6)	-	-	368 (13)	2206 (2)	2323 (3)
Sp	-0.38 (0.15)	33.76 (0.03)	59 (0)	-	-	-	-	7.3 (0.0)	296 (6)	-	-
Su	1.97 (0.19)	34.02 (0.02)	47 (6)	22.6 (0.9)	1.64 (0.17)	61.4 (7)	0.16 (0.10)	0.5 (0.2)	364 (13)	2164 (3)	2307 (8)
Au	2.38 (0.09)	34.20 (0.03)	63 (15)	-	-	-	-	-	394 (5)	-	-
HNLC											
Wi	-0.06 (0.23)	34.06 (0.01)	105 (29)	29.5 (0.6)	2.02 (0.07)	50.8 (1.8)	-	-	370 (3)	2191 (0)	2306 (1)
Sp	-0.16 (0.43)	33.79 (0.04)	49 (8)	-	-	-	0.20 (0.15)	3.4 (2.9)	310 (25)	-	-
Su	2.72 (0.16)	33.90 (0.02)	60 (9)	24.2 (0.7)	1.64 (0.18)	32.1 (8.2)	0.25 (0.13)	0.2 (0.0)	385 (6)	2153 (10)	2294 (11)
Au	2.89 (0.48)	34.04 (0.13)	56 (12)	-	-	-	-	-	389 (10)	-	-

Region	*SST*	*Salinity*	*MLD*	NO_3^-	PO_4^{3-}	SiO_4^{4-}	*dFe*	*Chl-a*	fCO_2	*DIC*	*TA*
Season	℃		*m*	$\mu mol\ kg^{-1}$	$\mu mol\ kg^{-1}$	$\mu mol\ kg^{-1}$	*nM*	$mg\ m^{-3}$	μatm	$\mu mol\ kg^{-1}$	$\mu mol\ kg^{-1}$
ACC											
Wi	-1.02 (0.23)	33.95 (0.00)	111 (12)	28.1 (0.7)	1.95 (0.11)	29.1 (0.5)	-	-	353 (20)	2175 (14)	2299 (4)
Sp	1.50 (0.32)	33.89 (0.03)	110 (9)	-	-	-	0.05 (0.02)	0.3 (0.1)	380 (8)	-	-
Su	3.13 (0.16)	33.84 (0.02)	65 (3)	21.1 (3.0)	1.39 (0.14)	11.6 (7.5)	0.05 (0.04)	1.2 (0.5)	346 (28)	2128 (11)	2287 (9)
Au	4.26 (0.21)	33.75 (0.02)	66 (4)	-	-	-	-	-	361 (3)	-	-
NSR											
Wi	0.37 (0.16)	34.00 (0.03)	136 (21)	28.2 (1.1)	1.88 (0.21)	33.0 (7.8)	-	-	374 (16)	2177 (5)	2298 (4)
Sp	1.65 (0.39)	33.90 (0.03)	97 (34)	-	-	-	0.06 (0.06)	0.6 (0.5)	387 (9)	-	-
Su	3.37 (0.22)	33.83 (0.01)	66 (3)	18.4 (3.3)	1.17 (0.38)	9.9 (7.7)	0.05 (0.04)	2.6 (1.7)	327 (24)	2121 (13)	2290 (1)
Au	4.30 (0.16)	33.76 (0.02)	58 (11)	-	-	-	-	-	363 (9)	-	-
GB											
Wi	0.08 (0.34)	34.03 (0.02)	124 (9)	28.5 (2.1)	1.98 (0.08)	47.2 (4.9)	-	-	444 (13)	2193 (2)	2291 (5)
Sp	1.83 (0.21)	33.89 (0.01)	88 (19)	-	-	-	0.14 (0.05)	1.9 (0.9)	372 (9)	-	-
Su	3.99 (0.64)	33.76 (0.07)	41 (18)	15.7 (1.7)	1.25 (0.30)	7.0 (5.1)	0.34 (0.26)	4.0 (2.2)	291 (27)	2107 (12)	2284 (4)
Au	4.17 (0.89)	33.74 (0.04)	65 (9)	-	-	-	-	-	331 (13)	-	-
PF											
Wi	-	-	-	-	-	-	-	-	-	-	-
Sp	4.33 (0.50)	33.90 (0.02)	62 (7)	-	-	-	0.06 (0.02)	1.7 (0.9)	361 (7)	-	-
Su	5.35 (0.28)	33.73 (0.08)	-	17.0 (0.0)	1.52 (0.01)	4.4 (0.4)	-	-	336 (8)	2115 (2)	2283 (3)
Au	5.69 (1.73)	33.78 (0.06)	71 (16)	-	-	-	-	-	360 (12)	-	-

7.12. Seasonal variations in sea surface fCO_2: a regional comparison

The eight hydrographic regions showed distinct seasonal patterns in seasonally averaged sea surface fCO_2 (Fig. 7.16). With sea ice present, usually until the summer (Table 7.4), sea surface fCO_2 in the WSC during winter and spring was supersaturated and represented a region of potential strong CO_2 outgassing with the removal of the sea ice cover. Similarly, ice covered surface waters at the SB were supersaturated with respect to atmospheric CO_2 during winter.

The development of ice edge blooms in the SIZ during the spring and summer thaw was accompanied by strong undersaturation in surface fCO_2 (Table 7.7 and Chapter 5). This could be observed in the four sub-regions that formed the SIZ: the WSC, the SB, the SACCF and part of the HNLC waters. The effects of southward sea ice retreat were first observed in the HNLC and SACCF regions, where the near-equilibrium concentrations of CO_2 in surface waters were transformed into seasonal minima during the spring. This pattern was repeated for the two southerly regions of the SIZ (the SB and the WSC) upon passing of the ice edge in summer.

By autumn, the four sub-regions of the SIZ were approaching pre-melt, pre-bloom conditions, with slight over saturation in the HNLC and SACCF regions from seasonal warming and slight undersaturation in the SB and WSC regions from declining blooms. With the exception of a decrease in fCO_2 due to the spring SIZ bloom, CO_2 saturation of the HNLC region increased from winter to autumn with a seasonal warming of 2.95 °C (Table 7.7). As the HNLC region partially overlaps with the SIZ it is often exposed to retreating sea ice, if the maximum sea ice extent is north of 57.5°S (Table 7.4). Therefore, ice edge blooms and associated CO_2 uptake are likely to be recurrent features of the otherwise HNLC region.

In the absence of strong photosynthetic activity and sea ice cover, surface water fCO_2 increased in the ACC and NSR regions with warming of 1.28 and 2.52 °C, respectively, during winter and spring (Table 7.8). By the summer, surface waters of the ACC and NSR were transformed into regions of CO_2 undersaturation that continued into the autumn, although slightly counteracted by seasonal warming. The GB displayed the largest seasonal variability in sea surface fCO_2. Strong supersaturation during winter rapidly changed through spring and into the summer, where development of the South Georgia bloom depleted surface

water macronutrients and DIC, driving strong CO_2 undersaturation (Table 7.8). This bloom had maximum extent and intensity during the summer (Table 7.3), which was probably supported by enhanced iron concentrations compared to the spring (Table 7.8). Sea surface fCO_2 at the PF followed a very similar trend to that at the SB, remaining undersaturated from spring to summer.

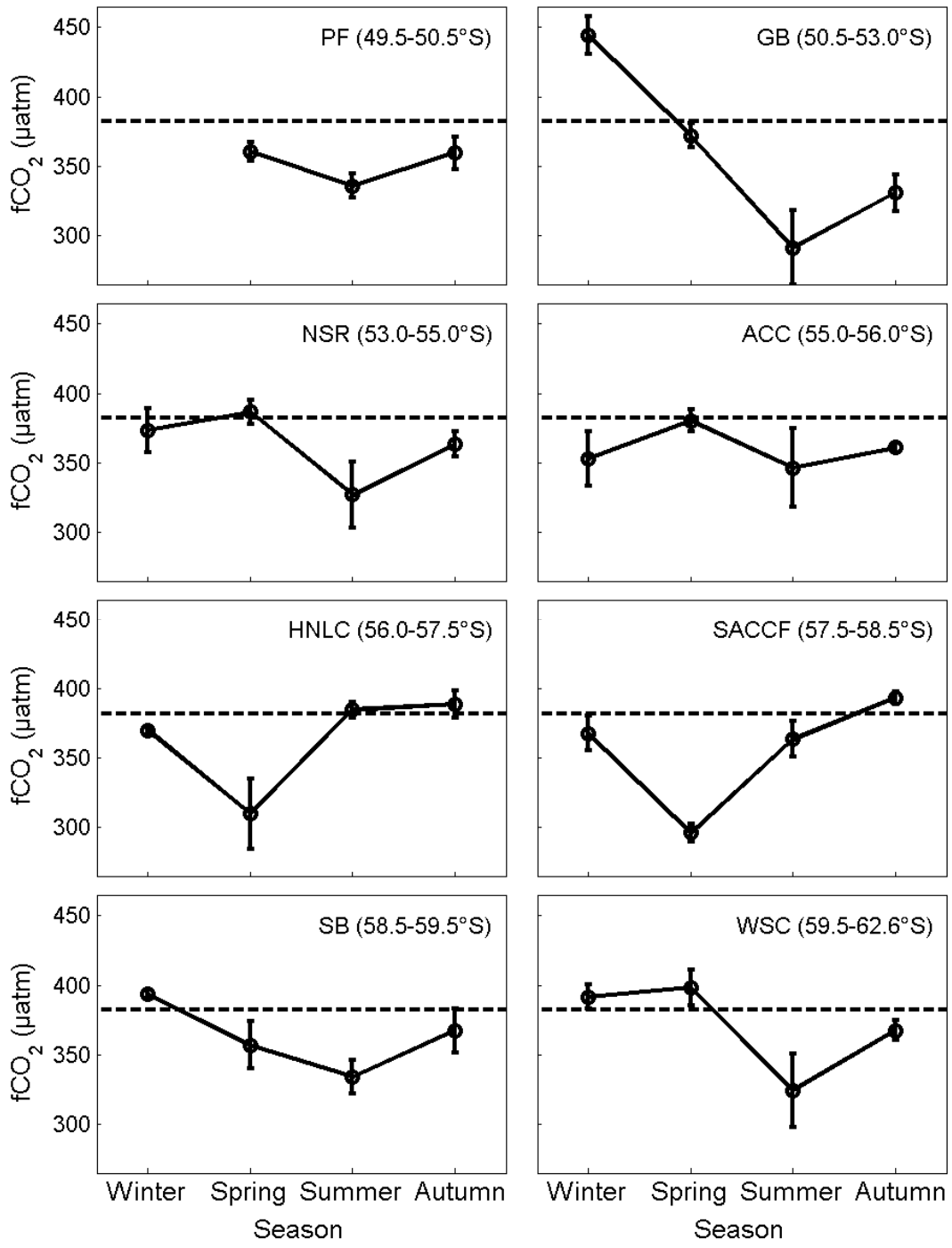

Figure 7.16. Seasonal variation in sea surface fCO_2 (µatm) for the Weddell-Scotia Confluence (WSC), Southern Boundary (SB), the Southern ACC Front (SACCF), high-nutrient low-chlorophyll (HNLC) waters, the ACC, the North Scotia Ridge (NSR), the Georgia Basin (GB) and the Polar Front (PF). Points represent the averages of all data in each sub-region for winter 2007, spring 2006, summer 2008 and autumn 2009. Error bars are the standard deviation of data. The average fCO_2(air) for 2006-2009 is shown (black dashed line).

7.13. Seasonal variations in sea surface fCO_2: property correlations

Across the Scotia Sea, the variation of sea surface fCO_2 and temperature for each season can be broadly described by three separate trends (Fig. 7.17a):

1. High fCO_2 beneath the cold, ice covered waters (winter and spring) rapidly decreases with a slight increase in temperature upon ice melt.
2. Increasing temperature from -1.00 to 3.00 °C corresponds to a strong increase in fCO_2 of 100-150 µatm from the region of ice melt to the HNLC waters.
3. From the HNLC region to the GB, the high fCO_2 is swiftly reduced through photosynthetic activity despite a slight increase in temperature.

Figure 7.17. (page 245) Sea surface fCO_2 (µatm) as a function of sea surface (a) temperature (°C), (b) salinity, (c) nitrate concentration (µmol kg^{-1}), (d) phosphate concentration (µmol kg^{-1}), (d) iron concentration and (e) chlorophyll-a concentration (chl-a, mg m^{-3}) in winter 2007 (blue), spring 2006 (green), summer 2008 (yellow) and autumn 2009 (red). The average fCO_2(air) for 2006-2009 is shown for reference (black dashed line).

Figure 7.18. (page 246) The latitudinal distribution of sea surface fCO_2 (µatm) and sea surface fCO_2 normalised to an average annual sea surface temperature of 2 °C ($fCO_{2\ T=2}$, µatm) during (a) winter 2007 fCO_2 (blue) and $fCO_{2\ T=2}$ (grey), (b) spring 2006 fCO_2 (green) and $fCO_{2\ T=2}$ (grey), (c) summer 2008 fCO_2 (yellow) and $fCO_{2\ T=2}$ (grey) and (d) autumn 2009 fCO_2 (red) and $fCO_{2\ T=2}$ (grey). The average fCO_2(air) for 2006-2009 is shown for reference (black dashed line). The approximate locations of bathymetry, fronts and hydrographic regions as in Figure 7.13.

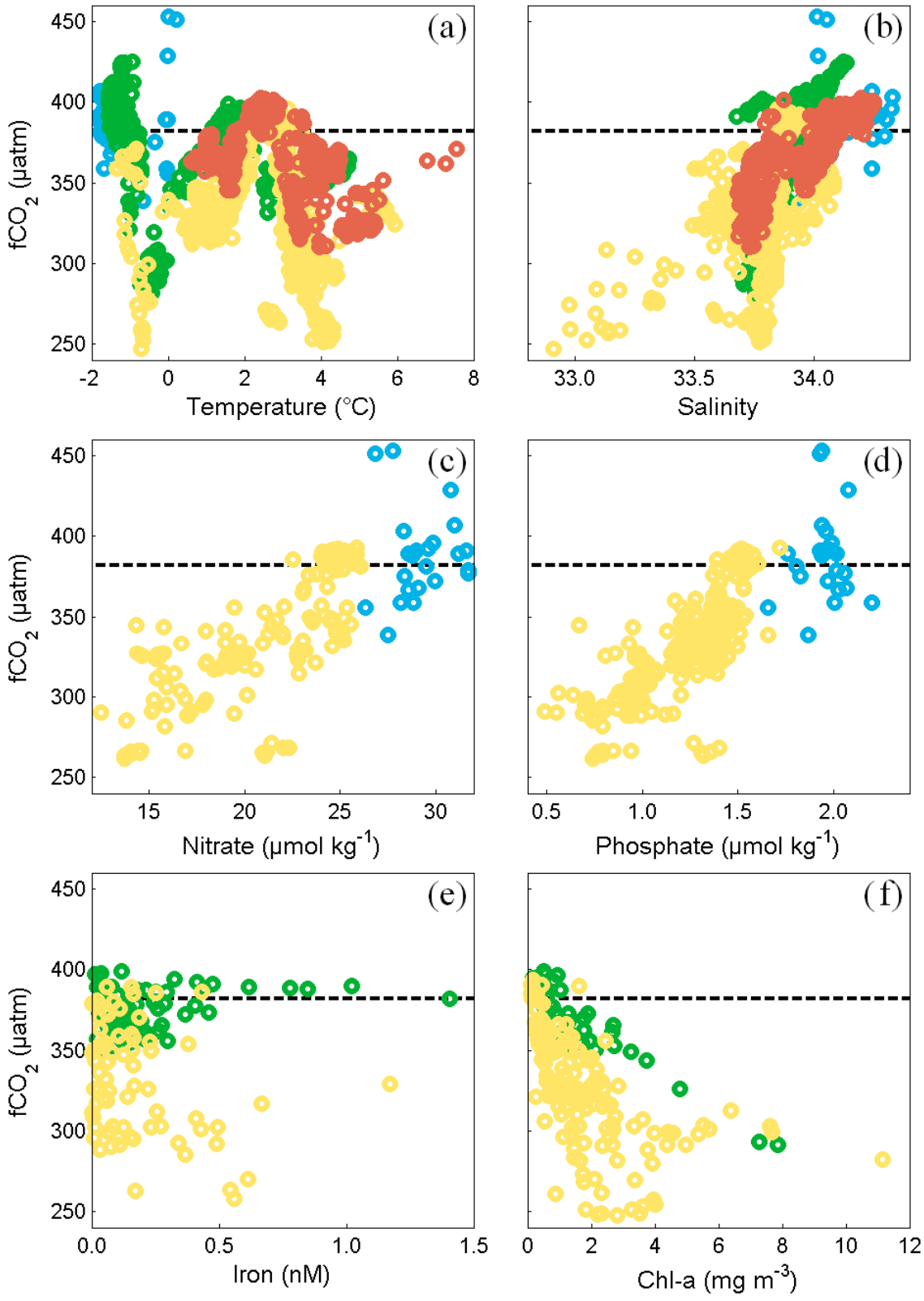
(a)
(b)
(c)
(d)
(e)
(f)
fCO2 (µatm)
Temperature (°C)
Salinity
Nitrate (µmol kg-1)
Phosphate (µmol kg-1)
Iron (nM)
Chl-a (mg m-3)

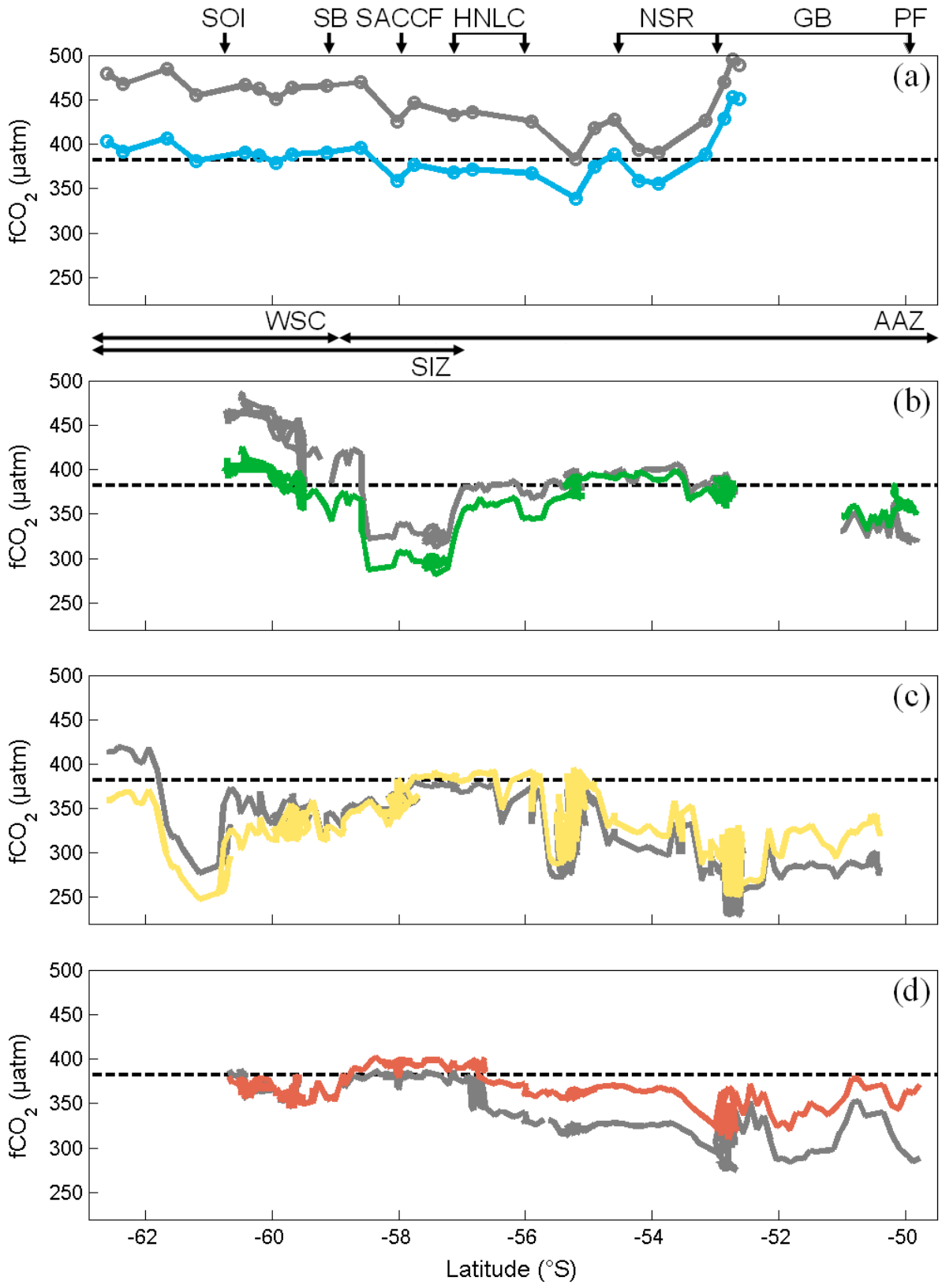
SOI
SB
SACCF
HNLC
NSR
GB
PF
(a)
WSC
AAZ
SIZ
(b)
(c)
(d)
fCO2 (µatm)
500
450
400
350
300
250
-62
-60
-58
-56
-54
-52
-50
Latitude (°S)

Exceptions to the three general trends are within the GB during winter and the warm waters of the PF where fCO_2 begins to slightly increase (spring and autumn). The effect of temperature can be further explored by comparison of fCO_2 at *in situ* temperature to fCO_2 normalised to average annual sea surface temperature along the transect of 2.00 °C ($fCO_{2\ T=2}$) (Fig. 7.18). The large undersaturation in the SIZ during spring and summer in $fCO_{2\ T=2}$ indicates the dominance of biological carbon uptake in this region (Fig. 7.18b-c). This is confirmed by elevated chlorophyll-a concentrations and reduced nutrient concentrations in the SIZ by the summer (Figs. 7.2e and 7.3). The similarity between fCO_2 and $fCO_{2\ T=2}$ in the HNLC waters verifies the significance of seasonal warming on the fCO_2 in the absence of large amounts of photosynthesis (Fig. 7.18b-d). The effect of biological carbon uptake in the South Georgia bloom is slightly counteracted by seasonal warming, as the difference between fCO_2 and $fCO_{2\ T=2}$ increases from spring to autumn (Fig. 7.18c-d).

The apparent correlation of fCO_2 and salinity is a result of the high fCO_2, saline waters beneath sea ice juxtaposed to low fCO_2, fresh waters at the receding ice edge (Fig. 7.17b). Sea surface fCO_2 decreased to below 300 μatm in the cold, fresh meltwaters in spring and summer (Fig. 7.17a-b). The greatest amount of sea ice melt had occurred by the summer, where fCO_2 was rapidly reduced by over 100 μatm, accompanied by an increase in chlorophyll-a to about 4 mg m^{-3} just north of the ice edge in the WSC (Fig. 7.2). The correlation between decreasing nitrate and phosphate concentrations, from winter to summer, and increasing phytoplankton biomass, indicated by chlorophyll-a content from spring to summer, with low fCO_2 is very strong (Fig. 7.17c-d). High winter macronutrient concentrations are utilised with increasing phytoplankton biomass through spring and summer, reducing fCO_2.

High concentrations of dFe were observed in surface waters between the SB and the South Orkney Islands from spring to summer (Fig. 7.2d), which corresponded to decreasing fCO_2 throughout the growing season (Fig. 7.17e). The generally higher iron concentrations in the fresher waters could include contributions from the melting sea ice. An inter-correlation between elevated iron concentrations, increased chlorophyll-a and reduced fCO_2 was evident across the Scotia Sea (Fig. 7.17e-f).

The large reduction in fCO_2 compared to summertime surface water chlorophyll-a content (Fig. 7.17f) could, in part, be due to the action of sea ice algae at the base of the ice floe (Gibson and Trull, 1999). The measured chlorophyll-a content in waters beneath sea ice is

likely to be an underestimation of phytoplankton biomass, as it does not include sea ice algae. The effect of ice algae probably contributes to the fCO_2-chlorophyll-a relationship of the SIZ of the Scotia Sea, in comparison to similar studies (Gibson and Trull, 1999; Bakker et al., 2008). Photosynthesis in surface waters beneath sea ice, and the development of blooms upon ice melt, prevent the large-scale release of CO_2 from the otherwise supersaturated waters that form during winter deep mixing and become capped by the ice (section 7.10.2), as shown in the Weddell Sea (Bakker et al., 2008) and WSC (Chapter 5). These trends establish the dominance of biological processes on the distribution of sea surface fCO_2 during spring and summer in the SIZ, discussed further in the following section.

7.14. Sea ice, blooms and CO_2

One principal area of elevated chlorophyll-a in the Scotia Sea was the SIZ, defined as the ocean north of the Weddell Sea to 57°S from maximum ice extent in winter 2007 (section 7.7.1). Four years of satellite chlorophyll-a data show that the SIZ blooms experience large inter-annual variability, with areal coverage ranging from 2 to 220 $\times$ 10^3 km^2 during the summer season in different years (Table 7.2). This result supports previous work where large inter-annual variability in marine productivity was observed from 1997 to 2005 across the Southern Ocean SIZ (Smith and Comiso, 2008). However, the general trend of stronger blooms in the summer and weaker blooms in the autumn was evident in all years (Figs. 7.5-7.8), as indicated by a ranking system based on bloom area and duration (Table 7.2). This variation tests the assumption of using a cruise in a single year to represent characteristic conditions of a given season (section 7.2). Although inter-annual variability in total sea ice cover, northward extent and ice edge blooms was observed from 2006 to 2009 (Table 7.4), the strong seasonal signal of the physical and biological processes associated with the winter advance and the spring-summer retreat of the sea ice had a dominant effect on the upper ocean waters of the SIZ (Fig. 7.2).

The distribution of sea surface fCO_2 in the WSC shows high values during the winter and spring and very low values during the summer (Fig. 7.16). From the comparison of satellite chlorophyll-a, sea ice and sea surface temperature data it can be concluded that the WSC was under sea ice during winter 2007 (Tables 7.4 and 7.7). Therefore, the WW carbonate parameters provide a good proxy for surface carbonate distributions beneath sea ice. The effect of sea ice cover is reflected in the relatively constant latitudinal distribution of sea

surface temperature, salinity, fCO_2, DIC and TA across the WSC in winter 2007 (Figs. 7.2 and 7.14). The coldest temperatures and highest salinity are consistent with advancing sea ice in August and September 2007 (Fig. 7.2). The seasonal deepening of the mixed layer (Fig. 7.2d) from autumn to winter, as a result of brine rejection during sea ice formation and increased wind speeds, leads to the entrainment of sub-surface waters and enrichment of DIC in the winter mixed layer. Winter DIC and TA showed homogeneity across the WSC with high concentrations of 2221 ± 3 and 2329 ± 3 μmol kg^{-1}, respectively, supporting the hypothesis of the rejection of carbonate-rich, saline brines upon and during sea ice formation (Rysgaard et al., 2007). Relatively constant winter mixed layer DIC was also observed in the SIZ south of Australia, where concentrations lay in a narrow range of 2182-2184 μmol kg^{-1} (Ishii et al., 2002). These processes bring about the winter conditions of cold, salty, nutrient-rich surface waters that are saturated in CO_2 (Fig. 7.12).

The increase in average fCO_2 in the WSC from winter to 398 μatm in early spring is consistent with trends observed in climatological fCO_2 in the SIZ, where increases up to 410 μatm (Takahashi et al., 2009) and to about 350 μatm at Prydz Bay, east Antarctica, were observed by early spring (Gibson and Trull, 1999). These seasonal increases suggest that throughout the winter the seawater carbonate chemistry is increasingly affected by deep vertical mixing into sub-surface waters supplied by upwelled CDW, increased respiration, remineralisation of organic matter and brine rejection (Nomura et al., 2006; Rysgaard et al., 2007). Beneath the growing ice sheet, the winter mixed layer becomes isolated from the atmosphere (Klatt et al., 2002), allowing fCO_2 to reach supersaturation.

The low light levels and shading from sea ice largely inhibited photosynthetic activity in the underlying water column, which was evident by the high concentrations of macronutrients (Table 7.7). At this time, the majority of the WSC acted as a potential winter source of CO_2 as indicated by positive ΔfCO_2 (Fig. 7.12), as previously observed in the sea ice regions of the Weddell Sea (Bakker et al., 1997; Bellerby et al., 2004; Bakker et al., 2008). However, sea ice cover would have largely inhibited any CO_2 flux out of the ocean, although recent work has suggested that CO_2 diffusion through the sea ice matrix can result in a small flux (Semiletov et al., 2004; Nomura et al., 2006).

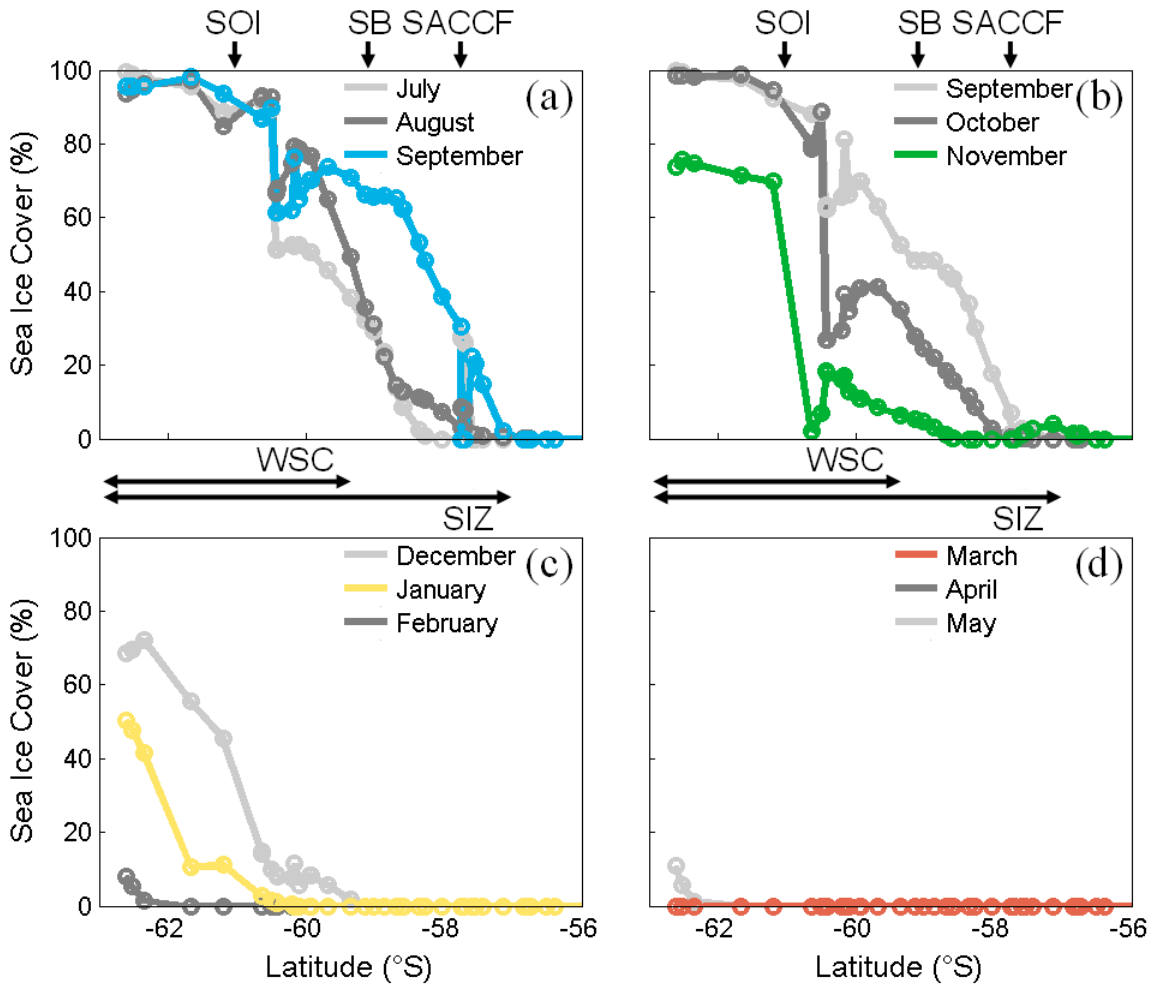

Figure 7.19. The latitudinal distribution of average monthly sea ice cover (%) for all stations along the transect in the SIZ (Figs. 7.9-7.11) in (a) September 2007 (blue), (b) November 2006 (green), (c) January 2008 (yellow) and (d) March 2009 (red). Data are also shown for the other two months (light and dark grey) in each season to evaluate the evolution of the sea ice cover (Stark et al., 2007).

Across the four sub-regions of the SIZ (WSC, SB, SACCF, HNLC) the southward retreating sea ice and subsequent bloom development was accompanied by strong fCO_2 undersaturation first at the SACCF-HNLC boundary and then in the WSC in the spring and summer, respectively (Fig. 7.12). The high macronutrient concentrations of the winter-spring period became largely reduced in the spring and summer SIZ blooms (Figs. 7.2d and 7.3). A distinct seasonal feature in sea surface fCO_2 occurred in spring, where waters of under- and supersaturation were found in close proximity (Fig. 7.12). The ice edge was located at around 59°S (Fig. 7.19b), where waters exhibited strong supersaturation of fCO_2 (Figs. 7.12).

Breaking up and melting of the sea ice near the South Orkney Islands allowed immediate outgassing of the winter CO_2 'reserve', especially where high wind speeds enhanced the air-sea CO_2 flux to 6.0 ± 2.7 mmol m^{-2} d^{-1} (Table 7.6 and Fig. 7.13c). In contrast, waters north of the ice edge (SB and SACCF) were a strong sink of atmospheric CO_2 up to 11.6 ± 1.2 mmol m^{-2} d^{-1} due to the extensive SIZ bloom of spring 2006 (Fig. 7.5). Surface waters were characterised by warm, fresh and shallow mixed layers that supported the large phytoplankton bloom (Fig. 7.2). The seasonal cruise JR161 intercepted the SIZ bloom in November 2006, which was the fourth strongest bloom (product rank of 12) in the SIZ from 2006-2009 (Table 7.2). Therefore the degree of DIC depletion and fCO_2 undersaturation attributed to 'spring' conditions from the JR161 dataset is likely to be greater than average spring conditions but still contributes to a realistic inter-seasonal discussion.

Sea ice seasonally covers large areas of the Southern Ocean and could represent a major source of bioavailable iron to support phytoplankton blooms upon ice melt (Sedwick et al., 2000). However, the persistent high sea surface iron concentrations between the SB and the South Orkney Islands from spring to summer (Fig. 7.2d) suggest that iron supply is not dominated by seasonal processes, such as sea ice retreat, and is therefore predominantly from other oceanic sources (section 1.4.3.2). These include the South Orkney Islands, the SSR (Fig. 7.1) or advection from waters that have passed over the shelf of the west Antarctic Peninsula (Dulaiova et al., 2009; Nolting et al., 1991; Sanudo-Wilhelmy et al., 2002; Ardelan et al., 2010) in addition to upwelling and advection within the ACC (Hoppema et al., 2003). The generally higher dFe concentrations during spring 2006 (≥ 1.4 nM) near the ice edge could, however, include contributions from the recently melted sea ice (Lannuzel et al., 2007; Lannuzel et al., 2008). This region was still beneath sea ice cover and as the fCO_2 remained at saturation levels with iron concentrations 0.5-1.5 nM, this suggests that light was limiting to phytoplankton growth during the spring (Boyd et al., 1999). Supersaturated fCO_2 at the lowest dFe concentrations in spring suggest iron and light co-limitation beneath ice covered waters of the WSC (Fig. 7.17e). By the summer with increased light and the absence of sea ice, sea surface fCO_2 had decreased by 50-100 μatm in the blooms across a similar range of iron concentrations.

The spring and summer thaw continued to expose the shallow and fresh surface waters (Fig. 7.2) to increased light levels and any iron present could act to seed the shallow mixed layer and promote phytoplankton growth. These processes are likely to contribute to the enhanced

chlorophyll-a that was observed from spring to summer in the SIZ of the Scotia Sea from 2006-2009 (Fig. 7.4). These biological events signify the start of the growing season and contribute to the observed reduction in sea surface fCO_2 and DIC (Figs. 7.2a and 7.14a). The transition from CO_2 saturated ice covered waters to CO_2 undersaturation during and upon ice melt was observed during spring 2006 (above) and summer 2008 (Chapter 5), which was ascribed to strong biological carbon uptake with a contribution from calcium carbonate processes in sea ice (Chapter 5).

The processes involved in water column stability and the seeding of phytoplankton communities occurred in similar patterns throughout the growing season and subsequently resulted in strong fCO_2 undersaturation that 'tracked' the southward retreating ice edge (Figs. 7.2). By autumn, the SIZ blooms had largely diminished and sea surface fCO_2 in the WSC had begun to return towards pre-bloom saturation values (Figs. 7.5-7.8 and 7.16). This has been attributed to low light levels instigating a limitation to phytoplankton growth, as iron supply within the upwelled UCDW, or from advection, was maintained (Hoppema et al., 2003; van Oijen et al., 2004). Autumnal light limitation, seasonal warming and reduced CO_2 uptake was most pronounced for the four southern sub-regions of the Scotia Sea (WSC, SB, SACCF, HNLC) (Fig. 7.16).

7.15. Transient CO_2 sinks across the ACC fronts

Large variability in seasonally averaged sea surface fCO_2 was observed at the SACCF, whereas the SB and PF were less variable and had remarkably similar trends with moderate undersaturation spring to autumn (Fig. 7.16). The SACCF separated more saline waters beneath the sea ice to the south from fresher waters to the north as its location was close to the upper limit of the SIZ at 57°S (Fig. 7.2c). High concentrations of DIC and TA were observed at the SB during the winter (Table 7.7) and have been attributed to the shoaling isohalines at this location, promoting upwelling of UCDW into the sub-surface water (Chapter 4).

During most of the winter, the SB and SACCF were beneath sea ice allowing DIC enrichment and supersaturation of fCO_2, due to vertical mixing and inhibited outgassing (section 7.12). Sea ice melt produced large scale freshening, firstly at the SACCF during spring and then at the SB during summer (Fig. 7.2c). Mixed layer depths became shallower by about 40-60 m at both fronts (Table 7.7). The receding ice edge (Fig. 7.19), increased light levels and enhanced iron concentrations stimulated the growth of phytoplankton blooms that swiftly reduced fCO_2

in the stratified surface waters (Fig. 7.2). The southward retreating sea ice had distinct effects on the phytoplankton activity and subsequently on the carbonate chemistry at both southern fronts. Depletion in DIC and TA between 20-50 μmol kg^{-1} from winter to summer at the SB and SACCF (Table 7.6 and Fig. 7.14) are due biological utilisation (DIC only), dilution by melting sea ice (mainly TA) and a small contribution from released brines where $CaCO_3$ precipitation has taken place (Chapter 5).

The effect on the seasonal fCO_2 distributions was largest at the SACCF, where sea ice had departed by October and a large, longer-lasting bloom had reduced sea surface fCO_2 by more than 50 μatm (Figs. 7.2 and 7.19). The SACCF was located in the centre of the SIZ bloom (Fig. 7.4) and represented the strongest fCO_2 undersaturation (Fig. 7.12) and CO_2 sink of -11.6 ± 1.2 mmol m^{-2} d^{-1} during spring 2006 (Fig. 7.13c and Table 7.6). This contributed to the observation of higher fCO_2 from winter to spring, where sea ice is present for longer, at the SB compared to the SACCF (Fig. 7.16).

Through the summer and into the autumn, sea surface temperatures and salinity increased in the SB and SACCF frontal regions due to seasonal warming and the absence of sea ice (Fig. 7.2b-c). The transformation of the SB to a moderate CO_2 sink of 4.6 ± 1.7 mmol m^{-2} d^{-1} by the summer (Fig. 7.13c and Table 7.6) is largely the result of biological carbon uptake despite surface warming of over 2°C (Table 7.7). The later initiation of the blooms at the SB usually means that they persist well into the summer, transforming the CO_2 saturated waters to a region of CO_2 undersaturation. Oppositely, the rapid increase in fCO_2, by up to 50 μatm, from spring to summer at the SACCF is due to the decaying bloom for a similar rate of surface water warming (Table 7.7). Upwelling of UCDW into sub-surface waters in the region of the SB and SACCF (Fig. 4.2) provides a sufficient iron flux into the upper ocean to support moderate production (de Barr et al., 1995; Hoppema et al., 2003; Blain et al., 2007). However, the main entrainment of upwelled UCDW occurs during the wind-driven deep mixing associated with autumn and winter conditions (Hoppema et al., 2003), which restricts the ability of the blooms to develop as light becomes limiting. Furthermore, transport within the Ekman layer (Fig. 1.1) removes up to 25% of the upwelled iron from the ACC before it can be utilised by phytoplankton (Hoppema et al., 2003). Therefore, phytoplankton biomass and the organic carbon pump are reduced through the autumn at the SB and SACCF (Figs. 7.5-7.8), allowing sea surface fCO_2 to reach saturation levels (Fig. 7.16) prior to the arrival of sea ice in the winter (Fig. 7.19).

Beyond the influence of sea ice, the PF had a smaller seasonal range in sea surface temperature, salinity and mixed layer depth compared to the SB and SACCF (Fig. 7.2 and Table 7.6). During each season, the surface expression of the PF could be identified by a sharp increase in temperature (Fig. 7.2b). This usually coincided with increases in salinity (Fig. 7.2c) and concentrations of macronutrients (Fig. 7.3). Seawater fCO_2 was undersaturated with respect to the atmosphere from spring to autumn (Fig. 7.16); a feature observed in spring 1992 in the presence of diatoms (Bakker et al., 1997). Relative to the SACCF, the SB and PF become the important sites for biological carbon uptake during the summer and autumn, representing sinks for atmospheric CO_2 of about 4 mmol m^{-2} d^{-1} (Fig. 7.13c and Table 7.6).

In contrast to the SB and SACCF, the waters of the PF have been found to be iron-rich and support phytoplankton blooms for longer, leading to persistent seasonal CO_2 undersaturation (Fig. 7.16) (de Baar et al., 1995; Smetacek et al., 1997; Bracher et al., 1999). With summer reductions in fCO_2, DIC and increases in chlorophyll-a, it is hypothesised that the PF is an area of annual uptake of atmospheric CO_2 between 2.3 and 4.5 mmol m^{-2} d^{-1} (Fig. 7.13c and Table 7.6) as a result of organic matter production through photosynthesis. This supports earlier observations of circumpolar enhanced export of particulate organic carbon (section 1.5.4.1) from diatom blooms in the PF region in the Atlantic (Rutgers van der Loeff, et al., 1997; Tremblay et al., 2002) and Pacific (Daly et al., 2001) sectors of the Southern Ocean. Increased water temperature, by over 1 °C from spring to summer (Table 7.8), would act to strongly compensate the biological decrease of fCO_2 (Fig. 7.18), however this is difficult to assess due to the meandering nature of the PF.

7.16. High-nutrient low-chlorophyll and CO_2 source waters

The HNLC waters showed relative seasonal homogeneity in sea surface fCO_2 with a general increase from winter to autumn (Fig. 7.16). The fCO_2 was close to saturation with respect to the atmosphere throughout the year with the distinct exception of spring. The large springtime variation is attributed to the SIZ blooms that often extended into the 'HNLC' latitude band, subsequently reducing the fCO_2. This was observed in the chlorophyll-a concentrations, which increased to 3.4 mg m^{-3} in spring 2006 (Fig. 7.2e and Table 7.7). However, by the summer the high chlorophyll-a concentrations had dissipated to less than 0.2 mg m^{-3} and were retained for the majority of the year, confirming the region as having HNLC conditions (Fig. 7.4 and Table 7.7).

Sea surface temperature increased by about 3 °C from winter to autumn, corresponding to an increase in fCO_2 by nearly 50 μatm (Table 7.7). In the absence of counteracting biological processes, this lead to a thermodynamically driven fCO_2 supersaturation in the central ACC (Fig. 7.12). However, a decrease in DIC up to 40 μmol kg^{-1} from winter to summer (Fig. 7.14a) indicated that biological carbon utilisation had occurred from the SIZ bloom that intruded the HNLC waters during the spring (section 7.12) and the standing stock of phytoplankton that remained in the upper ocean by the summer (section 6.11). Despite this, seasonal warming had a dominant effect on fCO_2 concentrations (Fig. 7.18). Similarly to the SACCF, initial CO_2 uptake at the start of the growing season evolved into an efflux of CO_2 of 2.3 ± 1.0 mmol m^{-2} d^{-1}, driven by summer warming (Fig. 7.13c and Table 7.6).

7.17. The South Georgia bloom and annual CO_2 uptake

The GB region showed the greatest range in sea surface fCO_2 with a seasonal difference of nearly 150 μatm (Fig. 7.16). The highest fCO_2 values of 444 ± 13 μatm occurred during winter (Table 7.8), making the region an especially strong source of CO_2 of 16.2 ± 4.1 mmol m^{-2} d^{-1} (Fig. 7.13c and Table 7.6). Salty surface waters combined with strong winds and surface cooling, produced deep mixed layers down to 120 m (Fig. 7.2f). From relatively low fCO_2 values during the autumn, these processes encouraged deep vertical mixing into sub-surface waters, which are supplied with DIC from upwelled UCDW (Chapter 4) with the influence of the SACCF in the GB (section 6.4). The DIC-rich sub-surface waters became entrained into the winter mixed layer with an ensuing increase in DIC (and DIC_{34}) to values close to 2190 μmol kg^{-1} (Fig. 7.14a), leading to increased sea surface fCO_2 by over 100 μatm by the winter (Fig. 7.16). Evidence of deep vertical mixing was observed over the NSR and into the GB, as wintertime enrichment of silicate, nitrate, and phosphate raised surface concentrations to 47.2, 28.5 and 2.0 μmol kg^{-1}, respectively (Table 7.8), alongside the supersaturated fCO_2.

With the onset of spring, water temperatures had warmed by nearly 1.75 °C and a notable freshening had taken place, reducing salinity by 0.14 units (Table 7.8). The upper ocean had become stratified with mixed layers of 88 ± 19 m. With increased light levels throughout the spring, the warmer and more stable water column presented conditions that encourage phytoplankton growth. Initiation of the South Georgia bloom in spring or early summer (Table 7.4) transformed the winter fCO_2 supersaturation (Fig. 7.12) with incremental decreases of about 70 μatm from the winter to spring and spring to summer (Fig. 7.16). Increased

chlorophyll-a, over 5 mg m^{-3}, in the GB coincided with surface water iron concentrations exceeding 1.0 nM (Figs. 7.2d-e and 7.17e-f). Inspection of sea surface conditions and circulation patterns downstream of South Georgia, in relation to other Southern Ocean islands, provides evidence for natural iron fertilisation (sections 6.13 and 6.14).

Continual warming and freshening of the sea surface, from glacial melt from South Georgia and sporadic precipitation events, occurred throughout the summer and into early autumn (Fig. 7.2 and Table 7.8). The water column maintained stratification with a shallowing of the mixed layer to 20-50 m. By the summer, the South Georgia bloom reached maximum extent and spread across the GB (Figs. 7.5-7.8). Based on the area and duration bloom ranks, the strongest South Georgia blooms always occurred during the summer months December-February (Table 7.3). Elevated chlorophyll-a concentrations of 2-12 mg m^{-3} corresponded to exceptionally undersaturated seawater fCO_2 between 250 and 300 μatm (Figs. 7.2 and 7.17e). The presence of diatoms in the bloom (Korb et al., 2010) was evident on the complete depletion of silicate in surface waters of the GB (Fig. 7.3c and Table 7.8).

The ΔfCO_2 and DIC reached annual minima for this region of -120 μatm and 2084 μmol kg^{-1}, respectively, in the core of the bloom (Fig. 7.12 and Table 7.8). These sea surface carbonate features turned the GB into the strongest seasonal sink for atmospheric CO_2 in the Scotia Sea of 12.0 ± 4.2 mmol m^{-2} d^{-1} (Fig. 7.13c and Table 7.6). This air-sea CO_2 flux (geographical limits, 53.0-50.5°S, average summer 2006-2009) in the GB was dominated by the CO_2 uptake of 15.1 ± 5.7 mmol m^{-2} d^{-1} in the South Georgia bloom (biological limits, 53.5-51.5°S, summer 2008) (Table 6.5). The strong sink for atmospheric CO_2 persisted into the autumn, although sea surface fCO_2 had increased on average by 40 μatm (Fig. 7.16) to weaken the sink to 9.6 ± 2.3 mmol m^{-2} d^{-1} (Fig. 7.13c and Table 7.6).

7.18. The role of the Scotia Sea in the marine carbon cycle

7.18.1. Annual source or sink of CO_2?

For each seasonal transect, instantaneous CO_2 fluxes were determined for every sea surface fCO_2 measurement with seasonally averaged wind speeds from QuikSCAT (Fig. 7.13c). The seasonal and annual flux of CO_2 for the Scotia Sea has been estimated by averaging the appropriate short term fluxes weighted for the latitudinal limit for each region (Table 7.9). Sea ice coverage, absence of photosynthetic activity and deep vertical mixing created a wintertime

CO_2 source of 2.9 ± 1.0 mmol m^{-2} d^{-1} along the transect in the Scotia Sea (Table 7.9). This would be dramatically enhanced if CO_2 exchange through the sea ice, assumed here to be negligible, takes place. The combination of the intense South Georgia bloom, the SIZ blooms at the receding ice edge and enhanced biological activity at the SB, SACCF and PF largely counteracted seasonal warming to create a strong oceanic CO_2 sink of 5.7 ± 1.4 mmol m^{-2} d^{-1} in the summer. The spring and autumn seasonal fluxes represent 'transitional' values between the annual maximum and minimum air-sea CO_2 fluxes of winter and summer, respectively. Finally, the seasonal analysis of the marine carbon cycle shows that the ocean along the transect from 62.6-49.5°S is an annual CO_2 sink of 6.2 ± 2.1 mmol m^{-2} d^{-1}. The relatively large standard deviation in the CO_2 fluxes reflects the variability and mosaic nature of the marine carbon cycle of the Scotia Sea.

Table 7.9. Seasonal and annual air-sea CO_2 fluxes (mmol m^{-2} d^{-1}) for the eight sub-regions of the Scotia Sea. Flux calculations as in Table 7.6. The annual regional flux is calculated from the average of the winter, spring, summer and autumn fluxes (equal weighting to each season) for each region weighted by latitude along the transect (13.1° latitude). Fluxes marked with * are assumed to be 0 due to sea ice cover. As no winter data exists for the PF a flux of 0 is estimated (**) based on comparable flux trends with the NSR and ACC regions. Standard deviation as for Table 7.6, in parentheses. Negative fluxes indicate oceanic uptake of CO_2.

Region	*Latitude* °S		*Air-sea CO_2 flux* *mmol m^{-2} d^{-1}*				
	Limits	*Total*	*Winter*	*Spring*	*Summer*	*Autumn*	*Annual*
WSC	-62.6/-59.5	3.1	0*	6.0 (2.7)	-6.2 (3.8)	-2.4 (1.5)	-2.6 (4.9)
SB	-59.5/-58.5	1.0	0*	-1.1 (2.9)	-4.6 (1.7)	-3.0 (2.9)	-8.7 (4.4)
SACCF	-58.5/-57.5	1.0	0*	-11.6 (1.2)	-1.2 (1.7)	1.9 (0.8)	-10.9 (2.2)
HNLC	-57.5/-56.0	1.5	-0.1 (0.5)	-9.2 (4.1)	2.3 (1.0)	2.0 (1.6)	-5.0 (4.5)
ACC	-56.0/-55.0	1.0	-3.4 (3.8)	2.2 (1.2)	-5.0 (4.7)	-3.0 (0.8)	-9.2 (6.2)
NSR	-55.0/-53.0	2.0	0.7 (3.3)	2.7 (1.3)	-6.9 (3.5)	-3.4 (1.6)	-6.9 (5.2)
GB	-53.0/-50.5	2.5	16.2 (4.1)	0.6 (1.5)	-12.0 (4.2)	-9.6 (2.3)	-4.8 (6.5)
PF	-50.5/-49.5	1.0	0**	-2.3 (1.2)	-4.5 (1.2)	-4.4 (2.1)	-11.2 (2.7)
Transect	-62.6/-49.5	13.1	2.9 (1.0)	-0.1 (0.9)	-5.7 (1.4)	-3.3 (0.7)	**-6.2 (2.1)**

A likely caveat is that the potentially strong CO_2 source waters beneath sea ice are liable to outgas to a certain extent upon immediate breaking and melting of the sea ice, before phytoplankton activity begins to reduce the fCO_2 (section 7.12). This scenario was encountered in spring 2006, where the ice edge was close to the South Orkney Islands (Fig. 7.19) and, just south of the SIZ bloom, waters were supersaturated in fCO_2 (Fig. 7.12). As the South Orkney Islands are within the WSC region, averaging of the data per sub-region implied that the whole region was a strong CO_2 source, despite the fact that at least half of the sea surface area was beneath sea ice (Fig. 7.19). This would lead to an overestimation of CO_2 released from the WSC region during spring (Tables 7.8-7.9). However, investigations have

shown that sea ice may be semi-permeable to CO_2 and some gas exchange may occur (Semiletov et al., 2004; Nomura et al., 2006) and it is also likely that leads and patches of open water would exist in the sea ice, prior to passage of the ice edge. Therefore, it is believed that any possible overestimation of the WSC region CO_2 flux, based on CO_2 source data north of the South Orkney Islands, is small.

7.18.2. Inter-annual variability and the future

Satellite derived chlorophyll-a concentrations from 2006 to 2009 showed the annual occurrence of mesoscale phytoplankton blooms in the SIZ and downstream of South Georgia (Figs. 7.5-7.8). These biological features represented vast areas of CO_2 undersaturation (Fig. 7.12) that created strong CO_2 sinks on seasonal timescales and have an important effect on the annual CO_2 flux of the Scotia Sea (Table 7.9). The SIZ blooms were initiated during spring at the receding ice edge, generally persisted through the summer and decayed by early autumn (Table 7.4). Large inter-annual variability existed in the month of bloom termination, ranging from October to May. A second variable is surface area, as some SIZ blooms covered the whole SIZ (63-57°S) and some just extended across 2° of latitude (Table 7.2). The South Georgia bloom was initiated during spring, had maximum coverage and intensity during summer and decayed by autumn (Table 7.4). Slight variation in the South Georgia bloom existed as initiation occurred in early summer in one year and in other the bloom had decayed by the end of the summer (Table 7.3). However, in all years the bloom occupied most of the GB and peaked in the summer (highest bloom ranks) with notable advection in the SACCF and PF, evident from the patterns of chlorophyll-a that lead out of the GB to the east (Fig. 7.4).

The seasonal CO_2 fluxes showed strong CO_2 uptake (a) to the north of the retreating sea ice (including the SACCF) in spring, (b) in the south of the SIZ (including the SB) in summer, tracking the ice edge, and (c) in the GB up to the PF in summer and autumn (Fig. 7.13c). However, biological features such as blooms are not confined within the limits of the sub-regions and have been shown to extend across the regional boundaries (section 7.16). In order to investigate this, the effects of the principle blooms of the SIZ and GB on oceanic CO_2 uptake were analysed by consideration of the area and duration of the bloom, irrespective of geographical limits (Tables 7.10 and 7.11). These ‘biological’ limits better capture the true biological effect on the marine carbon cycle during each season. As satellite chlorophyll-a data existed for each season for each year, inter-annual variability in bloom initiation, duration and

coverage can be investigated (Table 7.4) and its effects on the seasonal carbon cycle in the Scotia Sea can be explored.

Table 7.10. The average seasonal coverage (km^2), duration (days), ΔfCO_2(sea-air) (μatm) and CO_2 flux (mmol m^{-2} d^{-1}) for the seasonal ice zone blooms ([chl-a] ≥ 2.0 mg m^{-3}) from 2006 to 2009. The ΔfCO_2 and flux values are averages of all data (*n*) along the transect during spring 2006 (*n* = 13), summer 2008 (*n* = 26) and autumn 2009 (*n* = 12), within the average latitudinal limits. Air-sea CO_2 fluxes were calculated using seasonally averaged wind speeds with the Nightingale et al. (2000) relationship. Total flux (Tg C, where Tg is 10^{12} g C) is calculated using the tabulated averages for area, duration and flux in a given season. Standard deviation is shown in parentheses. Negative fluxes indicate oceanic uptake of CO_2.

Season	*Latitude*	*Longitude*	*Area*	*Duration*	*ΔfCO_2*	*Flux*	*Total flux*
	°S	*°W*	*10^3 km^2*	*days*	*μatm*	*mmol m^{-2} d^{-1}*	*Tg C*
Spring	-58.6/-57.8	-48.0/-42.5	31 (31)	48 (16)	-40 (23)	-7.3 (4.3)	-0.13 (0.16)
Summer	-59.5/-58.3	-44.5/-39.8	65 (104)	69 (27)	-31 (13)	-4.4 (1.9)	-0.24 (0.41)
Autumn	-59.3/-58.6	-45.9/-44.5	8 (12)	24 (20)	-12 (16)	-2.2 (2.9)	-0.01 (0.01)
Total							**-0.38 (0.44)**

Sea ice is an important component of the global climate system, where the extent, defined here as the area between the ice-ocean edges, is one of the major aspects (Gloersen and Campbell 1991). The sea ice extent affects the amount of light absorbed by the upper ocean, the organic carbon pump and the ocean-atmosphere exchange of heat, moisture and CO_2. As a result, the SIZ was a highly dynamic region, where large inter-annual variability in sea ice extent was accompanied by variations in phytoplankton blooms (as shown by high standard deviations relative to the seasonal means, Table 7.10), supporting previous observations (Smith and Comiso, 2008).

The years 2007 and 2008 represented maximum and minimum sea ice extent, respectively, both with weak and patchy blooms in the SIZ after ice melt (Table 7.4). This demonstrated the influence of sea ice on the biological activity of the Scotia Sea and accounted for the large

variations in average bloom features in spring and summer (Table 7.10). In contrast, 2006 represented a year of moderate sea ice cover that reached a northward maximum of 58°S in August (Fig. 7.9). Sea ice retreat began in September, exposing a large part of the SIZ to increased light levels, elevated dFe concentrations and a meltwater stabilised water column (Fig. 7.2). Subsequently, a large bloom was seeded by October 2006 (Figs. 7.5-7.6), which developed into the strongest bloom (rank 2, Table 7.2) with substantial biological carbon uptake (section 7.14) in the SIZ during the research period.

Despite the inter-annual variability, the bloom cycle of initiation, growth and decay occurred to some magnitude each year in the SIZ. The Scotia Sea data revealed a strong correlation between sea ice and biological activity (section 7.14); both of which are intrinsically linked to the carbonate chemistry of this region (Chapter 5). The presence of stronger jets in the ACC can often be observed in the SIZ as elevated chlorophyll-a was advected across the Scotia Sea by the SB and SACCF (Fig. 7.4). Aided by frontal transport and continual phytoplankton growth, the SIZ blooms often increased in areal coverage and duration into the summer. This contributed to a huge spatial uptake of CO_2 in the summer. For an average bloom coverage of 65,000 km^2 and average duration of 69 days, 0.24 ± 0.41 Tg C was transferred from the atmosphere to the upper ocean of the SIZ in the summer.

The average concentration of the entire Antarctic sea ice cover in December (1997-2006) (Fig. 7.20) corresponded with the observed inter-annual variability in the sea ice of the Scotia Sea, with a decadal variation in cover ranging from 55 to 65% (Smith and Comiso, 2008). The large inter-annual variability associated with the SIZ blooms, particularly during the summer, suggested that as much as 1.01 ± 0.72 Tg C was transferred from the atmosphere to the upper ocean of the SIZ for the substantial bloom of 2006/2007 that covered 220,000 km^2 and persisted for 87 days (Table 7.2). This gigantic CO_2 sink in the SIZ followed a winter of moderate sea ice extent in August and retreat by September (Table 7.4). Oppositely, the weak bloom of summer 2007/2008 removed as little as 0.01 ± 0.17 Tg C from the atmosphere over an area of about 2 km^2 for 31 days. This followed the ‘icy’ winter of 2007, where sea ice covered the whole SIZ and began a relatively late retreat.

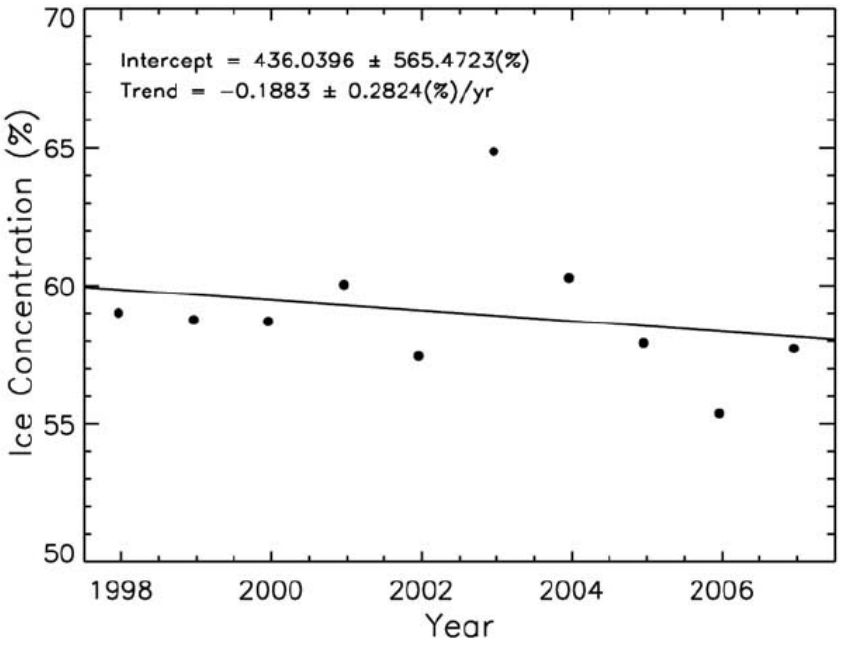

Figure 7.20. Mean Antarctic sea ice concentration (%) in December from 1997 to 2006 from the Special Sensor Microwave Imager (SSM/I) on the Defence Meteorological Satellite Program (DMSP) (Smith and Comiso, 2008).

These considerable variations in total CO_2 uptake, with differences of two orders of magnitude, further highlight the relationship between sea ice, phytoplankton and carbonate chemistry and show the vulnerability of the SIZ CO_2 sink to changes in sea ice and phytoplankton dynamics. Extreme wind events (up to 14 m s^{-1}) and grazing pressure have been determined as the major controls on ice edge blooms in the Weddell Sea during spring and summer (Lancelot et al., 1993). In contrast, wind speeds in the WSC, during spring and summer, were such that water stratification was maintained, encouraging phytoplankton growth, alongside substantial CO_2 uptake. The effect of zooplankton grazing was not examined. As for other Arctic and Antarctic sea ice studies, the inter-annual variability of the SIZ blooms of the Scotia Sea was closely correlated with the time of sea ice retreat (Wu, et al., 2007; Smith et al., 2008). Trends in sea ice concentration from 1997 to 2006 showed a decline in sea ice coverage by about 2% per decade (Fig. 7.20) (Smith and Comiso, 2008). Based on the results presented here, such a trend could weaken the SIZ blooms and subsequent biological carbon uptake of the Scotia Sea in the future (Montes-Hugo et al., 2009).

The largest and most intense South Georgia bloom was initiated in September 2007 and persisted for eight months before decaying in April 2008 (Table 7.4). During this time the

bloom extended across the whole GB with distinct advection of elevated chlorophyll-a within the SACCF and the PF (Fig. 7.7). The bloom during summer 2006/2007 was the weakest summer bloom over the four years (rank 20, Table 7.3), covering the northern part of the GB. Despite some degree of inter-annual variability, the seasonal initiation, growth and termination of the South Georgia bloom was the dominant signal. The bloom always reached maximum coverage and duration during summer (based on the highest bloom ranks), with relative inter-annual consistency (Tables 7.3). Therefore, average areal coverage and duration of the South Georgia bloom combined with fCO_2 measurements of summer 2008 (JR177) yields a representative estimate of 0.84 ± 0.38 Tg C transferred from the atmosphere to the upper ocean each summer (Table 7.11).

Table 7.11. The average seasonal coverage (km^2), duration (days), ΔfCO_2(sea-air) (μatm) and CO_2 flux (mmol m^{-2} d^{-1}) for the South Georgia bloom ([chl-a] ≥ 2.0 mg m^{-3}) from 2006 to 2009. The ΔfCO_2 and flux values are averages of all data (*n*) along the transect during spring 2006 (*n* = 7), summer 2008 (*n* = 26) and autumn 2009 (*n* = 52) within the average latitudinal limits. Air-sea CO_2 fluxes were calculated using seasonally averaged wind speeds with the Nightingale et al. (2000) relationship. Total flux (Tg C, where Tg is 10^{12} g C) is calculated using the tabulated averages for area, duration and flux in a given season. Standard deviation is shown in parentheses. Negative fluxes indicate oceanic uptake of CO_2.

Season	*Latitude*	*Longitude*	*Area*	*Duration*	*ΔfCO_2*	*Flux*	*Total flux*
	°S	*°W*	*10^3 km^2*	*days*	*μatm*	*mmol m^{-2} d^{-1}*	*Tg C*
Spring	-52.0/-51.0	-38.6/-36.9	16 (13)	50 (19)	-25 (9)	-4.4 (1.6)	-0.04 (0.04)
Summer	-52.6/-50.6	-40.7/-35.9	76 (16)	88 (2)	-67 (27)	-10.4 (4.2)	-0.84 (0.38)
Autumn	-52.8/-51.4	-40.9/-38.5	27 (25)	41 (27)	-50 (14)	-9.3 (2.5)	-0.13 (0.15)
Total							**-1.01 (0.41)**

The technique of 'biological' limits was employed to quantify the biological effect on the marine carbon cycle of the GB during summer 2008 (Chapter 6). At this time, the South Georgia bloom was the strongest summer bloom observed during the 2006-2009 research period, which was intercepted by the RRS *James Clark Ross* on cruise JR177 in early February 2008 (Table 7.1). The extensive bloom created a strong oceanic CO_2 sink of -15.1 ± 5.7 mmol m^{-2} day^{-1}, transferring 1.30 ± 0.45 Tg C from the atmosphere to the ocean during

summer 2008 (section 6.13). This indicated that the South Georgia bloom of summer 2007/2008 (Fig. 7.7) removed 0.30 Tg more carbon from the atmosphere than the average 1.01 ± 0.41 Tg C that was transferred from atmosphere from spring to autumn each year (Table 7.11). This further emphasizes the nature of inter-annual variability in the marine carbon cycle of the Scotia Sea.

The summation of the average sink fluxes of the Scotia Sea blooms during spring, summer and autumn was 1.39 ± 0.56 Tg C for a total average bloom area of 75×10^3 km^2 (Tables 7.10 and 7.11). Compared to the climatological estimate of the annual Southern Ocean sink flux of 0.06 Pg C (Takahashi et al., 2009) over 30.6×10^6 km^2, the blooms of the Scotia Sea accounted for over 2% of the total Southern Ocean CO_2 sink at only 0.2% of the areal coverage of the entire Southern Ocean.

7.19. Ocean acidification

7.19.1. The Scotia Sea and ocean acidification

Across the Scotia Sea, the action of the organic carbon pump in the SIZ and South Georgia blooms (sections 7.14 and 7.17) depleted the mixed layer DIC, giving the AASW concomitant high concentrations of carbonate ions ($[CO_3^{2-}]$) and increased pH_T (Figs. 4.4 and 7.21). The $[CO_3^{2-}]$ and aragonite saturation states reached summer maxima of 153 μmol kg^{-1} and 2.3, respectively, in the NSR-GB region (Fig. 7.14c-e). The elevated $[CO_3^{2-}]$ during the summer suggest that AASW is seasonally saturated with respect to aragonite.

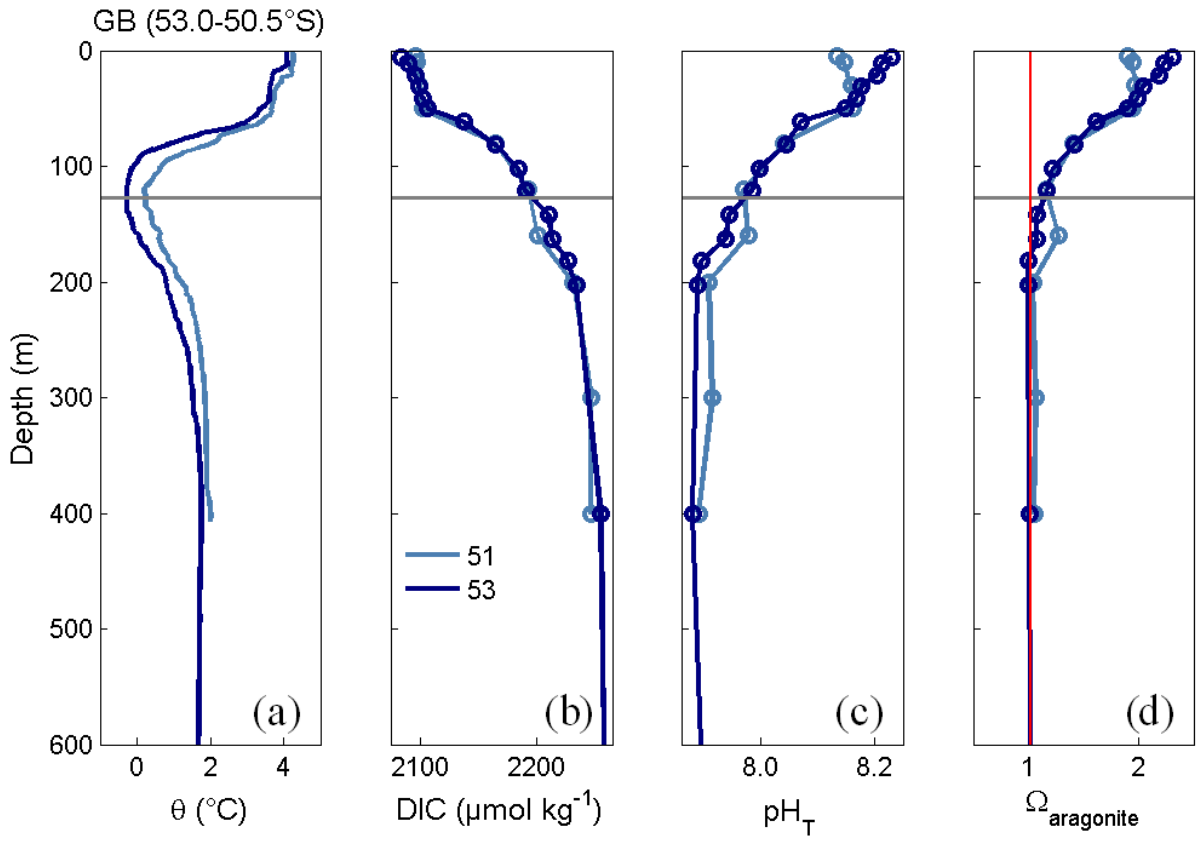

Figure 7.21. Vertical profiles of upper water column (a) potential temperature (θ, °C), (b) dissolved inorganic carbon (DIC, µmol kg^{-1}), (c) total pH (pH_T) and (d) aragonite saturation state (Ωaragonite) for Georgia Basin (GB) stations 51 and 53. The depth of the θ_{min} of the Winter Water is marked by the horizontal grey line and the limit of aragonite undersaturation (Ωaragonite < 1) is marked by a vertical red line in (d).

Increased vertical mixing during winter facilitated the ventilation and entrainment of sub-surface waters within the winter mixed layer where shoaling isohalines in the GB, at the SACCF and SB and frontal meanders provided a pathway for UCDW to upwell (Chapter 4). This was particularly evident in the regions of the SB, SACCF and in the GB (Fig. 4.2). Subsequently, wintertime surface water [CO_3^{2-}], pH_T and aragonite saturation states south of 59°S are reduced with a relatively homogeneity (Fig. 7.14c-e).

Aragonite saturation states are generally lowest at high latitudes due to increased solubility of CO_2, and hence elevated DIC concentrations, and increased solubility of carbonate minerals with decreasing temperature (section 1.5.2). Low saturation states (Ωaragonite < 1.3) were observed south of 59°S during summer and winter, with corresponding small seasonal

amplitudes (Figs 7.14e and 7.15e). These waters are beneath sea ice cover during winter and early spring and are close to the upwelling region of the SB (sections 4.2 and 7.12). Both of these factors contribute to DIC enrichment, carbonate depletion and low aragonite saturation states at the surface south of 59°S throughout the year.

Cold, saline and deep winter mixed layers in the GB were enriched in DIC, leading to fCO_2 supersaturation at the sea surface (Figs. 7.2 and 7.14). From the depth of the WW, a strong gradient in DIC existed into the surface waters (Fig. 7.21b). As UCDW is DIC-rich (Table 4.1), the upward movement of this water mass led to DIC enrichment below the thermocline at about 200 m depth. This was accompanied by a lowering of the pH_T and saturation state for aragonite from the base of the WW layer to about 200 m (Fig. 7.21c-d). Below 200 m, the water column was undersaturated with respect to aragonite. As a result of deep winter mixing to 100-200 m (Fig. 7.2f), winter AASW in the GB became relatively carbonate-poor (< 80 μmol kg^{-1}) and acidic with a aragonite saturation states less than 1.2 (Fig. 7.14). These processes contributed to the large seasonal amplitude in all sea surface carbonate parameters in the GB (Fig. 7.15) and increased the risk of ocean acidification, from bottom-up influences, in the northern Scotia Sea.

7.19.2. Ocean acidification in the Southern Ocean

In agreement with the Scotia Sea data (Fig. 7.14), empirical reconstructions of Southern Ocean data revealed a [CO_3^{2-}] minima, close to 90 μmol kg^{-1}, south of 60°S during the winter and maximum [CO_3^{2-}], up to 125 μmol kg^{-1}, between 55-50°S during the summer (McNeil and Matear, 2008). This also agrees with a basin scale average for surface [CO_3^{2-}] of 105 μmol kg^{-1} for the entire Southern Ocean (Orr et al., 2005). However, winter minima in [CO_3^{2-}] and pH_T of 79 μmol kg^{-1} and 7.98, respectively, were observed in the Scotia Sea in the GB. This is lower compared to the empirical data that indicate wintertime [CO_3^{2-}] of 125 μmol kg^{-1} and pH_T of 8.07 at the same latitude (McNeil and Matear, 2008).

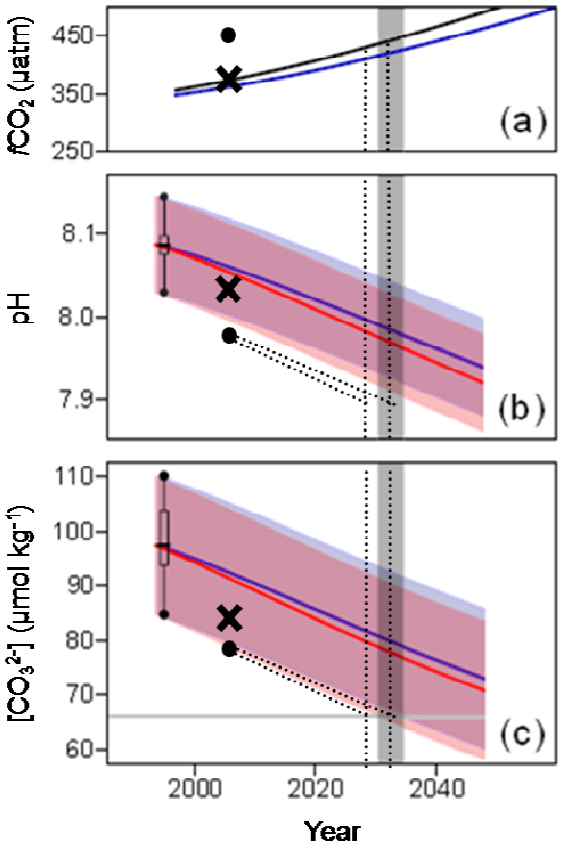

Figure 7.22. Observations and future predictions of sea surface acidification in the Southern Ocean, adapted from McNeil and Matear (2008). (a) fCO_2 (µatm) in air, IPCC IS92a emission scenario (black), and water (south of 60°S) from the CSIRO ocean carbon model (blue). Predictions of surface water (b) pH and (c) carbonate concentrations ($[CO_3^{2-}]$, µmol kg^{-1}) for atmospheric CO_2 equilibrium (red) and CO_2 disequilibrium (blue) conditions using the IPCC IS92a scenario. Observations from 1995 (b and c) are represented by box whisker plots (McNeil and Matear, 2008). Observations from the Scotia Sea for winter 2007 (b and c) are the average south of 60°S (cross) and the minimum from 55-50°S (filled circle). The $[CO_3^{2-}]$ that yields aragonite undersaturation is shown by a grey horizontal line in (c).

The strong summertime gradient in $[CO_3^{2-}]$ from 85 to 140 µmol kg^{-1} across the Scotia Sea and small seasonal amplitudes south of 59°S suggests that the region to the south of the SB will experience year-round aragonite undersaturation before 2040 (Fig. 7.22b-c). The large seasonal amplitudes in $[CO_3^{2-}]$ and pH_T of 60 µmol kg^{-1} and 0.2, respectively (Fig. 7.15c-d), extreme wintertime minima observed in the GB and undersaturation in the water column (Fig. 7.14c-d) suggest that calcifying organisms such as pteropods in this region may face wintertime aragonite undersaturation by 2030 (Fig. 7.22b-c), earlier than previous predictions

(McNeil and Matear, 2008; Orr et al., 2005). Such regions that experience substantial seasonal variability in surface water carbonate chemistry could be used as natural 'mesocosms' to investigate the response of calcifying organisms to future aragonite undersaturation. The degree of seasonal variability reported here has significant implications for future ocean acidification in the Scotia Sea.

7.20. Conclusion

Seasonal analysis of the marine carbon cycle of the Scotia Sea reveals the complexities and variations across diverse hydrographical and biogeochemical regions that exist in the Southern Ocean. The combination of satellite data over the 2006-2009 research period and *in situ* physical, chemical and biological observations during spring 2006, summer 2008 and autumn 2009 along a 1,400 km transect have enabled a detailed investigation into the processes that lead to seasonal and inter-annual variations in surface water carbonate chemistry. Wintertime (2007) conditions were inferred from parameters measured within the Winter Water during summer 2008. The transect encompassed several archetypal Southern Ocean regimes: sea ice, hydrographic fronts, HNLC waters and waters of the ACC in the open ocean, downstream of islands and over submarine ridges. In reference to the large seasonality observed within the sub-regions, implications for the future carbonate chemistry of the Scotia Sea have been described.

Four years of satellite derived chlorophyll-a and sea ice cover showed a general trend from maximum sea ice extent and no blooms in winter to widespread sea ice retreat and large blooms in summer. Maximum sea ice cover extended from 63° to 57°S during winter 2007 and defined the seasonal ice zone (SIZ) of the Scotia Sea. A strong correlation was observed between sea ice, ice edge phytoplankton blooms and subsequent undersaturation in fCO_2. The blooms of the SIZ exhibited large inter-annual variability in surface area and duration, supporting earlier observations (Smith and Comiso, 2008). Moderate sea ice advance and early retreat in winter and spring 2006 set up favourable conditions for phytoplankton bloom development in the SIZ. Prior to bloom development, break-up and melting of the sea ice revealed waters supersaturated with fCO_2 that outgassed at a rate of 6.0 ± 2.7 mmol m^{-2} d^{-1}. However, the action of the biological pumps and sea ice carbonate processes rapidly transformed the fCO_2 supersaturated waters to substantial fCO_2 undersaturation. During the three month lifetime of the bloom in spring and summer 2006-2007, 1.01 ± 0.72 Tg C was

transferred from the atmosphere to the ocean making this the strongest SIZ bloom during the research period. In contrast, following the 'icy' winter and late spring thaw of 2007, a weak bloom removed substantially less CO_2 (0.01 ± 0.17 Tg C) from the atmosphere.

The Southern Boundary (SB), Southern Antarctic Circumpolar Current Front (SACCF) and the Polar Front (PF) were transient CO_2 sinks during different seasons. The SACCF and the SB became strong CO_2 sinks (up to 11.6 ± 1.2 mmol m^{-2} d^{-1}) with the SIZ blooms that 'tracked' the southward retreating sea ice. The PF remained a CO_2 sink of 2.3-4.5 mmol m^{-2} d^{-1} from spring to autumn due to the ongoing phytoplankton activity in this region. In contrast, the HNLC waters of the central Scotia Sea were a consistent source of CO_2 of 2.0-2.3 mmol m^{-2} d^{-1} from summer to autumn due to seasonal warming.

Downstream of the island of South Georgia, extensive phytoplankton blooms developed each year and extended across the Georgia Basin (GB), reaching maximum strength every summer. These are recurrent features that created substantial and persistent undersaturation in sea surface fCO_2 up to -120 μatm to form the strongest seasonal sink for atmospheric CO_2 in the Scotia Sea of 12.0 ± 4.2 mmol m^{-2} d^{-1}. Through the action of the biological carbon pumps in the GB, the SIZ and at the three ACC fronts, the Scotia Sea transect was a summertime sink for atmospheric CO_2 of 5.7 ± 1.4 mmol m^{-2} d^{-1}.

By wintertime, the Scotia Sea was transformed into a CO_2 source 2.9 ± 1.0 mmol m^{-2} d^{-1} as sea ice growth, deep vertical mixing and little photosynthesis lead to enrichment of DIC and fCO_2 in the upper ocean. Waters near the SB, SACCF and in the GB were regions of strong wintertime fCO_2 supersaturation due to localised deep mixing and upwelling of DIC-rich CDW, with low concentrations of carbonate ($[CO_3^{2-}]$), into the sub-surface. The consistently low pH_T and $[CO_3^{2-}]$ (south of 59°S) and large seasonal amplitude in pH_T and $[CO_3^{2-}]$ (in the GB) indicated that these regions are particularly vulnerable to future sea surface aragonite undersaturation, possibly by 2030-2040. Waters beneath the thermocline in the GB were undersaturated with respect to aragonite. This scenario presents conditions of ocean acidification to calcifyers south of the Polar Front in the contemporary Scotia Sea.

The Scotia Sea from 62.6° to 49.5°S is an annual sink for atmospheric CO_2 of 6.2 ± 2.1 mmol m^{-2} d^{-1} using seasonally averaged wind speeds and the Nightingale et al. (2000) CO_2 flux relationship. The South Georgia bloom is a resilient and predictable element of this CO_2 sink,

transferring an average of 1.01 ± 0.41 Tg C from the atmosphere to the upper ocean from spring to autumn each year. The Scotia Sea blooms during spring, summer and autumn accounted for over 2% of the total Southern Ocean CO_2 sink (Takahashi et al., 2009).

The inter-annual variability in the SIZ blooms imposed large constraints on the CO_2 sink, transferring anywhere between 1.01 ± 0.72 Tg C and 0.01 ± 0.17 Tg C from the atmosphere to the upper ocean. Future climate change is likely to affect the sea ice-CO_2 relationship and the variable CO_2 sinks of the current SIZ could diminish through reduced sea ice coverage. The mosaic distribution and substantial seasonal amplitudes in sea surface carbonate chemistry of the Scotia Sea create a natural mesocosm to better understand and predict how future climatic changes may affect the distributions of air-sea CO_2 fluxes, pH and aragonite undersaturation for the contemporary and future Southern Ocean.

8. Conclusions and future work

8.1. Conclusions

The objective of this research was to investigate the marine carbon cycle of the Scotia Sea, Southern Ocean. The British Antarctic Survey (BAS) vessel RRS *James Clark Ross* typically spends 8 months in the Scotia Sea region and, with the installation of the new CASIX underway pCO_2 instrument in 2006, has generated a sea surface fCO_2 data set of over 2,500 measurements to date (Fig. 8.1). This work established a new surface water fCO_2 timeseries, a contribution to alleviating the paucity of fCO_2 data in this region (Takahashi et al., 2009).

An important component of this data set was the initiation of a 1,400 km transect across the Scotia Sea in austral spring 2006 and subsequent occupations in summer 2008 and autumn 2009. Sea surface fCO_2 measurements were made by the CASIX system (2006, 2008 and 2009) and a UEA system (2008). The CASIX instrument was acutely tested during an at-sea pCO_2 instrument intercomparison in summer 2008 (Chapter 3). Results demonstrated that the fCO_2 data generated by the CASIX instrument are of similar accuracy (7 μatm) and precision (3 μatm) to those obtained for sea surface fCO_2 measurements by other systems (Körtzinger et al., 2000), subsequently introducing an additional instrument into the oceanic pCO_2 community. Offsets between the CASIX and UEA CO_2 data sets were attributed differences in the instrument design and a series of recommendations were outlined in order to improve the accuracy of the CASIX seawater fCO_2 measurements.

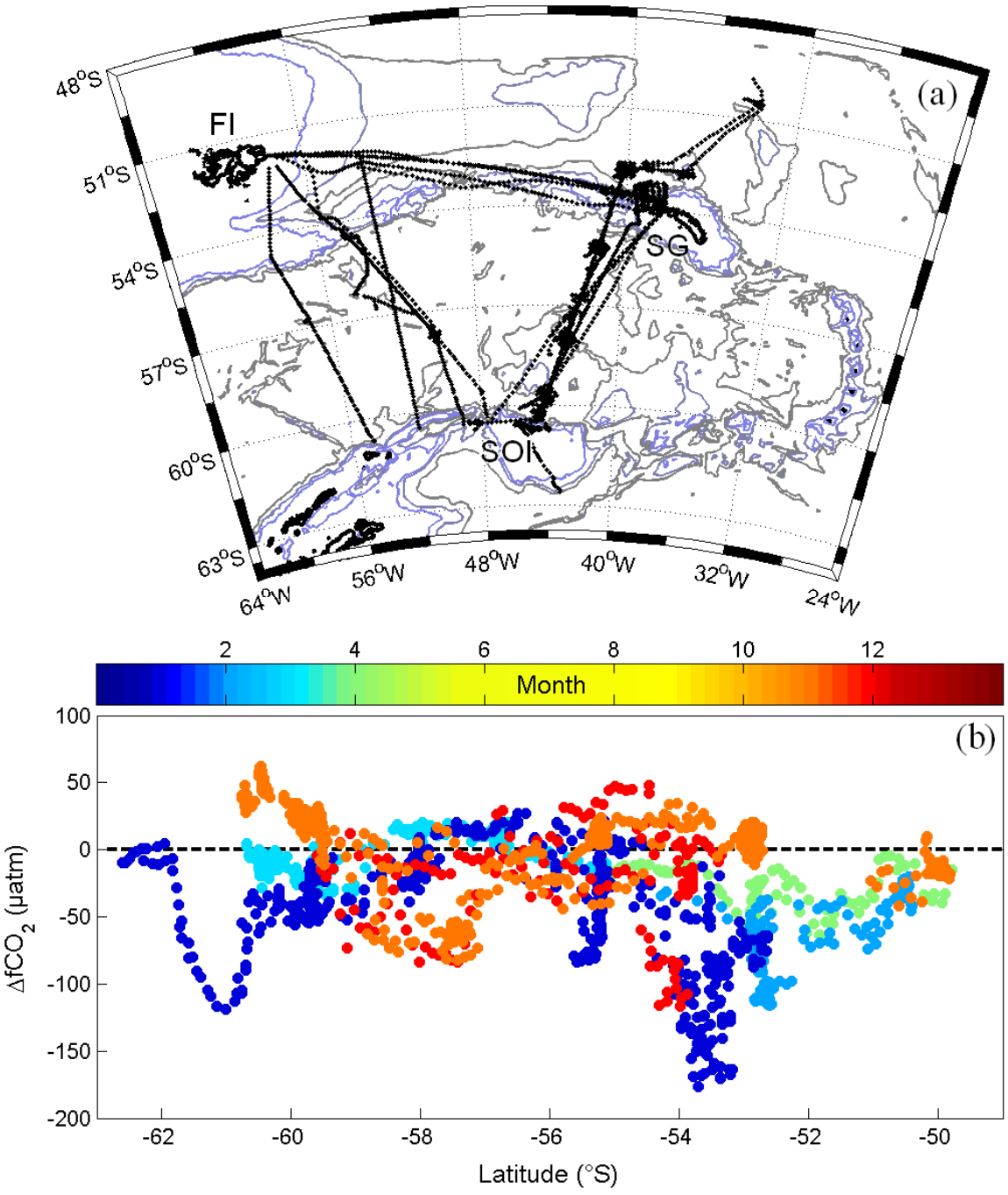

Figure. 8.1 Sea surface fCO_2 measurements collected in the Scotia Sea in 2006-2009. (a) the location of the fCO_2 measurements for the 14 cruises in the Scotia Sea (Table 2.1) and (b) the ΔfCO_2 (sea-air) (µatm) along the transect during seasonal cruises JR161, JR177 and JR200 and secondary cruises JR163/164, JR184, JR185, JR194/197 and JR188. The Falkland Islands (FI), South Orkney Islands (SOI) and South Georgia (SG) are identified. Data are coloured according to month. Depth contours in (a) are at 1000, 2000 and 3000 m (GEBCO, 2001).

The first deep carbonate measurements of the Scotia Sea were made in summer 2008 (Chapter 4) and are presented alongside hydrographic data in order to identify the principle water masses, hydrographic fronts and contemporary carbonate characteristics of the Scotia Sea. Antarctic Surface Water (AASW) was characterised by distinct summer minima in dissolved inorganic carbon (DIC) and total alkalinity (TA) and was supersaturated with respect to aragonite. The depth of the potential temperature minimum (θ_{min}) represented the remnant of the Winter Water (WW) and were used to infer the carbonate chemistry of AASW during the preceding winter (2007). Warm Upper Circumpolar Deep Water (UCDW) represented a voluminous reservoir of DIC in the ACC. Salty Lower Circumpolar Deep Water (LCDW) was distinctly enriched with alkalinity and was undersaturated with respect to aragonite. Warm Deep Water (WDW) was observed flowing out of the Weddell Sea, identified by a warm, saline core infiltrating the southern Weddell-Scotia Confluence (WSC).

Shoaling isohalines were observed throughout the water column upon intersection of the Southern ACC Front (SACCF) at 58°S and the Southern Boundary (SB) of the ACC at 59°S. Meanders in the SACCF were encountered in the central ACC (56-55°S) and in the Georgia Basin (GB), north of 53°S. Upwelling of DIC and nutrient rich UCDW at these locations contributed to (1) summertime enhanced phytoplankton biomass and net DIC depletion in the AASW and (2) enrichment of sub-surface waters that behaved as a supply of DIC-rich, carbonate-poor and low pH waters through increased vertical mixing during winter.

Contrasting concentrations of sea surface fCO_2, DIC and TA were observed in the marginal ice zone (MIZ) allowing a unique analysis the carbonate chemistry of Antarctic sea ice during the summer thaw (Chapter 5). The precipitation of carbonate minerals such as ikaite ($CaCO_3.6H_2O$) in sea ice brines have the net effect of decreasing DIC and TA, and increasing the fCO_2. Deficits in salinity normalised DIC and TA in the summer mixed layer of the MIZ were consistent with the release of brines from melting sea ice, where ikaite precipitation had taken place. Across the MIZ, ikaite precipitation accounted for up 12 ± 3 μmol kg^{-1}, or 13%, of the summer DIC deficit. Biological assimilation of carbon had the largest effect on summer DIC concentrations, resulting in deficits of 41 ± 1 μmol kg^{-1} at the receding ice edge.

The combined effects of biological carbon uptake and sea ice carbonate chemistry constituted a sea ice CO_2 pump and created substantial fCO_2 undersaturation of 95 μatm in the MIZ during summer. The original 'sea ice CO_2 pump' hypothesis proposed that the dissolution of

carbonate minerals in meltwater leads promotes CO_2 uptake from the atmosphere (Rysgaard et al., 2007; Rysgaard et al., 2009). The carbonate chemistry data for the Scotia Sea suggest that it is the transfer of DIC- and TA-poor brines into the surface water during ice melt, in the presence of phytoplankton blooms, that create a strong CO_2 sink during the summer. This research complements the identification of ikaite minerals in Antarctic sea ice (Papadimitriou et al., 2007; Dieckmann et al., 2008) and further highlights that complex, and not fully understood, carbonate chemistry processes are taking place in Antarctic sea ice with strong implications for CO_2 uptake in the polar oceans.

Waters downstream of South Georgia are amongst the most productive in the Southern Ocean, where extensive phytoplankton blooms occur each year (Atkinson et al., 2001; Korb and Whitehouse, 2004; Korb et al., 2008; Whitehouse et al., 2008). Shipboard and satellite surface chlorophyll-a concentrations identified regions of elevated chlorophyll-a, greater than 10 mg m^{-3}, in the core of the bloom that contrasted with upstream high-nutrient low-chlorophyll (HNLC) waters. The 'unproductive' HNLC waters held a small standing stock of chlorophyll-a and had a summertime DIC deficit of 2.2 ± 0.3 mol m^{-2}. This shows that HNLC waters of the ACC are more productive than commonly perceived, as suggested by Bakker et al. (2007), and illustrates some of the limitations in using satellite chlorophyll-a as an indicator of marine productivity.

The summer DIC deficit in the upper 100 m was 4.6 ± 0.8 mol m^{-2} in the bloom where substantial biological carbon uptake created an oceanic sink for atmospheric CO_2 of 15.1 ± 5.7 mmol m^{-2} d^{-1}. For the 90 day duration of the bloom that covered 80,000 km^2 of the GB, a total of 1.3 ± 0.5 Tg C was transferred from the atmosphere to the ocean through air-sea exchange. Sea surface distributions of dissolved iron across the AAZ provided evidence for iron enrichment downstream of South Georgia. Natural iron fertilisation and biologically mediated carbon uptake has been identified in the blooms downstream of sub-Antarctic islands of Crozet (Bakker et al., 2007) and Kerguelen (Jouandet et al., 2008). Compared to the spatial and temporal characteristics of the other island blooms, South Georgia was the strongest bloom, with a total summer DIC deficit of 4.4 ± 0.8 Tg C, almost twice that of the Kerguelen bloom. In a Southern Ocean context, the summertime DIC deficit of the South Georgia bloom was only superseded by blooms in the Ross Sea (Bates et al., 1998; Sweeney et al., 2000), firmly establishing the South Georgia bloom as the strongest region of biological carbon uptake in ice-free waters of the Southern Ocean.

The novel fCO_2 data obtained along the repeat transect in spring 2006, summer 2008 and autumn 2009 (Chapter 7) have established a new timeseries and will contribute valued autumnal data, a relatively undersampled season, to global fCO_2 datasets (CDIAC). Satellite derived chlorophyll-a and sea ice cover were used alongside *in situ* physical and biogeochemical observations to investigate the marine carbon cycle during the transition from wintertime CO_2 source to summertime CO_2 sink. Maximum sea ice cover extended from 63° to 57°S during winter 2007 and defined the seasonal ice zone (SIZ) of the Scotia Sea. A strong correlation was observed between sea ice, ice edge phytoplankton blooms and fCO_2 undersaturation, with distinct inter-annual variability. Moderate sea ice advance and early retreat set up conditions most favourable for phytoplankton bloom development. Early break-up and melting of the sea ice revealed waters supersaturated with fCO_2 that outgassed at a rate of 6.0 ± 2.7 mmol m^{-2} d^{-1}. The action of the biological pumps and sea ice carbonate processes rapidly transformed the fCO_2 supersaturated waters to substantial fCO_2 undersaturation. During the three month lifetime of the SIZ bloom in spring and summer 2006-2007, 1.01 ± 0.72 Tg C was transferred from the atmosphere to the ocean making this the strongest SIZ bloom during the research period.

The upwelled nutrient-rich CDW at the SACCF and the SB transformed the regions into transient CO_2 sinks (up to 11.6 ± 1.2 mmol m^{-2} d^{-1}) with the SIZ blooms that 'tracked' the southward retreating sea ice during the spring and summer thaw. The PF remained a CO_2 sink of 2.3-4.5 mmol m^{-2} d^{-1} due to a continuum of phytoplankton activity from spring to autumn. In contrast, the HNLC waters of the central ACC were a source of CO_2 of 2.0-2.3 mmol m^{-2} d^{-1} from summer to autumn due to seasonal warming. The substantial CO_2 undersaturation of the South Georgia bloom created an average summertime CO_2 sink of 12.0 ± 4.2 mmol m^{-2} d^{-1} across the GB. Through the action of the biological carbon pumps in the GB, the SIZ and at the three ACC fronts, the Scotia Sea was a summertime sink for atmospheric CO_2 of 5.7 ± 1.4 mmol m^{-2} d^{-1}.

By wintertime, the Scotia Sea was transformed into a CO_2 source of 2.9 ± 1.0 mmol m^{-2} d^{-1}. This was due to sea ice cover, little photosynthesis and upwelled CDW supplying the sub-surface water at the SACCF and SB with DIC. As a result, low pH and carbonate ion concentrations south of 59°S and in the GB drive strong seasonal amplitudes in aragonite saturation. These data re-enforce the empirical estimates of McNeil and Matear (2008) and

give a first prediction, based on localised *in situ* observations, of the onset of sea surface aragonite undersaturation in the Scotia Sea by 2030-2040. Waters beneath the thermocline in the GB were undersaturated with respect to aragonite, presenting conditions of ocean acidification to calcifyers south of the Polar Front.

The Scotia Sea from 62.6° to 49.5°S is an annual oceanic CO_2 sink of 6.2 ± 2.1 mmol m^{-2} d^{-1}. The South Georgia bloom is a resilient and predictable component of this CO_2 sink, transferring an average of 1.01 ± 0.41 Tg C from the atmosphere to the upper ocean during spring, summer and autumn each year. The Scotia Sea blooms accounted for over 2% of the current estimate for the total Southern Ocean CO_2 sink (Takahashi et al., 2009). The large inter-annual variability in the SIZ blooms imposed constraints on the CO_2 sink. Future climate change is likely to affect the sea ice-CO_2 relationship and the CO_2 sinks of the current SIZ could diminish. The distribution and substantial seasonal amplitudes in sea surface carbonate chemistry presented in this thesis show that the Scotia Sea is a 'mosaic' of Southern Ocean environments. The region can be considered as a natural mesocosm to better understand and predict how future climatic changes may affect the distributions of air-sea CO_2 fluxes, pH and aragonite undersaturation for the contemporary and future Southern Ocean.

8.2. Future work

The data presented in this thesis have added to our understanding of the role of the Southern Ocean in the global carbon cycle. With regular passages across Drake Passage, into sea ice, around South Georgia and up to the Polar Front, the RRS *James Clark Ross* is an ideal platform for carrying out CO_2 measurements to maintain observations of the dynamic Southern Ocean carbon cycle (Fig. 8.1). This should be done by continuation of the sea surface fCO_2 measurements on future cruises, to vastly improve the temporal coverage, and repeating the deep section transect with DIC and TA measurements in 5-10 years time to enable decadal changes to be evaluated (Bates et al., 1996; Jeandel et al., 1998; Feely et al., 2002; Feely et al., 2006; Metzl et al., 2009). This will allow a more thorough assessment of inter-annual variability.

This research highlighted interesting, and not fully understood, carbonate chemistry processes in Antarctic sea ice. To further investigate the influence of Antarctic sea ice carbonate chemistry on the marine carbon cycle, several time series that span the advance and retreat of the sea ice should be established. This could be carried out through shipboard analyses, but a

land or sea ice based campaign would provide optimal access and remove some logistical constraints of shipboard work. Ice coring and brine extraction in different ice types should complement the surface water analyses alongside high resolution, vertical hydrographic sampling in the upper ocean. Separation techniques should be implemented and optimised in order to identify the nature of any carbonate minerals present (Dieckmann et al., 2008). Small scale flux towers positioned over the ice sheet would complement the suite of oceanic parameters to investigate the potential for CO_2 exchange through sea ice (Semiletov et al., 2004; Nomura et al., 2006). The BAS research base, Rothera on the western Antarctic Peninsula would provide an ideal fieldwork site. As part of the BAS long term monitoring, the Rothera Oceanographic and Biological Time Series (RaTS) was established in 1997, carrying out station work every 5-7 days in Ryder Bay, northern Marguerite Bay (Clarke et al., 2008). The acquisition of carbonate chemistry parameters would neatly fit in with the work already carried out as part of RaTS.

Evidence suggested that the extensive South Georgia bloom is naturally iron fertilised (currently under investigation). The bloom had an estimated duration of 90 days, of which the RRS *James Clark Ross* was present for 5 days and carried out 3 hydrographic stations. Dedicated shipboard surveys from bloom initiation (October) to maximum extent (December) would better capture the scale of carbon uptake at different stages of the bloom development. The shipboard surveys should combine high frequency underway and station sampling, including autumn and winter repeat sections, across regions of low, moderate and high chlorophyll-a concentrations as determined from real time satellite images. Incorporation of winter sampling would validate the assumptions of using the temperature minimum as an indicator for Winter Water conditions, of which this and many seasonal carbon studies are based upon. The proposed reduction in aragonite saturation and effects on calcifying organisms should be tested at numerous localities, by *in situ* multi-depth netting and shipboard incubations to better predict effects of future ocean acidification to calcifyers in the Scotia Sea.

Glossary

AABW	Antarctic Bottom Water
AAIW	Antarctic Intermediate Water
AASW	Antarctic Surface Water
AAZ	Antarctic Zone
ACC	Antarctic Circumpolar Current
BAS	British Antarctic Survey
BATS	Bermuda Atlantic Time-series Study
CARBON-OPS	An operational UK air-sea carbon flux observation capability
CASIX	Centre for observation of Air Sea Interactions and fluXes
CDIAC	Carbon Data Information and Analysis Centre
CDW	Circumpolar Deep Water
CRM	Certified Reference Material
CTD	Conductivity, temperature, depth
DCM	Deep chlorophyll-a maxima
DIC	Dissolved inorganic carbon
DOC	Dissolved organic carbon
DOE	Department of Energy
FI	Falkland Islands
GB	Georgia Basin

GEBCO	General Bathymetric Chart of the Oceans
HNLC	High-nutrient low-chlorophyll
HOT	Hawaiian Ocean Time-series
IPCC	Intergovernmental Panel on Climate Change
JGOFS	Joint Global Ocean Flux Study
JR#	Cruise number # on RRS *James Clark Ross*
KERFIX	Kerguelen Fixed Station
LCDW	Lower Circumpolar Deep Water
MOC	Meridional overturning circulation
MODIS	MODerate resolution Imaging Spectroradiometer
NADW	North Atlantic Deep Water
NEGR	Northeast Georgia Rise
NOAA	National Oceanic and Atmospheric Administration
NSR	North Scotia Ridge
NWGR	Northwest Georgia Rise
MEB	Maurice Ewing Bank
MIZ	Marginal ice zone
MLD	Mixed layer depth
PF	Polar Front
PFZ	Polar Frontal Zone
PIC	Particulate inorganic carbon

POC	Particulate organic carbon
SACCF	Southern Antarctic Circumpolar Current Front
SB	Southern Boundary
SeaWiFS	Sea-viewing Wide Field-of-view Sensor
SG	South Georgia
SIZ	Seasonal ice zone
SOI	South Orkney Islands
SR	Shag Rocks
SSI	South Sandwich Islands
SSR	South Scotia Ridge
SST	Sea surface temperature
TA	Total Alkalinity
UCDW	Upper Circumpolar Deep Water
UEA	University of East Anglia
VINDTA	Versatile Instrument for the Determination of Titration Alkalinity
WDW	Warm Deep Water
WOCE	World Ocean Circulation Experiment
WSC	Weddell-Scotia Confluence
WW	Winter Water

References

Ackley, S.F. and Sullivan, C.W. 1994. Physical controls on the development and characteristics of Antarctic sea-ice biological communities - a review and synthesis. *Deep-Sea Res. I* **41**, 1583-1604.

Alvarez, M., Rios, A.F. and Roson, G. 2002. Spatio-temporal variability of air-sea fluxes of carbon dioxide and oxygen in the Bransfield and Gerlache Straits during Austral summer 1995-96. *Deep-Sea Res. II* **49**, 643-662.

Anderson, L.A. and Sarmiento, J.L. 1994. Redfield Ratios of remineralization determined by nutrient data analysis. *Global Biogeochem. Cyc.* **8**, 65-80.

Anderson, L.G., Falck, E., Jones, E.P., Jutterstrom, S. and Swift, J.H. 2004. Enhanced uptake of atmospheric CO_2 during freezing of seawater: A field study in Storfjorden, Svalbard. *J. Geophys. Res.* **109**, doi: 10.1029/2003JC002120.

Ardelan, M.V., Holm-Hansen, O., Hewes, C.D., Reiss, C.S., Silva, N.S., Dulaiova, H., Steinnes, E. and Sakshaug, E. 2010. Natural iron enrichment around the Antarctic Peninsula in the Southern Ocean. *Biogeosci.* **7**, 11-25.

Arhan, M., Naveira Garabato, A.C., Heywood, K.J. and Stevens, D.P. 2002. The Antarctic Circumpolar Current between the Falkland Islands and South Georgia. *J. Phys. Ocean.* **32**, 1914-1931.

Arrigo, K.R., Worthen, D., Schnell, A. and Lizotte, M.P. 1998. Primary production in Southern Ocean waters. *J. Geophys. Res.* **103**, 15587-15600.

Arrigo, K.R. and van Dijken, G.L. 2004. Annual changes in sea-ice, chlorophyll a, and primary production in the Ross Sea, Antarctica. *Deep Sea Res. II* **51**, 117-138.

Atkinson, A., Whitehouse, M.J., Priddle, J., Cripps, G.C., Ward, P. and Brandon, M.A. 2001. South Georgia, Antarctica: a productive, cold water, pelagic ecosystem. *Mar. Ecol. Prog. Ser.* **216**, 279-308.

Aumont, O. and Bopp, L. 2006. Globalizing from ocean in situ iron fertilization studies. *Global Biogeochem. Cycles* **20**, doi:10.1029/2005GB002591.

Bakker, D.C.E., de Baar, H.J.W. and Bathmann, U.V. 1997. Changes of carbon dioxide in surface waters during spring in the Southern Ocean. *Deep-Sea Res. II* **44**, 91-127.

Bakker, D.C.E., Nielsdóttir, M.C., Morris, P.J., Venables, H.J. and Watson, A.J. 2007. The island mass effect and biological carbon uptake for the subantarctic Crozet Archipelago. *Deep-Sea Res. II* **54**, 2174-2190.

Bakker, D.C.E., Hoppema, M., Schroder, M., Geibert, W. and de Baar, H.J.W. 2008. A rapid transition from ice covered CO_2-rich waters to a biologically mediated CO_2 sink in the eastern Weddell Gyre. *Biogeosci.* **5**, 1373-1386.

Bates, N.R., Michaels, A.F. and Knap, A.H. 1996. Seasonal and interannual variability of oceanic carbon dioxide species at the US JGOFS Bermuda Atlantic Time-series Study (BATS). *Deep-Sea Res. II* **43**, 347-383.

Bates, N.R., Hansell, D.A. and Carlson, C.A. 1998. Distributions of CO_2 species, estimates of net community production, and air-sea CO_2 exchanges in the Ross Sea polynya. *J. Geophys. Res.* **103**, 2883-2896.

Bathmann, U.V., Scharek, R., Dubischar, C., Klaas, C. and Smetacek, V. 1997. Chlorophyll and phytoplankton species distribution in the Atlantic sector of the Southern Ocean in spring. *Deep Sea Res. II* **44**, 51-68.

Bathmann, U.V. 1998. Ecology and biogeochemistry in the Atlantic sector of the Southern Ocean during austral spring: the first JGOFS expedition aboard RV *'Polarstern'*. *J. Marine Sys.* **17**, 77-85.

Belkin, I.M. and Gordon, A.L. 1996. Southern Ocean fronts from the Greenwich Meridian to Tasmania. *J. Geophys. Res.* **101**, 3675-3696.

Bednarsek, N. in preparation. PhD Thesis. University of East Anglia.

Bellerby, R.G.J., Hoppema, M., Fahrbach, E., de Baar, H.J.W. and Stoll, M.H.C. 2004. Interannual controls on Weddell Sea surface water fCO_2 during the autumn-winter transition phase. *Deep-Sea Res. I* **51**, 793-808.

Blain, S. Tréguer, P., Belviso, S., Bucciarelli, Denis, M., Desabre, S., Fiala, M., Jezequel, V.M., Le Fevre, J., Mayzaud, P., Marty, J.C. and Razouls, S. 2004. A biogeochemical study of the island mass effect in the context of the iron hypothesis: Kerguelen Islands, Southern Ocean. *Deep-Sea Res. I* **48**, 163-197.

Blain, S., Quéguiner, B., Armand, L., Belviso, S., Bombled, B., Bopp, L., Bowie, A., Brunet, C., Brussaard, C., Carlotti, F., Christaki, U., Corbière, A., Durand, I., Ebersbach, F., Fuda, J.-L., Garcia, N., Gerringa, L., Griffiths, B., Guigue, C., Guillerm, C., Jacquet, S., Jeandel, C., Lann, P., Lefèvre, D., Lo Monaco, C., Malits, A., Mosseri, J., Obernosterer, I., Park, Y.-H., Picheral, M., Pondaven, P., Remenyi, T., Sandroni, V., Sarthou, G., Savoye, N., Scouarnec, L., Souhart, M., Thuiller, D., Timmermans, K., Trull, T., Uitz, J., van Beek, P., Veldhuis, M., Vincent, D., Viollier, E., Vong, L. and

Wagener, T. 2007. Effect of natural iron fertilization on carbon sequestration in the Southern Ocean. *Nature* **446**, 1070-1075.

Boyd, P.W., Robinson, C., Savidge, G. and Williams, P.J. 1995. Water column and sea-ice primary productivity during Austral spring in the Bellingshausen Sea. *Deep Sea Res. II* **42**, 1177-1200.

Boyd, P.W., La Roche, J., Gall, M., Frew, R. and McKay, R.M.L. 1999. Role of iron, light and silicate in controlling algal biomass in subantarctic waters SE of New Zealand. *J. Geophys. Res.* **104**, 13395-13408.

Boyd, P.W., Watson, A.J., Law, C.S., Abraham, E.R., Trull, T., Murdoch, R., Bakker, D.C.E., Bowie, A., Charette, M., Croot, P., Downing, K., Frew, R., Gall, M., Hadfield, M., Hall, J., Harvey, M., La Roche, J.G.J., Liddicoat, M.R.L., Maldonado, M.T., McKay, R.M.L., Nodder, S., Pickmere, S., Pridmore, R., Rintoul, S.R., Safi, K., Waite, A. and Zeldis, J. 2000. A mesoscale phytoplankton bloom in the polar Southern Ocean stimulated by iron fertilization. *Nature* **407**, 695-702.

Boyd, P.W., Crossley, A.C., DiTullio, G.R., Griffiths, F.B., Hutchins, D.A., Queguiner, B., Sedwick, P.N. and Trull, T. 2001. Control of phytoplankton growth by iron supply and irradiance in the subantarctic Southern Ocean: Experimental results from the SAZ Project. *J. Geophys. Res.* **106**, 31573-31583.

Boyd, P.W. 2002. Environmental factors controlling phytoplankton processes in the Southern Ocean. *J. Phycol.* **38**, 844-861.

Boyd, P.W., Law, C.S., Wong, C.S., Nojiri, Y., Tsuda, A., Levasseur, M., Takeda, S., Rivkin, R., Harrison, P.J., Strzepek, R., Gower, J., McKay, R.M.L., Abraham, E.R., Arychuk, M., Barwell-Clarke, J., Crawford, W., Crawford, D., Hale, M., Harada, K., Johnson, K., Kiyosawa, H., Kudo, I., Marchetti, A., Miller, W., Needoba, J., Nishioka, J., Ogawa, H., Page, J., Robert, M., Salto, H., Sastri, A., Sherry, N., Soutar, T., Sutherland, N., Taira, Y., Whitney, F., Wong, S.-K.E. and Yoshimura, T. 2004. The decline and fate of an iron-induced subarctic phytoplankton bloom. *Nature* **428**, 549-553.

Boyd, P.W., Jickells, T., Law, C.S., Blain, S., Boyle, E.A., Buesseler, K.O., Coale, K.H., Cullen, J.J., de Baar, H.J.W., Follows, M., Harvey, M., Lancelot, C., Levasseur, M., Owens, N.P.J., Pollard, R.T., Rivkin, R., Sarmiento, J., Schoemann, V., Smetacek, V., Takeda, S., Tsuda, A., Turner, S. and Watson, A.J. 2007. Mesoscale Iron Enrichment Experiments 1993-2005: Synthesis and Future Directions. *Science* **315**, 612-617.

Bracher, A.U., Kroon, B.M.A. and Lucas, M.I. 1999. Primary production, physiological state and composition of phytoplankton in the Atlantic sector of the Southern Ocean. *Mar. Ecol. Prog. Ser.* **190**, 1-16.

Brainerd, K.E. and Gregg, M.C. 1995. Surface mixed and mixing layer depths. *Deep-Sea Res. I* **42**, 1521-1543.

Brandon, M.A., Murphy, E.J., Trathan, P.N. and Bone, D.G. 2000. Physical oceanographic conditions to the northwest of the sub-Antarctic Island of South Georgia. *J. Geophys. Res.* **105**, 23,983-23,996.

Broecker, W.S., Takahashi, T., Simpson, H.J. and Peng, T.-H. 1979. Fate of fossil fuel carbon dioxide and the global carbon budget. *Science* **206**, 409-418.

Broecker, W.S. and Peng, T.-H. 1982. *Tracers in the Sea*. Lamont-Doherty Geological Observatory, Palisades, N.Y.

Brown, P.J. 2008. PhD Thesis. *Natural and anthropogenic carbon dioxide fluxes in the subtropical North Atlantic*. University of East Anglia, pp. 249.

Bucciarelli, E., Blain, S. and Tréguer, P. 2001. Iron and manganese in the wake of the Kerguelen Islands (Southern Ocean). *Marine Chem.* **73**, 21-36.

Buma, A.G.J., de Baar, H.J.W., Nolting, R.F. and van Bennekom, A.J. 1991. Metal enrichment experiments in the Weddell-Scotia Seas: effects of iron and manganese on various plankton communities. *Limnol. Ocean.* **36**, 1865-1878.

Buma, A.G.J., Gieskes, W.W.C. and Thomsen, H.A. 1992. Abundance of cryptophyceae and chlorophyll b containing organisms in the Weddell-Scotia Confluence area in the spring of 1988. *Polar Biology* **12**, 43-52.

Caldeira, K. and Duffy, P.B. 2000. The role of the Southern Ocean in uptake and storage of anthropogenic carbon dioxide. *Science* **287**, 620-622.

Caldeira, K. and Wickett, M.E. 2003. Anthropogenic carbon and ocean pH. *Science* **425**, 365.

Callahan, J.E. 1972. The structure and circulation of deep water in the Antarctic. *Deep-Sea Res.* **19**, 563-575.

Canadell, J.G., Le Quéré, C., Raupach, M.R., Feild, C.B., Buitenhuis, E.T., Ciais, P., Conway, T.J., Gillett, N.P., Houghton, R.A. and Marland, G. 2007. Contributions to accelerating atmospheric CO_2 growth from economic activity, carbon intensity, and efficiency of natural sinks. *PNAS* **5**, 563-575.

Carmack, E.C. and Foster, T.D. 1975. Flow of water out of Weddell Sea. *Deep-Sea Res.* **22**, 711-724.

CDIAC Carbon Dioxide Information Analysis Centre, Environmental Sciences Division, Oak Ridge National Laboratory, US Department of Energy, Oak Ridge, TN, USA.

Chen, D., Busalacchi, A.J. and Rothstein, L.M. 1994. The roles of vertical mixing, solar radiation, and wind stress in a model simulation of the sea surface temperature seasonal cycle in the tropical Pacific Ocean. *J. Geophys. Res.* **99**, 20345-20359.

Ciattaglia, L., Colombo, T. and Masarie, K.A. 1999. Continuous measurements of atmospheric CO_2 at Jubany Station, Antarctica. *Tellus* **51B**, 713-721.

Coale, K.H., Johnson, K. S., Chavez, F. P., Buesseler, K. O., Barber, R. T., Brzezinski, M. A., Cochlan, W. P., Millero, F.J., Falkowski, P.G., Bauer, J.E., Wanninkhof, R.H., Kudela, R.M., Altabet, M.A., Hales, B.E., Takahashi, T., Landry, M. R., Bidigare, R. R., Wang, X., Chase, Z., Strutton, P. G., Friedrich, G. E., Gorbunov, M. Y., Lance, V. P., Hilting, A. K., Hiscock, M. R, Demarest, M., Hiscock, W. T., Sullivan, K. F., Tanner, S. J., Gordon, R. M., Hunter, C. N., Elrod, V. A., Fitzwater, S. E., Jones, J. L., Tozzi, S., Koblizek, M., Roberts, A. E., Herndon, J., Brewster, J., Ladizinsky, N., Smith, G., Cooper, D., Timothy, D., Brown, S.L., Selph, K.E., Sheridan, C.C., Twining B.S. and Johnson, Z.I. 2004. Southern Ocean Iron Enrichment Experiment: Carbon Cycling in High and Low-Si Waters. *Science* **304**, 408-414.

Comiso, J.C., Maynard, N.G., Smith, W.O. and Sullivan, C.W. 1990. Satellite Ocean Color Studies of Antarctic Ice Edges in Summer and Autumn. *J. Geophys. Res.* **95**, 9481-9496.

Comiso, J.C., McClain, C.R., Sullivan, C.W., Ryan, J.P. and Leonard, C.L. 1993. Coastal Zone Color Scanner pigment concentrations in the Southern Ocean and relationships to geophysical surface-features. *J. Geophys. Res.* **98**, 2419-2451.

Conkright, M. E. 2002. *World Ocean Database 2001, vol. 1, Introduction [CD-ROM]*, NOAA Atlas NESDIS, vol. 42, (ed. S. Levitus) Govt. Print. Off., Washington, D. C., pp. 159.

Cooper, D.J., Watson, A.J. and Ling, R.D. 1998. Variation of pCO_2 along a North Atlantic shipping route (U.K. to the Caribbean): A year of automated observations. *Marine Chem.* **60**, 147-164.

Clarke, A., Meredith, M.P., Wallace, M.I., Brandon, M.A. and Thomas, D.N. 2008. Seasonal and interannual variability in temperature, chlorophyll and macronutrients in northern Marguerite Bay, Antarctica. *Deep Sea Res. II* **55**, 1988-2006.

Craig, H. 1972. The GEOSECS Program: 1970-1971. *Earth Planet. Sci. Lett.* **16**, 47-49.

Craig, H. 1974. The GEOSECS Program: 1972-1973. *Earth Planet. Sci. Lett.* **23**, 63-64.

Daly, K.L., Smith, W.O., Johnson, G.C., DiTullio, G.R., Jones, D.R., Mordy, C.W., Feely, R.A., Hansell, D.A. and Zhang, J.-Z. 2001. Hydrography, nutrients, and carbon pools in the Pacific sector of the Southern Ocean: Implications for carbon flux. *J. Geophys. Res.* **106**, 7107-7124.

de Baar, H.J.W., Buma, A.G.J., Nolting, R.F., Cadee, G.C, Jacques, G. and Treguer, P.J. 1990. On iron limitation of the Southern Ocean - experimental observations in the Weddell and Scotia Seas. *Mar. Ecol. Progr. Ser.* **65**, 105-122.

de Baar, H.J.W. 1994. von Liebig's Law of the Minimum and Plankton Ecology (1899-1991). *Prog. Ocean.* **33**, 347-386.

de Baar, H.J.W., Jong, J.T.M., Bakker, D.C.E., Löscher, B.M., Veth, C. and Bathmann, U. 1995. Importance of iron for plankton blooms and carbon dioxide drawdown in the Southern Ocean. *Nature* **373**, 412-415.

Deacon, G.E.R. 1979. Weddell Gyre. *Deep-Sea Res*. **26**, 981-995.

Deacon, G.E.R. 1982. Physical and biological zonation in the Southern Ocean. *Deep-Sea Res*. **29**, 1-15.

Delille, B., Jourdain, B., Borges, A.V., Tison, J.L. and Delille, D. 2007. Biogas (CO_2, O_2, dimethylsulfide) dynamics in spring Antarctic fast ice. *Limnol. Oceanogr*. **52**, 1367-1379.

Dickson, A.G. and Millero, F.J. 1987. A comparison of the equilibrium constants for the dissociation of carbonic acid in seawater media. *Deep-Sea Res.* **34**, 1733-1743.

Dickson, A.G. 1981. An exact definition of total alkalinity and a procedure for the estimation of alkalinity and total inorganic carbon from titration data. *Deep-Sea Res.* **28**, 609-623.

DOE 2007. In: Guide to best practices for ocean CO_2 measurements (eds. A.G. Dickson, C.L. Sabine and J.R. Christian). PICES Special Publication 3, pp. 1-191.

Doney, S.C., Fabry, V.J., Feely, R.A. and Kleypas, J.A. 2009. Ocean Acidification: The Other CO_2 Problem. *Ann. Rev. Marine Sci.* **1**, 169-192.

Donlon, C.J. and Robinson, I.S. 1997. Observations of the oceanic thermal skin in the Atlantic Ocean. *J. Geophys. Res.* **102**, 18585-18606.

Dieckmann, G.S., Nehrke, G., Papadimitriou S., Göttlicher, J., Steininger, R., Kennedy, H., Wolf-Gladrow, D. and Thomas, D.N. 2008. Calcium carbonate as ikaite crystals in Antarctic sea ice. *Geophys. Res. Lett.*, **35**. doi:10.1029/2008GL033540.

Duce, R.A. and Tindale, N.W. 1991. Atmospheric transport of iron and its deposition in the ocean. *Limnol. Ocean.* **36**, 1715-1726.

Dulaiova, H., Ardelan, M.V., Henderson, P.B. and Charette, M.A. 2009. Shelf-derived iron inputs drive biological productivity in the southern Drake Passage. *Global Biogeochem. Cyc.* **23**, doi:10.1029/2008GB003406.

Draxier, R.R. and Hess, G.D., 1998. An overview of the HYSPLIT_4 modelling system for trajectories, dispersion and deposition. *Australian Meteorological Magazine*, **47**, 295-308.

Edwards, R. and Sedwick, P. 2001. Iron in East Antarctic snow: implications for atmospheric iron deposition and algal production in Antarctic waters. *Geophys. Res. Lett.* **38**, 3907-3910.

Elderfield, H. 2002. Carbonate Mysteries. *Science* **296**, 1618-1620.

Engel, A., Zondervan, I., Aerts, K., Beaufort, Benthien, A., Chou, L., Delille, B., Gattuso, J.-P., Harlay, J., Heemann, C., Hoffmann, L., Jacquet, S., Nejstgaard, J., Pizay, M.-D., Rochelle-Newall, E., Schneider, U., Terbrueggen, A. and Riebesell, U. 2005. Testing direct effects of CO_2 concentrations on a bllom of the coccolithophorid Emiliania huxleyi in mesocosm experiments. *Limnol. Ocean.* **50**, 493-507.

Eppley, R.W. 1972. Temperature and phytoplankton growth in the sea. *Fishery Bulletin* **70**, 1063-1085.

Erickson, D.J., Hernandez, J.L., Ginoux, P., Gregg, W.W. and McClain, C. 2003. Atmospheric iron delivery and surface ocean biological activity in the Southern Ocean and Patagonian region. *Geophys. Res. Lett.* **30**, doi:10.1029/2003GL017241.

Fabry, V.J. 1990. Shell growth rates of pteropod and heteropod mollusks and aragonite production in the open ocean: implications for the marine carbonate system. *J. Marine Res.* **48**, 209–222.

Fabry**,** V.J., Seibel, B.A., Feely, R.A., and Orr, J.C. 2008. Impacts of ocean acidification on marine fauna and ecosystem processes. *ICES J. Marine Sci.* **65**, 414–432.

Falkowski, P.G., Barber, R.T. and Smetacek, V. 2003. Biogeochemical Controls and Feedbacks on Ocean Primary Production. *Science* **281**, 200-206.

Feely, R.A., Boutin, J., Cosca, C.E., Dandonneau, Y., Etcheto, J., Inoue, H., Ishii, M., Le Quéré, C., Mackey, D., McPhaden, M., Metzl, N., Poisson, A. and Wannikhof, R. 2002. Seasonal and interannual variability of CO_2 in the Equatorial Pacific. *Deep Se Res. II* **49**, 2443-2469.

Feely, R.A., Sabine, C.L., Lee, K., Berelson, W., Kleypas, J., Fabry, V.J. and Millero, F.J. 2004. Impact of Anthropogenic CO_2 on the $CaCO_3$ System in the Oceans. *Science* **305**, 362-366.

Feely, R.A., Takahashi, T., Wannikhof, R., McPhaden, M., Cosca, C.E., Sutherland, S. and Carr, M.-E. 2006. Decadal variability of the air-sea CO2 fluxes in the equatorial Pacific Ocean. *J. Geophys. Res.* **111**, C07S03.

Feldman, G.C. and McClain, C.R., 2006a. Ocean Color Web, MODIS Reprocessing 1.1, NASA Goddard Space Flight Center. N. Kuring and S. W. Bailey.

Feldman, G.C. and McClain, C.R. 2006b. Ocean Color Web, SeaWiFS Reprocessing 5.1, NASA Goddard Space Flight Center. N. Kuring and S. W. Bailey.

Fennel, K., Abbott, M. R., Spitz, Y. H., Richman, J. G. and Nelson, D. M. 2003. Modelling Controls of phytoplankton production in the southwest Pacific Sector of the Southern Ocean. *Deep Sea Res. II* **50**, 769-798.

Foster, T.D. 1972. Haline convection in polynyas and leads. *J. Phys. Ocean.* **2**, 462-469.

Franck, V.M., Brzezinski, M.A., Coale, K.H. and Nelson, D.M. 2000. Iron and silicic acid concentrations regulate Si uptake north and south of the Polar Frontal Zone in the Pacific Sector of the Southern Ocean. *Deep Sea Res.* II **47**, 3315-3338.

Fung, I.Y., Meyn, S.K., Tegenh, I., Doney, S.C., John, J.G. and Bishop, J.K.B. 2000. Iron supply and demand in the upper ocean. *Global Biogeochem. Cyc.* **14**, 281-295.

Friis, K., Körtzinger, A. and Wallace, D.W.R. 2003. The salinity normalization of marine inorganic carbon chemistry data. *Geophys. Res. Lett.* **30**, doi:10.1029/2002GL015898.

Garrison, D.L., Ackley, S.F. and Buck, K.R. 1983. A Physical-Mechanism for Establishing Algal Populations in Frazil Ice. *Nature*, **306**, 363-365.

GEBCO, 2001. General Bathymetric Chart of the Oceans Digital Atlas. British Oceanographic Data Centre, Liverpool, U.K.

Geibert, W., Assmy, P., Bakker, D.C.E., Hanfland, C., Hoppema, M., Pichevin, L.E., Schröder, M., Schwarz, J.N., Stimac, I., Usbeck, R. and Webb, A. 2010. High productivity in an ice melting hot spot at the eastern boundary of the Weddell Gyre. *Global Biogeochem. Cyc.* **24**, doi:10.1029/2009GB003657.

Gervais, F. and Riebesell, U. 2002. Changes in primary productivity and chlorophyll-a in response to iron fertilization in the Southern Polar Frontal Zone. *Limnol. Ocean.* **47**, 1324-1335.

Gibson, J.A.E. and Trull, T.W. 1999. Annual cycle of fCO_2 under sea ice and in open water in Prydz Bay, east Antarctica. *Mar. Chem.* **66**, 187-200.

Gill, A.E. 1973. Circulation and bottom water production in Weddell Sea. *Deep-Sea Res.* **20**, 111-140.

Gleitz, M., Rutgers van de Loeff, M.M, Thomas, D.N., Dieckmann, G.S. and Millero, F.J. 1995. Comparison of summer and winter inorganic carbon, oxygen and nutrient concentrations in Antarctic sea ice brine. *Mar. Chem.* **51**, 81-91.

Gleitz, M., Grossmann, S., Scharek, R. and Smetacek, V. 1996. Ecology of diatom and bacterial assemblages in water associated with melting summer sea ice in the Weddell Sea, Antarctica. *Antarct. Sci.* **8**, 135-146.

Gloersen, P. and Campbell, W.J. 1991. Recent variations in Arctic and Antarctic sea ice covers. *Nature*, **352**, 33-36.

Gordon, A.L. and Huber, B.A. 1984. Thermohaline Stratification Below the Southern Ocean Sea Ice. *J. Geophys. Res.* **89**, 641-648.

Gouretski, V.V. and Danilov, A.I. 1993. Weddell Gyre - structure of the eastern boundary. *Deep-Sea Res. I* **40**, 561-582.

Gregg, W.W. and Casey, N.W. 2004. Global and regional evaluation of the SeaWiFS chlorophyll data set. *Remote Sensing Environ.* **93**, 463-479.

Hansson, I. 1973. A new set of acidity constants for carbonic acid and boric acid in seawater. *Deep Sea Res.* **20,** 461-78.

Hardman-Mountford, N.J., Moore, G., Bakker, D.C.E., Watson, A.J., Schuster, U., Barciela, R., Hines, A., Moncoiffé, G., Brown, J., Dye, S., Blackford, J., Somerfield, P.J., Holt, J., Hydes, D.J. and Aitken, J. 2008. An operational monitoring system to provide indicators of CO_2-related variables in the ocean. *ICES J. Marine Sci.* **65**, 1498-1503.

Heinze, C., Maier-Reimer E. and Winn, K. 1991. Glacial pCO_2 reduction by the World Ocean: experiements with the Hamburg carbon cycle model. *Paleoceanogr.* **6**, 395-430.

Helbling, E.W., Amos, A.F., Silva, N., Villafane, V. and Holm-Hansen, O. 1993. Phytoplankton distribution and abundance as related to a frontal system north of Elephant Island, Antarctica. *Antarct. Sci.* **5**, 25-36.

Hewes, C.D., Reiss, C.S., Kahru, M., Mitchell, B.G. and Holm-Hansen, O. 2008. Control of phytoplankton biomass by dilution and mixed layer depth in the western Weddell-Scotia Confluence. *Mar. Ecol. Prog. Ser.* **366**, 15-29.

Holeton, C.L., Nédélec, F., Sanders, R., Brown, L., Moore, C.M., Stevens, D.P., Heywood, K.J., Statham, P.J. and Lucas, C.H. 2005. Physiological state of phytoplankton communities in the southwest Atlantic sector of the Southern Ocean, as measured by fast repetition rate fluorometry. *Polar Biology* **29**, 44-52.

Holm-Hansen, O. and Mitchell, B.G. 1991. Spatial and temporal distribution of phytoplankton and primary production in the western Bransfield Strait region. *Deep-Sea Res. A* **38**, 961-980.

Holm-Hansen, O. and Hewes, C.D. 2004a. Deep chlorophyll-a maxima (DCMs) in Antarctic waters - I. relationships between DCMs and the physical, chemical, and optical conditions in the upper water column. *Polar Biology* **27**, 699-710.

Holm-Hansen, O., Naganobu, M., Kawaguchi, S., Kameda, T., Krasovski, I., Tchernyshkov, P., Priddle, J., Korb, R., Brandon, M., Demer, D., Hewitt, R.P., Kahru, M and Hewes, C.D. 2004b. Factors influencing the distribution, biomass, and productivity of phytoplankton in the Scotia Sea and adjoining waters. *Deep Sea Res. II* **51**, 1333-1350.

Holm-Hansen, O., Kahru, M. and Hewes, C.D. 2005. Deep chlorophyll-a maxima (DCMs) in pelagic Antarctic waters II. Relation to bathymetric features and dissolved iron concentrations. *Mar. Ecol. Progr. Ser.* **297**, 71-81.

Honjo, S. 2004. Particle export and the biological pump in the Southern Ocean. *Antarctic Sci.* **16**, 501-516.

Hoppema, M., Fahrbach, E., Schroder, M., Wisotzki, A. and de Baar, H.J.W. 1995. Winter-summer differences of carbon dioxide and oxygen in the Weddell Sea surface layer. *Mar.Chem.* **51**, 177-192.

Hoppema, M., Fahrbach, E., Stoll, M.H.C. and de Baar, H.J.W. 1998. Increase of carbon dioxide in the bottom water of the Weddell Sea, Antarctica. *Marine Chem.* **59**, 201-210.

Hoppema, M., Fahrbach, E., Stoll, M.H.C. and de Baar, H.J.W. 1999. Annual uptake of atmospheric CO_2 by the Weddell Sea derived from a surface layer balance, including estimations of entrainment and new production. *J. Marine Sys.* **19**, 219-233.

Hoppema, M., Stoll, M.H.C. and de Baar, H.J.W. 2000. CO_2 in the Weddell Gyre and Antarctic Circumpolar Current: austral autumn and early winter. *Mar. Chem.* **72**, 203-220.

Hoppema, M., de Baar, H.J.W., Fahrbach, E., Hellmer, H.H. and Klein, B. 2003. Substantial advective iron loss diminishes phytoplankton production in the Antarctic Zone. *Global Biogeochem. Cyc.* **17**, doi:10.1029/2002GB001957.

Hoppema, M., Middag, R., de Baar, H.J.W., Fahrbach, E., van Weerlee, E.M. and Thomas, H. 2007. Whole season net community production in the Weddell Sea. *Polar Biol.* **31**, 101-111.

Horner, R., Ackley, S.F., Dieckmann, G.S., Gulliksen, B., Hoshiai, Legendre, L., Melnikov, I.A., Reeburgh, W.S., Spindler, M. and Sullivan, C.W. 1992. Ecology of sea ice biota 1. Habitat, terminology, and methodology. *Polar Biology* **12**, 417-427.

Horner, R., Ackley, S.F., Dieckmann, G.S., Gulliksen, B., Hoshiai, Legendre, L., Melnikov, I.A., Reeburgh, W.S., Spindler, M. and Sullivan, C.W. 1992. Ecology of sea ice biota 1. Habitat, terminology, and methodology. *Polar Biology* **12**, 417-427.

Houghton J.T., Ding Y., Griggs D.J., Noguer M., van der Linden P.J., Xiaosu D. 2001. Climate change 2001: the scientific basis. In: *Contribution of Working Group I to the Third Assessment Report of the Intergovernmental Panel on Climate Change* Cambridge University Press. 944.

Hunt, B.P.V. and Hosie, G.W. 2006. The seasonal succession of zooplankton in the Southern Ocean south of Australia, part I: The seasonal ice zone. *Deep Sea Res. I* **53**, 1182-1202.

Iglesias-Rodriguez, M.D., Halloran, P.R., Rickaby, R.E.M., Hall, I.R., Colmenero-Hidalgo, E., Gittins, J.R., Green, D.R.H., Tyrrell, T., Gibbs, S.J., von Dassow, P., Rehm, E., Armbrust, E.V. and Boessenkool, K.P. 2008. Phytoplankton calcification in a high-CO_2 world. *Science* **320**, 336-340.

IOCCP, 2007. Surface Ocean CO_2 Atlas (SOCAT). In: *Surface Ocean CO_2 Variability and Vulnerabilities Workshop.* IOCCP Report No. 7, pp. 100.

IPCC, 2007. Contribution of Working Group I of the Fourth Assessment Report of the Intergovernmental Panel on Climate Change. In: *Climate change 2007: the physical science basis* (eds. S. Solomon, D. Quin, M. Manning, Z. Chen, M. Marquis, K.B. Averyt, M. Tignor, H.L. Miller). Cambridge University Press, Cambridge, pp. 996.

Ishii, M., Inoue, H.Y., Matsueda, H. and Tanoue, E. 1998. Close coupling between seasonal biological production and dynamics of dissolved inorganic carbon in the Indian Ocean sector and the western Pacific Ocean sector of the Antarctic Ocean. *Deep-Sea Res. I* **45**, 1187-1209.

Ishii, M., Inoue, H.Y. and Matsueda, H. 2002. Net community production in the marginal ice zone and its importance for the variability of the oceanic pCO_2 in the Southern Ocean south of Australia. *Deep-Sea Res. II* **49**, 1691-1706.

Jabaud-Jan, A., Metzl, N., Brunet, C., Poisson, A. and Schauer, B. 2004. Interannual variability of the carbon dioxide system in the southern Indian Ocean (20°S-60°S): the impact of a warm anomaly in austral summer 1998. *Global Biogeochem. Cyc.* **18**, doi:10.1029/2002GB002017.

Jacques, G. and Panouse, M. 1991. Biomass and composition of size fractionated phytoplankton in the Weddell-Scotia Confluence area. *Polar Biology* **11**, 315-328.

Jeandel, C., Ruiz-Pino, D., Gjarta, E., Poisson, A., Brunet, C., Charriaud, E., Dehairs, F., Delille, D., Fiala, M., Fravalo, C., Miquel, J.C., Park, H.Y., Pondaven, P., Queguiner, B., Razouls, S., Shauer, B. and Treguer, P. 1998. KERFIX, a permanent time-series station in the Southern Ocean: a presentation. *J. Marine Sys.* **17**, 555-569.

Jennings, J.C., Gordon, L.I. and Nelson, D.M. 1984. Nutrient depletion indicates high primary productivity in the Weddell Sea. *Nature* **309**, 51-54.

Jickells, T.D., An, Z.S., Anderson, K.K., Baker, A.R., Bergametti, G., Brooks, N., Cao, J.J., Boyd, P.W., Duce, R.A., Hunter, K.A., Kawahata, H., Kubilay, N., La Roche, J., Liss, P.S., Mahowald, N., Prospero, J.M., Ridgwell, A.J., Tegen, I. and Torres, R. 2005. Global iron connections between desert dust, ocean biogeochemistry and climate. *Science* **308**, 67-71.

Jouandet, M.P., Blain, S., Metzl, N., Brunet, C., Trull, T.W. and Obernosterer, I. 2008. A seasonal carbon budget for a naturally iron-fertilised bloom over the Kerguelen Plateau in the Southern Ocean. *Deep-Sea Res. II* **55**, 856-867.

Johnson, K.M., Sieburth, J.M., Williams, P.J.L. and Brandstrom, L. 1987. Coulometric total carbon dioxide analysis for marine studies - automation and calibration. *Mar. Chem.* **21**, 117-133.

Johnson, K. S., Gordon, R., and Coale, K.H. 1997. What controls iron concentrations in the world ocean? *Marine Chem.* **57**, 137-161.

Johnson, K.S., Chavez, F.P. and Frederich, G.E. 1999. Continental-shelf sediment as a primary source of iron for coastal phytoplankton. *Nature* **398**, 697-700.

Johnson, K.S. 2001. Iron supply and demand to the upper ocean: is extraterrestrial dust a significant source of bioavailable iron? *Global Biogeochem. Cyc.* **15**, 61-63.

Jones, E.P. and Coote, A.R. 1981. Oceanic CO_2 produced by the precipitation of $CaCO_3$ from brines in sea ice. *J. Geophys. Res.* **86**, 1041-1043.

Jones, E.P., Coote, A.R. and Levy, E.M. 1983. Effect of sea ice meltwater on the alkalinity of seawater. *J. Marine Res.* **41**, 43-52.

Joos, F. and Prentice, I.C. 2004. A paleo-perspective on changes in atmospheric CO_2 and climate. In: *The Global Carbon Cycle: Integrating Humans, Climate and the Natural World, SCOPE 62* (eds. C.B. Field and M.R. Raupach). Island Press, Washington DC, pp. 165-186.

Kang, S.H., Kang, J.S., Lee, S., Chung, K.H., Kim, D. and Park, M.G. 2001. Antarctic phytoplankton assemblages in the marginal ice zone of the northwestern Weddell Sea. *J. Plankton Res.* **23**, 333-352.

Key, R.M., Kozyr, A., Sabine, C.L., Lee, K., Wanninkhof, R., Bullister, J.L., Feely, R.A., Millero, F.J., Mordy, C. and Peng, T.-H. 2004. A global ocean carbon climatology: Results from Global Data Analysis Project (GLODAP). *Global Biogeochem. Cyc.* **18**, doi:10.1029/2004GB002247.

Key, R.M., Tanhua, T., Olsen, A., Hoppema, M., Jutterström, S., Schirnick, C., van Heuven, S., Kozyr, A., Lin, X., Velo, A., Wallace, D.W.R., and Mintrop, L. 2010. The CARINA data synthesis project: introduction and overview. *Earth Syst. Sci. Data*, **2**, 105-121.

Killawee, J.A., Fairchild, I.J., Tison, J.L., Janssens, L. and Lorrain, R. 1998. Segregation of solutes and gases in experimental freezing of dilute solutions: Implications for natural glacial systems. *Geochim. Cosmochim. Acta* **62**, 3637-3655.

Klatt, O., Roether W., Hoppema M., Bulsiewicz, K., Fleischmann, U., Rodehacke, C., Fahrbach, E., Weiss, R.F. and Bullister, J.L. 2002. Repeated CFC sections at the Greenwich Meridian in the Weddell Sea. *J. Geophys. Res.* **107**, doi:10.1029/2000JC000731.

Korb, R.E. and Whitehouse, M.J., 2004. Contrasting primary production regimes around South Georgia, Southern Ocean: large blooms versus high nutrient, low chlorophyll waters. *Deep-Sea Res. I* **51**, 721-738.

Korb, R.E., Whitehouse, M.J. and Ward, P. 2004. SeaWiFS in the southern ocean: spatial and temporal variability in phytoplankton biomass around South Georgia. *Deep Sea Res. II* **51**, 99-116.

Korb, R.E., Whitehouse, M.J., Thorpe, S.E. and Gordon, M. 2005. Primary production across the Scotia Sea in relation to the physico-chemical environment. *J. Mar. Sys.* **57**, 231-249.

Korb, R.E., Whitehouse, M.J., Atkinson, A. and Thorpe, S.E. 2008. Magnitude and maintenance of the phytoplankton bloom at South Georgia: a naturally iron replete environment. *Mar. Ecol. Progr. Ser.* **368**, 75-91.

Korb, R.E., Whitehouse, M.J., Gordon, M., Ward, P. and Poulton, A.J. 2010. Summer microplankton community structure across the Scotia Sea: implications for biological carbon export. *Biogeosci.* **7**, 343-356.

Körtzinger, A., Thomas, H., Schneider, B., Gronau, N., Mintrop, L. and Duinker, J.C. 1996. An at-sea intercomparison of two newly designed underway pCO_2 systems - encouraging results. *Mar. Chem.* **52**, 133-145.

Körtzinger, A., Mintrop, L., Wallace, D.W.R., Johnson, K.M., Neill, C., Tilbrook, B., Towler, P., Inoue, H.Y., Ishii, M., Shaffer, G., Torres Saavedra, R.F., Ohtaki, E., Yamashita, E., Poisson, A., Brunet, C., Schauer, B., Goyet, C. and Eischeid, G. 2000. The international at-sea intercomparison of fCO_2 systems during the R/V Meteor Cruise 36/1 in the North Atlantic Ocean. *Mar. Chem.* **72**, 171-192.

Krembs, C. and Engel, A. 2001. Abundance and variability of microorganisms and transparent exopolymer particles across the ice-water interface of melting first-year sea ice in the Laptev Sea (Arctic). *Mar. Biol.* **138**, 173-185.

Krembs, C., Eicken, H., Junge, K. and Deming, J.W., 2002a. High concentrations of exopolymeric substances in Arctic winter sea ice: implications for the polar ocean carbon cycle and cryoprotection of diatoms. *Deep Sea Res. I* **49**, 2163-2181.

Krembs, C., Tuschling, K. and von Juterzenka, K., 2002b. The topography of the ice-water interface - its influence on the colonization of sea ice by algae. *Polar Biology* **25**, 106-117.

Lalli, C.M. and Parsons, T.R. 1997. In: *Biological Oceanography An Introduction* Butterworth Heinemann.

Lancelot, C., Mathot, S., Veth, C. and Debaar, H. 1993. Factors controlling phytoplankton ice edge blooms in the Marginal Ice Zone of the northwestern Weddell Sea during sea ice retreat 1988 - field observations and mathematical modelling. *Polar Biology* **13**, 377-387.

Lannuzel, D., Schoemann, V., de Jong, J., Tison, J.L. and Chou, L. 2007. Distribution and biogeochemical behaviour of iron in the East Antarctic sea ice. *Mar. Chem.* **106**, 18-32.

Lannuzel, D., Schoemann, V., de Jong, J., Chou, L., Delille, B., Becquevort, S. and Tison, J.L. 2008. Iron study during a time series in the western Weddell pack ice. *Mar. Chem.* **108**, 85-95.

Law, R.M., Matear, R.J. and Francey, R.J. 2008. Comment on "Saturation of the Southern Ocean CO_2 sink due to recent climate change". *Science* **319**, 570a.

Le Quéré, C. and Metzl, N. 2003. Natural processes regulating the oceanic uptake of CO_2. In: *The Global Carbon Cycle: Integrating Humans, Climate and the Natural World, SCOPE 62* (eds. C.B. Field and M.R. Raupach). Island Press, Washington DC, pp. 243-255.

Le Quéré, C., Rödenbeck, C., Buitenhuis, E.T., Conway, T.J., Langenfelds, R., Gomez, A., Labuschagne, C., Ramonet, M., Nakazawa, T., Metzl, N., Gillet, N. and Heimann, M. 2007. Saturation of the Southern Ocean CO_2 sink due to recent climate change. *Science* **316**, 1735-1738.

Lee, K., Tong, L.T., Millero, F.J., Sabine, C.L., Dickson, A.G., Goyet, C., Park, G.-H., Wanninkhof, R., Feely, R.A. and Key, R.M. 2006. Global relationships of total alkalinity with salinity and temperature in surface waters of the world's oceans. *Geophys. Res. Lett.* **33**, doi:10.1029/2006GL027207.

Lewis, E. and Wallace, D. W. R. 1998. CO2SYS-Program developed for the CO_2 system calculations. Carbon Dioxide Inf. Anal. Centre. Report ORNL/CDIAC-105.

Liss, P.S. and Slater, P.G. 1974. Flux of gases across the air-sea interface. *Nature,* **247**, 181-184.

Liss, P.S. and Merlivat, L. 1986. Air-sea gas exchange rates: Introduction and synthesis. In: *The Role of Air-Sea Gas Exchange in Geochemical Cycling,* (ed. P. Buat-Menard). Reidel, Norwell, Mass., pp. 113-127.

Locarnini, R.A., Whitworth, T. and Nowlin, W.D. 1993. The importance of the Scotia Sea on the outflow of Weddell Sea Deep Water. *J. Marine Res.* **51**, 135-153.

Löscher, B.M., de Baar, H.J.W., de Jong, J.T.M., Veth, C. and Dehairs, F. 1997. The distribution of Fe in the Antarctic Circumpolar Current. *Deep-Sea Res. II* **44**, 143-187.

Marion, G.M. 2001. Carbonate mineral solubility at low temperatures in the Na-K-Mg-Ca-H-Cl-SO_4-OH-HCO_3-CO_3-CO_2-H_2O system. *Geochim. Cosmochim. Acta* **65**, 1883-1896.

Maldonado, M. T., Boyd, P.W., Harrison, P. J. and Price, N. M. 1999. Co-limitation of phytoplankton growth by light and Fe during winter in the NE subarctic Pacific Ocean. *Deep Sea Res. II* **46**, 2475-2485.

Martin, J.H. 1990. Glacial-interglacial CO_2 change: the iron hypothesis. *Paleoceanogr.* **5**, 1-13.

McNeil, B.I., Metzl, N., Key, R.M., Matear, R.J. and Corbiere, A. 2007. An empirical estimate of the Southern Ocean air-sea CO_2 flux. *Global Biogeochem. Cyc.* **21**, doi:

McNeil, B.I. and Matear, R.J. 2008. Southern Ocean acidification: A tipping point at 450-ppm atmospheric CO_2. *PNAS* **105**, 18860-18864.

Mehrbach, C., Culberson, C.H., Hawley, J.E. and Pytkowicz, R.M. 1973. Measurement of the apparent dissociation constants of carbonic acid in seawater at atmospheric pressure. *Limnol. Oceanogr*. **18**, 897-907.

Meiners, K.M., Papadimitriou, S., Thomas, D.N., Norman, L. and Dieckmann, G.S. 2009. Biogeochemical conditions and ice algal photosynthetic parameters in Weddell Sea ice during early spring. *Polar Biology* **32**, 1055-1065.

Meredith, M.P., Murphy, E.J., Cunningham, N.J., Wood, A.G., Korb, R.E., Whitehouse, M.J., Thorpe, S.E. and Vivier, F. 2003a. An anticyclonic circulation above the Northwest Georgia Rise, Southern Ocean. *Geophys. Res. Lett.* **30**, doi:10.1029/2003GL018039.

Meredith, M.P., Watkins, J.L., Murphy, E.J., Ward, P., Bone, D.G., Thorpe, S.E., Grant, S.A. and Ladkin, R.S. 2003b. Southern ACC Front to the northeast of South Georgia: Pathways, characteristics, and fluxes. *J. Geophys. Res.* **108**, doi:10.1029/2001JC001227.

Meredith, M.P., Brandon, M.A., Murphy, E.J., Trathan, P.N., Thorpe, S.E., Bone, D.G., Chernyshkov, P.P. 2005. Variability in hydrographic conditions to the east and northwest of South Georgia. *J. Marine Sys.* **53**, 143-167.

Meredith, M.P., Naveira Garabato, A.C., Gordon, A.L. and Johnson, G.C. 2008. Evolution of the Deep and Bottom Waters of the Scotia Sea, Southern Ocean, during 1995-2005. *J. Climate* **21**, 3327-3342.

Meskhidze, N., Nenes, A., Chameides, W.L., Luo, C. and Mahowald, N. 2007. Atlantic Southern Ocean productivity: fertilization from above or below? *Global Biogeochem. Cycl.* **21**.

Metzl, N. 2009. Decadal increase of oceanic carbon dioxide in Southern Indian Ocean surface waters (1991-2007). *Deep Sea. Res. II* **56**, 607-619.

Midorikawa, T., Nemoto, K., Kamiya, H., Ishii, M. and Inoue, H.Y. 2005. Persistently strong oceanic CO_2 sink in the western subtropical North Pacific. *Geophys. Res. Lett.* **32**, L05612.

Millero, F.J. 1995. Thermodynamics of the carbon dioxide system in the Oceans. *Geochim. Cosmochim. Acta.* **59**, 661–677.

Millero, F.J. 2007. The Marine Inorganic Carbon Cycle. *Chem Rev.* **107**, 308-341.

Millero, F.J., Feistel, R., Wright, D.G. and McDougall, T.J. 2008. The composition of standard seawater and the definition of the reference-composition Salinity Scale. *Deep Sea Res.* I **55**, 50-72.

Minas, H.J. and Minas, M. 1992. Net community production in high nutrient-low chlorophyll waters of the tropical and Antarctic Oceans - grazing vs iron hypothesis. *Oceanol. Acta* **15**, 145-162.

Mitchell, B.G., Brody, E.A., Holm-Hansen, O., McClain, C. and Bishop, J. 1991. Light limitation of phytoplankton biomass and macronutrient utilization in the Southern Ocean. *Limnol. Ocean.* **36**, 1662-1677.

Montes-Hugo, M., Doney, S.C., Ducklow, H.W., Fraser, W., Martinson, D., Stammerjohn, S.E. and Schofield, O. 2009. Recent Changes in Phytoplankton Communities Assoviated with Rapid Regional Climate Change Along the Western Antarctic Peninsula. *Science* **323**, 1470-1473.

Moore, J.K., Abbot, M.R. and Richman, J.G. 1999a. Location and dynamics of the Antarctic Polar Front from satellite sea surface temperature data. *J. Geophys. Res.* **104**, 3059-3073.

Moore, J.K., Abbot, M.R., Richman, J.G., Smith, W.O., Cowles, T.J., Coale, K.H., Gardner, W.D. and Barber, R.T. 1999b. SeaWiFS satellite ocean colour data from the Southern Ocean. *Geophys. Res. Lett.* **26**, 1465-1468.

Moore, J.K. and Abbot, M.R. 2000. Phytoplankton chlorophyll distributions and primary production in the Southern Ocean. *J. Geophys. Res.* **105**, 28709-28722.

Moore, J.K. and Abbot, M.R. 2002. Surface chlorophyll concentrations in relation to the Antarctic Polar Front: seasonal and spatial patterns from satellite observations. *J. Marine Sys.* **37**, 69-86.

Morel, F. M. M., Rueter, J. G. and Price, N. M. 1991. Iron nutrition of phytoplankton and its possible importance in the ecology of ocean regions with high nutrient and low biomass. *Oceanography* **4**, 56-61.

Morin, S., Marion, G.M., von Glasow, R., Voisin, D., Bouchez, J. and Savarino, J. 2008. Precipitation of salts in freezing seawater and ozone depletion events: a status report. *Atmos. Chem. Phys.* **8**, 7317-7324.

Mucci, A. 1983. The solubility of calcite and aragonite in seawater at various salinities, temperatures and on atmosphere total pressure. *Amer. J. Sci.* **283**, 780–799.

Naveira Garabato, A.C., Heywood, K.J. and Stevens, D.P. 2002a. Modification and pathways of Southern Ocean Deep Waters in the Scotia Sea. *Deep-Sea Res. I* **49**, 681-705.

Naveira Garabato, A.C., Strass, V.H. and Kattner, G. 2002b. Fluxes of nutrients in a three-dimensional meander structure of the Antarctic Polar Front. *Deep-Sea Res. II* **49**, 3771-3792.

Naveira Garabato, A.C., Stevens, D.P., Watson, A.J. and Roather, W. 2007. Short-circuiting of the overturning circulation in the Atlantic Circumpolar Current. *Nature* **447**, 194-197.

Nielsdóttir, M.C., Moore, C.M., Sanders, R., Hinz, D.J. and Achterberg, E.P. 2009. Iron limitation of the postbloom phytoplankton communities in the Iceland Basin. *Global Biogeochem. Cyc.* **23**, doi:10.1029/2008GB003410.

Nighingale, P.D., Malin, G., Law, C.S., Watson, A.J., Liss, P.S., Liddicoat, M.I., Boutin, J. and Upstill-Goddard, R.C. 2000. In situ evaluation of air-sea gas exchange parameterizations using novel conservative and volatile tracers. *Global Biogeochem. Cyc.* **14**, 373-387.

Nomura, D., Inoue, H.Y. and Yoyota T. 2006. The effect of sea-ice growth on air-sea CO_2 flux in a tank experiment. *Tellus* **58B**, 418-426.

Nolting, R.F., de Baar, H.J.W., Vanbennekom, A.J. and Masson, A. 1991. Cadmium, copper and iron in the Scotia Sea, Weddell Sea and Weddell Scotia Confluence (Antarctica). *Mar. Chem.* **35**, 219-243.

Nowlin, W.D. and Klinck, J.M. 1986. The physics of the Antarctic Circumpolar Current. *Rev. Geophys.* **24**, 469-491.

O'Reilly, J. E., Maritorena, S., Mitchell, B.G., Siegel, D.A., Carder, K.L., Garver, S.A., Kahru, M. and McClain, C. 1998. Ocean color chlorophyll algorithms for SeaWiFS. *J. Geophys. Res.* **103**, 24,937-24,953.

Orr, J.C., Fabry, V.J., Aumont, O., Bopp, L., Doney, S.C., Feely, R.A., Gnanadesikan, A., Gruber, N., Ishida, A., Joos, F., Key, R.M., Lindsay, K., Maier-Reimer, E., Matear, R., Monfray, P., Mouchet, A., Najjar, R.G., Plattner, G.-K., Rodgers, K.B., Sabine, C.L., Sarmiento, J.L., Schlitzer, R., Slater, R.D., Totterdall, I.J., Weirig, M.-F., Yamananka,

Y. and Yool, A. 2005. Anthropogenic ocean acification over the twenty-first century and its impact on calcifying organisms. *Nature* **437**, 681-686.

Orsi, A.H., Nowlin, W.D. and Whitworth, T. 1993. On the circulation and stratification of the Weddell Gyre. *Deep-Sea Res. I* **40**, 169-203.

Orsi, A.H., Whitworth, T. and Nowlin, W.D. 1995. On the meridional extent and fronts of the Antarctic Circumpolar Current. *Deep-Sea Res. I* **42**, 641-673.

Orsi, A.H., Johnson, G.C. and Bullister, J.L. 1999. Circulation, mixing, and production of Antarctic Bottom Water. *Progr. Oceanogr.* **43**, 55-109.

Papadimitriou, S., Kennedy, H., Kattner, G., Dieckmann, G.S. and Thomas, D.N. 2003. Experimental evidence for carbonate precipitation and CO_2 degassing during sea ice formation. *Geochim. Cosmochim. Acta* **68**, 1749-1761.

Papadimitriou, S., Thomas, D.N., Kennedy, H., Haas, C., Kuosa, H. and co-authors. 2007. Biogeochemical composition of natural sea ice brines from the Weddell Sea during early austral summer. *Limnol. Oceanogr.* **52**, 1809-1823.

Park, Y.-H. and Gamberoni, L. 1995. Large scale circulation and its variability in the south Indian Ocean. *J. Geophys. Res.* **100**, 24911-24930.

Park, Y.-H., Charriaud, E. and Fieux, M. 1998. Thermohaline structure of the Antarctic Surface Water/Winter Water in the Indian sector of the Southern Ocean. *J. Marine Sys.* **17**, 5-23.

Parsons, T.R., Maita, Y., Lalli, C.M. 1984. In: *A manual of chemical and biological methods for seawater analysis*. Pergamon Press, Oxford, 1-173 pp.

Patterson, S.L. and Sievers, H.A. 1980. The Weddell-Scotia Confluence. *J. Phys. Oceanogr.* **10**, 1584-1610.

Planquette, H., Statham, P.J., Fones, G.R., Charette, M.A., Moore, C.M., Salter, I., Nédélec, F.H., Taylor, S.L., French, M., Baker, A.R., Mahowald, N. and Jickells, T.D. 2007. Dissolved iron in the vicinity of the Crozet Islands, Southern Ocean. *Deep-Sea Res. II* **54**, 1999-2019.

Pollard, R.T. and Read, J.F. 2001. Circulation pathways and transports of the Southern ocean in the vicinity of the Southwest Indian Ridge. J. Geophys. Res. **106**, 2881-2898.

Pollard, R.T., Lucas, M.I. and Read, J.F. 2002. Physical controls on biogeochemical zonation in the Southern Ocean. *Deep-Sea Res. II* **49**, 3289-3305.

Pollard, R.T., Sanders, R., Lucas, M.I. and Statham, P.J. 2007. The Crozet Natural Iron Bloom and Export Experiemt (CROZEX). *Deep-Sea Res. II* **54**, 1905-1914.

Pondaven, P., Ragueneau, O., Tréguer, P., Hauvespre, A., Dezileua, L. and Reyss, J.L. 2000. Resolving the 'opal paradox' in the Southern Ocean. *Nature* **405**, 168-172.

Priddle, J., Boyd, I.L., Whitehouse, M.J., Murphy, E.J. and Croxall, J.P. 1998. Estimates of Southern Ocean primary production - constraints from predator carbon demand and nutreint drawdown. *J. Marine Sys.* **17**, 275-288.

Raven, J. A. 1990. Predictions of MN and Fe use Efficiencies of Phototrophic Growth as a Function of Light Availability for Growth and of C Assimilation Pathway. *New Phytologist* **116**, 1-18.

Reay, D.S., Priddle, S.J., Nedwell, D.B., Whitehouse, M.J., Ellis-Evans, J.C., Dueubert, C. and Connelly, D.P. 2001. Regulation by low temperature of phytoplankton growth and nutrient uptake in the Southern Ocean. *Marine Ecol. Prog. Ser.* **219**, 51-64.

Reid, J.L., Nowlin Jr., W.D. and Patzert, W.C. 1977.On the characteristics and circulation of the southwestern Atlantic Ocean. *J. Phys. Ocean.* **7**, 62-91.

Redfield, A.C., Ketchum, B.H. and Richards, F.A. 1963. The influence of organisms on the composition of seawater. In: *The Sea. Vol. 2. The Composition of Seawater* (ed. M.N. Hill). Wiley, New York, pp. 26-77.

Reid, J.L., Nowlin, W.D. and Patzert, W.C. 1977. On the characteristics and circulation of the southwestern Atlantic Ocean. *J. Phys. Ocean.* **7**, 62-91.

Revelle, R. and Suess, H.E. 1957. Carbon dioxide exchange between atmosphere and ocean and the question of an increase of atmospheric CO_2 during the past decades. *Tellus* **9**, 18-27.

Riebesell, U., Zondervan, I., Rost, B., Tortell, P.D., Zeebe, R.E. and Morel, F.M.M. 2000. Reduced calcification of marine plankton in response to increased atmospheric CO_2. *Nature* **407**, 364-367.

Rintoul, S.R. and Sokolov, S. 2001. Baroclinic transport variability of the Antarctic Circumpolar Current south of Australia (WOCE repeat section SR3). *J. Geophys. Res.* **106**, 2815-2832.

Rio, M.-H. and Hernandez, F. 2004. A mean dynamic topography computed over the world ocean from altimetry, in situ measurements, and a geoid model. *J. Geophys. Res.* **109**, doi:10.1029/2003JC002226.

Robertson, J.E. and Watson, A.J. 1992. Thermal skin effect of the surface ocean and its implications for CO_2 uptake. *Nature* **358**, 738-740.

Robinson, I.S., Wells, N.C., and Charnock, H. 1984. The sea surface thermal boundary layer and its relevance to the measurement of sea surface temperature by airborne and spaceborne radiometers. *Int. J. Rem. Sens.* 5, 19-45.

Royal Society. 2005. Ocean acidification due to increasing atmospheric carbon dioxide. Policy Document 12/05, The Royal Society, London. pp. 60.

Rubin, S.I., Takahashi, T., Chipman, D.W. and Goddard, J.G. 1998. Primary productivity and nutrient utilization ratios in the Pacific sector of the Southern Ocean based on seasonal changes in seawater chemistry. *Deep-Sea Res. I* **45**, 1211-1234.

Rutgers van der Loeff, M.M., Friedrich, J and Bathmann, U.V. 1997. Carbon export during the Spring Bloom at the Antarctic Polar Front, determined with the natural tracer ^{234}Th. *Deep-Sea Res. II* **44**, 457-478.

Rysgaard, S., Glud, R.N., Sejr, M.K., Bendtsen, J. and Christensen, P.B. 2007. Inorganic carbon transport during sea ice growth and decay: A carbon pump in polar seas. *J. Geophys. Res.* **112**, doi:10.1029/2006JC003572.

Rysgaard, S., Bendtsen, J., Pedersen, L.T., Ramlov, H. and Glud, R.N. 2009. Increased CO_2 uptake due to sea ice growth and decay in Nordic Seas. *J. Geophys. Res.* **114**, doi:10.1029/2008JC005088.

Sabine, C.L., Feely, R.A., Gruber, N., Key, R.M., Lee, K., Bullister, J.L., Wanninkhof, R., Wong, C.S., Wallace, D.W.R., Tilbrook, B., Millero, F., Peng, T.-H., Kozyr, A., Ono, T. and Rios, A. 2004. The oceanic sink for Anthropogenic CO_2. *Science* **305**, 367-371.

Sarmiento, J.L., Hughes, T.M.C., Stouffer, R.J. and Manabe, S. 1998. Simulated response of the ocean carbon cycling to anthropogenic carbon warming. *Nature* **393**, 245.

Sarmiento, J.L. and Gruber, N. 2006. *Ocean Biogeochemical Dynamic* Princeton University Press. Princeton, pp. 1-503.

Sarmiento, J.L. and Toggweiler, R. 1984. A new model for the role of the oceans in dtermining atmospheric pCO_2. *Nature* **308**, 621-624.

Sakshaug, E., Slagstad, D. and Holm-Hansen, O. 1991. Factors controlling the development of phytoplankton blooms in the Antarctic Ocean - a mathematical model. *Mar. Chem.* **35**, 259-271.

Sanudo-Wilhelmy, S.A., Olsen, K.A., Scelfo, J.M., Foster, T.D. and Flegal, A.R. 2002. Trace metal distributions off the Antarctic Peninsula in the Weddell Sea. *Mar. Chem.* **77**, 157-170.

Schlitzer, R. 2002. Carbon export fluxes in the Southern Ocean: results from inverse modelling and comparison with satellite based estimates. *Deep-Sea Res. II* **49**, 1623-1644.

Schröder, M. and Fahrbach, E. 1999. On the structure and the transport of the eastern Weddell Gyre. *Deep-Sea Res. II* **46**, 501-527.

Schuster, U. and Watson, A.J. 2007. A variable and decreasing sink for atmospheric CO_2 in the North Atlantic. *J. Geophys. Res.* **112**, doi:10.1029/2006JC003941.

Sedwick, P.N. and DiTullio, G.R. 1997. Regulation of algal blooms in Antarctic shelf waters by the release of iron from melting sea ice. *Geophys. Res. Lett.* **24**, 2515-2518.

Sedwick, P.N., DiTullio, G.R. and Mackay, D.J. 2000. Iron and manganese in the Ross Sea, Antarctica: seasonal iron limitation in Antarctic shelf waters. *J. Geophys. Res.* **105**, 11321-11336.

Semiletov, I., Makshtas, A., Akasofu, S.I. and Andreas, E.L. 2004. Atmospheric CO_2 balance: The role of Arctic sea ice. *Geophys. Res. Lett.* **31**, L05121.

Shim, J., Kang, Y.C., Kim, D. and Choi, S.-H. 2006. Distribution of net community production and surface pCO_2 in the Scotia Sea, Antarctica, during austral spring 2001. *Mar. Chem.* **101**, 68-84.

Siegenthaler, U. and Wenk, T. 1984. Rapid atmospheric CO_2.variations and ocean circulartion *Nature* **308**, 624-626.

Siegenthaler, U., Stocker, T.F., Monnin, E., Luethi, D., Schwander, J., Stauffer, B., Raynaud, D., Barnola, J.M., Fischer, H., Masson-Delmotte, V. and Jouzel, J. 2005. Stable carbon cycle-climate relationship during the late Pleistocene. *Science* **310**, 1313-1317.

Sievers, H.A. and Nowlin, W.D. 1984. The stratification and water masses at Drake Passage. *J. Geophys. Res.* **89**, 489-514.

Smetacek, V., de Baar, H.J.W., Bathmann, U.V., Lochte, K. and Rutgers van der Loeff, M.M. 1997. Ecology and biogeochemistry of the Antarctic Circumpolar Current during austral spring: a summary of Southern Ocean JGOFS cruise ANT X/6 of RV *Polarsten*. *Deep-Sea Res. II* **44**, 1-21.

Smith, I.J., Stevens, D.P., Heywood, K.J. and Meredith, M.P. 2010. The flow of the Antarctic Circumpolar Current over the North Scotia Ridge. *Deep-Sea Res. I* **57**, 14-28.

Smith, K.L., Robinson, B.H., Helly, J.J., Kaufmann, R.S., Ruhl, H.A., Shaw, T.J., Twining, B.S. and Vernet, M. 2007. Free-drifting icebergs: Hot spots of chemical and biological enrichment in the Weddell Sea. *Science* **317**, 478-482.

Smith, R.C., Martinson, D.G., Stammerjohn, S.E., Iannuzzi, R.A. and Ireson, K. 2008. Bellingshausen and western Antarctic Peninsula region: Pigment biomass and sea ice spatial/ temporal distributions and interannual variability. *Deep Sea Res. II* **55**, 1949-1963.

Smith, W.O. and Nelson, D.M. 1985. Phytoplankton bloom produced by a receding ice edge in the Ross Sea - spatial coherence with the density field. *Science* **227**, 163-166.

Smith, W.O. and Nelson, D.M. 1986. Importance of ice edge phytoplankton production in the Southern Ocean. *Bioscience* **36**, 251-257.

Smith, W.O. and Comiso, J.C. 2008. Influence of sea ice on primary productivity in the Southern Ocean: A satellite perspective. *J. Geophys. Res.* **113**, doi:10.1029/2007JC004251.

Sokolov, S. and Rintoul, S.R. 2007. On the relationship between fronts of the Antarctic Circumpolar Current and surface chlorophyll concentrations in the Southern Ocean. *J. Geophys. Res.* **112**, doi:10.1029/2006JC004072.

Stark, J.D., Donlon, C.J., Martin, M.J. and McCulloch, M.E. 2007. OSTIA: An operational, high resolution, real time, global sea surface temperature analysis system. In: *Marine Challenges: coastline to deep sea*. Conference proceedings. Oceans '07 IEEE Aberdeen.

Strass, V.H., Naveira Garabato, A.C., Pollard, R.T., Fischer, H.I., Hense, I., Allen, J.T., Read, J.F., Leach, H. and Smetacek, V. 2002. Mesoscale frontal dynamics: shaping the environment of primary production in the Antarctic Circumpolar Current. *Deep-Sea Res. II* **49**, 3735-3769.

Strzepek, R.F. and Harrison, P.J. 2004. Photosynthetic architecture differs in coastal and oceanic diatoms. *Nature* **431**, 689-692.

Stoll, M.H.C., de Baar, H.J.W., Hoppema, M. and Fahrbach, E. 1999. New early winter fCO_2 data reveal continuous uptake of CO_2 by the Weddell Sea. *Tellus* **51B**, 679-687.

Stoll, M.H.C., Thomas, H., de Baar, H.J.W., Zondervan, I.,de Jong, E., Bathmann, U.V. and Fahrbach, E. 2002. Biological versus physical processes as drivers of large oscillations of the air-sea CO_2 flux in the Antarctic marginal ice zone during summer. *Deep-Sea Res. I* **49**, 1651-1667.

Sunda, W. G. and Huntsman, S. A. 1997. Interrelated influence of iron, light and cell size on marine phytoplankton growth. *Nature* **390**, 389-392.

Sweeney, C., Smith, W.O., Hales, B., Bidigare, R.R., Carlson, C.A., Codispoti, L.A., Gordon, L.I., Hansell, D., Millero, F.J., Park, M.-O.K. and Takahashi, T. 2000. Nutrient and carbon removal ratios and fluxes in the Ross Sea, Antarctica. *Deep-Sea Res. II* **47**, 3395-3421.

Sweeney, C., Gloor, E., Jacobson, A.R., Key, R.M., McKinley, G., Sarmiento, J.L. and Wanninkhof, W. 2007. Constraining global air-sea gas exchange for CO_2 with recent bomb ^{14}C measurments. *Global Biogeochem. Cyc.* **21**, doi:10.1029/2006GB002784.

Tagliabue, A., Bopp, L., Dutay, J.C., Bowie, A.R., Chever, F., Jean-Baptiste, P., Bucciarelli, E., Lannuzel, D., Remenyi, T., Sarthou, G., Aumont, O., Gehlen, M and Jeandel, C. 2010. Hydrothermal contribution to the oceanic dissolved iron inventory. *Nature Geosci.* **3**, 252-256.

Takahashi, T., Olafsson, J., Goddard, J.G., Chipman, D.W. and Sutherland, S.C. 1993. Seasonal variation of CO_2 and nutrients in the high latitude surface oceans - a comparative-Study. *Global Biogeochem. Cyc.* **7**, 843-878.

Takahashi, T., Sutherland, S.C., Sweeney, C., Poisson, A., Metzl, N., Tilbrook, B., Bates, N., Wanninkhof, R., Feely, R.A., Sabine, C.L., Olafsson, J. and Nojiri, Y. 2002. Global sea-air CO_2 flux based on climatological surface ocean pCO_2, and seasonal biological and temperature effects. *Deep Sea Res. II* **49**, 1601-1622.

Takahashi, T., Sutherland, S.C., Wanninkhof, R., Sweeney, C., Feely, R.A., Chipman, D.W., Hales, B., Friederich, G., Chavez, F., Sabine, C.L., Watson, A.J., Bakker, D.C.E., Schuster, U., Metzl, Yoshikawa-Inoue, H., Ishii, M., Midorikawa, T., Nojiri, Y., Körtzinger, Steinhoff, T., Hoppema, M., Olafsson, J., Arnarson, T.S., Tilbrook, B., Johannessen, T., Olsen, A., Bellerby, R., Wong, C.S., Delille, B., Bates, N.R. and de Baar, H.J.W.. 2009. Climatological mean and decadal change in surface ocean pCO_2, and net sea-air CO_2 flux over the global oceans. *Deep-Sea Res. II* **56**, 554-577.

Timmermans, K.R., Gerringa, L.J.A., de Baar, H.J.W., van der Wagt, B., Veldhuis, M.J.W., de Jong, J.T.M. and Croot, P.L. 2001. Growth rates of large and small Southern Ocean diatoms in relation to availability of iron in natural seawater. *Limnol. Ocean.* **46**, 260-266.

Thoning, K.W., Tans, P.P. and Komhyr, W.D. 1989. Atmospheric Carbon-Dioxide at Mauna Loa Observatory 2. Analysis of the NOAA GMCC Data, 1974-1985. *J. Geophys. Res.* **94**, 8549-8565.

Thorpe, S.E., Heywood, K.J., Brandon, M.A. and Stevens, D.P. 2002. Variability of the Southern Antarctic Circumpolar Current Front north of South Georgia. *J. Mar. Sys*., **37**, 87-105.

Trathan, P.N., Brandon, M.A., Murphy, E.J. and Thorpe, S.E. 1997. Characterisation of the Antarctic Polar Frontal Zone to the north of South Georgia in summer 1984. *J. Geophys. Res.* **102**, 10483-10497.

Tranter, D.J. 1982. Interlinking of physical and biological processes in the Antarctic Ocean. *Ocean. Marine Biol. Ann. Rev.* **20**, 11-35.

Trembaly, J.E., Lucas, M.I., Kattner, G., Pollard, R., Strass, V.H., Bathmann, U. and Bracher, A. 2002. Significance of the Polar Frontal Zone for large-sized diatoms and new production during summer in the Atlantic sectror of the Southern Ocean. *Deep Sea Res. II* **49**, 3793-3811.

Tynan, C.T. 1998. Ecological importance of the Southern Boundary of the Antarctic Circumpolar Current. *Nature* **392**, 708-710.

van Oijen, T., van Leeuwe, M.A., Granum, E., Weissing, F.J., Bellerby, R.G.J., Gieskes, W.W.C. and da Baar, H.J.W. 2004. Light rather than iron controls photosynthate production and allocation in Southern Ocean phytoplankton populations during austral summer. *J. Plankton Res.* **26**, 885-900.

Venables, H.J. 2007. PhD Thesis. *Physical controls on the distribution of phytoplankton around the Crozet Plateau, Southern Ocean*. University of Southampton, pp. 242.

Vernet, M., Martinson, D., Ianuzzi, R., Stammerjohn, S., Kozlowski, W., Sines, K., Smith, R. and Garibotti, I. 2008. Primary production within the sea-ice zone west of the Antarctic Peninsula: 1-Sea ice, summer mixed layer and irradiance. *Deep Sea Res. II* **55**, 2068-2085.

Wallace, D.W.R. 2001. In: *Ocean circulation and Climate* (eds. G. Siedler, J. Church, W.J. Gould). Academic Press, San Diego, pp. 489-521.

Wanninkhof, R. 1992. Relationship between wind speed and gas exchange over the ocean. *J. Geophys. Res.* **97**, 7373-7382.

Ward, P., Whitehouse, M.J., Meredith, M., Murphy, E., Shreeve, R., Korb, R.E., Watkins, J., Thorpe, S., Woodd-Walker, R., Brierley, A., Cunningham, N., Grant, S. and Bone D. 2002. The Southern Antarctic Circumpolar Current Front: physical and biological coupling at South Georgia. *Deep-Sea Res. I* **49**, 2183-2202.

Watson, A.J., Bakker, D.C.E., Ridgwell, A.J., Boyd, P.W. and Law, C.S. 2000. Effect of iron supply on Southern Ocean CO_2 uptake and implications for glacial atmospheric CO_2. *Nature* **407**, 730-733.

Watson, A.J. and Orr, J.C. 2003. Carbon dioxide fluxes in the global ocean. In: *Ocean Biogeochemistry: The role of the Ocean Carbon Cycle in Global Change* (ed. M.J.R. Fasham). Springer-Verlag, Berlin.

Wefer, G. and Fischer, G. 1991. Annual primary production and export flux in the Southern Ocean from sediment trap data. *Marine Chem.* **35**, 597-613.

Weiss, R.F., Ostlund, H.G. and Craig, H. 1979. Geochemical studies of the Weddell Sea. *Deep-Sea Res.* **26**, 1093-1120.

Weiss, R.F. and Price, B.A. 1980. Nitrous-Oxide Solubility in Water and Seawater. *Marine Chem.* **8**, 347-359.

Whitehouse, M.J., Priddle, J. and Symon, C. 1996. Seasonal and annual change in seawater temperature, salinity, nutrient and chlorophyll a distributions around South Georgia, South Atlantic. *Deep Sea Res. I* **43**, 425-443.

Whitehouse, M.J., 1997. In: *Automated seawater nutrient chemistry*. British Antarctic Survey, Cambridge, pp. 1-14.

Whitehouse, M.J., Priddle, J. and Brandon, M.A. 2000. Chlorophyll/ nutrient characteristics in the water masses to the north of South Georgia, Southern Ocean. *Polar Biology* **23**, 373-382.

Whitehouse, M.J., Korb, R.E., Atkinson, A., Thorpe, S.E. and Gordon, M. 2008. Formation, transport and decay of an intense phytoplankton bloom within the high-nutrient low-chlorophyll belt of the Southern Ocean. *J. Mar. Sys.* **70**, 150-167.

Whitworth, T. and Nowlin, W.D. 1987. Water masses and currents of the Southern Ocean at the Greenwich Meridian. *J. Geophys. Res.* **92**, 6462-6476.

Whitworth, T., Nowlin, W.D., Orsi, A.H., Locarnini, R.A. and Smith, S.G. 1994. Weddell Sea shelf water in the Bransfield Strait and Weddell-Scotia Confluence. *Deep-Sea Res. I* **41**, 629-641.

Wu, Y., Peterson, I.K., Tang, C.L., Platt, T., Sathyendranath, S. and Yago-Fuentes, C. 2007. The impact of sea ice on the initiation of the spring bloom on the Newfoundland and Labrador Shelves. *J. Plankton Res.* **29**, 509-514.

Zeebe, R.E. and Wolf-Gladrow, D.A. 2001. Equilibrium. In: *CO_2 in Seawater: Equilibrium, Kinetics, Isotopes* (ed. D. Halpern). Elsevier, Amsterdam, pp. 1-83.

Zickfeld, K., Fyfe, J.C., Saenko, O.A., Eby, M. and Weaver, A.J. 2007. Response of the global carbon cycle to human-induced changes in Southern Hemisphere winds. *Geophys. Ress. Lett.* **34**, doi:10.1029/2006GL028797.

Zickfeld, K., Fyfe, J.C., Eby, M. and Weaver, A.J. 2008. Comment on "Saturation of the Southern Ocean CO_2 sink due to recent climate change". *Science* **319**, 570b.